Large Electroweak Corrections to Heavy WIMP Dark Matter Annihilation and Resummation

Kai Urban

Dissertation

Physik–Department T31
Technische Universität München

TECHNISCHE UNIVERSITÄT MÜNCHEN

Large Electroweak Corrections to Heavy WIMP Dark Matter Annihilation and Resummation

Kai Urban

Vollständiger Abdruck der von der Fakultät für Physik der Technischen Universität München zur Erlangung des akademischen Grades eines

Doktors der Naturwissenschaften

genehmigten Dissertation.

Vorsitzende:		Prof. Dr. Susanne Mertens
Prüfer der Dissertation:	1.	Prof. Dr. Martin Beneke
	2.	Prof. Dr. Alejandro Ibarra

Diese Dissertation wurde am 13.04.2021 bei der Technischen Universität München eingereicht und durch die Fakultät für Physik am 03.06.2021 angenommen.

Large Electroweak Corrections to Heavy WIMP Dark Matter Annihilation and Resummation

Große elektroschwache Korrekturen zu schwerer WIMP Dunkelmaterieannihilation und -resummation

Kai Urban

Abstract

In this thesis, we investigate large electroweak corrections to heavy WIMP dark matter annihilation. We calculate the one-loop potentials for arbitrary standard model representations in order to evaluate the non-relativistic Sommerfeld effect at NLO. Furthermore, we consider the resummation of electroweak Sudakov logarithms in the semi-inclusive $\chi^0\chi^0 \to \gamma + X$ annihilation process for wino and Higgsino dark matter to the NLL' order and combine both corrections to provide the most precise cross-section predictions to date.

Zusammenfassung

In dieser Dissertation werden elektroschwache Korrekturen zu schwerer WIMP Dunkelmaterieannihilation betrachtet. Wir untersuchen die Ein-Schleifenpotentiale für allgemeine Modelle mit beliebigen Standardmodelldarstellungen um den nicht-relativistischen Sommerfeldeffekt zu NLO zu bestimmen. Desweiteren betrachten wir die Resummation elektroschwacher Sudakovlogarithmen im semi-inklusiven $\chi^0\chi^0 \to \gamma + X$ Annihilationsprozess für wino und Higgsino Dunkelmaterie zur NLL' Ordnung und kombinieren beide Korrekturen zur präzisest bekannten Wirkungsquerschnittvorhersage.

Contents

1

Introduction

1.1 Dark matter - Evidence and properties

The nature of dark matter (DM) is certainly among the greatest unknowns in modern-day physics. The evidence for its existence ranges from the observation of velocity dispersions of galaxies and the finding that the dispersion is far too large to be supported by luminous matter only [1] in the 1930s, all the way to modern observations of the cosmic microwave background (CMB) [2]. It was the former observation, for which as a hypothetical explanation, a new non-luminous matter component was introduced, that was termed *Dunkle Materie* (dark matter) [1]. Today, the evidence for the existence of DM is overwhelming. The effect of DM can e.g., be observed in rotation curves [3, 4], strong [5] and weak [6] gravitational lensing, baryonic acoustic oscillations [7], the bullet cluster [8], to just list a few measurements.

It is surprising that despite the many observational hints, little is known about DM beyond its gravitational interaction. Among the empirically constrained properties is its electric charge, which has to vanish for the DM to be "dark",[1] the DM self-interactions [10], its lifetime being on cosmological timescales [11], and some model-independent constraints on the dark matter mass. However, without assuming a specific DM model, still a huge mass region is possible, ranging from dark matter masses of $m_\chi \sim 10^{-22}\,\text{eV}$ [12] to up to solar masses [13, 14] (for a more detailed discussion of model-independent constraints, we refer to the plethora of DM reviews in the literature, e.g., [15] and references therein).

A further property to which dark matter is typically classified is its velocity at the time of thermal decoupling. Simulations of large scale structure (LSS) formation can exclude hot (relativistic) dark matter as the dominant DM component [16]. To match the observed structure, cold dark matter (CDM), i.e., non-relativistic DM at the decoupling time or at most warm DM, is needed [17]. The reason CDM is very successful in the description of structure formation lies in the fact that after decoupling, density perturbations rise linearly, causing structures to grow hierarchically from small to large scales, in agreement with observations [18]. However, it has to be mentioned that there are some small-scale structure problems whose resolution is unclear within the CDM paradigm [19, 20].

Nevertheless, the relic abundance of DM in the concordance model of cosmology ΛCDM [17], is measured by the Planck satellite [2]

$$\Omega_{\text{DM}} h^2 = 0.120 \pm 0.001 \tag{1.1}$$

to an accuracy of better than a percent, where h is the Hubble constant in units of $100\,\text{km/s}\,\text{Mpc}$.

---

[1] In principle, there is also the possibility of "milli-charged dark matter". However, rather stringent bounds on the "milli-electric" charge exist [9].

The value implies about five times more dark matter than ordinary baryonic matter, with the rest of the energy budget of the universe essentially made up by dark energy.

1.2 The WIMP as a dark matter candidate

Despite the highly accurate knowledge of the DM density today, little is known of its particle physics properties.[2] Large mass ranges spanning over dozens of orders of magnitude are still possible, and a plethora of models can reproduce the observed abundance [23, 24]. Therefore, it is only natural to take some kind of guidance from other parts of physics to motivate possible dark matter candidates that also address further problems existing in cosmology, astro- or particle physics. On the particle physics side, two candidates have received particular attention over the last decades, as they also address some unknowns in particle physics. One is the axion and its connection to the strong CP problem [25, 26, 27], whilst the second being the weakly interacting massive particle (WIMP) (for a review, see, e.g., [28]).

For WIMPs, as for many other DM candidates, the relic abundance is set by the "freeze-out" mechanism [17, 29], assuming the standard cosmological evolution. In short, it is assumed that the dark matter is in thermal equilibrium with the SM plasma at some point in the early universe. As the expansion of the universe progresses, temperatures start to fall, and at some time, the annihilation and creation rates of the DM are of the size of the expansion rate of the universe, the Hubble rate. At this point, the DM annihilation ceases as the DM effectively does not see each other anymore; the abundance "freezes-out". Under usual assumptions for DM, the observed abundance is reproduced if the following relation between relic density and annihilation cross-section of the DM holds [17, 30][3]

$$\Omega_{\mathrm{DM}} h^2 \approx 0.1 \cdot \left(\frac{3 \cdot 10^{-26} \mathrm{cm}^3 \mathrm{s}^{-1}}{\langle \sigma v \rangle} \right) . \tag{1.2}$$

Any weak scale particle is naturally in the right ballpark for the cross-section $\langle \sigma v \rangle$. The numerical coincidence of the equality of weak-scale and freeze-out cross-section is also known as "WIMP miracle" [31], even though there is no connection between the abundance calculation and the electroweak scale. However, in particle physics, there are unresolved issues that hint at new physics around the weak or TeV-scale. This new physics typically also provides a dark matter candidate with the right abundance.

One of these issues that have sparked interest in new physics around the weak scale for decades is known as the electroweak hierarchy problem [32, 33]. In the standard model of particle physics (SM), the Higgs mass is described by a relevant operator, meaning it receives large quantum corrections under renormalization group evolution from large to small energies. Therefore, considerable fine-tuning is needed to find the Higgs mass at its observed value and not at the Planck scale (or any new physics scale above the electroweak scale), that one would naively expect to dominate the loop corrections.[4] Albeit a purely aesthetic criterion, the hierarchy problem has served as a guiding principle for beyond standard model (BSM) research over the past decades. Among the most popular resolutions of the hierarchy problem is certainly the concept

---

[2] This, of course, assumes dark matter to be some kind of particle. While also further possibilities exist that aim to explain the same observations as dark matter, e.g., modifying gravity [21] or dark matter from primordial black holes [22], at the present day, particle dark matter seems to be the most likely explanation for the observed missing mass problem.

[3] Up to corrections and refinements discussed at later stages of this thesis.

[4] Note that strictly speaking the hierarchy problem cannot be formulated within the Standard Model, as the Higgs mass is not calculable in the SM.

of supersymmetry (SUSY), which solves the hierarchy problem by introducing superpartners to the SM particles (for a review of SUSY, see, e.g., [34]). These superpartners are bosonic for the SM fermions and fermionic for the SM bosons, which means that they provide a correction to the Higgs mass of exactly opposite sign to the SM contribution. As long as the SUSY mass scale is not too large, this keeps the corrections to the Higgs mass small.

Furthermore, SUSY, in particular the minimal supersymmetric standard model (MSSM), provides WIMPs naturally as dark matter [31]. The usual candidates are the superpartners of the SM gauge sector, namely the wino, bino as partners of the electroweak gauge bosons and the Higgsinos as superpartners of the SM Higgs doublet. The four neutral Majorana fermions and two charged Dirac fermions that arise after electroweak symmetry breaking (EWSB) are called neutralinos and charginos. The lightest of the neutralinos represents a “textbook-like” WIMP candidate that would be produced by a freeze-out mechanism and reproduces the observed relic abundance for masses at the $\mathcal{O}(100\,\text{GeV})$ to a few TeV of DM mass m_χ [35, 36].

Limits of pure wino, Higgsino, bino are interesting, as they require a minimal set of parameters. If DM, for instance, would be a pure wino (with all other SUSY states decoupled), there is only one free parameter, the DM mass m_χ. Furthermore, if one assumes that the pure wino makes up all DM, m_χ is uniquely fixed.

Taking a more minimalistic perspective, the wino and Higgsino also appear in the context of “minimal dark matter” [37, 38]. The notion of minimal dark matter adds an extra SU(2) multiplet with minimal spin, isospin and hypercharge to the SM. The properties of these additions required for “minimal” dark matter are that the lightest component of the new multiplet is electrically neutral after EWSB and stable on cosmological scales. Furthermore, the interactions of the multiplet are only with the SM gauge group, i.e., only the mass of the dark matter is a free parameter. The multiplet size is constrained if a Landau pole in α_2 is to be avoided below the GUT/Planck scale [37]. The wino, as an $\text{SU}(2)_L$ triplet of Majorana fermions, and the Higgsino, as a doublet with hypercharge $Y = 1/2$, fall naturally into this larger class of models.[5]

1.3 Detection methods for electroweak WIMP dark matter

Typically, the experiments searching for WIMPs can be associated with three kinds of detection mechanisms: First dark matter production, e.g. at a collider such as the Large Hadron Collider (LHC), secondly direct detection, i.e. the scattering of dark matter at nuclear targets, and lastly, so-called indirect detection that maps the products of dark matter annihilation in astrophysical observations, e.g., photons or electrons. The typical thermal masses for the two primary models discussed in this thesis, the pure wino and Higgsino, are in the TeV-range, at around $(2.8-3)$ TeV or 1.1 TeV, respectively [36, 38, 39, 40].

For the electroweak WIMPs, the production and detection at a high-energy collider is a difficult task. The LHC can, for example, currently give a lower bound on the pure wino mass of about 500 GeV [41, 42]. The Higgsino is even harder to probe, and even constraining the mass or possibly discovering the Higgsino is only possible up to $m_\chi \approx (300-400)\,\text{GeV}$ given the projected final LHC data set [43]. Even at possible future high-energy colliders, e.g. the often discussed 100 TeV collider, a possible detection is also dependent on the precise specifications, the information used, the amount of collected data, and many other aspects, and remains a discussed subject in the literature [43, 44, 45, 46, 47]. A collider detection or final exclusion of

---

[5] In principle, all pure models with $Y \neq 0$ are already ruled out by direct detection constraints [37], however, they can typically be resurrected by introducing some non-minimal additions, e.g., small admixtures of other multiplets, that prevent DM/nucleon couplings via Z-exchange. For the case of the Higgsino, this is discussed in more detail in Chapter 4.

the thermal mass Higgsinos and winos at future colliders is therefore certainly not ensured.

Similarly, direct detection via DM-nucleon scattering proves challenging for both wino and Higgsino. For example, for the pure wino as DM, there is no direct Z- or Higgs coupling, and loop processes, therefore, determine the direct detection cross-section. The predicted spin-independent WIMP-proton scattering cross-section is $\sigma_{\mathrm{SI}} \approx 2 \cdot 10^{-47}\,\mathrm{cm}^2$ obtained within various effective field theory (EFT) approaches [48, 49, 50, 51, 52, 53, 54]. The value is close to the so-called "neutrino floor" for direct detection experiments if the wino is in the TeV-range [55]. Current direct detection experiments cannot constrain such cross-sections, and it is also not entirely clear if the next-generation direct detection experiments will be able to rule out or confirm the pure wino. For a review of the various experiments and constraints, see, e.g. [56]. For the Higgsino, the situation is even bleaker in direct detection. The cross-section is predicted well within the coherent neutrino background [49, 51, 54], making direct detection essentially impossible for this model.

Despite the grim prospects in direct detection and collider experiments for the thermal electroweak WIMPs, there is still potential to discover them through indirect detection (for a review, see e.g. [57]). The concept refers to the astronomical detection of DM annihilation or decay products, i.e., $\chi^0\chi^0$ annihilating into a SM final state. Indirect detection prospects profit from the large amount of DM in the universe, and telescopes, initially designed for other astrophysics or astronomy questions, are also sensitive to the SM final states considered. However, the typical challenges lie again in the weak DM coupling to the SM and the significant astrophysical uncertainties, e.g., DM profiles [58] and cosmic ray modeling [59]. Among the most popular final states to search for is a monoenergetic photon arriving in the detector, the so-called "line signal". The advantage of the photonic signal lies in the low astrophysical background and the possibility to hunt for a bump in the spectrum that is hard to explain by astrophysics. However, on the downside, as the dark matter does not directly couple to photons, the process can only start at one-loop.

The typical indirect detection telescopes that can constrain heavy WIMPs fall into two categories: Space-based and ground-based telescopes. The former can detect the high-energetic photon directly, whilst the latter relies on the detection using Cherenkov radiation produced in the atmosphere by the cosmic rays. The typical space-telescopes that constrain the electroweak WIMPs are EGRES [60], and especially in the last years, FERMI-LAT [61]. However, as their effective area and therefore their sensitivity drops sharply in the TeV-regime, most interesting for thermal electroweak WIMPs, ground-based telescopes are typically more sensitive to these models.

The ground-based telescopes that can detect the electroweak WIMPs in the TeV-range usually are Imaging Atmospheric Cherenkov Telescopes (IACT). Experiments such as VERITAS [62], MAGIC [63], HAWC [64] or H.E.S.S. [65] already cut into the relevant parameter space depending on the astrophysical assumptions made. Especially, the upcoming CTA experiment [66, 67] which is expected to improve the sensitivity to DM signals by at least an order of magnitude, will also be able to confirm or rule out most of the TeV-WIMP region, even under rather conservative assumptions on astrophysical uncertainties. Therefore, indirect detection provides the most promising and powerful avenue to test the thermal TeV-WIMPs to date.

1.4 Large loop effects in dark matter annihilation

Although the one-loop prediction for the neutralino annihilation into two photons or a photon and a Z-boson, i.e., the line signal, is known for more than 20 years [68, 69, 70], this result is not sufficient to constrain the wino and Higgsino as there are large corrections that significantly alter the forecast. The typical thermal masses of winos ($m_\chi \sim (2-3)\,\mathrm{TeV}$) and Higgsinos ($m_\chi \approx 1\,\mathrm{TeV}$), imply that there is a large scale ratio between DM mass and the electroweak (EW) scale $m_\chi/m_W \gg 1$. The largeness of this ratio causes several loop effects to produce large corrections to naive tree-level predictions. On the non-relativistic side, the so-called "Sommerfeld effect" [71], and in annihilation to exclusive or semi-inclusive final states, Sudakov logarithms [72], significantly modify the predicted cross-sections. The former was first pointed out for electroweak WIMPs in [73, 74], and arises as the massive electroweak gauge bosons $W^\pm, Z$ are from the DM perspective, light and essentially stable (at least on typical time scales of the dark matter annihilation). Ladder loop exchanges of these heavy gauge bosons are suppressed by factors of

$$\alpha_2 \frac{m_\chi}{m_W} \quad \text{or} \quad \frac{\alpha_2}{v} \tag{1.3}$$

in the non-relativistic regime, where v is the DM velocity. As for TeV DM, these ratios are of $\mathcal{O}(1)$, a special treatment is necessary, introducing potentials due to electroweak gauge boson exchange that after solving a Schrödinger equation resum these corrections. The resulting enhancement is known as the "Sommerfeld effect" or "Sommerfeld enhancement" after the QED calculation in [71]. After the initial calculation for winos and Higgsinos in indirect detection [74], it was found that also the freeze-out of WIMPs receives significant corrections due to the Sommerfeld effect [39]. In particular, many of the MSSM benchmark scenarios [36] and the class of minimal DM models [38] are subject to Sommerfeld effect corrections. However, the Sommerfeld enhancement is not restricted to electroweak WIMPs and has found applications in a plethora of other DM models and cosmological contexts. It was the anomalous positron excess in the PAMELA experiment [75] that initiated widespread interest in the Sommerfeld effect as a way to boost DM annihilation rates [76, 77] and popularized the effect in the literature.

A similar situation, albeit with massless gauge bosons, is present, e.g., in threshold annihilation at colliders or bound state physics for atomic systems. The modern tools to deal with potentials and other non-relativistic states are NRQCD and PNRQCD [78, 79, 80, 81] for the annihilation of quarkonia (and NRQED/PNRQED in the atomic physics setting [82, 83]). These effective theories allow for a systematic counting of the non-relativistic effects and their relative importance and have been worked out to high loop orders. The effective theories for the non-relativistic dark matter case, which are constructed in close analogy with their QED/QCD analogues, were first discussed in [84, 85, 86] and follow a similar logic. The phenomenology of the resulting potentials and the solution of the Schrödinger equation is quite different from QCD. The massive nature of the exchanged bosons leads to distinct enhancement with saturation, resonances, and other interesting effects that we will elude to at later stages of this thesis.

In exclusive and semi-inclusive DM annihilation, the second class of large corrections considered in this thesis plays a role, Sudakov double logarithms of the electroweak to the DM mass scale

$$\frac{\alpha_2}{\pi} \ln^2 \frac{m_W^2}{4m_\chi^2} \tag{1.4}$$

that arise at every order in perturbation theory. Again, if the DM mass is in the TeV-regime, these require resummation using renormalization group techniques. Similar to the non-relativistic toolbox, which is inspired by NRQCD, Sudakov resummation is also addressed in the collider context using soft-collinear effective theory (SCET) [87, 88, 89, 90]. SCET as an effective theory provides a natural way to deal with infrared (IR) soft and collinear physics that gives rise to the double logarithms. Whilst electroweak Sudakov logarithms in SCET were previously investigated in the collider context [91, 92], the application to the indirect detection process that involves further scales and challenges has only started to gather interest in the past years [93, 94, 95, 96, 97, 98, 99, 100, 101, 102]. In view, of the potentially large astrophysical uncertainties that enter indirect detection analyses, it is mandatory, to provide accurate particle physics predictions. The particle physics uncertainties are reducible by extending the calculations and therefore, not restricted by any possible experimental uncertainties or effects. Secondly, the particle physics differential cross-section enters the observed J-factors as a convolution with several astrophysical factors. Hence, it is desirable to reduce the error bars on the particle physics side as much as possible to not further bolster the, in any case, large uncertainties involved.

Outline. This thesis is organized as follows: We begin in Chapter 2, with a review of the method of regions approach to the calculation of loop corrections. Furthermore, we identify the necessary momentum modes needed to construct the corresponding effective theories in order to tackle the Sommerfeld effect and Sudakov resummation calculations. In Chapter 3, we discuss the construction of the non-relativistic effective theory for heavy electroweak WIMPs and discuss the NLO correction to the wino DM potentials. Following the wino calculation, we generalize the result for the NLO potential, in Chapter 4, to arbitrary $\mathrm{SU}(2)_L$ multiplets and hypercharges. Concluding the discussion of non-relativistic corrections to DM, in Chapter 5, we review the WIMP freeze-out computation and apply the insights of the NLO potentials to the wino model.

In the second part of this thesis, we deal with the description of the indirect detection endpoint spectrum and the resummation of electroweak Sudakov logarithms. We begin by examining the endpoint spectrum factorization for the process $\chi\chi \to \gamma + X$ in Chapter 6. We discuss the resummation of electroweak Sudakov logarithms and a selection of technical points for the wino and Higgsino endpoint spectrum in the following Chapter 7. Finally, in Chapter 8, we present the prediction for the endpoint spectrum for wino and Higgsino annihilation and combine the results for the NLO potentials (Chapters 3 and 4) with the resummed annihilation rates (Chapters 6 and 7). In Chapter 9, we conclude. A series of Appendices provide further technical details on the calculations discussed in the main text.

This thesis is mainly based on the following publications (and in some points extends upon the discussion therein)

- M. Beneke, A. Broggio, C. Hasner, K. Urban, and M. Vollmann, *Resummed photon spectrum from dark matter annihilation for intermediate and narrow energy resolution*, *JHEP* **08** (2019) 103, [`arXiv:1903.0870`]. [Erratum: JHEP 07, 145 (2020)]

- M. Beneke, R. Szafron, and K. Urban, *Wino potential and Sommerfeld effect at NLO*, *Phys. Lett.* **B800** (2020) 135112, [`arXiv:1909.0458`]

- M. Beneke, C. Hasner, K. Urban, and M. Vollmann, *Precise yield of high-energy photons from Higgsino dark matter annihilation*, *JHEP* **03** (2020) 030, [`arXiv:1912.0203`]

- M. Beneke, R. Szafron, and K. Urban, *Sommerfeld-corrected relic abundance of wino dark matter with NLO electroweak potentials*, *JHEP* **02** (2021) 020, [`arXiv:2009.0064`]

and work yet to appear

- M. Beneke and K. Urban, *in preparation*

- M. Beneke and K. Urban and M. Vollmann, *in preparation*

2

Radiative corrections to heavy WIMPs

For heavy WIMPs, the scale separation of electroweak and dark matter mass scale $m_Z \ll m_\chi$ leads to several enhanced corrections. In this Chapter, we motivate the origin of these corrections and identify the necessary ingredients for the EFT treatments detailed in the later parts of this thesis. We begin by reviewing the "method of regions" approach and discuss two illustrative examples of relevance in this thesis. Afterwards, we turn to identify the crucial momentum modes for the EFT construction. Finally, we discuss the factorization of annihilation effects and non-relativistic physics, that allows for the separate treatments of non-relativistic physics in Chapters 3, 4, 5, annihilation effects in Chapters 6, 7, and finally the combination of both in Chapter 8.

2.1 The method of regions

Evaluating loop integrals that involve many scales analytically, such as masses or kinematical parameters, can be challenging to practically impossible. However, in many physics situations, it is not necessary to know the full dependence on all parameters. Instead, one is interested in the leading behaviour in these parameters, e.g. to resum certain logarithmic corrections. The method of regions (sometimes also "strategy of regions") [105], provides a way to solve such loop integrals by expanding in the small parameters, simplifying intermediate loop integrals by the introduction of regions, and finally recovering the behaviour that could have also been extracted by expanding the full result. For a given loop integral, we can summarize the prescription in the following steps [106, 107]:

1. Divide the full loop integral into regions and expand the integrand in each region with respect to the small parameters in this region.

2. Perform the integration in each of the expanded regions over the entire integration domain of the loop momenta.

3. Set any scaleless integral to zero and add all expanded contributions.

This procedure reproduces the full result expanded in the small parameter, order by order. There are no counterexamples known to this method, and the corresponding asymptotic expansion is even proven in some cases. For more rigorous treatments and the current status of the method, see [106, 107, 108]. Below we provide two examples that exemplify the method and introduce the types of loop integrals encountered at later stages of this thesis.

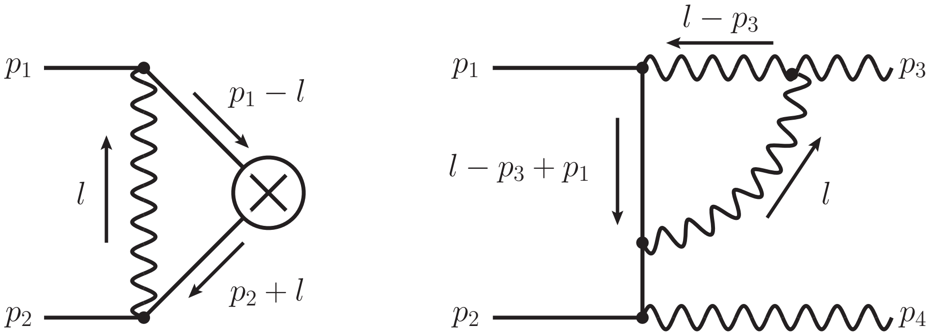

Figure 2.1: *Example diagrams corresponding to the loop integrals discussed in Sections 2.1.1 (left panel) and 2.1.2 (right panel).*

2.1.1 Example - massive gauge boson correction to threshold annihilation

As a first example, let us consider two heavy fermions of mass m_χ annihilating at an effective annihilation vertex, corrected by the exchange of a massive gauge boson of mass $m_W \ll m_\chi$, as depicted in Figure 2.1 (left panel). For simplicity, we drop any Dirac and momentum structure in the numerator and focus on the explicit integral. For the external fermion momenta, the threshold kinematics apply

$$p_1^\mu = p_2^\mu = m_\chi v^\mu \qquad v^\mu = (1,0,0,0)^T \,. \tag{2.1}$$

In this case, we can analytically solve the full integral and afterwards expand in the small ratio $\lambda = m_W/m_\chi$

$$\begin{aligned} I_1 &= \int [dl]\; \frac{1}{l^2 - m_W^2 + i\varepsilon} \cdot \frac{1}{(p_1 - l)^2 - m_\chi^2 + i\varepsilon} \cdot \frac{1}{(p_2 + l)^2 - m_\chi^2 + i\varepsilon} \\ &= \frac{i}{16\pi^2 m_\chi^2} \left[\ln \frac{m_\chi}{m_W} - \sqrt{\frac{4m_\chi^2}{m_W^2} - 1}\, \arctan\left(\sqrt{\frac{4m_\chi^2}{m_W^2} - 1} \right) \right] \\ &= \frac{i}{16\pi^2 m_\chi^2} \left[-\frac{\pi}{\lambda} - \ln\lambda + 1 + \frac{\pi}{8}\lambda + \mathcal{O}(\lambda^2) \right] \end{aligned} \tag{2.2}$$

where $[dl]$ is defined, in Eq. (A.1). We can also derive the result in the method of regions approach. To that end, we note three regions, a potential, hard and soft region, that contribute to this integral, following the above criteria. In the potential region, i.e., considering loop momenta of the scaling $(l^0, \mathbf{l}) \sim m_\chi(\lambda^2, \lambda)$, the result at $\mathcal{O}(\lambda^{-1})$ is given by

$$\begin{aligned} I_1^{\text{potential}}(\lambda^{-1}) &= \int [dl]\; \frac{-1}{\mathbf{l}^2 + m_W^2} \cdot \frac{1}{-\mathbf{l}^2 - 2m_\chi l^0 + i\varepsilon} \cdot \frac{1}{-\mathbf{l}^2 + 2m_\chi l^0 + i\varepsilon} \\ &= \frac{i}{16\pi^2 m_\chi^2} \left(-\frac{\pi}{\lambda} \right) \end{aligned} \tag{2.3}$$

which captures the full $1/\lambda$ enhanced correction. The first subleading correction $\mathcal{O}(\lambda^0)$ originates from the hard $(l^0, \mathbf{l}) \sim m_\chi(1,1)$

$$\begin{aligned} I_1^{\text{hard}}(\lambda^0) &= \int [dl]\; \frac{1}{l^2 + i\varepsilon} \cdot \frac{1}{(p_1 - l)^2 - m_\chi^2 + i\varepsilon} \cdot \frac{1}{(p_2 + l)^2 - m_\chi^2 + i\varepsilon} \\ &= \frac{i}{16\pi^2 m_\chi^2} \left(-\frac{1}{2\epsilon} - \frac{1}{2} \ln \frac{\mu^2}{m_\chi^2} + 1 \right) \,, \end{aligned} \tag{2.4}$$

and the soft region $(l^0, \mathbf{l}) \sim m_\chi(\lambda, \lambda)$

$$\begin{aligned}
I_1^{\text{soft}}(\lambda^0) &= \int [dl]\, \frac{1}{l^2 - m_W^2 + i\varepsilon} \cdot \frac{1}{-2m_\chi l^0 + i\varepsilon} \cdot \frac{1}{2m_\chi l^0 + i\varepsilon} \\
&= \frac{i}{16\pi^2 m_\chi^2} \left(\frac{1}{2\epsilon} + \frac{1}{2} \ln \frac{\mu^2}{m_W^2} \right) .
\end{aligned} \tag{2.5}$$

Adding the two regions, the $\mathcal{O}(\lambda^0)$ term of Eq. (2.2) is reproduced. Similarly, all subleading orders can be calculated, with the odd powers of λ originating from the potential region, whilst the even powers of λ are due to the hard and soft region. For example, the $\mathcal{O}(\lambda)$ term originates from the first subleading order in the potential region

$$\begin{aligned}
I_1^{\text{potential}}(\lambda) = \int [dl] \Bigg[& \frac{-(l^0)^2}{(\mathbf{l}^2 + m_W^2)^2} \cdot \frac{1}{-\mathbf{l}^2 - 2m_\chi l^0 + i\varepsilon} \cdot \frac{1}{-\mathbf{l}^2 + 2m_\chi l^0 + i\varepsilon} \\
& + \frac{-1}{\mathbf{l}^2 + m_W^2} \cdot \frac{-(l^0)^2}{(-\mathbf{l}^2 - 2m_\chi l^0 + i\varepsilon)^2} \cdot \frac{1}{-\mathbf{l}^2 + 2m_\chi l^0 + i\varepsilon} \\
& + \frac{-1}{\mathbf{l}^2 + m_W^2} \cdot \frac{1}{-\mathbf{l}^2 - 2m_\chi l^0 + i\varepsilon} \cdot \frac{-(l^0)^2}{(-\mathbf{l}^2 + 2m_\chi l^0 + i\varepsilon)^2} \Bigg] \\
= \frac{i}{16\pi^2 m_\chi^2} \cdot \left(\frac{\pi\lambda}{8} \right) &
\end{aligned} \tag{2.6}$$

and similar at higher orders. Note that the potential regions characteristically carry an additional factor of π compared to the soft and hard regions. The above regions can be viewed as an indicator of which modes to consider in the effective theory construction. For example, generically, for the non-relativistic EFT of heavy WIMPs, the hard modes will constitute the annihilation operators. The potential region, as the name suggests, gives rise to non-relativistic potentials. Finally, the soft region will contribute to corrections of the potential and the annihilation process, as discussed in later Chapters. However, it is important to remark that the regions only act as an indicator for the EFT construction; the method of regions expansion is not necessarily equivalent to the effective theory.

2.1.2 Example - exclusive annihilation of heavy DM

In the exclusive annihilation of two heavy DM particles into SM final states, additionally to the example above, further regions and diagrams contribute. In this example, we consider one of the contributing diagrams, depicted in Figure 2.1 (right panel). The following kinematics apply in the exclusive annihilation into photons

$$p_1^\mu = p_2^\mu = m_\chi v^\mu \,, \quad p_3^\mu = m_\chi n_+^\mu \,, \quad p_4^\mu = m_\chi n_-^\mu \,, \tag{2.7}$$

where we used the light-cone coordinates for the two final state bosons

$$n_+^\mu = (1,0,0,-1) \,, \quad n_-^\mu = (1,0,0,1) \,. \tag{2.8}$$

Finally, to finish this short interlude, let us introduce the decomposition into light-cone components

$$p^\mu = (n_- \cdot p)\, \frac{n_+^\mu}{2} + (n_+ \cdot p)\, \frac{n_-^\mu}{2} + p_\perp^\mu = p_+^\mu + p_-^\mu + p_\perp^\mu \tag{2.9}$$

to denote scaling of regions and to simplify integral notation. Dropping the numerator structure of Figure 2.1 (right panel), we are left with the integral depending on the two scales m_W, m_χ for which we assume $m_W < m_\chi$ to simplify the result

$$
\begin{aligned}
I_2 &= \int [dl]\, \frac{1}{(l-p_3+p_1)^2 - m_\chi^2 + i\varepsilon} \cdot \frac{1}{l^2 - m_W^2 + i\varepsilon} \cdot \frac{1}{(l-p_3)^2 - m_W^2 + i\varepsilon} \\
&\overset{\lambda\leq 1}{=} \frac{i}{64\pi^2 m_\chi^2} \left[+2\,\mathrm{Li}_2\left(\frac{2\left(\lambda^2-1\right)}{\lambda\left(\lambda+\sqrt{\lambda^2-4}\right)}\right) - 2\,\mathrm{Li}_2\left(\frac{2\left(\lambda^2-1\right)}{\lambda\left(\lambda+\sqrt{\lambda^2-4}\right)-2}\right) \right. \\
&\qquad -2\,\mathrm{Li}_2\left(\frac{2\left(\lambda^2-1\right)}{\lambda^2+\sqrt{\lambda^4+4}-2}\right) - 2\,\mathrm{Li}_2\left(\frac{2\left(1-\lambda^2\right)}{-\lambda^2+\sqrt{\lambda^4+4}+2}\right) \\
&\qquad +\ln^2\left(\frac{\lambda}{2}\left(\sqrt{\lambda^2-4}-\lambda\right)+1\right) - \ln^2\left(\frac{\lambda\left(\sqrt{\lambda^2-4}-\lambda\right)}{\lambda\left(\sqrt{\lambda^2-4}+\lambda\right)-2}\right) \\
&\qquad \left. -\ln^2\left(\frac{\sqrt{\lambda^4+4}-\lambda^2+2}{\sqrt{\lambda^4+4}+\lambda^2-2}\right)\right] \\
&= -\frac{i}{32\pi^2 m_\chi^2}\ln^2\frac{\lambda}{2} + \mathcal{O}(\lambda)
\end{aligned}
\tag{2.10}
$$

albeit the very complicate full result, as a function of dilogarithms Li_2 and double logarithms, the leading behaviour expanding in $\lambda \ll 1$, is a simple Sudakov double logarithm, which is common for these diagrams given the above kinematics. In the later Chapters, we will be concerned with the resummation of these logarithms, but for now, let us first investigate which regions reproduce this result within the method of regions. To do so, we first expand in the hard region $(l_+, l_-, l_\perp) \sim m_\chi(1,1,1)$

$$
\begin{aligned}
I_2^{\text{hard}} &= \int [dl]\, \frac{1}{(l-p_3+p_1)^2 - m_\chi^2 + i\varepsilon} \cdot \frac{1}{l^2 + i\varepsilon} \cdot \frac{1}{(l-p_3)^2 + i\varepsilon} \\
&= \frac{i}{64\pi^2 m_\chi^2}\left[-\frac{1}{\epsilon^2} - \frac{1}{\epsilon}\ln\frac{\mu^2}{4m_\chi^2} - \frac{1}{2}\ln^2\frac{\mu^2}{4m_\chi^2} + \frac{\pi^2}{12}\right]
\end{aligned}
\tag{2.11}
$$

which, as expected, only depends on the high energy scale m_χ. In this case, extending to the low-energy regions is not straightforward, as the corresponding integrals suffer from a rapidity divergence and are ill-defined in dimensional regularization alone. The phenomenon is sometimes referred to as “Collinear Anomaly” [109], and essentially indicates the appearance of the high-scale m_χ in low-energy regions. To obtain a meaningful result that reproduces the full theory, we need a further regulator on top of dimensional regularization. The formal discussion of the rapidity divergence is postponed to the endpoint spectrum factorization, discussed in Chapter 6. Which regions contribute to a given integral depends on the chosen rapidity regulator. This thesis uses the rapidity regulator first introduced in [110, 111]. For further details on the exact implementation, see Appendix E.1. In the final result summing all contributions, the rapidity regulator dependence needs to cancel. When expanding results in the regulators, one first needs to expand in the rapidity parameter η before expanding in the dimensional regularization parameter ϵ. Using the rapidity regulator η, we are left with the soft region $(l_+, l_-, l_\perp) \sim m_\chi(\lambda, \lambda, \lambda)$

$$
I_2^{\text{soft}} = \int [dl]\, \frac{1}{2m_\chi v\cdot l + i\varepsilon} \cdot \frac{1}{l^2 - m_W^2 + i\varepsilon} \cdot \frac{1}{-2m_\chi n_+\cdot l + i\varepsilon} \cdot \frac{\nu^\eta}{|(n_+ - n_-)\cdot l|^\eta}
$$

$$
\begin{aligned}
&= \frac{i}{64\pi^2 m_\chi^2}\left[\frac{1}{\epsilon^2} - \frac{2}{\epsilon\eta}\left(1+\ln\frac{\mu^2}{m_W^2}\right) + \frac{2}{\epsilon}\ln\frac{\mu}{\nu}\right. \\
&\qquad\left. + \frac{1}{2}\ln\frac{\mu^2}{m_W^2}\left(\ln\frac{\mu^2}{m_W^2} - 2\ln\frac{\nu^2}{m_W^2}\right) - \frac{\pi^2}{12}\right] , \qquad (2.12)
\end{aligned}
$$

and the collinear region $(l_+, l_-, l_\perp) \sim m_\chi(\lambda^2, 1, \lambda)$

$$
\begin{aligned}
I_2^{\text{collinear}} &= \int [dl]\, \frac{1}{-m_\chi n_+\cdot l + i\varepsilon}\cdot\frac{1}{l^2 - m_W^2 + i\varepsilon}\cdot\frac{1}{l^2 - 2m_\chi n_+\cdot l - m_W^2 + i\varepsilon}\frac{\nu^\eta}{|n_+\cdot l|^\eta} \\
&= \frac{i}{64\pi^2 m_\chi^2}\left[\frac{2}{\epsilon\eta}\left(1+\ln\frac{\mu^2}{m_W^2}\right) + \frac{1}{\epsilon}\ln\frac{\nu^2}{4m_\chi^2} + \ln\frac{\mu^2}{m_W^2}\ln\frac{\nu^2}{4m_\chi^2}\right] \qquad (2.13)
\end{aligned}
$$

with ν the rapidity analogue of the dimensional regularization scale μ. Adding the three contributions considered above, we recover the leading behaviour of (2.10)

$$
I_2^{\text{hard}} + I_2^{\text{soft}} + I_2^{\text{collinear}} = -\frac{i}{32\pi^2 m_\chi^2}\ln^2\frac{m_W}{2m_\chi} = -\frac{i}{32\pi^2 m_\chi^2}\ln^2\frac{\lambda}{2} \qquad (2.14)
$$

which exemplifies the power of the method of regions expansion. Furthermore, it gives us an insight into the origin of the Sudakov double logarithm, which ultimately will allow us to resum to all orders in perturbation theory. The above integrals also appear in the later matching calculations, as hard Wilson coefficients (hard region), soft function (soft region), and jet functions (collinear regions).

2.2 Relevant momentum modes and kinematics

Using the method of regions, further information on the kinematics, and information on experimental energy resolution, we can identify the modes expected to contribute to the respective effective theories, thereby aiding the construction of said effective theories in later Chapters.

2.2.1 Relic density - fully inclusive process

The physical observables investigated in this thesis, namely the dark matter relic abundance and the endpoint spectrum of photons in indirect detection, share that they involve the annihilation of two heavy non-relativistic DM fermions. Therefore, some parts of the calculation, e.g., the potentials, are universal and apply to both computations (as proven below). The relic abundance calculation depends on the total annihilation cross-section of the DM, i.e., we are interested in the inclusive DM annihilation cross-section. Requiring that the electroweak scale m_W is much below the dark matter mass scale m_χ, we expect the following modes to contribute from the method of regions analysis $l^\mu = (l^0, \mathbf{l})$:

$$
\begin{aligned}
\text{hard (h)} &: \quad l^\mu \sim m_\chi(1,1) \\
\text{soft (s)} &: \quad l^\mu \sim m_\chi(\lambda,\lambda) \\
\text{potential (p)} &: \quad l^\mu \sim m_\chi(\lambda^2,\lambda) \\
\text{ultrasoft (us)} &: \quad l^\mu \sim m_\chi(\lambda^2,\lambda^2) \qquad (2.15)
\end{aligned}
$$

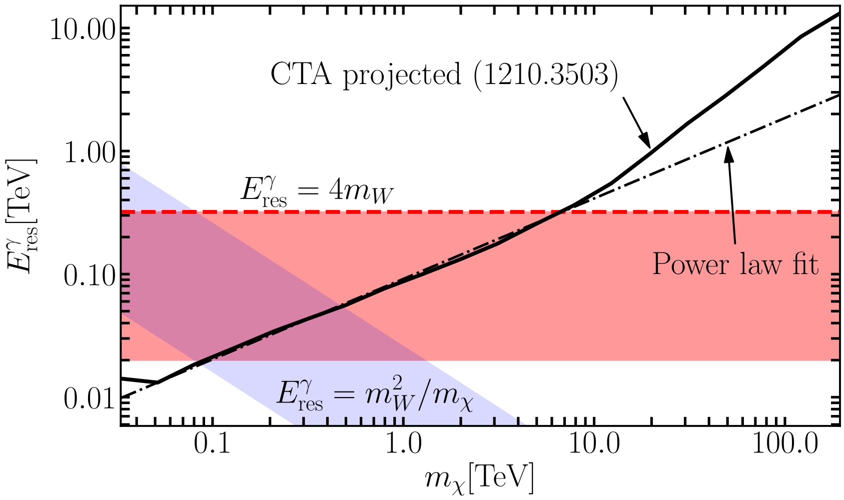

Figure 2.2: *Projected energy resolution of the CTA experiment (solid black line, from [112]), and the power-law fit* $E^\gamma_{\rm res} = 0.0915(E_\gamma/\text{TeV})^{0.653}$ *(dash-dotted) with* $E_\gamma \approx m_\chi$*. The dark-grey (red) and light-grey (blue) bands show where the intermediate and narrow resolution regimes described in the text, apply, respectively. The boundaries are defined as* $m_W[1/4, 4]$ *(intermediate resolution), and* $m_W^2/m_\chi[1/4, 4]$ *(narrow resolution)*

2.2.2 Indirect detection $\chi\chi \to \gamma + X$ - semi-inclusive/exclusive annihilation

In indirect detection, we are concerned with exclusive $\chi\chi \to \gamma\gamma$ or, more realistically, semi-inclusive $\chi\chi \to \gamma + X$ final states. The kinematics of this situation, i.e., two heavy non-relativistic dark matter particles that annihilate into SM particles, force a high energy photon to be detected at earth and a SM final state that recoils due to momentum conservation.

Which particles are possible inside the final state X depends on the resolution of the photon detector at earth. One of the final state particles is fixed to be a photon (in our convention, the anti-collinear direction $\bar{c}$), the kinematics of the annihilation imply that the unobserved recoiling final state X has invariant mass

$$p_X^2 = (p_1 + p_2 - p_\gamma)^2 = 4m_\chi^2 - 2(p_1 + p_2) \cdot p_\gamma = 4m_\chi\,(m_\chi - E_\gamma) \tag{2.16}$$

with p_1, p_2 the DM momenta at threshold, as defined in the preceding Section and $p_\gamma = E_\gamma n_+$. The energy resolution is defined as $E^\gamma_{\rm res} = m_\chi - E_\gamma$, meaning that the unobserved final state has invariant mass

$$p_X^2 = 4m_\chi E^\gamma_{\rm res}\,. \tag{2.17}$$

As the detector is assumed to have an energy resolution $E^\gamma_{\rm res} \ll m_\chi$, there are three parametric possibilities for the invariant mass of the recoiling state X. A regime $m_\chi^2 \gg m_W^2 \sim p_X^2$ where the invariant mass of the recoiling state is of the order of the electroweak scale,[1] a second regime where $m_\chi^2 \gg p_X^2 \sim m_\chi m_W \gg m_W^2$, and a third regime with $m_\chi^2 \gg p_X^2 \gg m_\chi m_W \gg m_W^2$. Translated into energy resolution of the detector, this leaves the three regimes:

$$\text{narrow}: \quad E^\gamma_{\rm res} \sim m_W^2/m_\chi$$

---

[1] This narrow regime (see below), extends also to $p_X^2 \ll m_W^2$, if small tweaks are applied, e.g., decoupling light-fermions if $p_X^2 < m_f^2$, with m_f a generic light-fermion mass. The corresponding modifications are discussed in the following Chapters in more detail.

$$\begin{aligned} \text{intermediate}: \quad & E^\gamma_{\text{res}} \sim m_W \\ \text{wide}: \quad & E^\gamma_{\text{res}} \gg m_W \end{aligned} \tag{2.18}$$

For the upcoming CTA experiment [66, 67, 113], which has a projected sensitivity to TeV γ-rays which is about an order of magnitude better than previous experiments, such as H.E.S.S. [65], we show the projected energy resolution in Figure 2.2 [112], as a function DM mass m_χ. We find that the projected energy resolution is well approximated in the region up to $m_\chi \approx 10\,\text{TeV}$, by a power-law fit ($E_\gamma = m_\chi$)

$$E^\gamma_{\text{res}} = 0.0915\,(E_\gamma/\text{TeV})^{0.653}\,. \tag{2.19}$$

Assuming that the resolution regimes apply within $[1/4, 4]m_W^2/m_\chi$ for narrow resolution, and $[1/4, 4]m_W$ for intermediate resolution, as indicated by the blue and red bands, respectively, we find that these two energy resolution regimes cover DM masses from $m_\chi \approx 100\,\text{GeV}$ up to $m_\chi \approx 10\,\text{TeV}$.[2]

In the case of the H.E.S.S. experiment [65], which currently puts the strongest indirect bounds on TeV dark matter, the typical energy resolution is $E^\gamma_{\text{res}}/E_\gamma \approx 10\%$. Therefore, meaning that the intermediate resolution regime, assuming the above boundaries, applies up to $\approx 3.2\,\text{TeV}$ covering both the range of the thermal wino and Higgsino.

In this thesis, we are mainly interested in the narrow and intermediate regimes. These cover the interesting mass region up to about 10 TeV, in which the wino and Higgsino have their thermal masses. Complementary work on the wide regime (albeit in a different formulation of the EFT) can be found in [98, 99].

Using the above insights on the scaling of the energy resolution, we find from a method of regions analysis that the following modes contribute to $\chi\chi \to \gamma + X$ ($l^\mu = (l_+, l_-, l_\perp)$)

$$\begin{aligned} \text{hard (h)}: \quad & l^\mu \sim m_\chi(1,1,1) \\ \text{hard-collinear (hc)}: \quad & l^\mu \sim m_\chi(1,\lambda,\sqrt{\lambda}) \\ \text{collinear (c)}: \quad & l^\mu \sim m_\chi(1,\lambda^2,\lambda) \\ \text{anti-collinear }(\bar{\text{c}}): \quad & l^\mu \sim m_\chi(\lambda^2,1,\lambda) \\ \text{soft (s)}: \quad & l^\mu \sim m_\chi(\lambda,\lambda,\lambda) \\ \text{potential (p)}: \quad & l^0 \sim m_\chi\lambda^2\,,\ \mathbf{l} \sim m_\chi\lambda \\ \text{ultrasoft (us)}: \quad & l^\mu \sim m_\chi(\lambda^2,\lambda^2,\lambda^2) \end{aligned} \tag{2.20}$$

where the hard-collinear mode only appears for intermediate resolution $E^\gamma_{\text{res}} \sim m_W$. These modes are the central ingredients for the factorization of the energy spectrum in Chapter 6, but for now, we will consider the factorization of potential modes from the annihilation process. This factorization allows a joint investigation of the potential correction for both relic abundance and indirect detection calculation.

2.3 Factorization of non-relativistic and annihilation dynamics

Let us consider a generic annihilation process for two heavy DM particles into arbitrary SM final states. The goal is to prove the factorization of the non-relativistic and annihilation dynamics. From the above mode discussion for relic abundance (2.15) and endpoint spectrum (2.20), we find that the only modes that could facilitate a cross-talk between the potentials and the annihilation process are either soft or ultrasoft.

---

[2] Note that the lower mass region $m_\chi \approx 100\,\text{GeV}$, even though possible by the detector, is not part of our EFT, as we aspire to sum large logarithms and the Sommerfeld ladder, which both rely on $m_\chi/m_W \gg 1$.

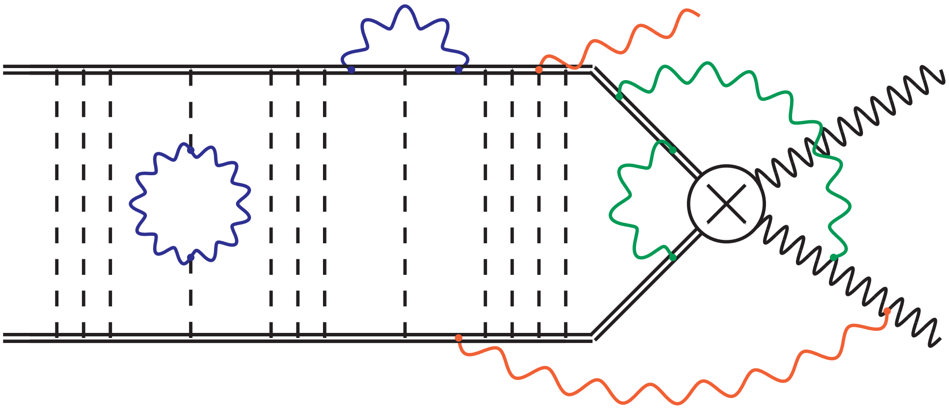

Figure 2.3: *Diagrammatic representation of the factorization argument presented in the text, Section 2.3. The green, and blue soft gauge boson emissions are possible, as they are not connected to the potential ladder (green) or connected to the ladder, but no momentum is routed through the annihilation vertex (blue). They constitute corrections to the annihilation process, and the potential, respectively. The red lines are not possible, at leading power in the effective theory, as they break the potential ladder, by throwing the non-relativistic DM propagators (solid double lines) off-shell.*

Considering the soft modes, and for simplicity, we also assume that the hard modes are integrated out, we are left with the possible situation schematically depicted in Figure 2.3. The Figure shows three types of soft corrections. In blue soft virtual loop corrections that are not routed through the annihilation vertex, these will constitute corrections to the potential. The green lines show corrections at the annihilation vertex, i.e., no potential loops between soft emission and the annihilation vertex. These virtual and real corrections constitute the soft functions that correct the hard annihilation process. Finally, soft emissions from inside the potential ladder are shown in red, either routed through the annihilation vertex (if virtual) or real emissions. These are the problematic modes, as they facilitate a cross-talk between annihilation and non-relativistic dynamics. However, as argued below, they do not contribute to leading power, as these soft emissions throw the potential propagators off-shell and thereby kill the Sommerfeld enhancement.

To see this more formally, let us consider, one of the ladder rungs in the potential region, stripping all unnecessary factors

$$\begin{aligned}
&\int [dl]\,\frac{-i}{(l-p)^2-m_W^2+i\varepsilon}\cdot\frac{-i}{(l-p')^2-m_W^2+i\varepsilon}\cdot\frac{i}{l^0+\frac{E}{2}-\frac{(\mathbf{l}+\mathbf{p})^2}{2m_\chi}+i\varepsilon}\cdot\frac{i}{-l^0+\frac{E}{2}-\frac{(\mathbf{l}+\mathbf{p})^2}{2m_\chi}+i\varepsilon}\\
&=\tilde{\mu}^{2\epsilon}\int\frac{d^{d-1}\mathbf{l}}{(2\pi)^{d-1}}\,\frac{i}{(\mathbf{l}-\mathbf{p})^2+m_W^2}\,\frac{-i}{E-\frac{(\mathbf{l}+\mathbf{p})^2}{m_\chi}+i\varepsilon}\,\frac{i}{(\mathbf{l}-\mathbf{p}')+m_W^2} \qquad (2.21)
\end{aligned}$$

where we dropped in the transition from first to the second line, the energy in the gauge boson propagator and systematically expanded to leading order in the NR expansion. The spatial momenta $\pm\mathbf{p}$, and $\pm\mathbf{p}'$ belong to the non-relativistic particles, before and after the scattering, respectively. We are essentially left with an insertion of the potential followed by a two-particle state NR propagator, followed again by an insertion of the potential. Extending this to arbitrary loops builds up the potential ladder. For a more detailed discussion on how the ladder is built up and the corresponding Green's function are constructed, see [86, 114]. If now, a soft correction is added to these ladder rungs, the non-relativistic fermion propagators are eikonalized, i.e.,

$$\frac{i}{l^0+\frac{E}{2}-\frac{(\mathbf{l}+\mathbf{p})^2}{2m_\chi}+i\varepsilon} \xrightarrow{(l^0,\mathbf{l})\sim m_\chi(\lambda,\lambda)} \frac{i}{l^0+i\varepsilon}\,. \tag{2.22}$$

Therefore, the enhanced nature of the loops ceases after such a soft emission, and there are two possibilities. First the soft loop can be closed inside the ladder (blue lines Figure 2.3). In this case, the enhancement is killed for the loops in which the soft momentum flows. However, after the loop is closed, the ladder enhancement continues as before (cf. Chapter 3). Therefore, these corrections correct the leading order potential ladder exchanges.

The second possibility, namely the soft correction, either routed through the annihilation vertex or as a real emission, kills the potential ladder to the right of the emission in Figure 2.3 (red lines). Hence, this is not possible at leading power unless the emission is to the right of the potential ladder, in which case, however, they would belong to the green category and constitute a correction to the annihilation process. Hence, there is no soft cross-talk between non-relativistic and annihilation dynamics.

Secondly, there is in principle also the possibility of ultrasoft modes facilitating such interdependence between the initial non-relativistic fermion state and the annihilation process. Fortunately, this is also not possible at leading power. For indirect detection, the reason is physically simple. The ultrasoft modes (in our case restricted to be photons) only couple to the total charge of the heavy DM two-particle state, which by assumption $\chi^0\chi^0 \to \gamma + X$ is zero. In the relic abundance calculation, there are also two-particle states with a non-vanishing net charge. However, the ultrasoft modes still drop at leading power, as the annihilation process is described by a local four-fermion operator, with overall charge zero (for more details, see explicit discussion in Chapter 3).

The above findings have profound consequences for the logic of this thesis. They allow us to consider corrections to the potential separate from annihilation corrections and apply the findings to various observables, independent of their process-dependent annihilation structure. Therefore, the next three Chapters 3, 4, 5 are devoted to the discussion of non-relativistic physics and its effects. Following this, there are two Chapters 6,7, that consider corrections to the annihilation process, however, independently from the non-relativistic dynamics, before finally we provide the combined effects in Chapter 8 for the endpoint spectrum in DM indirect detection.

3

NLO potentials for wino dark matter

In this Chapter, we discuss the calculation of the NLO potential. We start out with a detailed description of the non-relativistic effective theories that arise in the calculation. Afterwards, we choose the pure wino model, to illustrate the calculation, and to discuss the subtleties on renormalization schemes and other aspects. The next Chapter will generalize these results to arbitrary minimal models and discuss the generalization to non-zero hypercharge and arbitrary fermion representations. Furthermore, the non-relativistic EFT setup is a crucial ingredient in the factorization discussion in Chapter 6.

After setting up the EFT for generic heavy WIMPs, we discuss the calculation of the NLO potential by describing the $\chi^+\chi^- \to \chi^+\chi^-$ channel, that will include all possible diagram topologies, and effects of EWSB, such as γ-Z-mixing. In doing so, we introduce the on-shell renormalization scheme and discuss the gauge invariance of the result. Afterwards, we discuss the other possible co-annihilation channels and highlight the respective differences. Finally, we discuss the channels' asymptotic and full behaviours, provide fitting functions for easy implementation of the result, discuss the $\overline{\text{MS}}$ scheme and the top mass dependence of the result.

Finally, as a first illustration of the effects, we discuss the indirect detection mass spectrum without including Sudakov resummation effects, which are addressed in later Chapters. Most results presented in this Chapter were first given in [103, 104] in collaboration with M. Beneke and R. Szafron.

3.1 EFT of non-relativistic WIMPs

The effective field theory for non-relativistic heavy electroweak WIMPs was first discussed in [84, 85, 86], following the respective non-relativistic EFTs in QED and QCD [78, 79, 80, 81] for quarkonia [115]. In principle, we would like to discuss the potential non-relativistic theory for arbitrary heavy particles charged under the electroweak gauge group. While the derivation in this more general setup is very similar, there are some technical and notational subtleties, that however, do not provide any additional physics insights. Therefore, we specialize to the non-relativistic effective theory for wino DM and comment in every step on the possible extensions for other multiplets or including hypercharge. We begin our discussion with the wino Lagrangian added to the SM

$$\mathcal{L}_{\text{DM}} = \frac{1}{2}\,\overline{\chi}(x)\left(i\not{D} - m_\chi\right)\chi(x)\,, \tag{3.1}$$

where χ denotes an SU(2)-triplet of Majorana fermions and the covariant derivative is given by $D_\mu = \partial_\mu - ig_2 W^a_\mu T^a$. For generic models, the covariant derivative also gains a hypercharge component, however, only for a complex fermion/scalar field χ, which entails a different normalization of the kinetic term. As discussed in the previous Chapter, the modes relevant for the EFT construction are hard, soft, potential, and ultrasoft (cf. Section 2.2). We assume the power-counting, to follow $\lambda = m_W/m_\chi \sim v \sim \alpha_2$, where v is the non-relativistic velocity of the DM particles. Other scalings of v with respect to α_2 or λ do not change the construction of the non-relativistic theory, but give rise to different regimes (e.g., Coulombic if $\alpha_2 \sim v \gg \lambda$).

We begin constructing the EFT by matching to the non-relativistic EFT, which means in practice integrating out the hard modes. The matching procedure takes place in the unbroken electroweak phase. The theory then resembles NRQCD with an SU(2) gauge group, or for non-zero hypercharge an additional U(1). Therefore, we can extract the Feynman rules from the literature by adjusting group factors [114]. The non-relativistic Lagrangian terms that are relevant for our purposes are given by

$$\mathcal{L}_{\mathrm{NRDM}} = \chi^\dagger(x)\left(iD^0 + \frac{\mathbf{D}^2}{2m_\chi}\right)\chi(x)\,, \tag{3.2}$$

with only soft, potential, and ultrasoft modes being dynamic degrees of freedom.[1]

Following this, we can transition to the broken electroweak phase. The Lagrangian Eq. (3.2) takes the same form as above, with the difference, that the fields are now mass eigenstates instead of weak eigenstates as before. For the wino, this means that χ_a, where $a = 1, 2, 3$ in the unbroken theory, is replaced by the mass eigenstates $\chi^\pm = (\chi_1 \mp i\chi_2)/\sqrt{2}$ and $\chi^0 = \chi_3$. Furthermore, the masses of the fields have changed, due to massive gauge bosons in the heavy particle self-energies. As χ^0 and $\chi^\pm$ couple differently to the electroweak bosons, this leads to a mass splitting of $\delta m_\chi = m_{\chi^+} - m_{\chi^0} = 164.1\,\mathrm{MeV}$ [116] at two-loops.[2]

In the final transition to the potential non-relativistic theory, all soft fields and the potential gauge bosons are integrated out. In the end, this leads to four fermion operators, whose Wilson coefficient can be interpreted as the static potential. The leading-order (LO) potential arises from the potential gauge boson exchange at tree-level (TL), whilst soft loops correct the potentials. The final theory then contains only potential fermions and ultrasoft gauge bosons (which for $\lambda \sim \alpha_2 \sim v$ are restricted to be photons).[3] The Lagrangian of this potential non-relativistic DM (PNRDM) Lagrangian [84]

$$\begin{aligned}\mathcal{L}_{\mathrm{PNRDM}} = &\sum_{i=\pm,0} \chi^\dagger_{vi}(x)\left(iD^0_i(t,\mathbf{0}) - \delta m_i + \frac{\boldsymbol{\partial}^2}{2m_\chi} - e_i\, e\,\mathbf{x}\cdot\mathbf{E}(t,\mathbf{0})\right)\chi_{vi}(x)\\ &- \sum_{\{i,j\},\{k,l\}} \int d^3\mathbf{r}\, V_{\{ij\}\{kl\}}(r)\,\chi^\dagger_{vk}(t,\mathbf{x})\chi^\dagger_{vl}(t,\mathbf{x}+\mathbf{r})\chi_{vi}(t,\mathbf{x})\chi_{vj}(t,\mathbf{x}+\mathbf{r})\,,\end{aligned} \tag{3.3}$$

where e_i is the sign of the electric charge of fermion i in the positron charge units e. The electromagnetic covariant derivative is given by $iD^0_i = i\partial^0 + e_i e A^0$. We employ the convention that all fields in PNRDM are considered particle fields (cf. [84]). Again, if a model with hypercharge, different spin or similar is considered the Lagrangian takes the same form as above. However, the value of the mass splitting δm_i, as well as the Wilson coefficients (potentials), is

---

[1] Note that the non-relativistic Lagrangian has the same form if the corresponding non-relativistic field would be a Dirac fermion or a particle of arbitrary spin (even though the relativistic kinetic term carries possibly different canonical normalization).

[2] In the non-relativistic theory the mass difference arises from the soft correction to the dark matter propagator. Other than, e.g., in HQET or NRQCD, the gauge boson masses give rise to a linearly divergent integral in dimensional regularization, that corrects the DM mass, see Appendix A.1.3.

[3] For very large masses $m_\chi \sim \mathcal{O}(100\,\mathrm{TeV})$ there is the regime where $\lambda = m_W/m_\chi \sim \alpha_2^2$. For this regime, the ultrasoft W- and Z-boson emission is possible. In this regime, however, the potentials are essentially Coulombic, as the exchange momentum $\mathbf{k} \sim m_\chi\alpha_2 \sim m_\chi v \gg m_W$. Therefore, the theory resembles PNRQCD for scattering states, and working within the unbroken theory is appropriate.

model-dependent. Compared to the heavily studied QED/QCD cases in the literature, which obey structurally similar Lagrangians, the phenomenology in the above case is different. The broken gauge symmetry, e.g., leads to the possibility of off-diagonal potentials, as the fields χ_v are mass and not gauge eigenstates. The QED/QCD analogues are simultaneously mass and charge/gauge eigenstates and are therefore diagonal. Also, the matching coefficients $V(r)$ take different forms, as they arise from massive and massless gauge bosons (and at loop-level mixtures thereof).

To remove power-counting ambiguities, the ultrasoft fields in the gauge covariant derivative $D_i^0(t,\mathbf{0})$ and the electric field are multipole expanded around the center of mass, for simplicity chosen at the origin.[4] The electric field term $\mathbf{x}\cdot\mathbf{E}$ arises from ultrasoft photon emissions of the charged fermions and the potential $W^\pm$-bosons via equation-of-motion identities [117]. The term is of order $\mathcal{O}(\lambda^{3/2})$ and is an indication of the unbroken electromagnetic U(1). For next-to-leading order (NLO) considerations it is of higher-order in the counting.[5]

Even though ultrasoft interactions are higher-order than NLO, they are relevant if one is interested in DM bound-state formation rates, providing additional features in line searches and annihilation channels for relic abundance determination. For the wino, in the mass range of $(2-3)$ TeV the effect is irrelevant in indirect detection, as the single bound state, cannot be reached by an E1 or M1 transition [118] from the necessary initial ${}^1S_0$ scattering state. Furthermore, it is rather shallow, affecting the relic abundance prediction in the wino case only negligibly [119]. However, for larger multiplets, formation of bound states can significantly alter annihilation rates and have an observable impact.

The mass difference term $\delta m_i \sim \alpha_2 m_W \sim m_W^2/m_\chi$ has to be included at two-loops [116, 120] to reach NLO accuracy in the non-relativistic calculation, as the LO splitting is of the same order in power-counting as the kinetic energy. Other than for the wino, the two-loop mass-splitting is currently only available for the quintuplet model [121].

Therefore, the last piece to obtain NLO accuracy on the non-relativistic side for the wino is the potential $V_{\{ij\}\{kl\}}$ in (3.3). One-loop corrections to this term, first discussed in [103, 104], stem from the soft region and are the subject of the rest of this and the following Chapter. In principle, there is also the possibility of potentials more singular than r^{-1}. However, the vertex structure [114] forces them to appear at next-to-next-to-leading order (NNLO) or higher-order, as in QED/QCD.

3.1.1 Tree-level potentials

The leading order potentials stem from the expansion of tree-level gauge boson exchanges between two heavy lines. In the wino case, there are three two-particle state charge sectors $|Q|=0,1,2$. In the neutral sector, the momentum space potential reads

$$\tilde{V}^{Q=0}(\mathbf{k}) = i\,T^{\chi\chi\to\chi\chi}(\mathbf{k}) = \begin{pmatrix} 0 & -\frac{4\pi\alpha_2}{\mathbf{k}^2+m_W^2} & -\frac{4\pi\alpha_2}{\mathbf{k}^2+m_W^2} \\ -\frac{4\pi\alpha_2}{\mathbf{k}^2+m_W^2} & -\frac{4\pi\alpha}{\mathbf{k}^2}-\frac{4\pi\alpha_2 c_W^2}{\mathbf{k}^2+m_Z^2} & 0 \\ -\frac{4\pi\alpha_2}{\mathbf{k}^2+m_W^2} & 0 & -\frac{4\pi\alpha}{\mathbf{k}^2}-\frac{4\pi\alpha_2 c_W^2}{\mathbf{k}^2+m_Z^2} \end{pmatrix}, \tag{3.4}$$

---

[4] Choosing the center of mass at a point $\mathbf{a}$ results in an irrelevant phase due to translational invariance. Even though the multipole expansion explicitly breaks translational invariance, such differences are always of higher-order in the EFT counting, and can be successively reduced by including higher-order terms.

[5] In principle, the leading ultrasoft correction stems from the A^0 field in the covariant derivative, which is formally of order $\mathcal{O}(\lambda^{1/2})$. However, as the ultrasoft photons only couple to the overall charge of a given two-particle state Q, this never plays a role in the indirect detection annihilation process. The contribution also vanishes for overall charged states, such as $\chi^0\chi^\pm$ or $\chi^\pm\chi^\pm$ as ultrasoft Wilson lines drop from the local four-fermion operators describing the annihilation. An explicit one-loop calculation also checked this in the wino case.

where the entries refer to the $\chi^0\chi^0$, $\chi^+\chi^-$, $\chi^-\chi^+$ states, respectively, and $T^{\chi\chi\to\chi\chi}$ denotes the T-matrix in the specific $2 \to 2$ scattering channel. In the single-charged and double-charged sectors, the momentum space potentials are

$$\tilde{V}^{Q=\pm1}(\mathbf{k}) = \begin{pmatrix} 0 & \frac{4\pi\alpha_2}{\mathbf{k}^2+m_W^2} \\ \frac{4\pi\alpha_2}{\mathbf{k}^2+m_W^2} & 0 \end{pmatrix} \quad \text{and} \quad \tilde{V}^{Q=\pm2}(\mathbf{k}) = \frac{4\pi\alpha}{\mathbf{k}^2} + \frac{4\pi\alpha_2 c_W^2}{\mathbf{k}^2+m_Z^2}\,. \tag{3.5}$$

The entries refer to $\chi^0\chi^\pm$, $\chi^\pm\chi^0$ and $\chi^\pm\chi^\pm$, respectively. To resum the potential exchanges and to build up the characteristic ladder diagrams [86], the Schrödinger equation has to be solved. Although this is, in principle, also possible in momentum space, it is more convenient to work with the position space representation of the potential

$$V(r = |\mathbf{x}|) = \int \frac{d^3\mathbf{k}}{(2\pi)^3}\, e^{i\mathbf{k}\cdot\mathbf{x}}\, \tilde{V}(\mathbf{k})\,. \tag{3.6}$$

The necessary Fourier transforms (cf. Appendix B) lead to Coulomb and Yukawa potentials only.

The basis chosen above is referred to as method-I following [86]. It has the advantage that spin and angular momentum configuration of the initial state is irrelevant. However, the basis is redundant, as it contains information on states that are physically equivalent, e.g., $\chi^\pm\chi^0$ and $\chi^0\chi^\pm$. It is therefore conventional in non-relativistic EFTs [39, 86] to decompose the two-particle states according to their spin and angular momentum ${}^{2S+1}L_J$. The two example states are therefore cast by a single state $\chi^0\chi^\pm$ of definite L, S. The basis without redundancies and definite partial wave and spin configuration, are referred to as method-II, and automatically implement symmetries, e.g., that the identical Majorana fermions cannot exist in a state of odd $J = L + S$. In coordinate space, we find for the charge $Q = 0$ sector

$$V^{Q=0}(r)({}^1S_0) = \begin{pmatrix} 0 & -\sqrt{2}\alpha_2\frac{e^{-m_W r}}{r} \\ -\sqrt{2}\alpha_2\frac{e^{-m_W r}}{r} & -\frac{\alpha}{r} - \alpha_2 c_W^2\frac{e^{-m_Z r}}{r} \end{pmatrix}, \tag{3.7}$$

$$V^{Q=0}(r)({}^3S_1) = \begin{pmatrix} 0 & 0 \\ 0 & -\frac{\alpha}{r} - \alpha_2 c_W^2\frac{e^{-m_Z r}}{r} \end{pmatrix}. \tag{3.8}$$

The other charge sectors, angular momentum and spin configurations follow similar decompositions. The rules for the transition and a more detailed discussion of the bases is given in [86].

The calculation of the soft one-loop correction to the potential proceeds along the same lines. The T-matrix element in Eq. (3.4) is evaluated at the one-loop order. Afterwards, the Fourier transform between position and momentum space (3.6) can be executed. The more complicated structures arising from the one-loop corrections, lead to additional structures. Finally, let us mention that the transition from method-I and method-II is independent of the loop-order of the potential.

3.2 The $\chi^+\chi^- \to \chi^+\chi^-$ channel

As an example, for the one-loop correction to the potential, we examine the channel $\chi^+\chi^- \to \chi^+\chi^-$. While other channels are calculated similarly $\chi^+\chi^- \to \chi^+\chi^-$ has the illustrative advantage that all possible diagram topologies contribute, and the effects of EWSB, e.g., through γ-Z-mixing play a delicate role. The diagrams that contribute are shown in Figure 3.1 and have to be understood as expanded in the soft region of the threshold expansion [105]. In practice, this

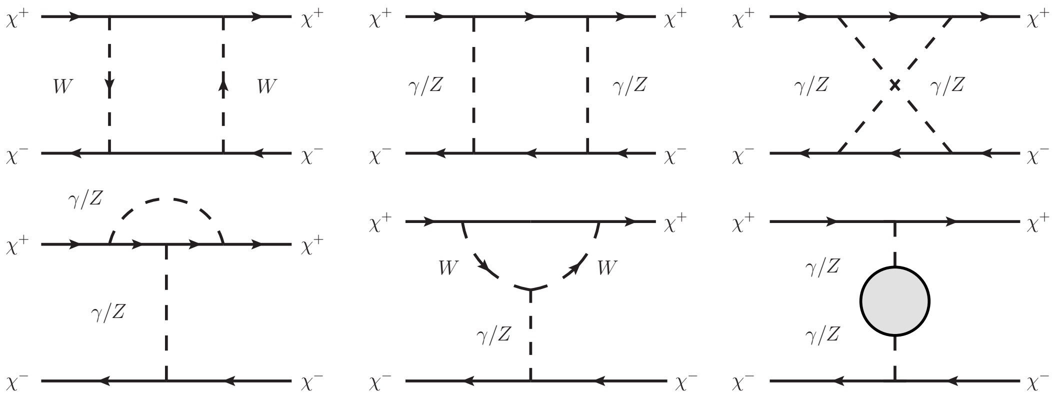

Figure 3.1: *The one-loop topologies contributing to the $\chi^+\chi^- \to \chi^+\chi^-$ channel excluding field renormalization, counterterm and tadpole topologies. Arrows on the fermion and gauge boson lines indicate electric charge flow.*

means that non-relativistic fermion propagators become static eikonal ones, as they are thrown off-shell by soft momenta (2.22). In principle, the mass difference appears together with the kinetic energy if $\chi^\pm$ propagators are considered. However, the mass difference drops as well, as $E \sim \delta m_\chi \sim m_\chi \lambda^2$. Note that in the ordinary box diagram, the pinched poles $l^0 \pm i\varepsilon$ are not picked up. The pinch poles are part of the LO potential iterations through the characteristic ladder diagrams (see above).

Topology-wise, the NLO correction calculation is very similar to the analogue calculation in QCD (where the one-loop correction is already known since the seventies [122, 123, 124]). However, the difficulties of the calculation in the SM+DM case arise from the fact that the gauge bosons now can be massive. Furthermore, the heavy fermionic states are not weak eigenstates, but instead, charge eigenstates. The results for the topologies are presented in Appendix A.

Box and crossed box diagrams cancel if they involve the same particles, similar to photon boxes in QED. Therefore, only the W-boson box leads to a non-zero contribution, as electric charge conservation forbids the crossed counterpart. The self-energies and counterterms mix the photon and Z, and contain all SM particles. We evaluate them in general covariant gauge using `FeynArts` [125], `FORMCalc` [126], and `Package-X` [127], and checked them against the Feynman gauge results (excluding tadpoles) in [128].

Finally, let us comment on the non-abelian vertex correction (second diagram in the second row of Figure 3.1). This diagram vanishes in Feynman gauge. Feynman gauge preserves the gauge boson polarization and the static interaction with the fermions projects on the gauge boson propagators' zero-component. In general covariant R_ξ-gauge the diagram is non-vanishing and required for a gauge parameter independent result. Therefore, the only missing piece is the employed renormalization scheme, which we discuss below.

3.2.1 The on-shell renormalization scheme

We renormalize all ultraviolet (UV) divergences in the on-shell scheme following [128].[6] As the characteristic scale of a potential momentum exchange is the electroweak scale, the input

---

[6] In the literature on electroweak corrections, several renormalization schemes are referred to as "on-shell" scheme, which differ by the input parameters and are suited for different applications. In high-energy applications, e.g., at colliders, for the DM potential or in the Sudakov resummation calculation presented in later Chapters, where the relevant energy scale is m_Z, it is customary to renormalize $\alpha_{\rm os}(m_Z)$ to avoid large logarithms of light fermion masses over the electroweak scale.

parameters at m_Z present a natural choice. They are

$$\alpha_{\text{os}}(m_Z),\, m_W,\, m_Z,\, m_t,\, m_H \tag{3.9}$$

and we set the CKM-matrix to unity. The counterterms in this scheme are

$$\delta m_W^2 = \text{Re}\,\Sigma_T^{WW}(m_W^2)\,, \qquad \delta m_Z^2 = \text{Re}\,\Sigma_T^{ZZ}(m_Z^2) \tag{3.10}$$

for the gauge boson masses, and

$$2\delta Z_e|_{\alpha_{\text{os}}(m_Z)} = \left.\frac{\partial \Sigma_T^{\gamma\gamma}(k^2)}{\partial k^2}\right|_{W,f=t}^{k^2=0} - \frac{2s_W}{c_W}\frac{\Sigma_T^{\gamma Z}(0)}{m_Z^2} + \text{Re}\frac{\Sigma_T^{\gamma\gamma}(m_Z^2)|_{f\neq t}}{m_Z^2} \tag{3.11}$$

for the electromagnetic coupling at the Z-resonance. The self-energies Σ_T are evaluated with all fermions massless, except the top quark. We use dimensional regularization and drop scaleless integrals. As we consider the light fermions massless, the charge must be renormalized at m_Z (or any other mass scale μ, where the approximation $m_f \ll \mu$ holds), as the Thomson limit does not exist if massless fermions are present. To provide a compact notation at later stages, the following counterterms for the Weinberg angle are useful

$$\begin{aligned}
s_W^{(0)} &= s_W + \delta s_W\,, \qquad c_W^{(0)} = c_W + \delta c_W\,,\\
\frac{\delta c_W}{c_W} &= \frac{1}{2}\left(\frac{\delta m_W^2}{m_W^2} - \frac{\delta m_Z^2}{m_Z^2}\right) = \frac{1}{2}\text{Re}\left(\frac{\Sigma_T^{WW}(m_W^2)}{m_W^2} - \frac{\Sigma_T^{ZZ}(m_Z^2)}{m_Z^2}\right)\,,\\
\frac{\delta s_W}{s_W} &= -\frac{c_W^2}{s_W^2}\frac{\delta c_W}{c_W}\,.
\end{aligned} \tag{3.12}$$

Finally, we comment on the treatment of tadpole diagrams in our scheme. In the electroweak theory, tadpole diagrams are omnipresent, and various approaches are possible. Regardless of the tadpole scheme adopted, their contribution has to cancel in physical observables [128], meaning we could drop tadpoles altogether. Nevertheless, we decide to keep the tadpoles, as gauge boson self-energies including tadpoles are gauge invariant on-shell [129]. Therefore, also the counterterms for couplings and gauge boson masses are gauge invariant, including tadpoles [129, 130]. This becomes useful in checking gauge invariance of the final result and makes the necessary cancellations more transparent.[7]

3.2.2 The momentum space potential at NLO

Combining the diagrams in Figure 3.1 with the on-shell scheme above, the one-loop correction to $\chi^+\chi^- \to \chi^+\chi^-$ reads

$$\begin{aligned}
\delta V_{\chi^+\chi^-\to\chi^+\chi^-} = &-\frac{4\pi\alpha_2 s_W^2}{\mathbf{k}^2}\Bigg[2\,I_{\text{vertex}}(\alpha_2 c_W^2, m_Z) + 2\,I_{3\,\text{gauge}}^{WW} + \frac{\Sigma_T^{\gamma\gamma}(-\mathbf{k}^2)}{\mathbf{k}^2}\\
&\qquad + 2\,\delta Z_e + 4\,\delta Z_{\chi^+}\Bigg]\\
&-\frac{4\pi\alpha_2 c_W^2}{\mathbf{k}^2 + m_Z^2}\Bigg[2\,I_{\text{vertex}}(\alpha_2 c_W^2, m_Z) + 2\,I_{3\,\text{gauge}}^{WW} + \frac{\Sigma_T^{ZZ}(-\mathbf{k}^2)}{\mathbf{k}^2 + m_Z^2} - \frac{\delta m_Z^2}{\mathbf{k}^2 + m_Z^2}
\end{aligned}$$

---

[7] If we would consider Higgs potentials, i.e., the Higgs mass would appear at tree-level, we would need to specify a tadpole renormalization constant, to properly define the Higgs mass at one-loop. As we do not consider Higgs potentials at any point in this thesis, and hence the Higgs mass only appears at one-loop, we omit the explicit tadpole renormalization.

$$
\begin{aligned}
&\left. +2\,\delta Z_e - \frac{2}{c_W^2}\frac{\delta s_W}{s_W} + 4\,\delta Z_{\chi^+} \right] \\
&- \frac{4\pi\alpha_2}{\mathbf{k}^2(\mathbf{k}^2+m_Z^2)}\,(-2 s_W c_W)\,\Sigma_T^{\gamma Z}(-\mathbf{k}^2) + I_{\text{box}}(\alpha_2, m_W; \alpha_2, m_W) \qquad (3.13)
\end{aligned}
$$

in terms of box, vertex and self-energy functions, and the counterterms. The explicit results can be found in Appendix A in Feynman and general covariant R_ξ-gauge. The first large square bracket corresponds to the correction to the Coulomb potential, namely the vertex corrections (A.6/A.19) and (A.7/A.22), the photon self-energy (A.26/A.27/A.28), the renormalization of the coupling (3.11) and the wave-function of the DM field (A.10). The equation numbers refer to the Feynman and R_ξ-gauge results, respectively. The second large bracket corrects the tree Z-exchange, which is analogous, apart from the additional term $\delta s_W/s_W$ from (3.12) due to the different coupling, and the δm_Z^2 mass counterterm (3.10). The last line originates from γ-Z-mixing (A.29/A.30/A.31) and the box term due to the exchange of two W-bosons (A.3/A.16). The latter two are the only terms that are not directly associated with one of the tree terms (though the γ-Z-mixing contribution could be partial-fractioned and grouped with the tree terms).

3.2.3 Gauge-invariance of the potential correction

The potential correction (3.13) is gauge invariant and pole-free. The inclusion of the tadpoles in the self-energies ensures that the on-shell self-energies are gauge parameter independent. Therefore the electric charge counterterm δZ_e, the Weinberg angle counterterms δs_W, and the Z-boson mass counterterm are δm_Z^2 are individually gauge invariant.

The explicit cancellation of gauge parameters between box, vertex, and self-energy topologies is analogous to the SM, but the respective topologies expanded in the soft and non-relativistic limits. For an in-depth discussion of the SM gauge cancellation, see, e.g., [130]. Furthermore, let us note that the cancellation between wave-function renormalization and vertex correction (lower left topology in Figure 3.1) is only partial. Contrary to the analogue, e.g., in HQET, the potential correction is derived in the mass basis, and not in the weak eigenbasis, which leaves remnant terms, exactly needed to cancel the gauge parameters of the other topologies.

For convenience at later stages, and as the fermionic self-energies are gauge invariant by themselves, we split the potential correction into three separate pieces:

1. An electroweak part, that includes all bosonic contributions, meaning the Yang-Mills and Higgs part of the SM self-energies, or put differently, all non-fermionic contributions to the SM self-energies. Note that the counterterms are split into pieces that originate from the electroweak self-energies and terms created by fermionic loops.
2. A light fermionic contribution that incorporates all massless fermion loops, except
3. the third generation quarks. They are separated for illustrative purposes, as they contain massive contributions due to massive top-loops (again also including the respective parts of the counterterms). Although taken massless, the bottom quark cannot be put into the light-fermionic category, as, e.g., in the W-self-energy, the top- and bottom-quarks are tied together, as they form an SU(2) doublet.

3.3 The remaining co-annihilation channels

The calculation of the NLO correction for the potentials in the other co-annihilation channels proceeds similarly. For the $\chi^0\chi^0 \to \chi^0\chi^0$ channel, where the TL potential is vanishing, only box

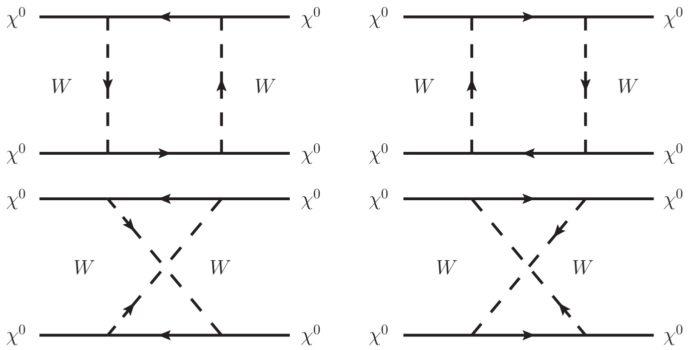

Figure 3.2: *All diagrams contributing to the $\chi^0\chi^0 \to \chi^0\chi^0$ channel. Arrows on the fermion and gauge boson lines indicate electric charge flow. The contribution vanishes due to the cancellation of box and crossed box graphs.*

and crossed diagrams are possible, cf. Figure 3.2. As the coupling of W's for the wino is purely vectorial (similar to photon boxes in QED), the diagrams only differ by an overall sign, and hence cancel, such that

$$\delta V_{\chi^0\chi^0\to\chi^0\chi^0} = 0\,. \tag{3.14}$$

In the off-diagonal channel $\chi^0\chi^0 \to \chi^+\chi^-$ due to W-exchange at TL, we find that the topologies depicted in Figure 3.3 contribute. The class of topologies is the same as in the $\chi^+\chi^- \to \chi^+\chi^-$ channel (adapted to the net exchange of one electric charge unit between the upper and lower fermion line). A special comment is in order on the box topologies: crossed box diagrams are not possible, as the χ^0 couples only to W-bosons. Therefore, the boxes are always comprised of one W and either photon or Z-boson. The complete correction in the off-diagonal channel reads

$$\begin{aligned}\delta V_{\chi^0\chi^0\to\chi^+\chi^-} = \;& \delta V_{\chi^+\chi^-\to\chi^0\chi^0} \\ = \;& -\frac{4\pi\alpha_2}{\mathbf{k}^2+m_W^2}\Bigg[2\,I_{\text{vertex}}(\alpha_2,m_W) + 2\left(I^{W\gamma}_{\text{3gauge}} + I^{WZ}_{3\text{ gauge}}\right) + 2\,\delta Z_{\chi^0} + 2\,\delta Z_{\chi^+} \\ & \qquad + \frac{\Sigma_T^{WW}(-\mathbf{k}^2)}{\mathbf{k}^2+m_W^2} - \frac{\delta m_W^2}{\mathbf{k}^2+m_W^2} + 2\delta Z_e - 2\frac{\delta s_W}{s_W}\Bigg] \\ & + I_{\text{box}}(\alpha_2,m_W;\alpha_2 c_W^2,m_Z) + I_{\text{box}}(\alpha_2,m_W;\alpha,0)\,.\end{aligned} \tag{3.15}$$

The terms correspond to the vertex corrections (A.6/A.19), the triple gauge vertex diagrams (A.7/A.21/A.20), the DM wave function renormalization constants for $\chi^0\chi^0$ (A.9/A.23) and $\chi^+\chi^-$ (A.10/A.24). Furthermore, there is the W-boson self-energy (A.36/A.37/A.38) and the mass counterterm (3.10), as well as the counterterms associated with the tree-level coupling (3.11/3.12). In the last line, the box topologies with unequal non-zero masses (A.2/A.16) and one vanishing mass (A.4/A.17) appear. The equation numbers, as before, refer to Feynman and R_ξ-gauge result, respectively.

With these channels, the Sommerfeld correction to the indirect detection cross-section can be calculated, as shown in [103] and later in this Chapter. For the relic abundance calculation, we furthermore need the $Q = \pm 1$ and $Q = \pm 2$ channels. In the $Q = \pm 1$ channel, $\chi^0\chi^\pm \to \chi^\pm\chi^0$, the topologies are similar to the $\chi^0\chi^0 \to \chi^+\chi^-$ channel, as the tree-level potentials are equal up to a minus sign. For the box topologies, only the crossed box is now possible due to charge flow, rendering the correction in this channel exactly the negative one of the $\chi^0\chi^0 \to \chi^+\chi^-$ channel

$$\delta V_{\chi^0\chi^\pm\to\chi^0\chi^\pm} = -\delta V_{\chi^0\chi^0\to\chi^+\chi^-}\,. \tag{3.16}$$

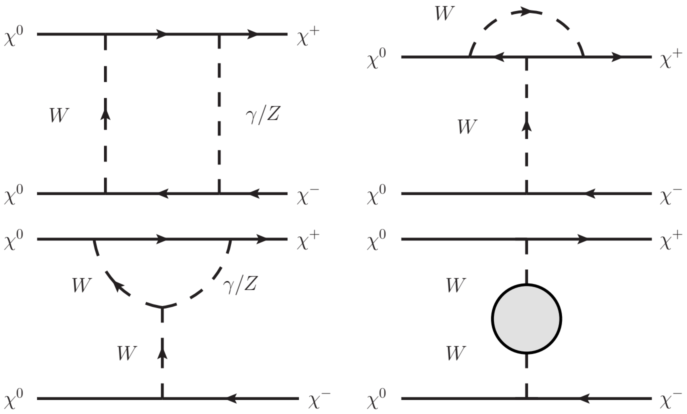

Figure 3.3: *The one-loop topologies contributing to the $\chi^0\chi^0 \to \chi^+\chi^-$ channel excluding field renormalization, counterterm and tadpole topologies. Arrows on the fermion and gauge boson lines indicate electric charge flow.*

Similarly, we find for the $Q = \pm 2$ channel $\chi^\pm\chi^\pm \to \chi^\pm\chi^\pm$, that the correction is identical up to an overall minus sign to the channel $\chi^+\chi^- \to \chi^+\chi^-$, as the same structures associated to the tree-level potential are involved. Furthermore, only the crossed W-box is now possible due to charge flow, compared with the ordinary W-box in the corresponding $Q = 0$ channel $\chi^+\chi^- \to \chi^+\chi^-$. Therefore, we find

$$\delta V_{\chi^\pm\chi^\pm \to \chi^\pm\chi^\pm} = -\delta V_{\chi^+\chi^- \to \chi^+\chi^-} \,. \tag{3.17}$$

The equality of the correction for the channels for $|Q| = 1, 2$ with the corresponding $Q = 0$ channels is a first manifestation that the correction is only tied to the gauge boson exchanged at tree-level, as will be proven in Chapter 4. The gauge invariance for all the co-annihilation channels can be checked as for the $\chi^+\chi^- \to \chi^+\chi^-$ channel above. Finally, we also check for all channels that in the limit $m_W \to m_Z$ (i.e., $s_W \to 0, c_W \to 1$) we reproduce previously known results for the Higgsed SU(2) theory [131, 132]. More precisely, we compared the unrenormalized potentials with Eq. 16 of [131], analytically. The renormalized result is not compared, as [131] does not fully specify the renormalization scheme.

3.4 Analysis of the channels

The results of the previous paragraphs allow an analysis of the potential correction in various limits. For practical applications, such as calculating the Sommerfeld enhancement, the position space representation of the potentials is most convenient. However, as not all Fourier transforms are analytically possible, we also consider the momentum space representation to understand the potential correction's asymptotic behaviour. The analytic and numerical transforms required to obtain the position space potential at NLO are given in Appendix B.

In the following, we discuss the two non-zero charge neutral channels, as the other channels are either vanishing or related to those by a minus sign. The results and asymptotic behaviours also have further applications, as they will constitute the full correction for the pure SU(2) projection of the potential, as is detailed in the following Chapter 4.

The result for the $\chi^+\chi^- \to \chi^+\chi^-$ channel, i.e., the exchange of γ and Z-boson with coupling to T^3 at tree-level is shown in Figure 3.4. The off-diagonal W-boson exchange potential at tree-level in the $\chi^0\chi^0 \to \chi^+\chi^-$ channel, is shown in Figure 3.5. The results were obtained using

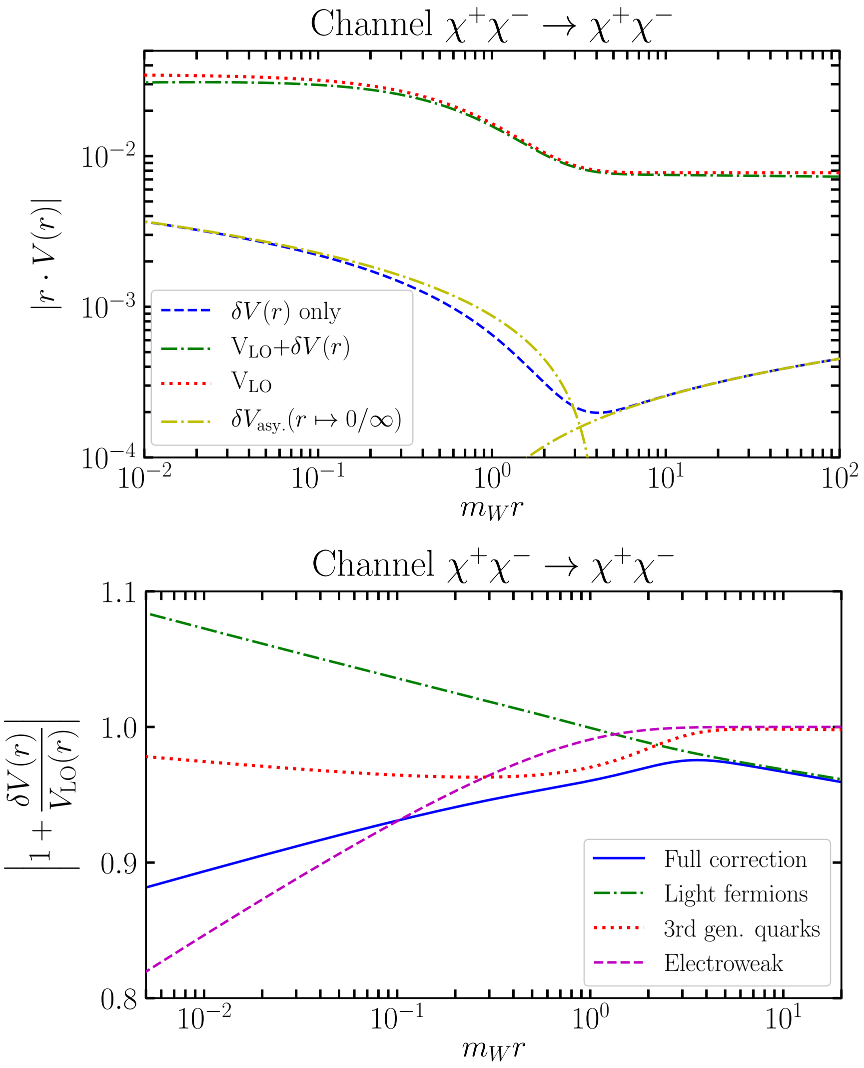

Figure 3.4: *The NLO correction to the potential in the channel $\chi^+\chi^- \to \chi^+\chi^-$. The upper panel shows the modulus of the potential $|r \cdot V(r)|$ for the LO and NLO potential, the NLO contribution only, and the small and large-distance asymptotic behaviour. In the lower panel, we show the ratio of the full NLO potential to the LO potential (blue solid), and separately for the three gauge invariant pieces identified in the text (other curves).*

the following input parameters for the numerics and plots: the on-shell electromagnetic coupling $\alpha = \alpha_{\mathrm{os}}(m_Z) = 1/128.943$ at the Z-mass, and the gauge boson masses $m_W = 80.385\,\mathrm{GeV}$ and $m_Z = 91.1876\,\mathrm{GeV}$. The SU(2) coupling and the Weinberg angle are determined by the on-shell relations $\alpha_2 = \alpha_{\mathrm{os}}(m_Z)/s_W^2$ and $c_W = m_W/m_Z$. Furthermore, we need the Higgs-boson and top-quark mass, for which we take the on-shell masses $m_H = 125\,\mathrm{GeV}$ and $m_t = 173.1\,\mathrm{GeV}$. The uncertainty of these parameters is small enough to be ignored for practical purposes, except for the top-quark mass, as discussed below.

3.4.1 The asymptotic behaviour of the NLO potentials

To assess the NLO potentials' behaviour, we start by examining the asymptotic regions of large and small momentum exchange or small and large distance, respectively. As not all Fourier

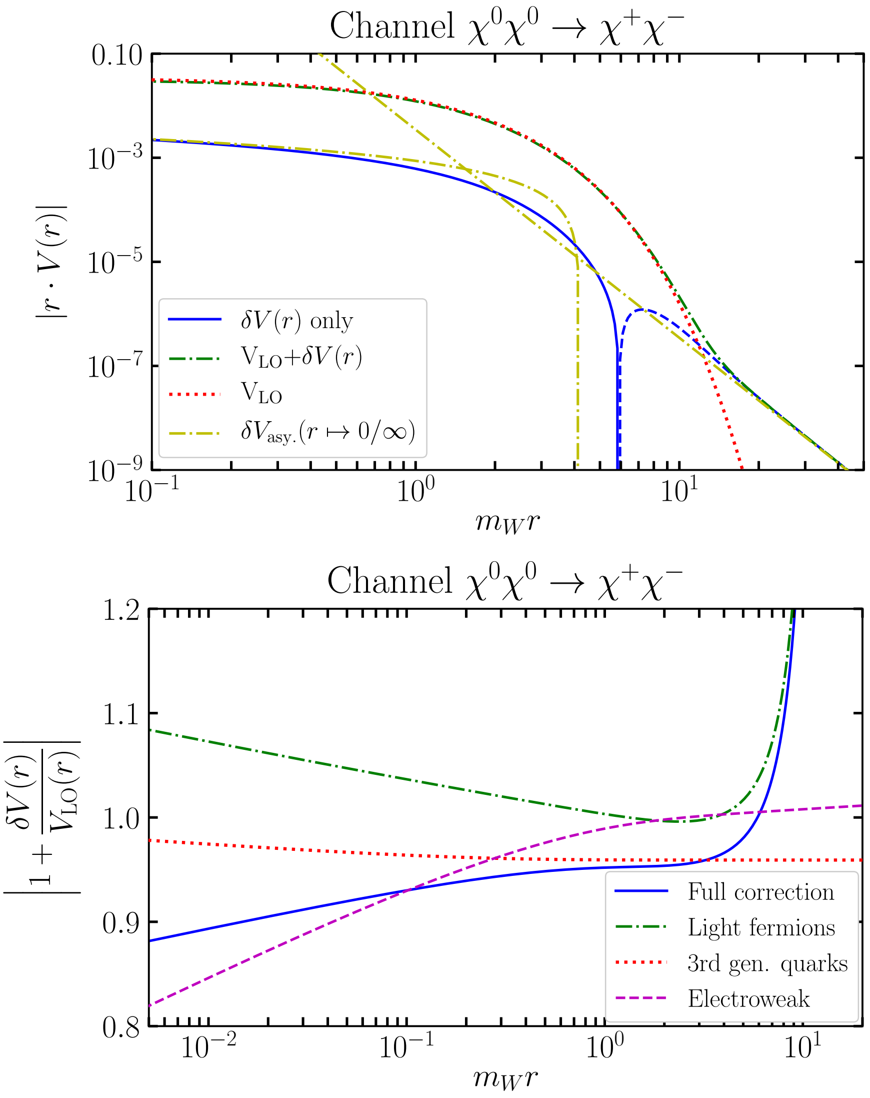

Figure 3.5: *The NLO correction to the potential in the channel $\chi^0\chi^0 \to \chi^+\chi^-$. The upper panel shows the modulus of the potential $|r \cdot V(r)|$ for the LO and NLO potential, the NLO contribution only and the asymptotic behaviours. The change from solid to dashed for the blue $\delta V(r)$ curve marks its change of sign. In the lower panel, we show the ratio of the NLO to the LO potential for the full correction, and for the three gauge invariant pieces, which illustrates their different behaviour.*

transforms are analytically available, we discuss the results in $|\mathbf{k}|$-space, where we have full analytic control of each term. We do so for each of the gauge invariant pieces discussed above and emphasize the origins of the corrections and the respective dominant contributions.

The $r \to 0$ / $\mathbf{k}^2 \to \infty$ limit

The large momentum exchange region $|\mathbf{k}| \to \infty$ shows the same analytic behaviour for both the $\chi^0\chi^0 \to \chi^+\chi^-$ and $\chi^+\chi^- \to \chi^+\chi^-$ channels, as the SU(2) symmetry is effectively restored in this limit. For the light fermionic contribution, we find

$$\delta V_{\text{light ferm.}}(\mathbf{k}^2 \to \infty) = -\frac{3\alpha_2^2}{\mathbf{k}^2}\left(\ln\frac{\mathbf{k}^2}{m_Z^2} - \frac{c_W^2}{s_W^2}\ln\frac{m_W^2}{m_Z^2}\right) . \tag{3.18}$$

This is similar to the QED/QCD analogue, as the prefactor of the logarithmic term is proportional to the SU(2) beta function contribution of light fermions. Similarly, for the third generation quarks, the asymptotic behaviour is

$$\delta V_{\text{3rd gen. quarks}}(\mathbf{k}^2 \to \infty) = -\frac{\alpha_2^2}{\mathbf{k}^2}\left(\ln\frac{\mathbf{k}^2}{m_Z^2} + A(m_W, m_Z, m_t)\right) , \tag{3.19}$$

where the prefactor is again the SU(2) beta function contribution of the third generation quarks. The function $A(m_W, m_Z, m_t)$ is a complicated function of the W-, Z- and top-mass given in Appendix C. To permille accuracy in the interval of ±10 GeV around the on-shell top mass $m_{t,\text{os}} = 173.1\,\text{GeV}$ it is approximated by $A(m_W, m_Z, m_t) = -17.1808 - 4.99861 \cdot 10^{-4}\,\text{GeV}^{-2} \times (m_t^2 - m_{t,\text{os}}^2)$. Finally, the electroweak (i.e., gauge and Higgs-boson) contribution is

$$\delta V_{\text{electroweak}}(\mathbf{k}^2 \to \infty) = \frac{\alpha_2^2}{\mathbf{k}^2}\left(\frac{43}{6}\ln\frac{\mathbf{k}^2}{m_Z^2} + B(m_W, m_Z, m_H)\right) , \tag{3.20}$$

where to this piece, contrary to the fermionic pieces, also the non-self-energy topologies contribute. The prefactor of the logarithm is the non-fermionic part of the SU(2) beta function, which underlines the analogy to QED/QCD. $B(m_W, m_Z, m_H)$ is a function of the Higgs, W- and Z-mass given in Appendix C and evaluates for on-shell parameters to -1.03577. The analytic result displays an interesting manifestation of the screening theorem [133]. Even though individual terms are Higgs-mass dependent up to m_H^6, B itself is only logarithmically dependent on the Higgs mass m_H.[8] Therefore, any possible Higgs mass uncertainty is, in practice, negligible.

In order to assemble the full asymptotic behaviour, we define

$$\Delta = \frac{3c_W^2}{s_W^2}\ln\frac{m_W^2}{m_Z^2} - A(m_W, m_Z, m_t) + B(m_W, m_Z, m_H) , \tag{3.21}$$

which allows to write the $r \to 0$ short-distance asymptotics of the position space potential as

$$\begin{aligned}\delta V^{r\to 0}_{\chi^+\chi^-\to\chi^+\chi^-}(r) &= \delta V^{r\to 0}_{\chi^0\chi^0\to\chi^+\chi^-}(r) \\ &= \frac{\alpha_2^2}{2\pi r}\left(-\beta_{0,\text{SU(2)}}\left(\ln(m_Z\, r) + \gamma_E\right) + \frac{1}{2}\Delta\right) \\ &\approx \frac{\alpha_2^2}{2\pi r}\left(-\beta_{0,\text{SU(2)}}\ln(m_Z\, r) + 4.92585\right) ,\end{aligned} \tag{3.22}$$

where γ_E is the Euler-Mascheroni constant and $\beta_{0,\text{SU(2)}} = 43/6 - 1 - 3 = 19/6$. Of the numerical coefficient, the light-fermion term makes up -1.3188, the third generation quarks 8.59038, the electroweak terms -0.51788, and Euler-Mascheroni constant associated with the logarithm

---

[8] Note though that B (and for that matter all other such functions in the asymptotic behaviour) is derived under the assumption that imaginary and real parts can be extracted, as for SM masses. This means using a Higgs mass of, e.g., 115 GeV or 135 GeV, in the function B is valid. However, if the Higgs mass, would be taken below the W-mass, the extraction of real/imaginary parts is different, and B takes a different form than the one given in Appendix C. For realistic mass values, all functions take the form given in Appendix C. In any case, one can always go back to the expressions Eqs. (3.13) and (3.15), which are valid for arbitrary masses.

-1.82785. The identical short distance behaviour in both channels, can also be seen by comparing Figures 3.4 and 3.5.

The logarithm $\ln(m_Z r)$, in principle, poses a conceptual problem as it grows arbitrarily large for $r \to 0$, even exceeding the tree-level potential, and hence constituting a breakdown of perturbation theory. This can be dealt with in the $\overline{\text{MS}}$ renormalization scheme discussed later, which absorbs these logarithms. For the practical calculation of the Sommerfeld effect, using the on-shell potentials presents no problem. The dominant contribution to the solution of the Schrödinger equation comes from the region $m_Z r \sim 1$, as necessitated by the construction of the EFT and the difference between renormalization schemes is of higher-order in this region. We also checked this numerically.

The $r \to \infty$ / $\mathbf{k}^2 \to 0$ limit

In a similar fashion, we can analyze the opposite limit, namely $r \to \infty$ / $\mathbf{k}^2 \to 0$. In this case, however, the channels behave differently as we probe the IR limit of the potential and become sensitive to the underlying gauge bosons and their masses. Whilst before, in the $r \to 0$ / $\mathbf{k}^2 \to \infty$, i.e., the UV-limit, the gauge boson masses are irrelevant, and electroweak symmetry is essentially restored, making the correction universal. We begin by examining the $\chi^+\chi^- \to \chi^+\chi^-$ channel. For the light-fermionic contribution, we find

$$\delta V^{(+-)(+-)}_{\text{light ferm.}}(\mathbf{k}^2 \to 0) = -\frac{76}{9}\frac{\alpha^2}{\mathbf{k}^2}\ln\frac{\mathbf{k}^2}{m_Z^2} + \mathcal{O}(\mathbf{k}^0)\,, \tag{3.23}$$

where the prefactor is the light-fermionic contribution to the electromagnetic beta function, by all massless fermions except the bottom quark. The behaviour underlines, the cutoff of the Z-boson at tree-level and the takeover of the long-range electromagnetic Coulomb potential. Similarly, the third-generation quark contribution is dominated by the massless $b\bar{b}$-quark loops, resulting in

$$\delta V^{(+-)(+-)}_{\text{3rd gen. quarks}}(\mathbf{k}^2 \to 0) = -\frac{4}{9}\frac{\alpha^2}{\mathbf{k}^2}\ln\frac{\mathbf{k}^2}{m_Z^2} + \mathcal{O}(\mathbf{k}^0) \tag{3.24}$$

where the massive top contribution is exponentially suppressed in the large r limit. The electroweak part of the potential is also sub-leading, as all loops that appear in the calculation are massive. The leading term for $\mathbf{k}^2 \to 0$ is given by

$$\delta V^{(+-)(+-)}_{\text{electroweak}}(\mathbf{k}^2 \to 0) = \frac{\alpha_2^2}{m_W^2}\,C(m_W, m_Z, m_H)\,, \tag{3.25}$$

where the function $C(m_W, m_Z, m_H)$ is given in Appendix C and for on-shell parameters evaluates to 3.67219. Even though it does not contribute to the asymptotic behaviour, the result is a good check of the calculation through its m_H dependence, which is only logarithmic. As the four fermion scattering amplitude in the full theory needs to obey the screening theorem [133], the screening property is inherited if the amplitude is expanded in the non-relativistic/soft limit, which is equivalent to the EFT diagrams.

This means that combining all separately gauge invariant contributions, the correction is dominated by the massless fermion loops in $\Sigma_T^{\gamma\gamma}$ correcting the photonic Coulomb potential, and hence we obtain the purely abelian asymptotic behaviour

$$\delta V^{r\to\infty}_{\chi^+\chi^-\to\chi^+\chi^-}(r) = \frac{\alpha^2}{2\pi r}(-\beta_{0,\text{em}})(\ln(m_Z r) + \gamma_E)\,, \tag{3.26}$$

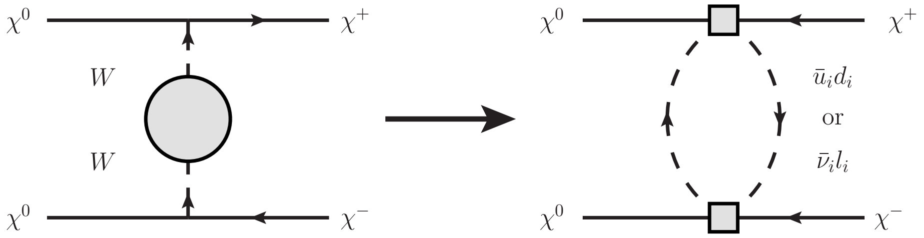

Figure 3.6: *The relevant one-loop self-energy, that in the large distance, small momentum exchange region, gives the long range asymptotic* (3.28) *in the channel* $\chi^0\chi^0 \to \chi^+\chi^-$.

where $\beta_{0,\text{em}} = -80/9$ is the electromagnetic beta function coefficient for all SM fermions except the top quark. The asymptotic behaviour starts to dominate the NLO correction around $m_W r \geq 5$ as can be seen in Figure 3.4.

For the off-diagonal channel $\chi^0\chi^0 \to \chi^+\chi^-$ the asymptotic behaviour also originates from the massless fermion loops. The relevant terms in the expansion are

$$\delta V^{(00)(+-)}_{\text{light ferm.}}(\mathbf{k}^2 \to 0) = \frac{1}{3}\, n_{\text{ld}}\, \alpha_2^2 \ln \frac{\mathbf{k}^2}{m_W^2} \left(\frac{m_W^2}{(\mathbf{k}^2 + m_W^2)^2} - \frac{1}{\mathbf{k}^2 + m_W^2} \right), \tag{3.27}$$

which scales as $\mathbf{k}^2 \ln(\mathbf{k}^2/m_Z^2)$ for $\mathbf{k}^2 \to 0$ and we dropped the constant term that originates from exponentially suppressed terms in position space. n_{ld} denotes the number of massless fermion doublets, in our case $n_{\text{ld}} = n_{\text{lepton doub.}} + n_{\text{quark doub.}} \cdot N_c = 9$. The Fourier transforms for the individual terms are discussed in detail in Appendix B. After expanding for large r, we find

$$\delta V^{(00)(+-),r\to\infty}_{\text{light ferm.}}(r) = -\frac{n_{\text{ld}}\, \alpha_2^2}{\pi m_W^4 r^5} = -\frac{12\alpha_2}{\pi m_W^4 r^5}\, \frac{\Gamma_W}{m_W}\,. \tag{3.28}$$

where Γ_W is the width of the W-boson at one-loop in the EFT. The power-like behaviour is a consequence of taking the SM fermions except the top quark to be massless. Schematically, the diagrammatic explanation for the long-range potential is shown in Figure 3.6.[9] The W-width $m_W\Gamma_W = \text{Im}\,\Sigma_T^{WW}(m_W^2)$ originates, in this case, as it is entirely composed of the massless fermion doublets. Only the light-fermionic terms have a non-vanishing imaginary part. In the W-boson self-energy, the only term that exhibits an imaginary part stems from massless logarithms $\ln \mathbf{k}^2$ that are responsible for the r^{-5} behaviour, which explains why the prefactor of these logarithms coincides with the width.

The behaviour of the NLO potential in this region constitutes formally a breakdown of perturbation theory,[10] as for $r \gg 1/m_W$, the correction exceeds the exponentially decreasing tree-level potential, as can be seen in Figure 3.5. In the phenomenological applications discussed later, this does not pose a problem, as the Sommerfeld effect is dominated by the region $m_W r \sim 1$. We numerically checked that the region where the power-like asymptotic behaviour dominates the NLO potential does not affect the Sommerfeld factors significantly.

The light fermions are in reality, of course, not massless. A formal treatment of the $r \to 0$ limit would require a further matching step, where we integrate out the W-mass, as depicted in Figure 3.6. The resulting theory has the same r^{-5} asymptotic as predicted above. Subsequently,

---

[9] A similar result is known for the long-range force due to massless neutrinos in atomic physics [134]. While the long-range force is universal, the dependence on fermion mass is different for Dirac, and Majorana fermions [135] due to different coupling structures.

[10] The r^{-5} tail is physical, as at one-loop the light-fermions enter the potential for the first time. From a perturbation theory standpoint though a different EFT would need to be employed.

one could then match onto theories where the light SM fermion doublets become successively massive. The fermionic contributions are then cut off at distances $r \sim 1/m_f$, where m_f is the mass of the fermion in question, similar to the third-generation quark contribution discussed below.

The third-generation quark and the electroweak contribution are subdominant for $r \to 0$, as they start with a constant term in the expansion around $\mathbf{k}^2 = 0$ and are therefore exponentially suppressed.[11] Explicitly, we find

$$\delta V^{(00)(+-)}_{\text{3rd gen. quarks}}(\mathbf{k}^2 \to 0) = \frac{\alpha_2^2}{m_W^2}\, D(m_W, m_Z, m_t)\,, \tag{3.29}$$

$$\delta V^{(00)(+-)}_{\text{electroweak}}(\mathbf{k}^2 \to 0) = \frac{\alpha_2^2}{m_W^2}\, E(m_W, m_Z, m_H)\,, \tag{3.30}$$

where the functions D, E are given in Appendix C and evaluate for on-shell values to 14.6515 and 2.76239, respectively. Again the screening theorem is fulfilled by these expressions. Furthermore, let us note another breakdown of perturbation theory in these contributions (and in the light-fermion terms). The gauge boson mass renormalization behaves as

$$\frac{\delta m_W^2}{(\mathbf{k}^2 + m_W^2)^2} \quad \to \quad \frac{\delta m_W^2}{8\pi m_W}\exp(-m_W r)\,, \tag{3.31}$$

compared to the tree-level $\exp(-m_W r)/r$, therefore at some point exceeding the tree-level contribution. However, these terms are subdominant compared to the light-fermion tail and hence contribute even less to the Sommerfeld factor. Dyson resummation would cure this behaviour and result in potentials of the form $\exp(-(m_W^2 + \delta m_W^2)^{1/2} r)/r$.

The full asymptotic behaviour for $r \to \infty$ in the off-diagonal $\chi^0\chi^0 \to \chi^+\chi^-$ channel is given by the light-fermionic contribution

$$\delta V^{r\to\infty}_{\chi^0\chi^0\to\chi^+\chi^-}(r) = -\frac{n_{\text{ld}}\,\alpha_2^2}{\pi m_W^4 r^5} = -\frac{12\alpha_2}{\pi m_W^4 r^5}\,\frac{\Gamma_W}{m_W}\,, \tag{3.32}$$

which explains the steep increase around $m_W r \approx 10$ in Figure 3.5. Furthermore, in this Figure we also note the exponential suppression of the electroweak and third-generation quark contributions.

3.4.2 The complete NLO corrections

The exact NLO potential interpolates between the $r \to 0$ and $r \to \infty$ asymptotics. The most significant deviations from the asymptotics are observed around $m_W r \sim 1$, which is the crucial region to accurately determine the Sommerfeld effect. Therefore it is not sufficient to simply glue the asymptotics together. For an accurate determination, either the full numerically calculated potential or the fitting functions provided in [103] have to be used. For the off-diagonal potentials in (3.7) and (3.8), they read

$$\begin{aligned}
\delta V^{\text{fit}}_{\chi^0\chi^0\to\chi^+\chi^-} &= -\delta V^{\text{fit}}_{\chi^0\chi^\pm\to\chi^\pm\chi^0} \\
&= \frac{2595\alpha_2^2}{\pi r} \times \begin{cases} \exp\left[-\dfrac{79\left(L-\frac{787}{12}\right)\left(L-\frac{736}{373}\right)\left(L-\frac{116}{65}\right)\left(L^2-\frac{286L}{59}+\frac{533}{77}\right)}{34\left(L-\frac{512}{19}\right)\left(L-\frac{339}{176}\right)\left(L-\frac{501}{281}\right)\left(L^2-\frac{268L}{61}+\frac{38}{7}\right)}\right], & x < x_0 \\[2ex] -\exp\left[-\dfrac{13267\left(L-\frac{76}{43}\right)\left(L-\frac{28}{17}\right)\left(L+\frac{37}{30}\right)\left(L^2-\frac{389L}{88}+\frac{676}{129}\right)}{5\left(L-\frac{191}{108}\right)\left(L-\frac{256}{153}\right)\left(L+\frac{8412}{13}\right)\left(L^2-\frac{457L}{103}+\frac{773}{146}\right)}\right], & x > x_0 \end{cases}
\end{aligned} \tag{3.33}$$

---

[11] Note that also the light-fermionic contribution, exhibits a constant exponentially suppressed term. However, the difference for third-generation quarks and the electroweak contribution is that no terms of the form $\ln \mathbf{k}^2$ appear in the expansion at higher orders, which could cause long-range potentials.

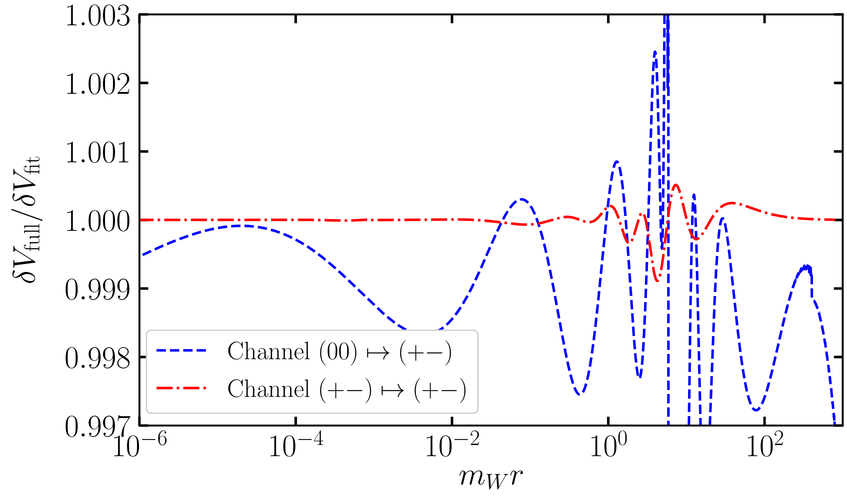

Figure 3.7: *Ratio of the numerical Fourier transform of the potential correction to the fitting functions in the variable $x = m_W r$ for the channel $(00) \to (+-)$ (blue/dashed) and $(+-) \to (+-)$ (red/dot-dashed). The relative difference stays in the permille range for both channels, except for a small point around $x_0 = 555/94$, which is due to a slightly different position in the sign change of $\delta V_{\rm full}$ and $\delta V_{\rm fit}$.*

and for the diagonal ones

$$\begin{aligned}\delta V^{\rm fit}_{\chi^+\chi^-\to\chi^+\chi^-} &= -\delta V^{\rm fit}_{\chi^\pm\chi^\pm\to\chi^\pm\chi^\pm}\\ &= \frac{\delta V^{r\to\infty}_{\chi^+\chi^-\to\chi^+\chi^-}}{1+\frac{32}{11}x^{-\frac{22}{9}}} + \frac{\delta V^{r\to 0}_{\chi^+\chi^-\to\chi^+\chi^-}}{1+\frac{7}{59}x^{\frac{61}{29}}} + \frac{\alpha}{r}\left[\frac{-\frac{1}{30}+\frac{4}{135}\ln x}{1+\frac{58}{79}x^{-\frac{17}{15}}+\frac{1}{30}x^{\frac{119}{120}}+\frac{8}{177}x^{\frac{17}{8}}}\right],\end{aligned} \tag{3.34}$$

where $x = m_W r$, $x_0 = 555/94$ and $L = \ln x$. The fitting functions provide permille accuracy for the Sommerfeld factors relevant in indirect detection [103] (cf. Section 3.5). In general, the correction to the Coulomb and Z-Yukawa potential is closer to the full numerical result. The reason is the sign change for the W-Yukawa potential at $x_0 = 555/94$. This sign change is set by the distance where the light-fermion contribution starts to dominate the correction.

The accuracy of the full numerical Fourier transform compared to the fitting functions is shown in Figure 3.7. The fitting functions approximate the full result to better than a permille for the channel $\chi^+\chi^- \to \chi^+\chi^-$ and a few permille in the case of $\chi^0\chi^0 \to \chi^+\chi^-$. The slightly worse performance of the fitting function in the latter channel originates from the fact that two fitting functions are needed to account for the solution's sign change at x_0. Using the fitting functions provides accurate results at the sub permille level (off-resonance) and on the few permille level on resonance, as will be shown in Section 3.5.

The full correction for very small (large) r is significant due to the logarithmic (power-like) behaviour. However, these regions contribute little to Sommerfeld factors. In the relevant region $m_W r \sim 1$, the NLO correction to the potentials is in the few percent range. The interplay of the various corrections determines the complete NLO result. For example, for $r \to 0$ in both, the $\chi^+\chi^- \to \chi^+\chi^-$ and $\chi^0\chi^0 \to \chi^+\chi^-$ channels, the correction due to light fermions is of opposite sign to the electroweak contribution.

3.4.3 Scheme conversion to $\overline{\rm MS}$-couplings

Perturbation theory breaks down at short distances for the results above, due to the short-distance SU(2)-beta function logarithms. This behaviour originates in on-shell renormalization at the scale m_Z, which is suitable for calculating the Sommerfeld effect but leads to logarithms of the form $\ln(m_Z\, r)$.

To absorb these running coupling logarithms at small distances, a change of renormalization scheme to the $\overline{\text{MS}}$-scheme using running couplings evaluated at the scales $\mu = e^{-\gamma_E}/r$ or $\mu^2 = \mathbf{k}^2$ in position or momentum space, respectively, is necessary. To this end, the on-shell coupling is converted to the $\overline{\text{MS}}$-scheme using

$$\begin{aligned} \alpha_{\overline{\text{MS}}}(m_Z) &= \alpha_{\text{os}}(m_Z)\left[1 + 2\,\delta Z_e|_{\alpha_{\text{os}}(m_Z)} - 2\,\delta Z_e|_{\alpha_{\overline{\text{MS}}(m_Z)}}\right] \\ &= \alpha_{\text{os}}(m_Z)\left[1 + \frac{\alpha_{\text{os}}(m_Z)}{4\pi}\left(\frac{382}{27} + 7\ln\frac{m_W^2}{m_Z^2} - \frac{16}{9}\ln\frac{m_t^2}{m_Z^2}\right)\right] \\ &= 0.00780372\,, \end{aligned} \tag{3.35}$$

with on-shell renormalization factors given in Section 3.2.1. Furthermore, we need the Weinberg angle in the $\overline{\text{MS}}$ scheme.[12] In the literature, one finds different definitions of the $\overline{\text{MS}}$ Weinberg angle. We choose [136, 137]

$$s^2_{W,\overline{\text{MS}}}(m_Z) = s^2_{W,\text{os}}(m_Z)\left[1 + 2\,\frac{\delta s_W}{s_W}\bigg|_{\text{os}} - 2\,\frac{\delta s_W}{s_W}\bigg|_{\overline{\text{MS}}}\right] = 0.232486\,, \tag{3.36}$$

where δs_W was defined in (3.12) and on-shell parameters used for all terms involved. For numerics in the $\overline{\text{MS}}$ scheme, we use the $\overline{\text{MS}}$ top mass $\overline{m}_t(\overline{m}_t) = 163.35\,\text{GeV}$. To keep notation short, from here on couplings in the $\overline{\text{MS}}$-scheme are denoted by a hat.[13]

Using the above input values, the issue of large short-distance logarithms for $r \to 0$ can be revisited. To do so, we convert the $\overline{\text{MS}}$-coupling at m_Z to the coupling at an arbitrary scale μ by expanding the running couplings to fixed order. For the two couplings $\hat{\alpha}_1, \hat{\alpha}_2$, this means

$$\hat{\alpha}_1(\mu) = \hat{\alpha}_1(m_Z) + \frac{\hat{\alpha}_1^2(m_Z)}{4\pi}\beta_{0,Y}\ln\frac{m_Z^2}{\mu^2} + \dots \tag{3.38}$$

$$\hat{\alpha}_2(\mu) = \hat{\alpha}_2(m_Z) + \frac{\hat{\alpha}_2^2(m_Z)}{4\pi}\beta_{0,\text{SU(2)}}\ln\frac{m_Z^2}{\mu^2} + \dots \tag{3.39}$$

and hence the Weinberg angles can be expanded as

$$\hat{s}_W^2(\mu) = \hat{s}_W^2(m_Z) + \frac{\hat{\alpha}_2(m_Z)\hat{s}_W^2(m_Z)}{4\pi}\left[\beta_{0,Y}\hat{s}_W^2(m_Z) - \beta_{0,\text{SU(2)}}\hat{c}_W^2(m_Z)\right]\ln\frac{m_Z^2}{\mu^2} + \dots \tag{3.40}$$

---

[12] Note that to absorb the logarithms in the case of the wino, a scheme conversion of only α_2 would be sufficient. However, in view of the more general models examined in Chapter 4 that will involve α_1 and α_2 (or respective Weinberg angles), we choose to convert α and s_W (or implicitly α_1, α_2).

[13] Note that to make the $\overline{\text{MS}}$-scheme, in which two couplings are converted, consistent one of the gauge bosons masses becomes a derived quantity. By convention m_W is chosen, as it is known to a lesser precision than the Z-mass,

$$\hat{m}_W^2(\mu) = \hat{c}_W^2(\mu)m_Z^2\,. \tag{3.37}$$

Note, however, that for the plots, we use m_W at its on-shell value. For short-distances, the gauge boson masses play a subleading role, making possible differences small. Furthermore, using $\hat{m}_W$ also makes the momentum to position space conversion a nuisance, as now also the denominators of propagators depend on $\ln\mathbf{k}^2$. As the difference in the region $r \to 0$, where the $\overline{\text{MS}}$-scheme is the more appropriate renormalization scheme, is anyways of higher-order, and we do not use the $\overline{\text{MS}}$-scheme for numerical predictions of observables related to the potential, restricting to the on-shell value does not change the analysis considerably.

and analogously for $\hat{c}_W^2$. Therefore using the $\overline{\text{MS}}$-scheme at scale $\mu^2 = \mathbf{k}^2$, we can write the tree-level W-Yukawa potential in momentum space as

$$-\left.\frac{4\pi\hat{\alpha}_2(\mu)}{\mathbf{k}^2+m_W^2}\right|_{\mu^2=\mathbf{k}^2} = -\frac{4\pi\hat{\alpha}_2(m_Z)}{\mathbf{k}^2+m_W^2}\left(1+\frac{\hat{\alpha}_2(m_Z)}{4\pi}\beta_{0,\text{SU}(2)}\ln\frac{\mathbf{k}^2}{m_Z^2}\right) . \tag{3.41}$$

For $|\mathbf{k}| \to \infty$, this exactly cancels the logarithmic contribution in the asymptotic behaviour (3.22). The cancellation is also visible for each of the separately gauge invariant corrections, when splitting the beta function into $\beta_{0,\,\text{SU}(2)} = 19/6 = 43/6 - 1 - 3$, where terms correspond to the electroweak, third-generation quark, and light-fermion contributions. In position space, the expansion for $\mu = e^{-\gamma_E}/r$ leads to,

$$-\left.\frac{\hat{\alpha}_2(\mu)}{r}e^{-m_W r}\right|_{\mu=e^{-\gamma_E}/r} = -\frac{\hat{\alpha}_2(m_Z)}{r}e^{-m_W r}\left(1-\frac{\hat{\alpha}_2(m_Z)}{2\pi}\beta_{0,\text{SU}(2)}\ln\left(m_Z r e^{\gamma_E}\right)\right) , \tag{3.42}$$

which cancels the logarithms for $r \to 0$. The $\overline{\text{MS}}$ scheme presented here applies to momenta and distances of $\mathbf{k}^2 > m_W^2$ and $1/r > m_W$.[14]

For the tree-level Coulomb and Z-Yukawa potential, the logarithms for $r \to 0$ are also cancelled by switching to $\overline{\text{MS}}$

$$-\left.\frac{4\pi\hat{\alpha}(\mu)}{\mathbf{k}^2}\right|_{\mu^2=\mathbf{k}^2} = -\frac{4\pi\hat{\alpha}(m_Z)}{\mathbf{k}^2}\left(1+\frac{\hat{\alpha}(m_Z)}{4\pi}\left(\beta_{0,\text{SU}(2)}+\beta_{0,Y}\right)\ln\frac{\mathbf{k}^2}{m_Z^2}\right), \tag{3.44}$$

$$\begin{aligned}-\left.\frac{4\pi\hat{\alpha}_2(\mu)\hat{c}_W^2(\mu)}{\mathbf{k}^2+m_Z^2}\right|_{\mu^2=\mathbf{k}^2} &= -\frac{4\pi\hat{\alpha}_2(m_Z)\hat{c}_W^2(m_Z)}{\mathbf{k}^2+m_Z^2}\left[1+\frac{\hat{\alpha}_2(m_Z)}{4\pi}\right.\\ &\quad\left.\times\left(\beta_{0,\text{SU}(2)}(1+\hat{s}_W^2(m_Z))-\beta_{0,Y}\frac{\hat{s}_W^4(m_Z)}{\hat{c}_W^2(m_Z)}\right)\ln\frac{\mathbf{k}^2}{m_Z^2}\right] ,\end{aligned} \tag{3.45}$$

where we have used the beta function for the hypercharge $\beta_{0,Y} = -41/6 = -1/6 - 11/9 - 49/9$ (split into electroweak, third-generation quarks and light fermions). As expected from the tree-level potential, since $\hat{\alpha} + \hat{\alpha}_2\hat{c}_W^2 = \hat{\alpha}_2$, entirely due to the T^3T^3 coupling, at high-energies/small-distances, the hypercharge contribution is decoupled and drops in the asymptotic behaviour (3.22). A similar argument works in position space.

In Figure 3.8, we show the absolute value of the potential in the $\overline{\text{MS}}$-scheme using the position space conversion (3.42) and one-loop running couplings at the scale $\mu = e^{-\gamma_E}/r$. While the NLO and LO potentials diverge for small r in the on-shell scheme due to the breakdown of perturbation theory, the NLO correction always remains small in the $\overline{\text{MS}}$-scheme. The correct

---

[14] Although the expansions in position and momentum space are equivalent in the high-energy limit $r \to 0\,/\,\mathbf{k}^2 \to \infty$ (up to higher-order constant terms), they differ fundamentally in the low-energy limit. The reason is hidden in the fact, that the Fourier transform of $\hat{\alpha}_2(\mathbf{k}^2)$ is proportional to r^{-3}. For example, the Fourier transform of (3.41) together with the NLO terms (3.15) leads to the large-r asymptotics

$$V^{r\to\infty,\overline{\text{MS}}}_{\chi^0\chi^0\to\chi^+\chi^-}(r) = -\beta_{0,\text{SU}(2)}\frac{\hat{\alpha}_2^2}{2\pi m_W^2 r^3} , \tag{3.43}$$

while in position space the asymptotics is the same as for the on-shell potential (3.28) (exchanging the couplings). A more detailed discussion of the Fourier transform that leads to this behaviour is found in Appendix B. The r^{-3} dependence is not a conceptual problem for two reasons. First, similar to the on-shell case (3.28) that shows an r^{-5} behaviour, another EFT would need to be constructed that integrates out the massive bosons and keeps only light fermions dynamical, whilst also decoupling the heavy particles from the running coupling. Secondly, the $\overline{\text{MS}}$-scheme is designed to absorb the logarithms that grow large for $r \to 0\,/\,\mathbf{k}^2 \to \infty$ and is therefore not expected to work in the opposite limit anyway.

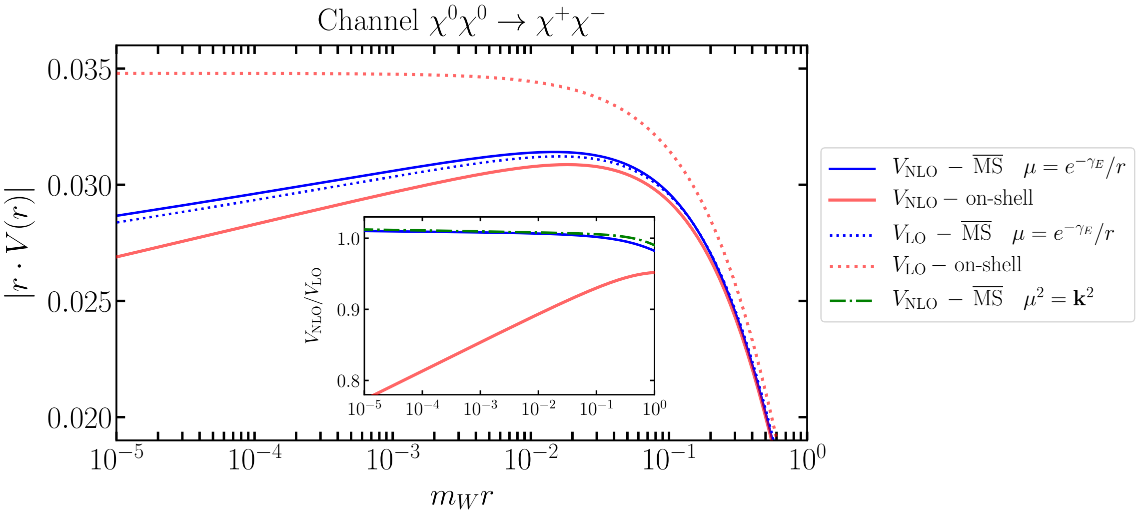

Figure 3.8: *The NLO (solid) and LO potential (dotted) $|r \cdot V(r)|$ in the $\overline{\mathrm{MS}}$-scheme using $\mu = e^{-\gamma_E}/r$ (blue) and in the on-shell scheme (red) for the channel $\chi^0\chi^0 \to \chi^+\chi^-$. The inset shows the ratio of the NLO potential to the LO potential for with same colour coding. In addition the dashed-dotted (green) line shows the $\overline{\mathrm{MS}}$-scheme potential with running coupling at $\mu^2 = \mathbf{k}^2$ implemented before Fourier transformation to position space.*

short-distance behaviour is already present at tree-level, due to the use of the running scale. The inset of Figure 3.8, which shows the ratio of the NLO to the LO potential, further emphasizes this point. It also shows that it does not matter whether the running coupling is implemented in position or momentum space, as it should be.

The $\overline{\mathrm{MS}}$-scheme is the better scheme for large momenta or small distances, as the correction and tree-level potential remain close. Solving the Schrödinger equation to obtain the Sommerfeld effect technically probes all momentum regions. Hence, it is not clear which scheme is superior for the calculation of the Sommerfeld effect. We investigate the impact on the Sommerfeld corrected prediction for indirect detection in the end of this Chapter, and find that the Sommerfeld factor changes for various $\overline{\mathrm{MS}}$ approximations and the on-shell result are compatible with differences of the size of well-behaved electroweak corrections beyond the one-loop order considered here. Therefore, we use the on-shell result for the correction for the predictions presented from hereon. It is important, though, to note that the control over the $r \to 0$ limit is a crucial check of our result and proves perturbative control.

3.4.4 Top-quark mass dependence

The only input parameter with considerable uncertainty and non-negligible impact on the NLO potential is the top-quark mass. The top-quark mass first enters the potential at one-loop, and the dependence on it is not only logarithmic but quadratic. At this point, it would be possible to use the pole mass $m_t = 173.1\,\mathrm{GeV}$ or the corresponding $\overline{\mathrm{MS}}$-mass (at four loops) $\overline{m}_t(\overline{m}_t) = 163.35\,\mathrm{GeV}$. At one-loop, the top-quark mass ambiguity is not fixed by scheme considerations, and both values present legitimate choices. The difference of $10\,\mathrm{GeV}$ is by far the largest uncertainty of all input parameters. The parameters that enter at leading order, i.e., the gauge boson masses and couplings, have a reduced scheme dependence at NLO and are known rather precisely in any case. The only other parameter without reduced scheme dependence, is the Higgs boson mass. However, the NLO potential is only logarithmically dependent on

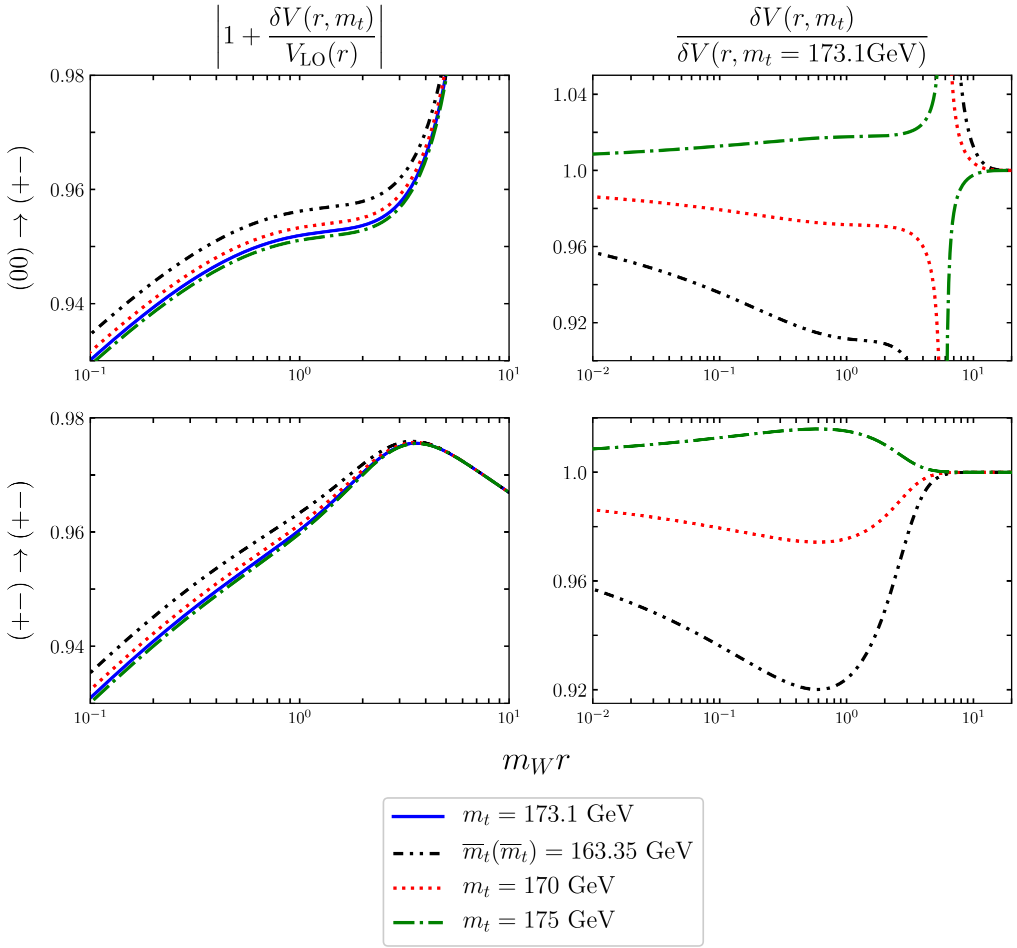

Figure 3.9: *Ratio of the NLO potential to the LO potential (left panel) and the ratio of the correction vs. the correction for the reference value $m_t = 173.1\,\text{GeV}$ (right panel) for various values of top mass. The upper panel gives the channel $(00) \to (+-)$ and the lower panel $(+-) \to (+-)$. The lines refer to $m_t = 173.1$ GeV (blue/solid), 163.35 GeV (black/dot-dot-dashed), 170 GeV (red/dotted), and 175 GeV (green/dot-dashed) all in the on-shell renormalization scheme for the couplings.*

the Higgs boson mass due to screening [133] and the Higgs mass is known to a good precision. Therefore, the top-mass introduces clearly the largest uncertainty on the potential at NLO.

Let us begin our investigation of top-mass dependence by examining its impact on the asymptotic behaviours. At large-distances light fermions dominate the NLO correction, making the top-mass dependence negligible. At small distances, the top-mass enters in the function $A(m_W, m_Z, m_t)$ given in Appendix C, that controls the size of the Coulomb term in the $r \to 0$ asymptotics. We find

$$\frac{A(m_W, m_Z, \overline{m}_t(\overline{m}_t))}{A(m_W, m_Z, m_t)} = 1 + 2.92 \cdot 10^{-5} \frac{1}{\text{GeV}^2} \left[\overline{m}_t(\overline{m}_t)^2 - (173.1\,\text{GeV})^2\right] = 0.904\,, \tag{3.46}$$

where the last number is given for $\overline{m}_t(\overline{m}_t) = 163.35\,\text{GeV}$. Therefore, we expect changes of the order of $10\,\%$ in the third quark-generation part of the potential. For the non-logarithmic term in (3.22) this means

$$m_t = 173.1\,\text{GeV}: \quad 4.92585 \quad \to \quad \overline{m}_t(\overline{m}_t) = 163.35\,\text{GeV}: \quad 4.09563\,, \tag{3.47}$$

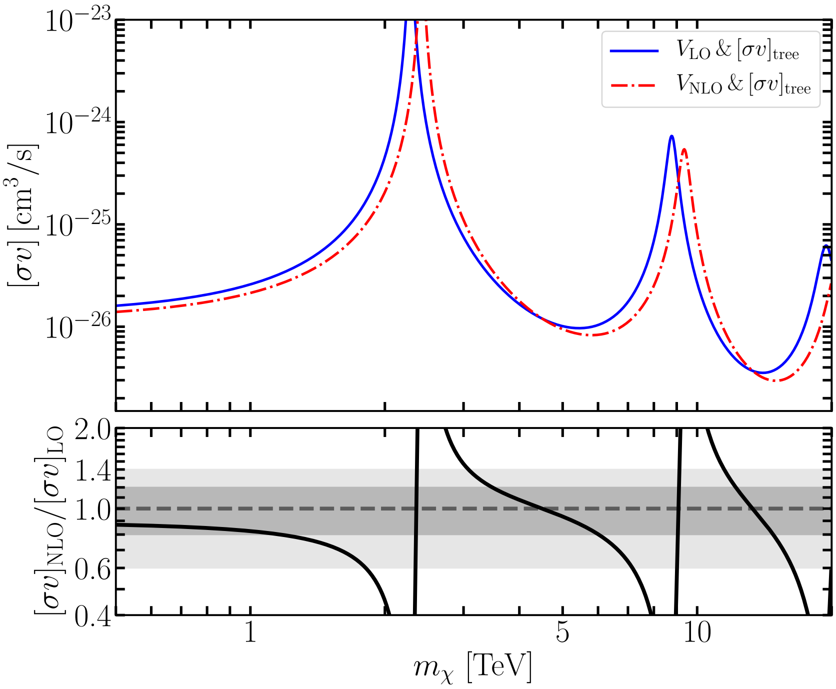

Figure 3.10: *$[\sigma v]$ for $\chi^0\chi^0 \to \gamma + X$ at tree-level, calculated with LO (solid/blue), and the NLO (dash-dotted/red) potential at a DM velocity $v = 10^{-3}$. The lower panel shows the ratio of the NLO to LO result with dark (light) grey bands to visualize the 20% (40%).*

which is a 17 % decrease of the Coulombic behaviour coefficient for $r \to 0$ for the full correction to the potential. However, in this region, the logarithmic term contributes, which is of similar size, decreasing the correction's effect to roughly 10 % on the NLO correction.

Figure 3.9 shows the ratio of the full NLO potential to the LO potential for a range of r centered around $1/m_W$ for different values for the top mass (left panel). As outlined above, the top-mass dependence is most relevant at short and intermediate distances, as it is cut off at large distances. At short distances, the dependence on the top-mass is reduced by the logarithmic term dominating more and more. In the $\overline{\mathrm{MS}}$-scheme, where the logarithms are absorbed for $r \to 0$, the ratio of the different top-mass NLO potentials becomes constant. In the right panel of the Figure, we depict the ratio to the default value $m_t = 173.1\,\mathrm{GeV}$. In both channels shown, the top mass changes the NLO correction by up to 10 %, with the largest changes around $m_W r \sim 1$. Note that the singularity in the ratio for the $\chi^0\chi^0 \to \chi^+\chi^-$ channel originates from the slightly different sign change in $\delta V(r, m_t)$ for the various top masses, and hence is an artefact of taking the ratio.

3.5 Sommerfeld effect in indirect detection

Equipped with above results, we take a first look at a physical prediction that can be done using the NLO potential, namely the indirect detection cross-section (here without the resummation effects associated with the annihilation process, discussed in later Chapters). The discussion helps to assess the impact of the NLO potential, allows some intuition for the relic abundance prediction discussed in Chapter 5, and helps to set up the SCET discussion surrounding the indirect detection prediction in Chapter 8. Furthermore, with this calculation, we have available a test of the fitting functions, their quality, the effect of using $\overline{\mathrm{MS}}$ potentials, and the top quark

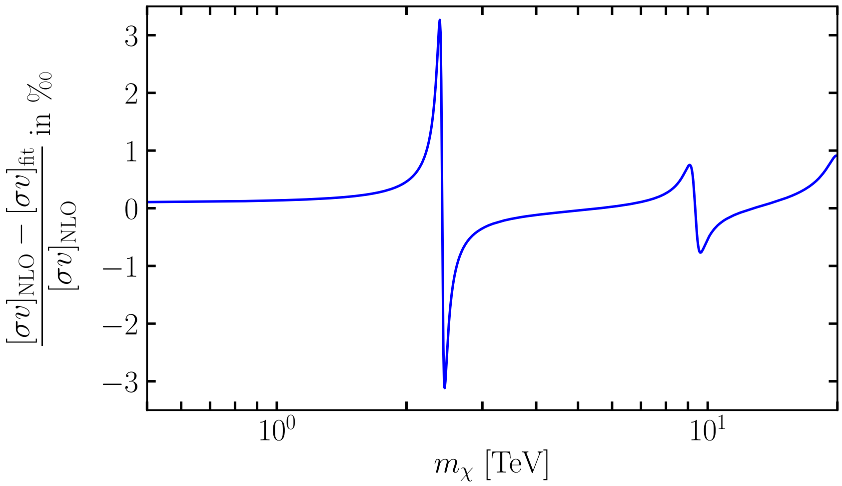

Figure 3.11: *Relative error in permille of the Sommerfeld enhanced cross-section using the full NLO potential vs. the fitting function for the relevant range of values of DM mass* m_χ.

mass dependence, all discussed conceptually in the previous Section. We refrain from providing technical details on the indirect detection calculation, as this is discussed in detail in later Chapters. In this Section, we are mainly concerned with the qualitative changes in the behaviour from LO to NLO potential. The precise numerical values are discussed in combination with Sudakov resummation in Chapter 8. In this sense, the tree-level indirect detection is merely a convenient choice to discuss the qualitative behaviour of the Sommerfeld effect and assess the size of the expected non-relativistic corrections.

In Figure 3.10, we show the annihilation cross-section times velocity $[\sigma v]$ calculated with the LO (solid/blue) and the NLO (dashed/red) potential in the mass range $m_\chi = 0.5 \ldots 20$ TeV for the DM particle.[15] This mass region covers the onset of the Sommerfeld enhancement at small masses, the predicted mass value of the dark matter relic abundance $m_\chi = 2.88\,\mathrm{TeV}$ [40], and the first two zero-energy resonances. At these resonances, the potential starts to support a bound state in the spectrum. Schematically, the enhancement factor S is proportional to

$$S \sim \frac{1}{E - E_{\mathrm{BS}}} \tag{3.48}$$

where E is the kinetic energy of the two-particle state and E_{BS} the bound state binding energy. At the resonance mass values, the bound state energy is zero, leading to a $S \sim v^{-2}$ resonant enhancement of the cross-section.[16] Away from resonance, a significant enhancement is observed, that saturates at small velocity values, due to the binding energy.

The LO and NLO curve are distinguishable on a logarithmic plot, which already indicates that the effect of going to NLO is significant and larger than the expected few percent of a typical electroweak correction. The reason lies in the shifted location of the zero-energy resonances. The full NLO potential is slightly weaker than the LO potential (see above). Hence, at NLO, the bound states are supported in the spectrum only for larger mass values. The first two Sommerfeld resonances shift from 2.283 (8.773) TeV at LO to 2.419 (9.355) TeV at NLO.

This is visible in the lower panel of Figure 3.10, where the ratio of the NLO to LO prediction is shown. Near resonance, the ratio evidently blows up. Still, also off-resonance, the correction is

---

[15] Note that without Sommerfeld enhancement, the LO prediction for the annihilation cross-section $\chi^0\chi^0 \to \gamma + X$ vanishes.

[16] At very low velocities in the absolute vicinity of the resonance, the cross-section result becomes unreliable and violates partial-wave unitarity. In that case, a further treatment would be necessary [138, 139, 140, 141].

typically larger than 20% for a large mass range and always larger than the typical $3 - 4\%$ of an electroweak loop correction.

To check the quality of the fitting functions, we show in Figure 3.11 the accuracy of the indirect detection cross-section when instead of the exact computation of the NLO potential, the fitting functions are used. The error is at most $0.3\,\%$ near the first resonance and usually substantially smaller. The first and second resonance positions themselves change by only 0.1 GeV, 0.2 GeV, respectively.

The top-mass uncertainty of the potential translates into a small effect on the Sommerfeld factor [103]. For example, the location of the first (second) Sommerfeld resonance is shifted due to the NLO potential correction from 2.283 TeV to 2.408 (9.311) TeV instead of 2.419 (9.355) TeV when the $\overline{\text{MS}}$-mass $\overline{m}_t(\overline{m}_t) = 163.35\,\text{GeV}$ instead of $m_t = 173.1\,\text{GeV}$ is adopted. This effect is small enough to be ignored for the following assessments, hence in the following we will stick with the pole mass value $m_t = 173.1\,\text{GeV}$.

Using $\overline{\text{MS}}$-couplings as discussed in Section 3.4.3, and for concreteness, the position space conversion outlined there, leads to the resonances appearing at 2.368 (9.166) TeV for the TL $\overline{\text{MS}}$ potential, and the NLO correction 2.391 (9.240) TeV. Note that, part of the observed shift is due to using the $\overline{\text{MS}}$-top mass $\overline{m}_t(\overline{m}_t)$ (see above) in the $\overline{\text{MS}}$-potential correction. Furthermore, as expected, the TL and NLO $\overline{\text{MS}}$ results are close, as the main effect is captured by resumming the leading coupling logarithms and furthermore converting to the one-loop $\overline{\text{MS}}$ couplings (cf. Eqs. (3.35), (3.36)).

4

NLO potentials for general SM multiplets

In the previous Chapter, we discussed the potential correction for the wino dark matter model. We find that some channels, e.g., $\chi^0\chi^0 \to \chi^+\chi^-$ and $\chi^0\chi^\pm \to \chi^\pm\chi^0$ obtain the same NLO correction up to a minus sign, that is already present for the tree-level potential. Furthermore, we observe that the gauge parameter cancellation between the various potential correction pieces is very delicate and involves several highly complicated terms. Together with the fact that some topologies and corrections, e.g., self-energies, are only tied to the exchanged gauge boson, this leads to the suspicion that some structure is to be unveiled, resulting in universal features across models. In this Chapter, we investigate the NLO potential for minimal dark matter [37, 38] or more generally arbitrary electroweak representations and charges and prove the universal nature of the NLO correction independent of the heavy particle model. In particular, we show that the NLO correction is only tied to the exchanged gauge boson at tree-level. All information pertaining to the external heavy particle is contained in the tree-level potential.

4.1 The tree-level potential for arbitrary SM representations

The electroweak Feynman rules for the heavy particles (fermions/scalars/...) only depend on the representation under $\mathrm{SU}(2)_L$ and $\mathrm{U}(1)_Y$. To construct the potential for arbitrary SU(2) representations in the broken phase, we work in the charge basis in which T_R^3 is diagonal, i.e., $Q = T_R^3 + Y$. In principle, the entries of $T_R^\pm$ are only fixed up to an arbitrary phase normalization for each multiplet component. For consistency with minimal DM, any convention is fine, as long as it leads to the same SU(2) invariant mass term for all components of the multiplet [38]. We choose the convention in which the (off-diagonal) entries of $T_R^\pm$ are real for concreteness. A generic spin-j representation is constructed using [142]

$$\begin{aligned}
\left\langle j, m_1 \middle| T_R^3 \middle| j, m_2 \right\rangle &= m_2\, \delta_{m_1,m_2} \\
\left\langle j, m_1 \middle| T_R^+ \middle| j, m_2 \right\rangle &= \sqrt{\frac{(j+m_2+1)(j-m_2)}{2}}\, \delta_{m_1,m_2+1} \\
\left\langle j, m_1 \middle| T_R^- \middle| j, m_2 \right\rangle &= \sqrt{\frac{(j+m_2)(j-m_2+1)}{2}}\, \delta_{m_1,m_2-1}
\end{aligned} \tag{4.1}$$

from which we can derive the generic tree-level potential for minimal dark matter [37, 38] and arbitrary SM representations, as the assumption of DM is at no point needed in the calculation (the same holds for the NLO correction). The only formal requirement is that the multiplet has a mass much larger than the electroweak scale $m_\chi \gg m_Z$, and, of course, that it couples to the

SM in the first place. The tree-level potential involving the exchange of a W-boson reads

$$\begin{aligned} V^{W}_{(ij),(kl)} &= (-1)^{n_Q}\frac{4\pi\alpha_2}{\mathbf{k}^2+m_W^2}\left(T^{+}_{R,ik}T^{-}_{R,jl}+T^{-}_{R,ik}T^{+}_{R,jl}\right) \\ &= (-1)^{n_Q}V^{W}_{\text{tree}}\left(T^{+}_{R,ik}T^{-}_{R,jl}+T^{-}_{R,ik}T^{+}_{R,jl}\right), \end{aligned} \tag{4.2}$$

where $n_Q = 0$ if the $|Q_i| + |Q_j| = |Q_k| + |Q_l|$ and $n_Q = 1$ otherwise. The factor $(-1)^{n_Q}$ expresses the possible minus sign due to "fermion flow" (note that in the particle/particle convention employed in our calculation, this sign is part of the Feynman rule). The introduction of n_Q is pure convenience and is mainly chosen to allow compact results as the corresponding diagrams only differ by signs. Furthermore, we remark that for the linear combination $T^+T^- + T^-T^+$ only one term can be non-zero in a given channel.

For the tree-level potentials involving γ and Z-exchange the potential reads (note that in this case $i = k$ and $j = l$ as T^3 and Y are diagonal)

$$\begin{aligned} V^{\gamma/Z}_{(ij),(ij)} &= +\frac{4\pi\alpha}{\mathbf{k}^2}(T^3_{R,ii}+Y_i)(T^3_{R,jj}+Y_j) + \frac{4\pi\alpha}{\mathbf{k}^2+m_Z^2}\frac{c_W^2T^3_{R,ii}-s_W^2Y_i}{s_Wc_W}\cdot\frac{c_W^2T^3_{R,jj}-s_W^2Y_j}{s_Wc_W} \\ &= \left(\frac{4\pi\alpha}{\mathbf{k}^2}+\frac{4\pi\alpha}{\mathbf{k}^2+m_Z^2}\frac{c_W^2}{s_W^2}\right)T^3_{R,ii}T^3_{R,jj} + \left(\frac{4\pi\alpha}{\mathbf{k}^2}-\frac{4\pi\alpha}{\mathbf{k}^2+m_Z^2}\right)(T^3_{R,ii}Y_j+T^3_{R,jj}Y_i) \\ &\quad + \left(\frac{4\pi\alpha}{\mathbf{k}^2}+\frac{4\pi\alpha}{\mathbf{k}^2+m_Z^2}\frac{s_W^2}{c_W^2}\right)Y_iY_j \\ &= V^{T3T3}_{\text{tree}}\,T^3_{R,ii}T^3_{R,jj} + V^{T3Y}_{\text{tree}}(T^3_{R,ii}Y_j+T^3_{R,jj}Y_i) + V^{YY}_{\text{tree}}\,Y_iY_j \\ &= V^{T3T3}_{(ij)(ij)} + V^{T3Y}_{(ij)(ij)} + V^{YY}_{(ij)(ij)}, \end{aligned} \tag{4.3}$$

where we distinguish Y_i and Y_j, as if j is part of the antiparticle multiplet of i, then $Y_i = -Y_j$ and in the complex fermion (scalar) case then $T^3_{ii} = -T^3_{jj}$. For real fermions (scalars), hypercharge is $Y = 0$. We split the tree-level terms into three pieces, as we expect the correction to them to be separately gauge invariant. The correction to T^3T^3 and YY should be gauge invariant, as we can write models where $T^3 \neq 0, Y = 0$ and vice versa. As the corrections to T^3T^3 and YY are gauge invariant, also the correction to T^3Y has to be gauge invariant separately, even though it is only non-vanishing if both T^3 and Y are non-vanishing.

For simplicity, we have chosen both heavy particles in the same $\mathrm{SU}(2)_L$-representation. In principle, we could have also selected a case with two different representations R, R' (with also possibly different hypercharge $Y_R, Y_{R'}$), the essence of the derivation above, and the following arguments for the potential correction do not depend on this. However, most terms would be duplicated. So for notational simplicity, we avoid the case of different representations, as in such cases, typically mixing between the R and R'-multiplets, via Higgs-interactions is allowed. As we do not cover the Higgs potentials (as they are not relevant for minimal DM), and we do not have the correction to Higgs potentials readily available, we omit this case.

4.2 The potential correction at NLO

In the following, we present the relevant linear combinations and extract the "Casimir-like" scaling of the NLO corrections. We restrict to presenting the result for the potential correction. The detailed evaluation of the correction topology by topology and the corresponding group algebra is presented in Appendix D. The results for the loop integrals are given in Appendix A.

4.2.1 Off-diagonal W-boson exchange

The result for the off-diagonal W-Yukawa potential reads

$$\begin{aligned}\delta V^{W}_{(ij),(kl)} = {} & V^{W}_{(ij),(kl)} \left(2\delta Z_e - 2\frac{\delta s_W}{s_W} + \frac{\Sigma_T^{WW}(-\mathbf{k}^2) - \delta m_W^2}{\mathbf{k}^2 + m_W^2} + 2\left(I^{W\gamma}_{3\,\text{gauge}} + I^{WZ}_{3\,\text{gauge}}\right)\right) \\ & + (-1)^{n_Q}(T^+_{R,ik}T^-_{R,jl} + T^-_{R,ik}T^+_{R,jl}) \left[-I_{\text{box}}\left(\alpha_2, m_W; \alpha, 0\right) - I_{\text{box}}\left(\alpha_2, m_W; \alpha\frac{c_W^2}{s_W^2}, m_Z\right)\right] \\ & + \delta V^{W}_{(ij),(kl)}\Big|_{\text{WF/vertex}} \end{aligned} \tag{4.4}$$

where the individual terms and the origin of the prefactors are presented in Appendix D. Let us comment on the vertex and wave-function contribution $\delta V^{W}_{(ij),(kl)}\Big|_{\text{WF/vertex}}$ at this point. The individual contributions, namely wave-function renormalization and vertex correction, are proportional to further factors differing from the tree-level linear combination. However, in the linear combination, the terms cancel exactly so that always the tree-level factor times a universal term is left over.

For the full potential correction, the crucial observation is that all terms are proportional to the tree-level factor $(-1)^{n_Q}(T^+_{R,ik}T^-_{R,jl} + T^-_{R,ik}T^+_{R,jl})$. Therefore, for the off-diagonal W-Yukawa potentials, we can always write

$$V^{W,\text{NLO}}_{(ij),(kl)} = (-1)^{n_Q}\left(T^+_{R,ik}T^-_{R,jl} + T^-_{R,ik}T^+_{R,jl}\right)\left(V^W_{\text{tree}} + \delta V^W_{1-\text{loop}}\right) \tag{4.5}$$

where $\delta V^W_{1-\text{loop}}$ does not depend on any of the properties of the heavy particles but only on the low-energy properties of the broken theory. Therefore, we find a "Casimir-like" scaling, similar to the QCD result, also in the broken theory. The explicit expression is the same as in the wino case (stripping the factor $(-1)^{n_Q}$)

$$\delta V^W_{1-\text{loop}} = -\delta V_{\chi^0\chi^0\to\chi^+\chi^-} = \delta V_{\chi^0\chi^\pm\to\chi^\pm\chi^0} \tag{4.6}$$

where the wino results refer to Eqs. (3.15) and (3.16), respectively. Furthermore, this implies that the analysis for the off-diagonal channel in the wino (Section 3.4) applies in all off-diagonal channels, regardless of the model, as only the overall prefactor changes. The correction to the tree-level potential at one-loop is only sensitive to the low-energy properties of the exchanged W-boson. All information on the heavy particles and their respective representations is already present at tree-level and does not impact the potential at NLO.

4.2.2 The photon and Z-boson exchanges

Similar, to the above results for the off-diagonal channel, in the diagonal channels involving photon and Z-exchange, we also find universal behaviour for the individual pieces. The T^3T^3 projection at tree-level reads

$$\begin{aligned}\delta V^{T3T3}_{(ij),(ij)} = {} & +\frac{4\pi\alpha}{\mathbf{k}^2}\left(T^3_{R,ii}T^3_{R,jj}\right)\left(2\delta Z_e + \frac{\Sigma_T^{\gamma\gamma}(-\mathbf{k}^2)}{\mathbf{k}^2}\right) \\ & + \frac{4\pi\alpha}{\mathbf{k}^2 + m_Z^2}\left(T^3_{R,ii}T^3_{R,jj}\right)\frac{c_W^2}{s_W^2}\left(2\delta Z_e + 2\frac{\delta c_W}{c_W} - 2\frac{\delta s_W}{s_W} + \frac{\Sigma_T^{ZZ}(-\mathbf{k}^2) - \delta m_Z^2}{\mathbf{k}^2 + m_Z^2}\right) \\ & + \frac{4\pi\alpha}{\mathbf{k}^2(\mathbf{k}^2 + m_Z^2)}\left(T^3_{R,ii}T^3_{R,jj}\right)\frac{-2c_W}{s_W}\Sigma_T^{\gamma Z}(-\mathbf{k}^2) + V^{T3T3}_{(ij),(ij)}\left(2I^{WW}_{3\,\text{gauge}}\right)\end{aligned}$$

$$+ \delta V^{T3T3}_{(ij),(ij)}\Big|_{\text{vertex/WF}} - T^3_{R,ii}T^3_{R,jj} I_{\text{box}}\left(\alpha_2, m_W; \alpha_2, m_W\right) , \tag{4.7}$$

for the T^3Y contribution

$$\begin{aligned}\delta V^{T3Y}_{(ij),(ij)} = &+ \frac{4\pi\alpha}{\mathbf{k}^2}\left(T^3_{R,ii}Y_j + T^3_{R,jj}Y_i\right)\left(2\delta Z_e + \frac{\Sigma^{\gamma\gamma}_T(-\mathbf{k}^2)}{\mathbf{k}^2}\right) \\ &- \frac{4\pi\alpha}{\mathbf{k}^2+m_Z^2}\left(T^3_{R,ii}Y_j + T^3_{R,jj}Y_i\right)\left(2\delta Z_e + \frac{\Sigma^{ZZ}_T(-\mathbf{k}^2) - \delta m_Z^2}{\mathbf{k}^2+m_Z^2}\right) \\ &+ \frac{4\pi\alpha}{\mathbf{k}^2(\mathbf{k}^2+m_Z^2)}\left(T^3_{R,ii}Y_j + T^3_{R,jj}Y_i\right)\left(\frac{s_W}{c_W} - \frac{c_W}{s_W}\right)\Sigma^{\gamma Z}_T(-\mathbf{k}^2) \\ &+ \delta V^{T3Y}_{(ij),(ij)}\Big|_{\text{vertex/WF}} + V^{T3Y}_{(ij),(ij)} I^{WW}_{3\,\text{gauge}} ,\end{aligned} \tag{4.8}$$

and finally for the Y^2 part

$$\begin{aligned}\delta V^{YY}_{(ij),(ij)} = &+ \frac{4\pi\alpha}{\mathbf{k}^2}\left(Y_iY_j\right)\left(2\delta Z_e + \frac{\Sigma^{\gamma\gamma}_T(-\mathbf{k}^2)}{\mathbf{k}^2}\right) \\ &+ \frac{4\pi\alpha}{\mathbf{k}^2+m_Z^2}\frac{s_W^2}{c_W^2}\left(Y_iY_j\right)\left(2\delta Z_e - 2\frac{\delta c_W}{c_W} + 2\frac{\delta s_W}{s_W} + \frac{\Sigma^{ZZ}_T(-\mathbf{k}^2) - \delta m_Z^2}{\mathbf{k}^2+m_Z^2}\right) \\ &+ \frac{4\pi\alpha}{\mathbf{k}^2(\mathbf{k}^2+m_Z^2)}\left(Y_iY_j\right)\frac{2s_W}{c_W}\Sigma^{\gamma Z}_T(-\mathbf{k}^2) + \delta V^{YY}_{(ij),(ij)}\Big|_{\text{vertex/WF}} .\end{aligned} \tag{4.9}$$

The observation is the same as for the W-exchange, all contributions are proportional to the respective tree-level factors, and the potential correction, therefore, obeys a “Casimir-like” scaling. Consequently, we can write

$$\begin{aligned}V^{\gamma/Z,\text{NLO}}_{(ij),(ij)} &= V^{T3T3}_{(ij),(ij)} + \delta V^{T3T3}_{(ij),(ij)} + V^{T3Y}_{(ij),(ij)} + \delta V^{T3Y}_{(ij),(ij)} + V^{YY}_{(ij),(ij)} + \delta V^{YY}_{(ij),(ij)} \\ &= T^3_{R,ii}T^3_{R,jj}\left(V^{T3T3}_{\text{tree}} + \delta V^{T3T3}_{\text{1-loop}}\right) + \left(T^3_{R,ii}Y_j + T^3_{R,jj}Y_i\right)\left(V^{T3Y}_{\text{tree}} + \delta V^{T3Y}_{\text{1-loop}}\right) \\ &\quad + Y_iY_j\left(V^{YY}_{\text{tree}} + \delta V^{YY}_{\text{1-loop}}\right)\end{aligned} \tag{4.10}$$

and apply our analysis to the respective $\delta V_{\text{1-loop}}$ pieces independent of the precise representations for the heavy particle. Again, we find that the potential correction in all instances arises only from low-energy properties of the underlying gauge theory (in this case, the SM) and is tied to the tree-level exchange.

For the T^3T^3 contribution, we can infer the result from the wino channels, and the corresponding analysis, e.g., of the asymptotic behaviour and the fitting functions, applies. Therefore, we write

$$\delta V^{T3T3}_{\text{1-loop}} = -\delta V_{\chi^+\chi^-\to\chi^+\chi^-} = \delta V_{\chi^\pm\chi^\pm\to\chi^\pm\chi^\pm} \tag{4.11}$$

where the wino channels are given in Eqs. (3.13) and (3.17), respectively.

Finally, before turning to the analysis of the new channels, let us remark that at one-loop (at least for pure multiplets, i.e., without Higgs exchange), we do not induce potentials in channels in which the tree-level contribution vanishes. The explicit proof is provided in Appendix D; however, one can also understand this intuitively. If the tree-level potential vanishes, the only possibility for loop topologies are box diagrams. However, as noted above, to cancel the box diagrams gauge dependence, a delicate combination of self-energies, and other terms is needed.

As these other combinations vanish, as they arise from tree-level diagrams, we would not have expected induced potentials at one-loop in any case.

Another possibility to phrase the universality is to consider the SM in a Coulomb gauge formulation [143]. In Coulomb gauge, all soft corrections connected to the heavy particle vanish. Therefore, only the usual box diagram with the potential region, i.e., the leading-order potential ladder and the Coulomb gauge SM self-energies, contribute. As the self-energies are independent of the heavy particle and only tied to the tree-level exchange boson, the correction is necessarily proportional to the tree-potential, as in QCD. Hence, there is a "Casimir"-type scaling of the one-loop correction.

4.3 Analysis of the channels

The above results allow us to repeat the analysis of the potential correction similar to the case of the wino, Section 3.4, now for general SM multiplets. As the W-Yukawa potential and the T^3T^3-part have already appeared in the discussion of the wino potential correction, we do not repeat the analysis of Section 3.4.1. We focus on the new corrections, and in particular, also repeat the splitting into respective gauge invariant subparts (namely light fermions, third-generation quarks, and the electroweak part).

The potential corrections to the tree-potential V_{tree}^{T3Y} and V_{tree}^{YY} are shown in Figures 4.1 and 4.2, respectively. We begin with the analysis of the asymptotic behaviour before turning to the full correction and, in the end, provide some general comments and an example on how to construct the potential correction for an explicit model, in our case, the pure Higgsino model.

4.3.1 Asymptotic behaviour

T^3Y - linear combination

For the projection onto the T^3Y-component, we have at small distance

$$\delta V^{T^3Y}(r\to 0) = \text{const.} \tag{4.12}$$

which also holds for each gauge invariant sub piece individually. We can understand the origin of this behaviour from the tree-level linear combination. The Fourier transformation has two regions in the method of regions expansion for $r \to 0$. First, there is $\frac{1}{r} \sim |\mathbf{k}| \gg m_Z$, which in dimensional regularization evaluates to

$$\begin{aligned}
\tilde{\mu}^{2\epsilon}\int \frac{d^{d-1}\mathbf{k}}{(2\pi)^{d-1}}\, e^{i\mathbf{k}\cdot\mathbf{r}}\, \frac{4\pi\alpha}{\mathbf{k}^2+m_Z^2} &= \tilde{\mu}^{2\epsilon}\int \frac{d^{d-1}\mathbf{k}}{(2\pi)^{d-1}}\, e^{i\mathbf{k}\cdot\mathbf{r}} \sum_{n=0}^{\infty} \frac{4\pi\alpha}{\mathbf{k}^2}\left(-\frac{m_Z^2}{\mathbf{k}^2}\right)^n \\
&\overset{\frac{1}{r}\sim|\mathbf{k}|\gg m_Z}{\approx} \sum_{n=0}^{\infty} \tilde{\mu}^{2\epsilon}\int \frac{d^{d-1}\mathbf{k}}{(2\pi)^{d-1}}\, e^{i\mathbf{k}\cdot\mathbf{r}}\, \frac{4\pi\alpha}{\mathbf{k}^2}\left(-\frac{m_Z^2}{\mathbf{k}^2}\right)^n \\
&= \frac{\alpha}{r}\cosh(m_Z r) \overset{r\to 0}{\longrightarrow} \frac{\alpha}{r}\left(1+\frac{1}{2}m_Z^2r^2+\mathcal{O}(m_Z^4r^4)\right)\,.
\end{aligned} \tag{4.13}$$

This correctly captures all attractive contributions of the Yukawa potential and reproduces the leading Coulomb behaviour for $r \to 0$. However, it completely misses the Yukawa potential's screening contributions. Therefore, in the case in which the leading Coulomb behaviour cancels for $r \to 0$ with other tree-level terms, we need to consider also the second region, where $|\mathbf{k}| \sim m_Z \ll \frac{1}{r}$. In this case, there is no expansion for the momentum space potential, though one can expand the exponential in the Fourier transform. The resulting integrals are divergent

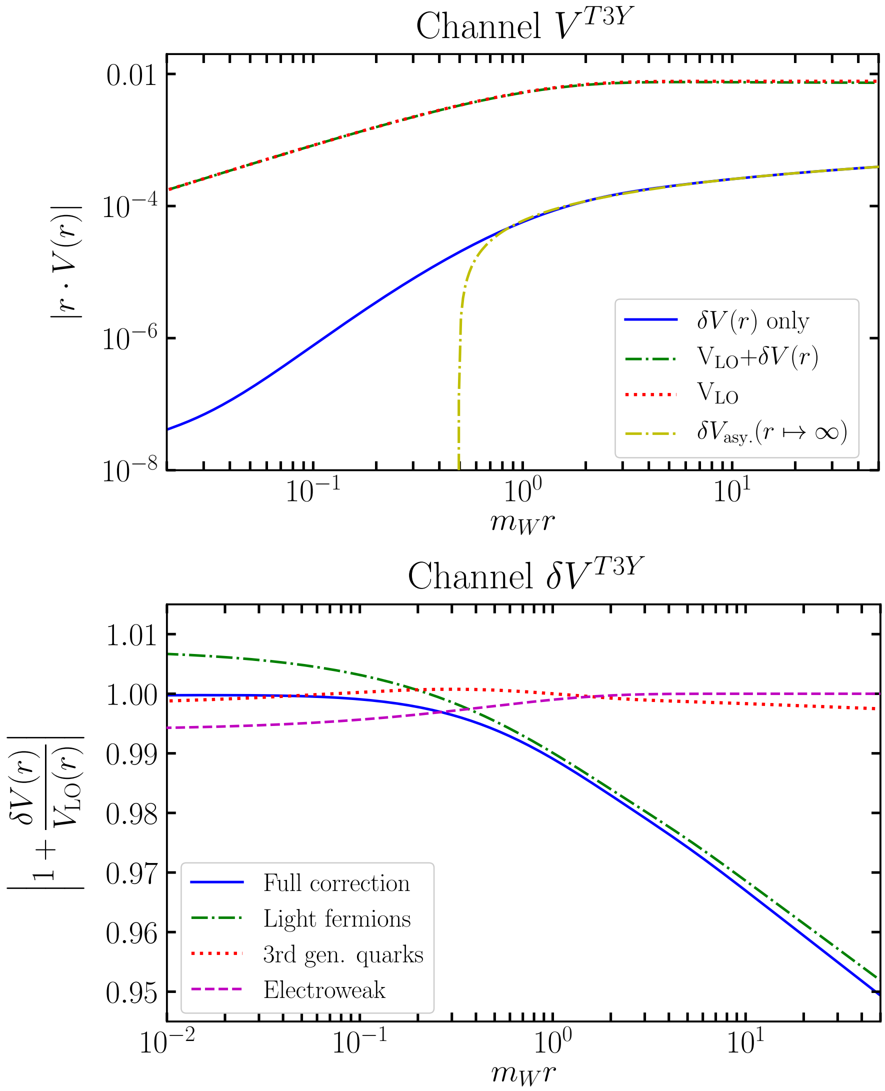

Figure 4.1: *The NLO correction to the tree potential V^{T3Y}_{tree}. The upper panel shows the modulus of the potential $|r \cdot V(r)|$ for the LO and NLO potential, the NLO contribution only, and the large-distance asymptotic behaviour (the change from solid to dashed for the correction only line, indicates the sign change of this term). In the lower panel, we show the ratio of the full NLO potential to the LO potential (blue solid) and separately for the three gauge invariant pieces identified in the text (other curves).*

(e.g., the leading piece linearly that also appears in other contexts later, cf. Sections 5.1.2 and A.1.3). The integrals evaluate to

$$\begin{aligned}
\tilde{\mu}^{2\epsilon} \int \frac{d^{d-1}\mathbf{k}}{(2\pi)^{d-1}}\, e^{i\mathbf{k}\cdot\mathbf{r}} \frac{4\pi\alpha}{\mathbf{k}^2+m_Z^2} &= \tilde{\mu}^{2\epsilon} \int \frac{d^{d-1}\mathbf{k}}{(2\pi)^{d-1}} \frac{4\pi\alpha}{\mathbf{k}^2+m_Z^2} \sum_{n=0}^{\infty} \frac{(i\mathbf{k}\cdot\mathbf{r})^n}{n!} \\
&\overset{\frac{1}{r} \gg |\mathbf{k}| \sim m_Z}{\approx} \sum_{n=0}^{\infty} \tilde{\mu}^{2\epsilon} \int \frac{d^{d-1}\mathbf{k}}{(2\pi)^{d-1}} \frac{4\pi\alpha}{\mathbf{k}^2+m_Z^2} \frac{(i\mathbf{k}\cdot\mathbf{r})^n}{n!} \\
&= \frac{\alpha}{r}\sinh(-m_Z r) \xrightarrow{r\to 0} \frac{\alpha}{r}\left(-m_Z r - \frac{1}{6} m_Z^3 r^3 + \mathcal{O}(m_Z^5 r^5)\right) \quad (4.14)
\end{aligned}$$

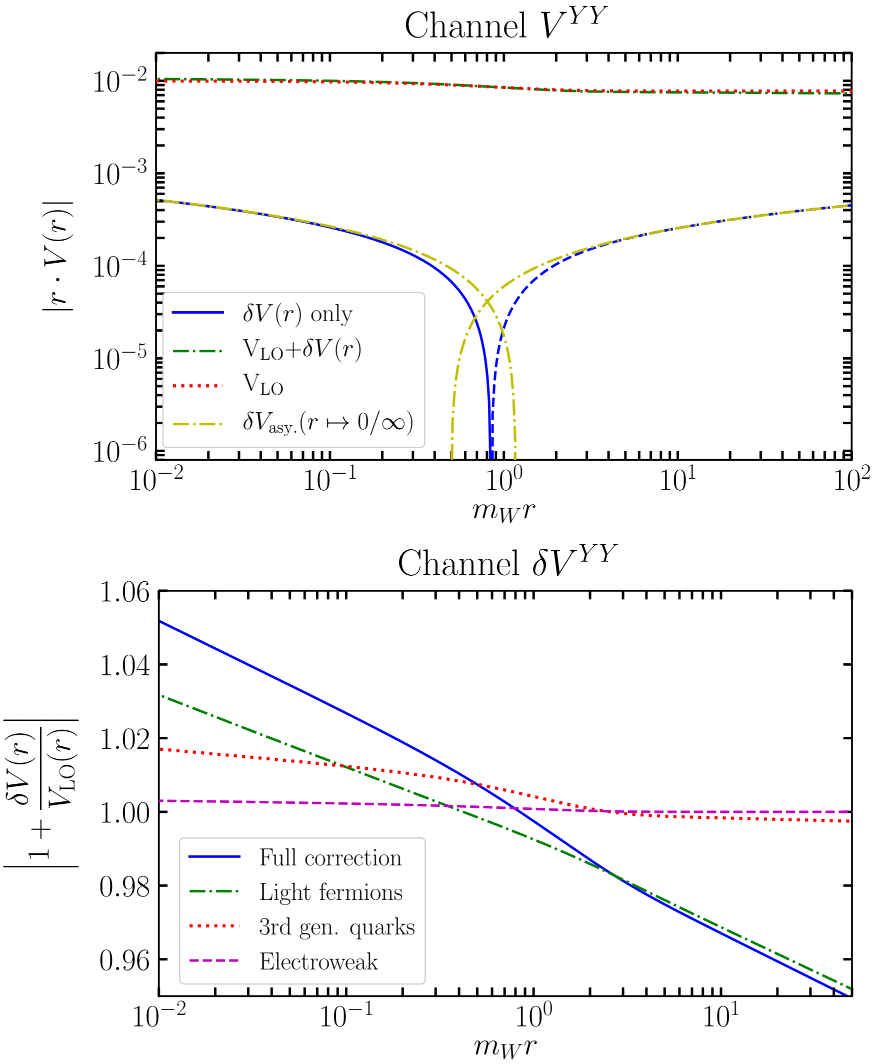

Figure 4.2: *The NLO correction to the tree potential V^{YY}_{tree}. The upper panel shows the modulus of the potential $|r \cdot V(r)|$ for the LO and NLO potential, the NLO contribution only, and the large-distance asymptotic behaviour. In the lower panel, we show the ratio of the full NLO potential to the LO potential (blue solid) and separately for the three gauge invariant pieces identified in the text (other curves).*

which captures all screening contributions of the Yukawa potential. Therefore for the T^3Y projection at tree-level, we find

$$V^{T3Y}_{\mathrm{tree}}(r) = \frac{\alpha}{r} - \frac{\alpha}{r}\, e^{-m_Z r} \quad \xrightarrow{r \to 0} \quad \alpha m_Z \tag{4.15}$$

the leading term for $r \to 0$ is constant and arises from the region $m_Z \sim |\mathbf{k}| \ll \frac{1}{r}$ in a method of regions expansion, i.e., the expansion of the Fourier transform. In the NLO potential, a similar cancellation happens, as again the leading pieces from the region $m_Z \ll |\mathbf{k}| \sim \frac{1}{r}$ cancel, as, in the high-momentum exchange region, SU(2) and U(1) disentangle. The leading correction therefore comes from the same region as for the tree-potential $|\mathbf{k}| \sim m_Z \ll \frac{1}{r}$. However, in this case, for the complicated one-loop structures, e.g. the SM self-energies, the analytic extraction proves difficult. The light-fermionic contribution coefficient can be extracted, as all Fourier transforms are analytically available, and one can just Taylor expand around $r = 0$. For electroweak and third-generation quark contribution, this is not possible due to the unknown Fourier transform. The coefficients can be extracted numerically, or one could try to extract them analytically by simplifying the loop structures. In essence, the latter amounts to solving various two-loop integrals in $d = 3$.

Physically though, in any realistic scenarios, if the T^3Y projection is non-vanishing, the T^3T^3 and YY components are also present and have the leading contribution from $m_Z \ll |\mathbf{k}| \sim \frac{1}{r}$. Therefore, they are orders of magnitude larger in the $r \to 0$ limit. The above considerations are interesting from a conceptual standpoint but have a negligible impact on any practical results. For example, at $m_W r \approx 0.1$, $|r \cdot V(r)|$ of the T^3Y component is already below 10^{-6} (cf. Figure 4.1), whilst for the YY component, we find $2.5 \cdot 10^{-4}$ (cf. Figure 4.2), more than two orders of magnitude larger. The difference becomes even larger for smaller distances, as $|r \cdot V(r)|$ increases for YY, whilst it linearly decreases for T^3Y.

At large distances for T^3Y, we find the long-distance correction to the tree-level Coulomb potential

$$\delta V^{T^3Y}_{\text{light ferm.}}(\mathbf{k}^2 \to 0) = \frac{76}{9}\frac{\alpha^2}{\mathbf{k}^2}\ln\frac{\mathbf{k}^2}{m_Z^2} + \mathcal{O}(\mathbf{k}^0)\,, \tag{4.16}$$

$$\delta V^{T^3Y}_{\text{3rd gen. quarks}}(\mathbf{k}^2 \to 0) = \frac{4}{9}\frac{\alpha^2}{\mathbf{k}^2}\ln\frac{\mathbf{k}^2}{m_Z^2} + \mathcal{O}(\mathbf{k}^0)\,, \tag{4.17}$$

$$\delta V^{T^3Y}_{\text{electroweak}}(\mathbf{k}^2 \to 0) = \frac{\alpha_2^2 s_W^2}{m_W^2} F(m_W, m_Z, m_H)\,, \tag{4.18}$$

with the function $F(m_W, m_Z, m_H)$ given in the Appendix C, which obeys the screening theorem [133] (as all the following m_H dependent functions) and evaluates to -0.61209 for on-shell parameters. In position space, we find for the full correction

$$\delta V^{T3Y}_{r\to\infty}(r) = \frac{\alpha^2}{2\pi r}\left(-\beta_{0,\text{em}}\right)\left(\ln(m_Z r) + \gamma_E\right) \tag{4.19}$$

where $\beta_{0,\text{em}} = -80/9$ is the electromagnetic beta function coefficient, as is also visible in Figure 4.1.

YY - linear combination

In the case of δV^{YY}, the small distance behaviour is similar to the δV^{T3T3} contribution, however, with SU(2) and U(1) interchanged

$$\delta V^{YY}_{\text{light ferm.}}(\mathbf{k}^2 \to \infty) = \frac{\alpha_1^2}{\mathbf{k}^2}\left(\frac{49}{9}\ln\frac{\mathbf{k}^2}{m_Z^2} + \frac{3c_W^2}{s_W^2}\ln\frac{m_W^2}{m_Z^2}\right) \tag{4.20}$$

$$\delta V^{YY}_{\text{3rd gen. quarks}}(\mathbf{k}^2 \to \infty) = \frac{\alpha_1^2}{\mathbf{k}^2}\left(\frac{11}{9}\ln\frac{\mathbf{k}^2}{m_Z^2} + G(m_W, m_Z, m_t)\right) \tag{4.21}$$

$$\delta V^{YY}_{\text{electroweak}}(\mathbf{k}^2 \to \infty) = \frac{\alpha_1^2}{\mathbf{k}^2}\left(\frac{1}{6}\ln\frac{\mathbf{k}^2}{m_Z^2} + H(m_W, m_Z, m_H)\right)\,. \tag{4.22}$$

The functions $G(m_W, m_Z, m_t)$ and $H(m_W, m_Z, m_H)$ are given in Appendix C. G can be approximated to sub permille accuracy in the interval of $\pm 10\,\text{GeV}$ around the on-shell top-mass $m_{t,\text{os}} = 173.1\,\text{GeV}$, by $G(m_W, m_Z, m_t) = 11.9389 + 4.40457 \cdot 10^{-4}\,\text{GeV}^{-2} \times (m_t^2 - m_{t,\text{os}}^2)$, for all other parameters at on-shell values. The function H evaluates to 2.53229 for on-shell parameters.

For the full asymptotic behaviour, we define

$$\Delta_2 = \frac{3c_W^2}{s_W^2}\ln\frac{m_W^2}{m_Z^2} + G(m_W, m_Z, m_t) + H(m_W, m_Z, m_H)\,, \tag{4.23}$$

which in the YY-sector takes the form

$$\begin{aligned} \delta V^{YY}_{r\to 0}(r) &= \frac{\alpha_1^2}{2\pi r}\left(-\beta_{0,Y}\left(\ln(m_Z r) + \gamma_E\right) + \frac{1}{2}\Delta_2\right) \\ &\approx \frac{\alpha_1^2}{2\pi r}\left(-\beta_{0,Y}\ln(m_Z r) + 1.97247\right) \end{aligned} \tag{4.24}$$

where $\beta_{0,Y} = -\frac{49}{9} - \frac{11}{9} - \frac{1}{6} = -\frac{41}{6}$, and the last line provides the numerical value for on-shell parameters. Of the numerical coefficient, the light-fermion term makes up -4.46142, the third-generation quarks 5.26395, the electroweak terms 1.16994 and the Euler-Mascheroni constant associated with the logarithm -3.94431.

Again at large distances, we identify the leading correction due to the electromagnetic beta function, and a subleading contribution from the electroweak part

$$\delta V^{YY}_{\text{light ferm.}}(\mathbf{k}^2 \to 0) = \frac{76}{9}\frac{\alpha^2}{\mathbf{k}^2}\ln\frac{\mathbf{k}^2}{m_Z^2} + \mathcal{O}(\mathbf{k}^0)\,, \tag{4.25}$$

$$\delta V^{YY}_{\text{3rd gen. quarks}}(\mathbf{k}^2 \to 0) = \frac{4}{9}\frac{\alpha^2}{\mathbf{k}^2}\ln\frac{\mathbf{k}^2}{m_Z^2} + \mathcal{O}(\mathbf{k}^0)\,, \tag{4.26}$$

$$\delta V^{YY}_{\text{electroweak}}(\mathbf{k}^2 \to 0) = \frac{\alpha_2^2 s_W^2}{m_W^2} I(m_W, m_Z, m_H) \tag{4.27}$$

with the function $I(m_W, m_Z, m_H) = 0.75918$ for on-shell parameters, given in functional form in Appendix C. Therefore, at large distances, in position space we find

$$\delta V^{YY}_{r\to\infty}(r) = \frac{\alpha^2}{2\pi r}\left(-\beta_{0,\text{em}}\right)\left(\ln(m_Z r) + \gamma_E\right)\,. \tag{4.28}$$

Note that different to the SU(2) analogue (3.13), the beta function behaviours for small and large distances have equal signs for δV^{YY}, as both correspond to an abelian symmetry, as can be seen in the lower panel of Figure 4.2. Also, note that for small masses, all functions contribute to the beta function behaviour. The electroweak contribution is hardly visible, as it is only 1/41 of the full coefficient.

Special linear combinations

The $\mathrm{U}(1)_{\text{em}}$ beta function appears at large distances, in δV^{T3T3}, δV^{T3Y}, and δV^{YY}, as they all contribute to the correction of the tree-level photon exchange. It is only when this tree-level exchange vanishes, due to particular combinations of T^3 and Y, that a different dynamic shows up. In channels in which one of the involved heavy DM particles is neutral $T^3_{ii} = -Y_i$, i.e., if only a Z-boson is exchanged at tree-level and the Coulombic contribution vanishes, the asymptotic behaviour is different. The origin is similar as for the W-boson exchange at tree-level (cf. Section 3.4.1). However, as now hypercharge is involved, the possibilities are richer than in the wino case.

We begin by considering the case, with $T^3_{ii} = -Y_i$ and $T^3_{jj} = -Y_j$, i.e., neutral-neutral channels as is relevant for indirect detection, if the hypercharge of the multiplet is non-zero. In such a case, the relevant linear combination is

$$\delta V^{T3T3-2T3Y+YY}_{Z-\text{only}} = \delta V^{T3T3} - 2\delta V^{T3Y} + \delta V^{YY} \tag{4.29}$$

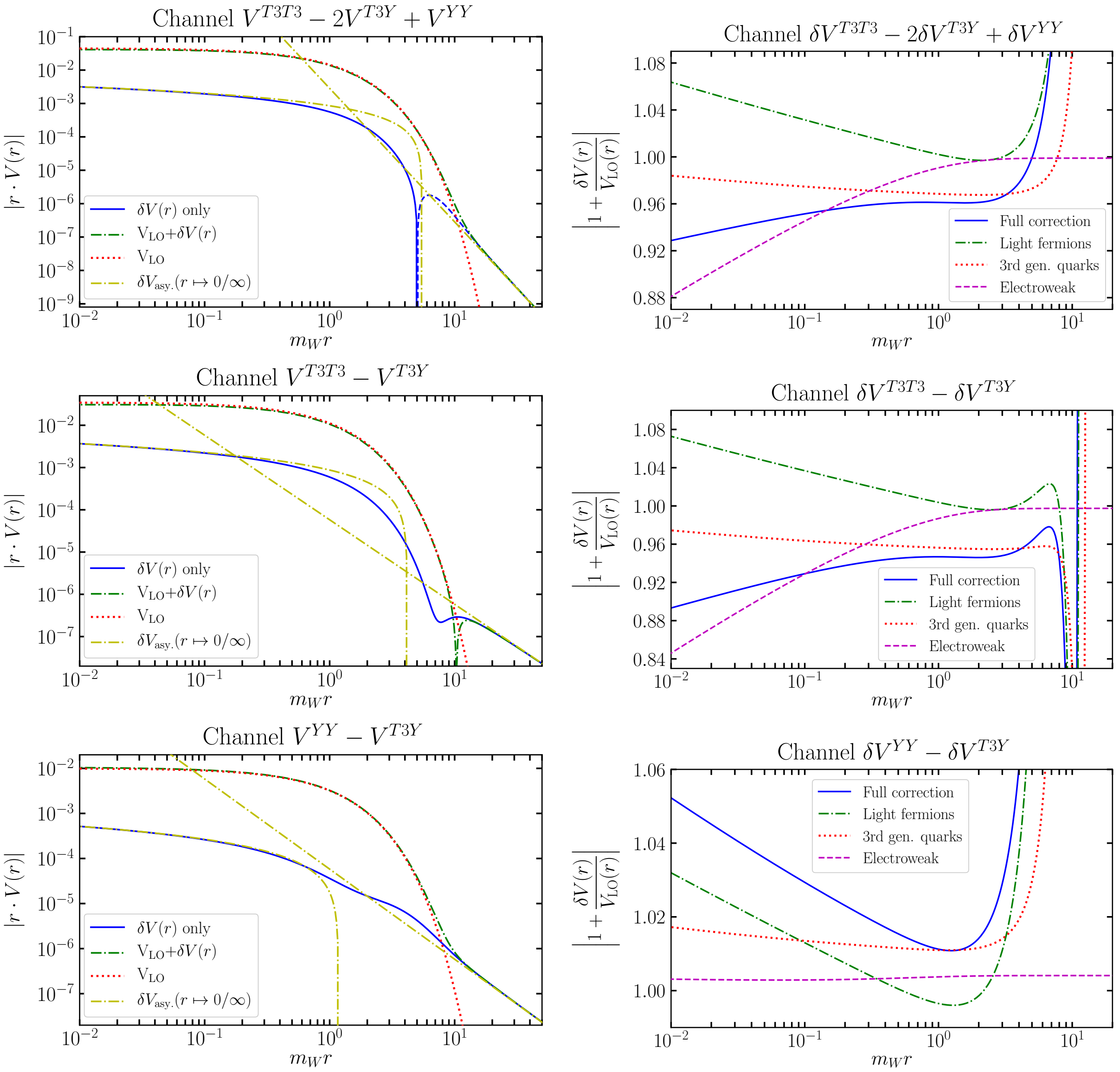

Figure 4.3: *The NLO correction to the tree-level Z-boson only exchange potentials discussed in the text. The left panel shows the modulus of the potential $|r \cdot V(r)|$ for the LO and NLO potential, the NLO contribution only, and the large-distance asymptotic behaviour (the change from solid to dashed for the correction only line, indicates the sign change of this term). In the right panel, we show the ratio of the full NLO potential to the LO potential (blue solid) and separately for the three gauge invariant pieces identified in the text (other curves). The upper plots correspond to the linear combination given in* (4.29)*, the middle and lower plots to the linear combinations in* (4.31).

and the physics is the same as in the W-boson channel. We effectively find a 4-Fermi theory with a long-distance potential induced by massless fermion exchange at large distances. Note that for the Z, now also the third generation quarks contribute, as $b\bar{b}$ loops are possible. The asymptotic behaviour, therefore, is

$$\delta V^{r\to\infty}_{Z-\text{only}}(r) = \frac{12\alpha}{\pi s_W^2 c_W^2 m_Z^5 r^5}\left\{\frac{\alpha m_Z}{c_W^2 s_W^2}\left[\left(\frac{27-54s_W^2+76s_W^4}{36}\right)+\left(\frac{9-12s_W^2+8s_W^4}{72}\right)\right]\right\}$$

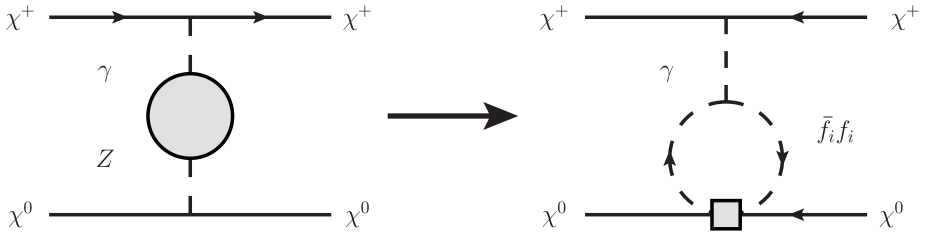

Figure 4.4: *The relevant one-loop self-energy, that in the large distance, small momentum exchange region, gives the long range asymptotic* (4.31) *for* $\delta V^{T3T3} - \delta V^{T3Y}$ *and* $\delta V^{YY} - \delta V^{T3Y}$.

$$= \frac{12\alpha}{\pi s_W^2 c_W^2 m_Z^4 r^5} \frac{\Gamma_Z}{m_Z} \tag{4.30}$$

where the Z-width is given by $m_Z \Gamma_Z = \mathrm{Im}\Sigma_T^{ZZ}(m_Z^2)$. In the first line, inside the curly brackets, the terms indicate the light fermionic and third-generation quark (i.e., $b\bar{b}$-loops) contributions to the Z-width, respectively. The behaviour is shown in the upper panel of Figure 4.3. Note the similarity of the Z-only to the W-exchange correction in off-diagonal channels, cf. Figure 3.5.

However, the above restriction of all heavy particles involved being neutral, if only a Z-boson is exchanged at tree-level, is only sufficient for the charge-0 sector of the potentials. In relic abundance calculations, in the charged sectors, a case may appear, where only one heavy particle is neutral, and still only a Z can be exchanged (e.g., the $+0 \to +0$-channel in the Higgsino case). Without loss of generality, let us assume that the heavy particle i is neutral $T^3_{ii} = -Y_i$ and the particle j is charged $T^3_{jj} \neq -Y_j$. The linear combination for the corrections turns out to be

$$-Y_i T^3_{jj} \left(\delta V^{T3T3} - \delta V^{T3Y}\right) + Y_i Y_j \left(\delta V^{YY} - \delta V^{T3Y}\right) , \tag{4.31}$$

and hence the two relevant linear combinations are $\delta V^{T3T3} - \delta V^{T3Y}$ and $\delta V^{YY} - \delta V^{T3Y}$. The difference to before is now that a photon can couple to the charged fermion, and therefore at large distances, the situation displayed in Figure 4.4 may appear. Compared to the charge-0 sector, the extra photon propagator leads to a r^{-3} asymptotic. We find

$$\begin{aligned} \left(\delta V^{T3T3} - \delta V^{T3Y}\right)(r \to 0) &= -\left(\delta V^{YY} - \delta V^{T3Y}\right)(r \to 0) \\ &= -\frac{\alpha_1 \alpha_2}{18\pi m_Z^2 r^3} \left\{ \left(38c_W^2 - 38s_W^2 - 11\right) + \left(2c_W^2 - 2s_W^2 + 1\right) \right\} \end{aligned} \tag{4.32}$$

where the terms in the curly brackets correspond to light fermions and third-generation quarks, respectively. The terms originate from $\Sigma_T^{\gamma Z}$ as indicated above. The asymptotics for $T^3T^3 - T^3Y$ and $YY - T^3Y$ are of opposite sign, as for $T^3_{jj} = -Y_j$, we need to recover (4.30) and hence the r^{-3} behaviour needs to cancel in that case. This can also be seen in Figure 4.3, adding the middle and lower panel (and adjusting for the absolute value) generates the upper panel.

Also, let us note that this way, no Coulombic contribution, can be induced. Naively, one might consider the electroweak contribution to $\Sigma_T^{\gamma Z}$ to create an effective photon vertex. However, the renormalized self-energy $\hat{\Sigma}_T^{\gamma Z}(\mathbf{k}^2 \to 0) = \mathcal{O}(\mathbf{k}^2)$ needs to vanish for zero-momentum exchange in the absence of massless particles, to have a well-defined Thomson limit [128]. Hence we do not introduce a Coulomb potential at long distances due to the electroweak contribution, which only entails massive terms.

4.3.2 Full corrections and fitting functions

Similar to the case of the wino, we provide fitting functions that mimic the full Fourier transform that is only possible numerically, to a sufficient precision for practical applications. As the wino case already contains the necessary fitting functions for the off-diagonal and T^3T^3-exchanges, we do not repeat them here. They are found in Eqs. (3.33) and (3.34)

$$\delta V^{W}_{\text{fit}}(r) = -\delta V^{\text{fit,wino}}_{\chi^0\chi^0\to\chi^+\chi^-}(r) = \delta V^{\text{fit,wino}}_{\chi^0\chi^\pm\to\chi^\pm\chi^0}(r)\,, \tag{4.33}$$

$$\delta V^{T3T3}_{\text{fit}}(r) = -\delta V^{\text{fit,wino}}_{\chi^+\chi^-\to\chi^+\chi^-}(r) = \delta V^{\text{fit,wino}}_{\chi^\pm\chi^\pm\to\chi^\pm\chi^\pm}(r)\,. \tag{4.34}$$

For the YY potentials as the correction changes sign, we define two fitting functions, one above and one below the sign change position at $x_1 = \frac{718}{853}$, where $x = m_W r$

$$\delta V^{YY}_{\text{fit}}(r) = \begin{cases} \dfrac{\delta V^{YY}_{r\to 0}}{1+\frac{97}{12306436}e^{-\frac{484}{119}x}} - \dfrac{\alpha^2}{r}\dfrac{\frac{71}{104}+\frac{145}{2109}x}{1+\frac{262}{185}e^{-\frac{961}{412}x}} + \dfrac{\frac{41}{19r}+\frac{42}{11}m_W}{1+126870\,e^{\frac{484}{119}x}}\,, & x \le x_1 \\[2ex] \dfrac{\delta V^{YY}_{r\to\infty}}{1+e^{\frac{356}{185}-\frac{191}{179}x}} + \dfrac{\alpha^2}{r}\left[\dfrac{-\frac{85336}{177}-\frac{272x}{21}}{1+e^{\frac{398}{373}x-\frac{127}{66}}} + \dfrac{\frac{4402}{9}-\frac{959\sqrt{x}}{93}+\frac{564x}{35}}{1+e^{\frac{643}{602}x-\frac{2157}{1120}}}\right]\,, & x > x_1 \end{cases} \tag{4.35}$$

The result is permille accurate except in the absolute vicinity of the sign change, shown in Figure 4.5, where the ratio of the full numerical result to the fitting function is shown in the upper panel.

The channel T^3Y should not be separately fitted, as its asymptotic behaviour for $r \to 0$ contains subleading terms compared to the full correction in any given model (cf. (4.12)). To circumvent this problem, we fit T^3Y together with T^3T^3 in the linear combination $T^3T^3 + T^3Y$. In any given model, one can therefore build the appropriate linear combination of T^3T^3, T^3Y and YY, from the fitting functions of $T^3T^3, T^3T^3 + T^3Y, YY$, except for the special power-like asymptotic behaviours for which we provide separate fit functions below. The fitting function for $T^3T^3 + T^3Y$ that approximates the result to permille accuracy (cf. Figure 4.5 - upper panel) over the entire range of r reads

$$\left(\delta V^{T3T3} + \delta V^{T3Y}\right)_{\text{fit}}(r) = \frac{\delta V^{T3T3}_{r\to 0}}{1+\frac{62}{161}x^{\frac{203}{185}}} + \frac{2\,\delta V^{T3T3}_{r\to\infty}}{1+\frac{807}{280}x^{-\frac{267}{268}}} + \frac{\frac{\alpha}{r}\left(-\frac{77}{57}+\frac{71}{485}L-\frac{64}{263}L^2\right)}{\left(1+\frac{268}{7}x^{-\frac{220}{109}}\right)\left(1+\frac{686}{145}x^{\frac{48}{43}}\right)}\,, \tag{4.36}$$

where $L = \ln x$. Note that even though this provides permille accuracy, subtracting the fitting function for T^3T^3 from the above result does not provide an accurate description of T^3Y, as the subleading terms that enter T^3Y and are sometimes the dominant contribution are not resolvable, due to the different fitting procedures.

As discussed above, for special linear combinations of T^3 and Y, we find different asymptotic behaviours for $r \to \infty$. To this end, we provide further fitting functions for these linear combinations, as the above fitting functions do not cancel to the accuracy needed to reveal the power-like r^{-3} and r^{-5} behaviours for $r \to \infty$, even though they are permille level accurate. We begin with the linear combination $T^3T^3 - 2T^3Y + YY$, relevant in indirect detection, that acquires an r^{-5} asymptotic at large distances where the sign change is located at $x_2 = \frac{1382}{275}$

$$\left(\delta V^{T3T3} - 2\delta V^{T3Y} + \delta V^{YY}\right)_{\text{fit}}(r)$$

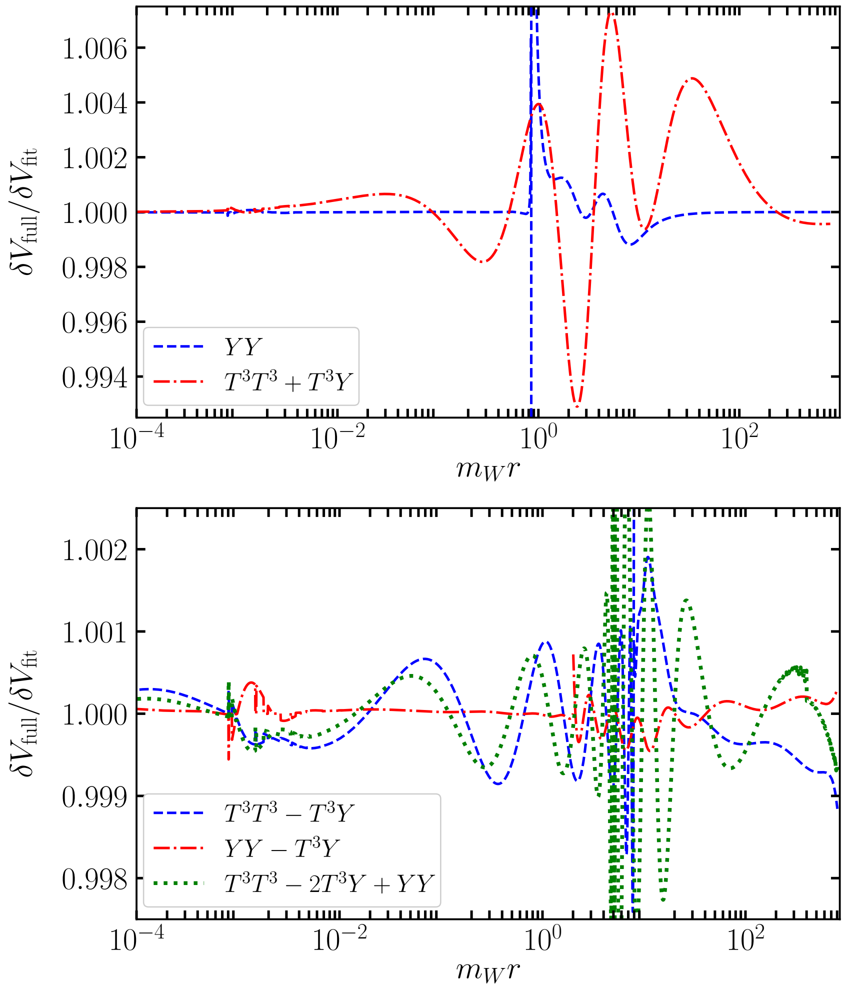

Figure 4.5: *Ratio of the numerical Fourier transform of the potential correction to the fitting functions in the variable $x = m_W r$ for the channels YY (blue/dashed) and $T^3T^3 + T^3Y$ (red/dash-dotted) in the upper panel. In the lower panel, the same ratio is shown for the channels with power-like large distance asymptotic behaviours $T^3T^3 - T^3Y$ (blue/dashed), $YY - T^3Y$ (red/dash-dotted) and $T^3T^3 - 2T^3Y + YY$ (green/dotted).*

$$= \frac{\alpha^2}{r}\begin{cases} -\exp\left[\frac{597\left(L-\frac{1667}{108}\right)\left(L-\frac{837}{503}\right)\left(L-\frac{55}{34}\right)\left(L-\frac{961}{911}\right)\left(L^2-\frac{1715}{563}L+\frac{2072}{587}\right)}{83\left(L-\frac{841}{31}\right)\left(L-\frac{292}{133}\right)\left(L-\frac{1733}{1054}\right)\left(L-\frac{2105}{1302}\right)\left(L^2-\frac{729}{263}L+\frac{1422}{451}\right)}\right], & x \leq x_2 \\ \exp\left[-\frac{3710\left(L-\frac{637}{396}\right)\left(L+\frac{2999}{875}\right)\left(L^2-\frac{7506}{1819}L+\frac{1097}{240}\right)\left(L^2-\frac{5789}{2180}L+\frac{2399}{1326}\right)}{933\left(L-\frac{398}{247}\right)\left(L-\frac{933}{613}\right)\left(L+\frac{2137}{662}\right)\left(L^2-\frac{2785}{664}L+\frac{8311}{1749}\right)}\right], & x > x_2 \end{cases} . \tag{4.37}$$

Finally, we also fit the cases with the r^{-3} asymptotic, which are also better fitted with two functions despite not changing sign. The linear combination $T^3T^3 - T^3Y$ is fitted by

$$\left(\delta V^{T3T3} - \delta V^{T3Y}\right)_{\rm fit} = -\frac{\alpha^2}{r}\begin{cases} \exp\left[\frac{1823\left(L-\frac{262}{15}\right)\left(L-\frac{100}{91}\right)\left(L^2-\frac{641}{145}L+\frac{1226}{177}\right)\left(L^2-\frac{1434}{341}L+\frac{4709}{1052}\right)}{243\left(L-\frac{1549}{52}\right)\left(L-\frac{925}{319}\right)\left(L^2-\frac{1438}{351}L+\frac{642}{151}\right)\left(L^2-\frac{595}{158}L+\frac{1491}{281}\right)}\right], & x \leq x_3 \\ \exp\left[-\frac{902\left(L-\frac{1229}{169}\right)\left(L-\frac{29}{279}\right)\left(L^2-\frac{1331}{278}L+\frac{327}{56}\right)\left(L^2-\frac{2920}{747}L+\frac{1013}{258}\right)}{\left(L-\frac{3891}{535}\right)\left(L+\frac{5687}{13}\right)\left(L^2-\frac{627}{131}L+\frac{391}{67}\right)\left(L^2-\frac{811}{207}L+\frac{661}{169}\right)}\right], & x > x_3 \end{cases} , \tag{4.38}$$

with $x_3 = \frac{950}{119}$. The linear combination $YY - T^3Y$ is fitted by

$$\begin{aligned}
&\left(\delta V^{YY} - \delta V^{T3Y}\right)_{\text{fit}} \\
&= \frac{\alpha^2}{r}\begin{cases}
\exp\left[\frac{518\left(L-\frac{496}{19}\right)\left(L+\frac{106}{283}\right)\left(L^2-\frac{392}{185}L+\frac{827}{394}\right)\left(L^2+\frac{67}{189}L+\frac{1473}{158}\right)}{83\left(L-\frac{395}{8}\right)\left(L-\frac{747}{236}\right)\left(L^2-\frac{659}{445}L+\frac{193}{108}\right)\left(L^2+\frac{347}{2171}L+\frac{677}{81}\right)}\right] & x \leq x_4 \\
\exp\left[\frac{1636\left(L-\frac{837}{79}\right)\left(L+\frac{147}{397}\right)\left(L^2-\frac{1073}{265}L+\frac{801}{173}\right)\left(L^2-\frac{1805}{727}L+\frac{2630}{1127}\right)}{11\left(L-\frac{687}{64}\right)\left(L-\frac{1981}{24}\right)\left(L^2-\frac{2457}{601}L+\frac{520}{111}\right)\left(L^2-\frac{449}{179}L+\frac{312}{115}\right)}\right] & x > x_4
\end{cases}, \qquad (4.39)
\end{aligned}$$

where x_4 is given by $x_4 = \frac{379}{189}$. The numerical quality of the special asymptotics fitting functions is shown in Figure 4.5 lower panel. As can be observed, except in the vicinity of the sign changes, all fitting functions are permille to even sub permille level accurate over the entire interesting r-range for computing the Sommerfeld factor.[1]

As a validation, we tested the computation of the NLO Sommerfeld factors with the fitting functions for the higgsino model in indirect detection (cf. Sections 4.4 and 8.2), and find comparable accuracy to the corresponding wino calculation (cf. Figure 3.11). The largest discrepancies are again seen in the resonance's absolute vicinity and are at maximum about two permille for the cross-section prediction. For mass values off-resonance, the fitting functions provide even sub permille accuracy for the Sommerfeld factors. Similar accuracy is also expected for other observables, models, and the two fitting functions not tested by this procedure $T^3T^3 - T^3Y$ and $YY - T^3Y$.

4.3.3 General comments

Let us make a few general remarks without repeating the full analysis as in the case of the wino. We find similar breakdowns of perturbation theory, for $r \to 0$, due to the beta function logarithms, as in the wino in the channel δV^{YY} (the channel δV^{T3Y} does not suffer this problem, due to the cancellation discussed above). Introducing the $\overline{\text{MS}}$-running couplings, as outlined in Section 3.4.3 for the wino, absorbs these logarithms. The same restrictions, e.g., at large r, apply. However, as phenomenology does not change considerably, we do not repeat the discussion.

On the issue of the top mass dependence of the result, the individual functional dependence is similar to the wino case in the component δV^{YY}, as exemplified for G below Eq. (4.22). In the T^3Y component, we expect a similar dependence. However, as it is always subdominant in the small r region and of the order of subleading corrections to T^3T^3 and YY, it does not warrant further investigation in this region. Furthermore, the top quark does not play a role in the large r Coulomb correction, making the top mass dependence of the T^3Y linear combination irrelevant from a phenomenological standpoint.

Finally, the results allow the construction of the NLO correction for arbitrary electroweak charged models which obey $m_\chi \gg m_Z$ and $m_\chi \alpha_2 \sim m_Z$ (as otherwise, a different EFT applies), as outlined for the Higgsino example below. Our results also are an integral part for models involving Higgs potentials, such as the MSSM. In that case, however, the correction to the Higgs potentials and depending on the gauge considered to the tree-level Goldstone and longitudinal gauge boson potentials would need to be worked out. As long as the contribution due to Higgs potentials is small, our results should already approximate the full result. As the mass difference between various parts of the multiplet is only known to two-loop order for the wino and the Majorana quintuplet [116, 120, 121], unfortunately, we can only claim full NLO accuracy on the non-relativistic side for these two models.

---

[1] Note that for the asymptotic regions $x \gtrsim 10^2$ and $x \lesssim 10^{-2}$ one can also use the asymptotic behaviours given in the previous Section. Possible differences are permille level or even below.

4.4 Higgsino potential at NLO - an explicit example

As an example of how one can implement the above results, let us discuss the Higgsino model, an SU(2) doublet with hypercharge $Y = 1/2$ of Dirac fermions, which will be relevant in later Chapters. In the charge-0 and -1 sector, we find using the rules given above

$$\begin{aligned} V^{Q=0}_{\text{tree}}(r) &= \begin{pmatrix} -\frac{1}{4}\left(V^{T3T3}_{\text{tree}} - 2V^{T3Y}_{\text{tree}} + V^{YY}_{\text{tree}}\right) & -\frac{1}{4}V^{W}_{\text{tree}} \\ -\frac{1}{4}V^{W}_{\text{tree}} & -\frac{1}{4}\left(V^{T3T3}_{\text{tree}} + 2V^{T3Y}_{\text{tree}} + V^{YY}_{\text{tree}}\right) \end{pmatrix} \\ &= \begin{pmatrix} -\frac{\alpha}{4s_W^2c_W^2r}e^{-m_Zr} & -\frac{\alpha_2}{2r}e^{-m_Wr} \\ -\frac{\alpha_2}{2r}e^{-m_Wr} & -\frac{\alpha}{r} - \frac{(s_W^2-c_W^2)^2\alpha}{4s_W^2c_W^2r}e^{-m_Zr} \end{pmatrix} \end{aligned} \tag{4.40}$$

$$V^{Q=1}_{\text{tree}}(r) = -\frac{1}{4}\left(V^{T3T3}_{\text{tree}} - V^{T3Y}_{\text{tree}}\right) + \frac{1}{4}\left(V^{YY}_{\text{tree}} - V^{T3Y}_{\text{tree}}\right) = \frac{(c_W^2 - s_W^2)\alpha_2}{4s_W^2c_W^2r}e^{-m_Zr} \tag{4.41}$$

with the entries corresponding to $\chi^0_D\overline{\chi}^0_D$, $\chi^+\chi^-$ for $Q = 0$ and $\chi^0_D\chi^+$ for $Q = 1$ (the other charge 1 potentials, e.g. $\chi^0_D\chi^-$, are equal). Note that typically no charge 2 sector is considered in the Higgsino case, as the corresponding annihilation matrix vanishes. For the NLO correction, this means

$$\delta V^{Q=0}_{1-\text{loop}} = \begin{pmatrix} -\frac{1}{4}\left(\delta V^{T3T3} - 2\delta V^{T3Y} + \delta V^{YY}\right) & -\frac{1}{4}\delta V^{W} \\ -\frac{1}{4}\delta V^{W} & -\frac{1}{4}\left(\delta V^{T3T3} + 2\delta V^{T3Y} + \delta V^{YY}\right) \end{pmatrix} \tag{4.42}$$

$$\delta V^{Q=1}_{1-\text{loop}} = -\frac{1}{4}\left(\delta V^{T3T3} - \delta V^{T3Y}\right) + \frac{1}{4}\left(\delta V^{YY} - \delta V^{T3Y}\right) \tag{4.43}$$

where either the full results discussed above or the fitting functions can be used to obtain accurate results. Note that all possible fitting functions are needed in the Higgsino if relic abundance is to be considered.

Direct detection experiments already rule out the pure Higgsino due to the Z-coupling of χ^0_D. Splitting $\chi^0_D = \chi^0_1 + i\chi^0_2$ into two Majorana fermions, with a small mass splitting $\delta m_N \gtrsim \mathcal{O}(100\,\text{keV})$ between χ^0_1 and χ^0_2, introduced by some UV completion of the model, the Higgsino is still a perfectly viable DM candidate. Furthermore, note that this mass splitting due to small admixtures of winos and binos in supersymmetric scenarios is the rule rather than the exception. The relevant charge-0 channel in method-II notation [86], for spin $S = 0$, therefore can be written as

$$\begin{aligned} &V^{Q=0,S=0}_{\text{Majorana, tree}} \\ &= \begin{pmatrix} 0 & -\frac{1}{4}\left(V^{T3T3}_{\text{tree}} - 2V^{T3Y}_{\text{tree}} + V^{YY}_{\text{tree}}\right) & -\frac{1}{2\sqrt{2}}V^{W}_{\text{tree}} \\ -\frac{1}{4}\left(V^{T3T3}_{\text{tree}} - 2V^{T3Y}_{\text{tree}} + V^{YY}_{\text{tree}}\right) & 0 & -\frac{1}{2\sqrt{2}}V^{W}_{\text{tree}} \\ -\frac{1}{2\sqrt{2}}V^{W}_{\text{tree}} & -\frac{1}{2\sqrt{2}}V^{W}_{\text{tree}} & -\frac{1}{4}\left(V^{T3T3}_{\text{tree}} + 2V^{T3Y}_{\text{tree}} + V^{YY}_{\text{tree}}\right) \end{pmatrix} \\ &= \begin{pmatrix} 0 & -\frac{\alpha}{4s_W^2c_W^2r}e^{-m_Zr} & -\frac{\alpha_2}{2\sqrt{2}r}e^{-m_Wr} \\ -\frac{\alpha}{4s_W^2c_W^2r}e^{-m_Zr} & 0 & -\frac{\alpha_2}{2\sqrt{2}r}e^{-m_Wr} \\ -\frac{\alpha_2}{2\sqrt{2}r}e^{-m_Wr} & -\frac{\alpha_2}{2\sqrt{2}r}e^{-m_Wr} & -\frac{\alpha}{r} - \frac{(s_W^2-c_W^2)^2\alpha}{4s_W^2c_W^2r}e^{-m_Zr} \end{pmatrix} \end{aligned} \tag{4.44}$$

where the columns and rows correspond to $\chi^0_1\chi^0_1$, $\chi^0_2\chi^0_2$ and $\chi^+\chi^-$, respectively. The NLO correction correspondingly is obtained with $V^{AB}_{\text{tree}} \to \delta V^{AB}_{1-\text{loop}}$. The mass differences are cast as a corresponding matrix $2\delta m^{\text{hig.}} = \text{diag}\,(0, 2\delta m_N, 2\delta m)$ with $\delta m_N = m_{\chi^0_2} - m_{\chi^0_1}$.

Besides the above, there is, in principle, a $\chi_1^0\chi_2^0$ potential in the charge-0 sector. However, as it does not mix with $\chi_1^0\chi_1^0$, it is not relevant for indirect detection. Also note, the above small mass splitting is irrelevant in the Higgsino relic abundance case. It only becomes relevant at temperatures where the freeze-out process is already complete, i.e., using the above χ_D^0, χ^+ potentials is sufficient for this calculation. Equipped with these results, relic abundance and indirect detection calculations for the Higgsino model are possible.

5

Relic density for wino dark matter

As a second example for the NLO electroweak potential effects, we discuss the relic abundance calculation for wino dark matter. We begin by reviewing the WIMP relic abundance calculation under the freeze-out assumption and then apply the formalism to the wino model. The calculation using NLO potentials was first presented in [104] in collaboration with M. Beneke and R. Szafron. The same analysis is not repeated for the Higgsino model with NLO potentials, as already the inclusion of the LO Sommerfeld effect has negligible impact on the relic abundance prediction (see, e.g. [36, 38]). Therefore, re-performing the analysis does not promise new exciting insights.

5.1 Relic abundance calculation

Here we briefly review the dark matter relic abundance calculation to establish the notation and formulas for the following discussion, mostly following [86]. The discussion is generic for the coannihilation of WIMPs [29, 144] under rather general assumptions, stated below. For the pure wino, including Sommerfeld enhancement, the results were first presented in [39] and in the context of minimal DM in [38]. For the full MSSM including Sommerfeld enhancements and $\mathcal{O}(v^2)$ effects in the annihilation cross-sections this was first achieved in [36, 84, 85, 86].

The thermal relic abundance of the dark matter is obtained by solving the Boltzmann equation for the number density [145]

$$\frac{dn(t)}{dt} + 3H(t)n(t) = -\left\langle \sigma_{\text{eff}} v \right\rangle \Big(n^2(t) - n_{\text{eq}}^2(t)\Big)\,, \tag{5.1}$$

where $n = \sum_i n_i$ is the sum of the individual number densities of all co-annihilating particles (for the wino $i = 0, +, -$). The equation depends upon the Hubble rate H, the equilibrium number density $n_{\text{eq}} = \sum_i n_{\text{eq},i}$, and the thermally-averaged cross-section $\langle \sigma_{\text{eff}} v \rangle$, which is discussed in detail below. Eq. (5.1) is valid under the assumption that Maxwell-Boltzmann statistics, instead of Fermi-Dirac statistics for fermions or Bose-Einstein statistics for bosons, can be employed. For typical freeze-out temperatures of $T_f \sim m_\chi/20$ this is an excellent approximation. Furthermore, the description relies on the fact that the DM particles remain in kinetic equilibrium with the SM plasma till freeze-out ends [146].

For practical calculations, it is useful to reformulate (5.1) in terms of comoving quantities. To this end, we introduce the yield $Y = n/s$ defined as the ratio of particle number density n to the entropy density of the cosmic comoving frame s. Given that the entropy per comoving volume is conserved, the change of n and s due to the universe's expansion is the same. $ds/dt = -3Hs$ and therefore the term involving the Hubble rate H drops in (5.1). Furthermore, the time variable t is unhandy, as the effective annihilation cross-section $\langle \sigma_{\text{eff}} v \rangle$ will depend on the particles kinetic energy and therefore on the temperature T. Therefore, we introduce the variable $x = m_\chi/T$ as an evolution variable, after which the Boltzmann equation reads

$$\frac{dY}{dx} = \frac{1}{3H}\frac{ds}{dx}\,\langle\sigma_{\text{eff}}v\rangle\left(Y^2 - Y_{\text{eq}}^2\right) \tag{5.2}$$

with $Y_{\text{eq}} = n_{\text{eq}}/s$. Now only the Hubble rate H remains to be fixed using the Friedmann equation. Assuming a radiation dominated universe during DM freeze-out, the Hubble rate can be related to the energy density, and the Boltzmann equation takes the final form

$$\frac{dY}{dx} = -\sqrt{\frac{\pi}{45G}}\,\frac{g_*^{1/2}m_\chi}{x^2}\,\langle\sigma_{\text{eff}}v\rangle\left(Y^2 - Y_{\text{eq}}^2\right)\,, \tag{5.3}$$

where G is Newtons constant and the parameter $g_*^{1/2}$ is given by

$$g_*^{1/2} = \frac{h_{\text{eff}}(T)}{g_{\text{eff}}^{1/2}(T)}\left[1 + \frac{1}{3}\frac{d(\ln h_{\text{eff}}(T))}{d(\ln T)}\right]\,. \tag{5.4}$$

The parameters $g_{\text{eff}}, h_{\text{eff}}$ are defined in terms of the energy and entropy density, respectively

$$\rho(T) = g_{\text{eff}}(T)\frac{\pi^2}{30}T^4 \quad , \quad s(T) = h_{\text{eff}}(T)\frac{2\pi^2}{45}T^3\,. \tag{5.5}$$

The effective degrees of freedom $g_{\text{eff}}, h_{\text{eff}}$ are functions that interpolate between the full SM value and the value today. For temperatures of $(100 - 400)$ MeV, i.e., during the QCD phase transition, these functions show a steep increase that depends on the exact modelling of the phase transition. This modelling is typically not relevant for TeV-scale DM without Sommerfeld enhancement as the DM is frozen out before. However, with Sommerfeld enhancement, the late time annihilations may also deplete the DM density during the QCD phase transition, making accurate modelling, e.g. on the lattice, necessary. For the solution of the Boltzmann equation, we adopt the implementation of [147] using the plots and tables given there. For temperatures below $T = 1\,\text{MeV}$, and above $T = 280\,\text{GeV}$, we supplement the table, with results of [148].

From the Boltzmann equation (5.3), one can easily understand the freeze-out dynamics. Assuming that we start at some initial x in equilibrium with the thermal plasma, initially $Y = Y_{\text{eq}}$. For small x, the difference between Y and Y_{eq} will remain small, and Y closely follows the equilibrium distribution, which falls exponentially. At some point (for typical TeV-WIMPs around $x \sim 20$), the prefactor $\sim \langle\sigma_{\text{eff}}v\rangle$ is not able to provide the necessary change anymore for Y to follow Y_{eq} closely, and effectively the annihilations cease. The dark matter "freezes out". Including the potentials does not change the general picture. However, the velocity dependence of the cross-section can partially compensate the $1/x^2$ factor. Therefore, the freeze-out process can be prolonged over a longer period and shifted to later times (smaller temperatures).

After solution of the Boltzmann equation, the obtained yield at present time $Y_0 = Y(x_0)$ is linearly related to the DM relic abundance

$$\Omega_{\text{DM}}h^2 = \frac{\rho_{\text{DM}}}{\rho_{\text{crit.}}}h^2 = \frac{m_\chi s_0 Y_0}{\rho_{\text{crit.}}}h^2 \tag{5.6}$$

where the critical energy density is given by $\rho_{\text{crit.}} = 1.05368 \cdot 10^{-5}\,\text{GeV}\,\text{cm}^{-3}\,h^2$. This can be compared to the results by Planck $\Omega_{\text{DM}}h^2 = 0.1205$ [2] to determine the mass for which the WIMP under consideration would constitute the full DM relic abundance.

5.1.1 Thermally-averaged cross-section

The relevant quantity that is still missing for the solution of the Boltzmann equation is the thermally-averaged cross-section. It is the crucial quantity in the sense that the particle physics (and therefore the NLO potentials) enter the relic abundance calculation at this point. The thermally-averaged cross-section in a co-annihilation scenario is given by

$$\langle \sigma_{\text{eff}} v \rangle = \sum_{i,j} \langle \sigma_{ij} v_{ij} \rangle \, \frac{n_{i,\text{eq}} n_{j,\text{eq}}}{n_{\text{eq}}^2} \tag{5.7}$$

where $\langle \sigma_{ij} v_{ij} \rangle$ are the thermally-averaged cross-sections for the individual processes. The result can be translated to the expression in the CM-frame (which allows us to use the NR annihilation cross-sections to $\mathcal{O}(v^2)$ of [85]) [29, 144]

$$\langle \sigma_{\text{eff}} v \rangle = \frac{T}{n_{\text{eq}}^2} \sum_{i,j} \frac{g_i g_j}{4\pi^4} \int_{(m_i+m_j)^2}^{\infty} ds \, (\sigma_{ij} v_{\text{rel}}) \; p_{ij} \; \frac{s^2 - (m_i^2 - m_j^2)^2}{4s} \; K_1\!\left(\frac{\sqrt{s}}{T}\right) \tag{5.8}$$

with g_i the internal spin degrees of freedom, so for the fermions considered later $g_i = 2$. The further quantities are given by

$$p_{ij} = \frac{1}{\sqrt{s}} \sqrt{\frac{s^2}{4} - \frac{s}{2}(m_i^2 + m_j^2) + \frac{(m_i^2 - m_j^2)^2}{4}} \tag{5.9}$$

$$n_{\text{eq}} = \frac{T}{2\pi^2} \sum_i g_i \, m_i^2 \, K_2\left(\frac{m_i}{T}\right) \tag{5.10}$$

where K_1, K_2 refer to the modified Bessel functions of the second kind. The Bessel functions in their large argument expansion provide the characteristic suppression for decoupling channels $\sim e^{-(m_i+m_j-2m_\chi)/T}$ relative to the annihilation cross-section of the lightest DM particles.

5.1.2 Technical implementation of the relic abundance calculation

The calculation of the relic density can be divided into several steps. To determine the thermally-averaged cross-section, a velocity/temperature-dependent expression in each of the co-annihilation channels $\sigma_{ij} v_{ij}$, cf. Eq. (5.8), has to be produced. We use the annihilation matrices $\hat{f}(^{2S+1}L_J)$ up to $\mathcal{O}(v^2)$, conveniently tabulated in Appendix C of [85]. For definiteness, we use one-loop $\overline{\text{MS}}$ couplings evolved to the natural scale of the hard annihilation process $\mu = 2m_\chi$. The necessary Sommerfeld factors, for the DM state $\chi_i \chi_j$ in the partial-wave configuration $^{2S+1}L_J$ of angular momentum L and spin S is given by [86]

$$S_{ij}[\hat{f}(^{2S+1}L_J)] = \frac{\left[\psi^{(L,S)}_{e_4 e_3,\,ij}\right]^* \hat{f}^{\chi\chi\to\chi\chi}_{\{e_1e_2\}\{e_4e_3\}}(^{2S+1}L_J)\, \psi^{(L,S)}_{e_1e_2,\,ij}}{\hat{f}^{\chi\chi\to\chi\chi}_{\{ij\}\{ij\}}(^{2S+1}L_J)|_{\text{LO}}} \,. \tag{5.11}$$

The wave functions $\psi^{(L,S)}_{e_1e_2,\,ij}$ describe the scattering of the state ij into another state e_1e_2, and are evaluated at $\mathbf{r} = 0$. They are obtained solving the Schrödinger equation at the origin. We implement the variable phase method described in [86], to which we also point for further details on the solution and the derivation of the Sommerfeld factors. As input, we need the NLO potentials in a numerically accessible and quickly evaluable form. Therefore, we precalculate the NLO potentials numerically and create interpolating functions as an input for the differential equation solver. The Schrödinger equation is then solved from an initial vale $x_0 = m_\chi v r_0 = 10^{-7}$ to a large value x_∞.[1] The latter is determined adaptively starting from an initial $x_\infty^{\text{initial}} = (m_\chi/\text{TeV})$, by requiring that doubling x_∞ does change the Sommerfeld factor by less than three permille, till the procedure terminates. Near the $\chi^+\chi^-$-threshold, convergence is sometimes hard to reach. Therefore, we abort the procedure for $x_\infty > 10^4$, which does not pose a severe problem, as the threshold region where this happens is rather narrow, the behaviour around the true value is oscillating, and we also scan the threshold very accurately. Therefore, the inaccuracies of $\sim 1\%$ due to the termination above x_∞, tend to average out for the thermally-averaged cross-section and have a negligible impact on the final cross-section prediction. The co-annihilation cross-section in the channel ij, used for the thermal average (5.8), is given by[2]

$$\begin{aligned}\sigma^{\chi_i\chi_j\to\,\text{light}}\, v_{\text{rel}} =\, & S_{ij}[\hat{f}(^1S_0)]\, \hat{f}^{\chi\chi\to\chi\chi}_{\{ij\}\{ij\}}(^1S_0) + S_{ij}[\hat{f}(^3S_1)]\, 3\, \hat{f}^{\chi\chi\to\chi\chi}_{\{ij\}\{ij\}}(^3S_1) \\ & + \frac{\vec{p}_{ij}^{\,2}}{M_{ij}^2} \Big(S_{ij}[\hat{g}_\kappa(^1S_0)]\, \hat{g}^{\chi\chi\to\chi\chi}_{\{ij\}\{ij\}}(^1S_0) + S_{ij}[\hat{g}_\kappa(^3S_1)]\, 3\, \hat{g}^{\chi\chi\to\chi\chi}_{\{ij\}\{ij\}}(^3S_1) \\ & + S_{ij}\Big[\frac{\hat{f}(^1P_1)}{M^2}\Big]\, \hat{f}^{\chi\chi\to\chi\chi}_{\{ij\}\{ij\}}(^1P_1) + S_{ij}\Big[\frac{\hat{f}(^3P_{\mathcal{J}})}{M^2}\Big]\, \hat{f}^{\chi\chi\to\chi\chi}_{\{ij\}\{ij\}}(^3P_{\mathcal{J}})\Big)\,. \end{aligned} \tag{5.12}$$

We tabulate the above cross-section in all co-annihilation channels using 100 velocity points distributed logarithmically between $v = 10^{-4}$ and 1. In addition, we add further points around the two-particle thresholds, for $\chi^\pm\chi^\pm, \chi^+\chi^-$ at $v = \sqrt{2\delta m_\chi/m_\chi}$ and at the threshold for $\chi^0\chi^\pm$, which is located at $v = \sqrt{\delta m_\chi/m_\chi}$. In total, we use around 150 points for each of the co-annihilation channels.

The results of this procedure are monotonically interpolated and then integrated for the velocity/temperature-dependent thermally-averaged annihilation cross-section. We calculate the thermal average for 20 points per decade logarithmically distributed between $x = m_\chi/T = 1$ to 10^8. The resulting table is again monotonically interpolated and used as an input for the Boltzmann equation solver, that solves (5.3) from $x = 1 - 10^8$ using the initial condition $Y(1) = Y_{\text{eq}}(1)$. For concreteness, we extract the value of Y_∞ from $Y(10^8)$.

5.2 NLO relic density - wino model

Using the above procedures and definitions, we proceed to determine the wino relic abundance. Let us recap, that the first zero-energy bound-state resonance for the $\chi^0\chi^0$ $(^1S_0)$ total annihilation cross-section is located at $m_\chi = 2.282\,\text{TeV}$ for the LO potential and at $2.419\,\text{TeV}$ for the NLO potential. The Sommerfeld factor for the total cross-section is slightly different from the one for $\gamma + X$ considered in [103] or in Section 3.5, since in the latter case, only the $\chi^+\chi^- \to \chi^+\chi^-$ component of the annihilation matrix enters. Therefore, in that case, only the wave-function components $\psi_{(00)(+-)}$ and $\psi_{(+-)(00)}$ are probed. On the other hand, for the relic abundance

---

[1] Note that x appears twice, once in the solution of the Schrödinger equation $x = mvr$, and once in the Boltzmann equation $x = m_\chi/T$. For consistency with [86], we keep this notation. Whichever definition applies should be clear from the context.

[2] There is a scheme-dependence for the $\mathcal{O}(v^2)$ S-wave Sommerfeld factors $S_{ij}[\hat{g}\kappa(^1S_0)]$, $S_{ij}[\hat{g}_\kappa(^1S_0)]$ in (5.12) in the factor κ. To obtain this expression, an equation-of-motion identity is used, see Section 4.4 of [86]. As the exchange bosons can be massive, an additional term from the Lippmann-Schwinger equation arises from a linearly divergent loop integral, cf. Section A.1.3. Though finite, the result is scheme-dependent. The dependence would cancel against the one-loop hard annihilation matrices, which are not known. This scheme-dependence is already present for the LO potential. Adding the NLO potential contributions neither improves the situation nor is straightforward, as there are richer structures for the loop integral at NLO. Therefore, we stick in the determination of κ to the LO factor, as adding the NLO terms would not improve upon the scheme-dependence, and second and more importantly, the corrections from the $\mathcal{O}(v^2)$ terms are small in practice, as discussed later.

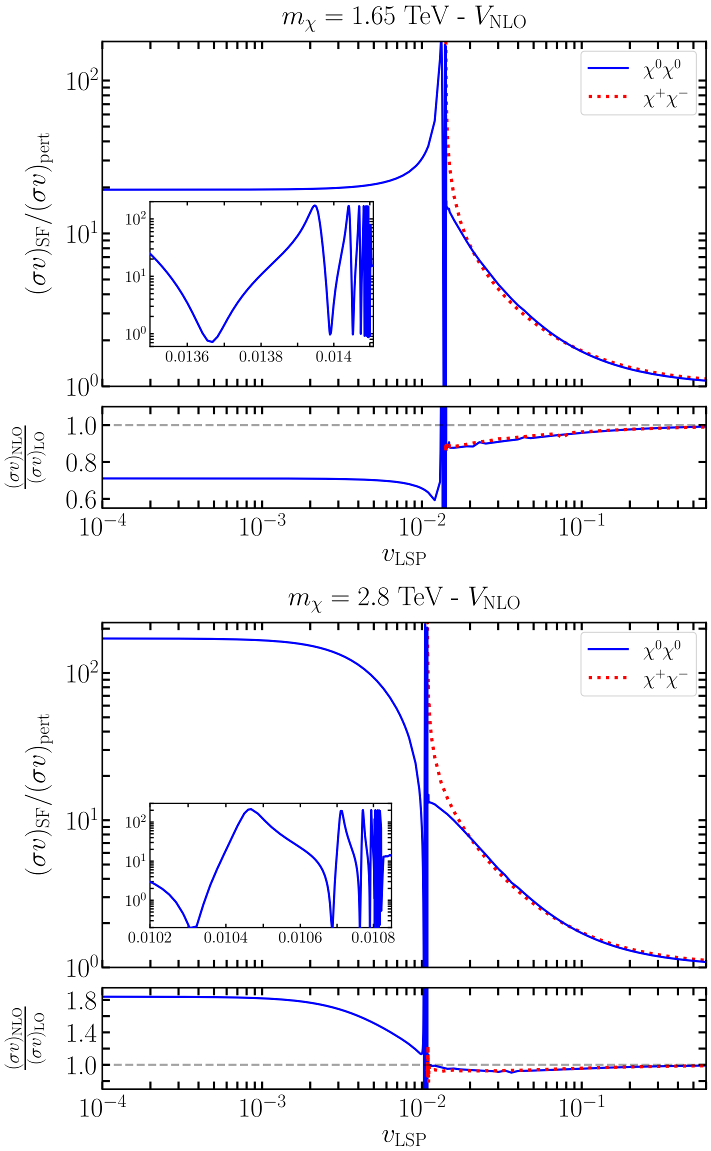

Figure 5.1: *The Sommerfeld factors for the two channels $\chi^0\chi^0$ and $\chi^+\chi^-$ computed with the NLO potential for $m_\chi = 1.65$ TeV (upper panel) and 2.8 TeV (lower panel) as a function of DM velocity. The inset zooms into the region around $v_{\rm LSP} = \sqrt{2\delta m_\chi/m_\chi}$, where Coulomb bound states cause a rapid oscillation in the Sommerfeld factor. Below each panel, the effect of the NLO correction to the potential is highlighted by showing the ratio of NLO to LO Sommerfeld factor.*

calculation, the annihilation matrix is non-zero in all entries $\chi^0\chi^0/\chi^+\chi^- \to \chi^0\chi^0/\chi^+\chi^-$ and the Sommerfeld calculation is sensitive to all components of the wave function. Nevertheless, the resonance masses for the co-annihilation channels are the same within sub-GeV accuracy as those for the annihilation to $\gamma + X$.

5.2.1 Sommerfeld factors in individual channels

To assess the effect of the NLO potential on the Sommerfeld factors, we examine the cross-section in the two most important charge-zero annihilation channels $\chi^0\chi^0, \chi^+\chi^-$ in Figure 5.1 as functions of χ^0 velocity. The two panels show mass values below and above the first bound-state resonance. A prominent increase in the $\chi^+\chi^-$ Sommerfeld factor is seen at $v_{\mathrm{LSP}} = \sqrt{2\delta m_\chi/m_\chi}$, which is due to the $\chi^+\chi^-$ threshold. The small spikes slightly below the threshold value correspond to the Coulomb bound states of $\chi^+\chi^-$ [36], shown enlarged, in the inset of Figure 5.1. Formally, at the $\chi^+\chi^-$-threshold, the Sommerfeld factor turns infinite, as the relative velocity of the charged DM two-particle state is

$$v_{+-} = 2\,\mathrm{Re}\sqrt{\left(m_\chi v_{\mathrm{LSP}}^2 - 2\delta m_\chi\right)/\left(m_\chi + \delta m_\chi\right)} \;\to\; 0\,, \tag{5.13}$$

where v_{LSP} is the velocity of the lightest DM particle χ^0. However, this will not spoil the abundance calculation, as in the thermal average, the $1/v_{+-}$ divergence is regulated by the integration measure $d^3\mathbf{v}_{+-} = v_{+-}^2 dv_{+-} d\Omega$. For velocity values below the threshold, only the $\chi^0\chi^0$ channel is present, and the Sommerfeld factor can be seen to saturate around $v \lesssim 10^{-3}$.

In the subtended panel of each plot, we show the ratio of NLO to LO Sommerfeld factor. For small values of v_{LSP} below the $\chi^+\chi^-$ threshold, the NLO potential causes $\mathcal{O}(1)$ corrections to the cross-section, as already observed for indirect detection in Section 3.5. For velocity values above the $\chi^+\chi^-$ threshold, the correction is on the order of a few percent as expected for a one-loop electroweak correction. This leads to two important observations: First, the resonance effect and related the $\mathcal{O}(1)$ corrections for indirect detection using the NLO potential are a small velocity effect and require the heavier state to be decoupled. Secondly, it is a priori not clear if the NLO relic abundance will be larger or smaller at a given mass value, as the relic abundance prediction weighs the different velocity regimes. While there is a generic suppression before decoupling of the heavier state, the correction can be much larger in the resonant regime below threshold and enhance the cross-section, thereby prolonging freeze-out.

5.2.2 Thermally-averaged annihilation cross-section

The relevant particle-physics quantity in determining the relic abundance is the thermally-averaged annihilation cross-section $\langle \sigma_{\mathrm{eff}} v\rangle$ shown in Figure 5.2 for the same mass values as above and at the resonance mass values of LO and NLO potential. For small $x \lesssim 10$, the non-relativistic approximation is inaccurate, and in principle, a relativistic calculation to determine the annihilation cross-section would be necessary. The final relic abundance is only negligibly affected by this inaccuracy, as the freeze-out process starts around $x \sim 20$. At this point, the non-relativistic approximation is already very precise, as we include $\mathcal{O}(v^2)$ corrections. At large x values around $x \sim m_\chi/\delta m_\chi$, a small drop in the Born approximation is visible, that corresponds to the decoupling of the $\chi^+\chi^-$-channel. For the Sommerfeld enhanced results, the cross-section saturates at a constant value for large x, except at the resonances, where a $1/v^2 \sim x$ enhancement persists.

As already discussed for the Sommerfeld factors above, below the first resonance, the cross-section obtained using the NLO potential is always smaller than using the LO potential. For mass values above the first resonance of the NLO potential, the annihilation cross-section using the NLO potentials may also be larger than in the LO case. However, even at the NLO resonance mass value $m_\chi = 2.42$ TeV, the prediction exceeds the LO result only around $x \gtrsim 100$. This corresponds to the generic large v, early time, suppression of the Sommerfeld factors above. Only when the resonant enhancement plays a major part in the thermal average, i.e., as soon as the heavy states decouple, the NLO prediction exceeds the LO result. The reason is the slightly weaker NLO potential, which leads to less enhancement, except in the late-time regime.

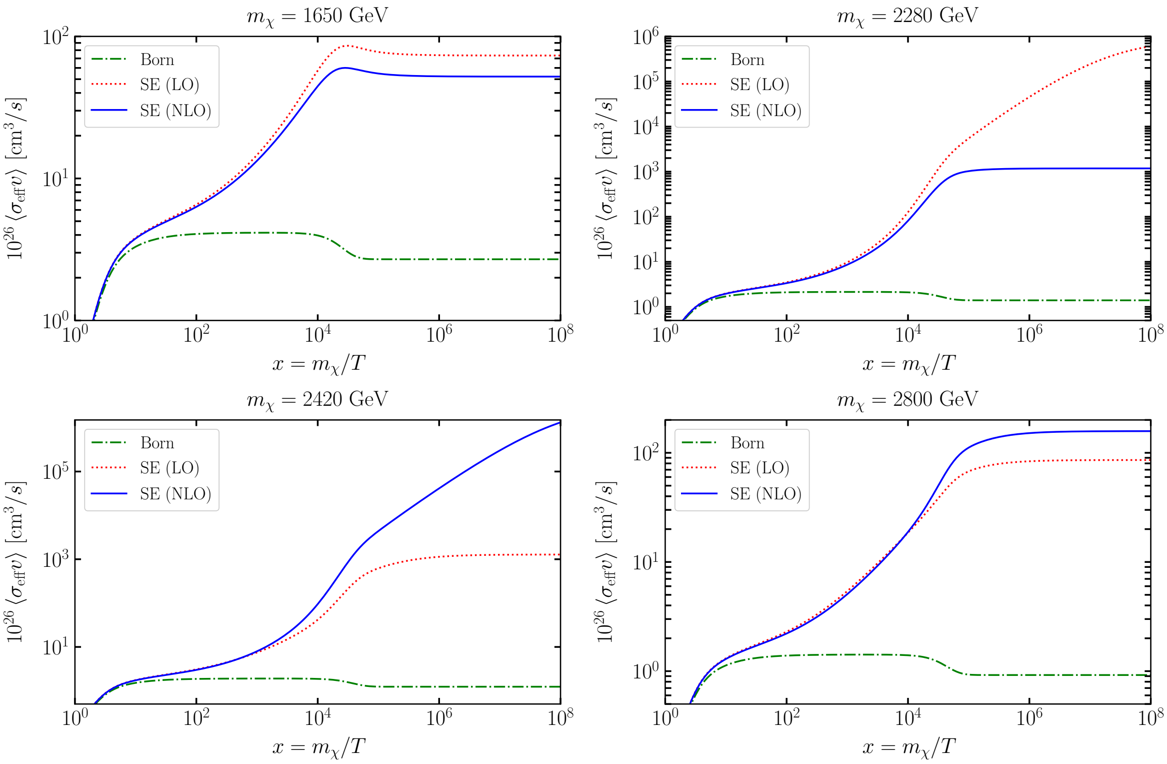

Figure 5.2: *The thermally-averaged cross-section $\langle\sigma_{\rm eff}v\rangle$ in the Born approximation (green/dot-dashed), and with the Sommerfeld enhancement from the LO (dotted/red) and NLO (solid/blue) potential as a function of $x = m_\chi/T$. We show $\langle\sigma_{\rm eff}v\rangle$ for mass values below the first resonance ($m_\chi = 1.65$ TeV) and above ($m_\chi = 2.8$ TeV), and near the first resonance of the LO ($m_\chi = 2.28$ TeV) and the NLO ($m_\chi = 2.42$ TeV) potential.*

5.2.3 The dark-matter yield Y

When solving the Boltzmann equation (5.3), the above observations on thermally-averaged cross-section and Sommerfeld factors translate into the yield Y as a function of x as shown in Figure 5.3. The plots show the ratio to the prediction using only the Born cross-section without Sommerfeld enhancement. Till $x \sim (20-30)$, the ratio stays at unity, as the freeze-out process has not yet begun. For higher x, the Sommerfeld enhanced yields are smaller than their Born equivalent, as the increased cross-section depletes the DM abundance more, thereby extending freeze-out. Away from bound-state resonances around $x \sim 10^4$ also the Sommerfeld enhanced freeze-out process completes, and the ratio of yields becomes constant. It is only at the resonance mass values that the late time $1/v^2 \sim x$ enhancement starts a further depletion of $\mathcal{O}(1)$, as shown for the LO and NLO resonant mass values (upper right and lower left panel, respectively).

Similar to the above considerations, we can also transfer the thermally-averaged cross-section observations to the yields. At early times, i.e., for low x, the NLO yield is always larger than the LO yield, as the annihilation cross-section is generically smaller. At the resonance mass value, the late-time annihilations can overpower the LO depletion, which can lead to an inverted picture. As the effect of late-time annihilations hinges on the resonant enhancement, this is only possible at the resonant mass values, as for other masses, even though the late-time cross-section might be larger, the freeze-out process is already complete.

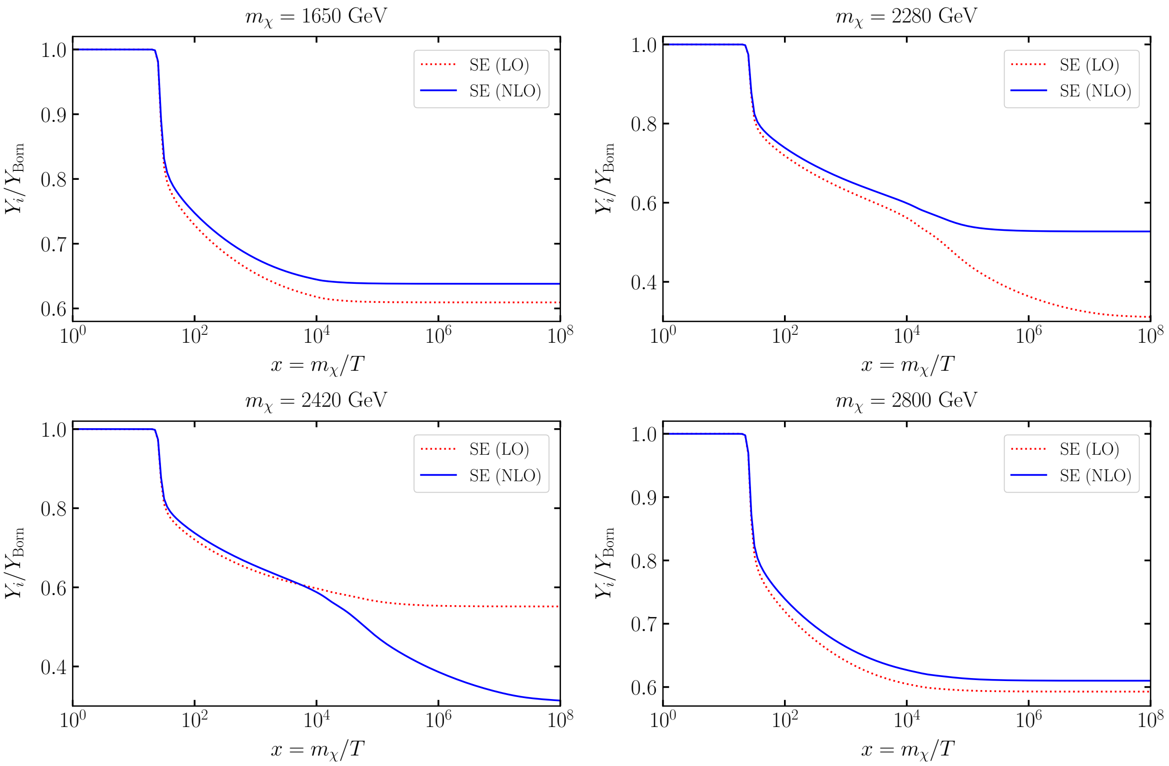

Figure 5.3: *The ratio Y_i/Y_{Born} as a function of $x = m_\chi/T$ for several values of m_χ as in Figure 5.2. The perturbative yield Y_{Born} is computed with the Born cross-section only, while the Y_i include the LO (dotted/red) and the NLO Sommerfeld potential (solid/blue).*

5.2.4 The wino relic abundance

Finally, we can use the yield at present-day and relate it to the observed DM relic abundance (5.6). In Figure 5.4, we show the predicted relic abundance for a given wino DM mass value, using the Born approximation, LO and NLO potentials. As already noted in the literature [36, 39, 40], the LO Sommerfeld effect leads to a significant $\mathcal{O}(20-30\%)$ correction of the predicted DM mass.

The correction obtained by including the NLO potential is in comparison rather mild, being about $(2-5)\,\%$ smaller than the LO potential prediction, away from resonance. In the vicinity of the resonance mass value, the corrections grow larger, as is also visible by the subtended ratio plot of NLO to LO prediction. The observed abundance $\Omega_{\mathrm{DM}}h^2 = 0.1205$ [2] is shown as an indication, and reached for a wino mass of 2.842 TeV with NLO potentials compared to 2.886 TeV at LO (and 2.207 TeV using Born cross-section only). As a comparison, the inclusion of $\mathcal{O}(v^2)$ terms results in a $(1-3)\,\%$ correction, i.e., is of similar size.

The uncertainty on the NLO potential calculation is hard to quantify. The largest remaining theoretical uncertainty arises presumably from the one-loop corrections to the hard annihilation matrices. The dominant logarithmic parts are already taken into account using running couplings, which has a sizeable effect. As an example, we consider $m_\chi = 3\,\mathrm{TeV}$ close to the observed abundance value. The relevant coupling ratio, that quantifies the effect of using running couplings is given by $\hat{\alpha}_2^2(2\times 3\,\mathrm{TeV})/\hat{\alpha}_2^2(m_Z) = 0.867$. We can estimate the non-logarithmic parts by comparing to the Sudakov resummation presented in the following Chapters or in [100, 101]. In this case, the non-logarithmic hard corrections are about $2\,\%$ of the tree-level value. For the total annihilation cross-section, it is expected that they are of similar size. Therefore, the above

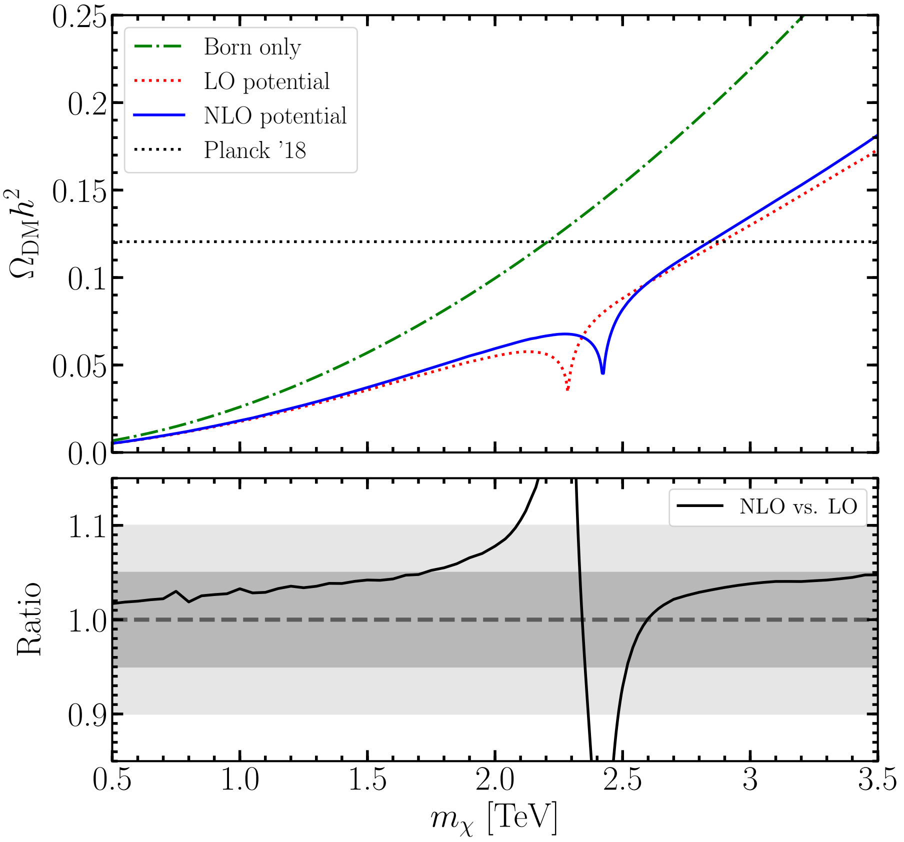

Figure 5.4: *Wino DM relic abundance as function of DM mass m_χ computed with Born cross-sections (dashed-dotted/green), including Sommerfeld enhancement with the LO (dotted/red), and the NLO potential (solid/blue). The horizontal line shows the observed relic abundance. In the lower panel, the ratio of the NLO to LO Sommerfeld-corrected relic abundance is shown. The dark (light) grey bands mark the 5 (10)% variations. Except in the vicinity of the resonances the NLO correction is a few percent. The small wiggles in the ratio plot are due to numerical inaccuracies of the calculation.*

result is probably accurate to a few percent in addition to the non-particle physics uncertainties on the calculation, such as effective numbers of degrees of freedom $g_*^{1/2}$.

6

SCET for dark matter indirect detection

Up to this point, we have mainly covered non-relativistic corrections to DM annihilation. As outlined in Chapter 2, for semi-inclusive (exclusive) processes, there are further enhanced corrections that need specialized treatment. In this Chapter, we proof factorization for the observable $\chi^0\chi^0 \to \gamma + X$, in a generic heavy fermionic minimal DM model in the narrow $E^\gamma_{\rm res} \sim m_W^2/m_\chi$ and intermediate $E^\gamma_{\rm res} \sim m_W$ resolution regime. For a discussion of factorization and resummation in the wide $m_\chi \gg E^\gamma_{\rm res} \gg m_W$ regime, see [98, 99]. The presentation in this Chapter is a generalization of the discussion in [101] for wino DM. We also borrow some notation introduced in [149] to cover the hypercharge case. Originally, the narrow resolution endpoint factorization was introduced in [100]. The additions and modifications that lead to the intermediate resolution case were initially worked out between M. Beneke, A. Broggio and the author. Similarly, the factorization theorem for the Higgsino case was first presented in [102] and worked out as a simple generalization of the wino case by C. Hasner, M. Vollmann and the author.

6.1 Electroweak soft-collinear effective theory

After the proof of factorization between non-relativistic and annihilation dynamics (cf. Chapter 2) and the respective corrections to NR physics discussed at length in previous Chapters, we turn to the discussion of soft-collinear factorization and the corrections to the annihilation process. The corresponding soft-collinear EFT for the $\gamma + X$ endpoint spectrum, is an admixture of SCET$_{\rm I}$ and SCET$_{\rm II}$ [87, 88, 89, 90], as can, e.g., be seen from the corresponding discussion of modes and integrals in Chapter 2. Depending on the virtuality, two different Lagrangians come into play. Suppose the virtuality of the modes is much larger than the electroweak scale masses. In that case, the theory resembles an unbroken SU(2) $\otimes$ U(1) SCET$_{\rm I}$ theory, whilst for virtualities of order of the electroweak scale, the electroweak masses play a role and an SCET$_{\rm II}$-type theory in the broken phase has to be considered [91, 92].

For simplicity, we restrict to the discussion of the gauge boson Lagrangians, as the gauge boson fields will directly appear in the annihilation operators. The treatment of SM fermion fields is in close analogy to the QCD case. Let us begin from the unbroken SCET Lagrangian

$$\mathcal{L}_{\rm SCET-I} = \mathcal{L}_c + \mathcal{L}_{\bar{c}} + \mathcal{L}_{\rm soft} \tag{6.1}$$

where the individual Lagrangians correspond to the collinear, anti-collinear and soft fields, respectively. Before discussing the Lagrangians, decoupling transformations and EWSB in the SCET formalism, we introduce the conventions for the covariant derivatives, fields strengths, and so on. In agreement with the previous Chapters, we use

$$D_\mu = \partial_\mu + ig_1 B_\mu Y - ig_2 W^a_\mu T^a_{\rm SU(2)} \tag{6.2}$$

for the gauge covariant derivatives. As most of the decoupling transformations and field redefinitions are identical up to the exchange of fields and couplings between $\mathrm{SU}(2)_L$ and $\mathrm{U}(1)_Y$, we define a new vector of unbroken SM gauge boson fields that includes the B field, in addition to the SU(2) gauge fields W^a [149]

$$A^a_\mu = \left(W^1_\mu, W^2_\mu, W^3_\mu, B_\mu\right)^T \quad , \quad T^a = \left(g_2 T^1_{\mathrm{SU}(2)}, g_2 T^2_{\mathrm{SU}(2)}, g_2 T^3_{\mathrm{SU}(2)}, -g_1 Y\right)^T \tag{6.3}$$

where the couplings are absorbed, and the relative minus sign between W and B fields in the covariant derivative is part of the generator matrix. Note that the first three entries of the generator matrix are understood as operating on the SU(2) space, whilst the fourth only acts on hypercharge, or put differently $\left[T^i_{\mathrm{SU}(2)}, Y\right] = 0$. Fields without a gauge index are interpreted as $A_\mu = A^a_\mu T^a$, and the gauge covariant derivative is written in the compact form

$$D_\mu = \partial_\mu - i A^a_\mu T^a = \partial - i A_\mu \,. \tag{6.4}$$

The field strength tensors are defined as usual

$$F^{a,\mu\nu} T^a = i \left[D^\mu, D^\nu\right] \tag{6.5}$$

note that there is no additional factor $1/g_2$ or similar, as the couplings are part of T^a. The covariant derivatives in this expressions are to be evaluated for the indices $a = 1, 2, 3$ as $D_{\mathrm{SU}(2)}$, i.e., D_μ with $Y = 0$. For $a = 4$, we use $D_{\mathrm{U}(1)}$ dropping the g_2 term in D_μ and setting $Y = 1$. All fields are split into their respective low-energy modes[1]

$$A^\mu \to A^\mu_s + A^\mu_c + A^\mu_{\bar{c}} \,. \tag{6.6}$$

The collinear fields contain hard-collinear and collinear modes. The two types of collinear modes can be split after EWSB is implemented. In the following, we use the terms collinear and hard-collinear interchangeably, unless necessary for physics reasons in which case we state so. Similarly, the soft-fields also contain what are later ultrasoft interactions. After EWSB, the ultrasoft pieces, which are purely photonic for the DM masses considered in this thesis, appear separately. The soft gauge boson Lagrangian is the same as the SM gauge boson Lagrangian with all fields understood as soft[2]

$$\mathcal{L}_{\mathrm{soft}} = -\frac{1}{4}\left(F^{a,\mu\nu}_s F^s_{a,\mu\nu}\right) \,. \tag{6.7}$$

The collinear c and anti-collinear $\bar{c}$ Lagrangians are equal upon interchange $c \leftrightarrow \bar{c}$ (and respectively $n_+ \leftrightarrow n_-$), i.e., it is sufficient to discuss either of the two. Therefore, we consider only the collinear gauge boson Lagrangian

$$\mathcal{L}_c = -\frac{1}{4}\left(F^{a,\mu\nu}_c F^a_{c,\mu\nu}\right) + (D^\mu \varphi_c)^\dagger D_\mu \varphi_c \,, \tag{6.8}$$

where φ_c is the collinear Higgs doublet added for demonstrative purposes. The field strength tensor is defined as above, though the constituting covariant derivatives are to be understood

---

[1] Here, we assume that the hard matching step is already performed, even though we will only discuss it subsequently.

[2] We refrain from the customary SM notation $-\frac{1}{2}\operatorname{tr} W_{\mu\nu} W^{\mu\nu}$ for the SU(2) part of the field strength tensor, as this would lead to relative factors of two between hypercharge and SU(2) bosons, and spoil the advantage of the above compact notation, in the following.

as expanded in the large components [150]. Therefore, acting on a collinear field, the covariant derivative reads

$$D^\mu = \partial^\mu - iA_c^\mu - in_- A_s(x_- + x_\perp)\frac{n_+^\mu}{2} \tag{6.9}$$

where the light-cone vector/decompositions are defined in Section 2.1.2. At leading power $n_- A_s$ appears, as compared to the corresponding collinear component, this term is not suppressed.[3] Hence, the soft field is also to be evaluated at the multipole expanded position $x_- + x_\perp$.

As the (anti-)collinear fields have a large momentum component, that is not power-suppressed, e.g., as $n_+\partial A_c(x) \sim \lambda^0 A_c(x)$, an infinite tower of collinear operators needs to be considered. This infinite tower can be summed and manifests as non-locality in the position of the collinear fields that the annihilation Lagrangian is integrated over (see later discussion Section 6.3). It is customary (and, for further considerations, also very convenient) to change into a basis of manifestly collinear gauge invariant fields. We introduce the collinear Wilson line [89]

$$W_c(x) = P\exp\left[i\int_{-\infty}^{0} ds\, n_+ \cdot A_c^C(x + sn_+)\, T^C\right], \tag{6.10}$$

with P the path-ordering symbol. At this point, the advantage of the above notation becomes clear. We can work with one Wilson line for the collinear sector containing both SU(2) and U(1) fields, and furthermore, we do not have to worry about different couplings, as they are absorbed into the “generators”. In terms of the collinear Wilson lines, we can introduce the gauge collinear building blocks for the Higgs doublet and the gauge bosons

$$\Phi_c(x) = W_c^\dagger(x)\varphi_c(x)\,, \tag{6.11}$$

$$\mathcal{A}_c^{B,\mu}(x)T^B = \mathcal{A}_c^\mu(x) = W_c^\dagger\left[iD^\mu W_c\right](x) = \int_{-\infty}^{0} ds\, n_+ \cdot \left[W_c^\dagger F_c^{\nu\mu} W_c\right](x + sn_+)\,. \tag{6.12}$$

Finally, to completely rewrite the Lagrangian in terms of collinear gauge-invariant building blocks, we also introduce a new (curly) covariant derivative and field strength tensor

$$\mathcal{D}^\mu = W_c^\dagger D^\mu W_c = \partial_\mu - i\mathcal{A}_c\,, \qquad \mathcal{F}^{a,\mu\nu}T^a = i\left[\mathcal{D}^\mu, \mathcal{D}^\nu\right]\,. \tag{6.13}$$

Analogous to QCD, see e.g. [151], the terms $n_\pm \mathcal{A}_c$ can be eliminated by the Wilson lines (6.10) and the equation of motion. Therefore, the collinear degrees of freedom are represented by transverse fields. There are no direct collinear interactions with the anti-collinear fields, as such interactions lead to hard modes that are not part of the effective theory anymore. However, both collinear and anti-collinear fields are still connected by the exchange of soft modes. We can decouple the soft and (anti-)collinear interactions by performing a field redefinition in terms of the soft Wilson lines

$$Y_\pm(x) = P\exp\left[-i\int_0^{\infty} ds\, n_\mp \cdot A_s^C(x + sn_\mp)\, T^C\right] \tag{6.14}$$

and hence, we have

$$\mathcal{A}_c^B(x) = Y_+^{BC}(x_-)\mathcal{A}_c^{C(0)}(x)\,, \quad \mathcal{A}_{\bar{c}}^B = Y_-^{BC}(x_+)\mathcal{A}_{\bar{c}}^{C(0)}(x)\,. \tag{6.15}$$

The generators T^A are to be understood in the adjoint representation for the gauge boson decoupling. The same decoupling is also performed on the collinear Higgs field, in which case, T^A is part of the fundamental representation.

---

[3] Note that there is no additional soft kinetic term induced by the collinear kinetic term $-(1/4)F_c^{\mu\nu}F_{c,\mu\nu}$, as the term is collinear gauge invariant and a gauge in which $n_- A_s = 0$ could be chosen.

For the hard-collinear field, the above presentation is sufficient, as its virtuality is of order $m_\chi m_W \gg m_W^2$, and hence can be evaluated in the unbroken theory. However, the anti-collinear direction, i.e., the detected photon is sensitive to the electroweak scale,[4] and hence EWSB needs to be implemented. The gauge boson mass terms follow swiftly from the Higgs kinetic term by using the vacuum expectation value

$$\begin{aligned}(\mathcal{D}^\mu \Phi_c)^\dagger \mathcal{D}_\mu \Phi_c &= (n_+\partial\Phi_c)^\dagger\, n_-\mathcal{D}\Phi_c + (n_-\mathcal{D}\Phi_c)\, n_+\partial\Phi_c + (\mathcal{D}_\perp\Phi_c)^\dagger\, \mathcal{D}_{\perp,\mu}\Phi_c \\ &\xrightarrow{\Phi_c=(0,v/\sqrt{2})} \frac{g_2^2 v^2}{8}\left(\mathcal{A}^{1,\mu}_{\perp c}\mathcal{A}^{1}_{\perp c,\mu} + \mathcal{A}^{2,\mu}_{\perp c}\mathcal{A}^{2}_{\perp c,\mu}\right) + \frac{v^2}{8}\left(g_2\mathcal{A}^{3,\mu}_{\perp c} + g_1\mathcal{A}^{4,\mu}_{\perp c}\right)^2 \qquad (6.16)\end{aligned}$$

where as expected only the transversal part of the collinear fields acquires the mass. Changing from the weak basis to the mass basis, i.e., splitting the above into the SM $W^\pm$ bosons $\mathcal{W}^\pm = (\mathcal{A}^1 \mp i\mathcal{A}^2)/\sqrt{2}$, the Z boson $\mathcal{Z} = c_W\mathcal{A}^3 + s_W\mathcal{A}^4$ and the photon $\gamma = s_W\mathcal{A}^3 - c_W\mathcal{A}^4$, the mass terms in the Lagrangian are[5]

$$m_W^2\mathcal{W}^+_\mu\mathcal{W}^{\mu,-} + \frac{m_Z^2}{2}\mathcal{Z}_\mu\mathcal{Z}^\mu\,. \qquad (6.17)$$

We drop the Higgs terms from hereon, as they are not necessary anymore for any of the following considerations, and mainly served the illustrative purpose of showing how gauge boson masses arise for the (anti-)collinear fields in the SCET formalism.

6.2 Non-relativistic decoupling

In Section 2.3, we argued that the non-relativistic dynamics, i.e., the potentials and connected the Sommerfeld enhancement, are always factorized from the annihilation process at leading power. In short, there is no cross-talk due to soft modes between annihilation and the NR process. Nevertheless, the NR fermion fields still enter the annihilation operators, and soft corrections connected to the effective annihilation process are still allowed.[6]

As the leading soft-NR interactions are eikonal, we decouple the soft interactions using a Wilson line field redefinition as above for the gauge bosons entering the annihilation operator Eq. (6.14). The soft decoupling redefinition for the fields reads

$$\chi_{va}(x) = Y_{v,ab}(x_0)\chi^{(0)}_{vb}(x)\,, \qquad (6.18)$$

with the soft Wilson line $Y_v(x)$ defined as

$$Y_v(x) = \mathrm{P}\exp\left[i\int_{-\infty}^{0} dt\, v\cdot A_s^C(x+vt)\,T^C\right]\,, \qquad (6.19)$$

where T^C are the generators in the SU(2) representation (or in the case of $C = 4$ hypercharge) of the DM fermion, and $v^\mu = (1, \mathbf{0})^T$. The states χ_v should be understood in the unbroken EW basis, as part of the NRDM Lagrangian Eq. (3.2). In this sense, the transformation is similar to

---

[4] For narrow resolution, the hard-collinear mode is not present, and also the collinear modes are sensitive to m_W. Furthermore, possible mass effects connected to the hard-collinear modes are also sensitive to the electroweak scale. Both need to be calculated using the broken Lagrangian.

[5] The W-mass, and Z-mass are defined as usual, as $m_W^2 = g_2^2v^2/4$, $m_Z^2 = (g_1^2 + g_2^2)v^2/4$, respectively, in terms of the Higgs vacuum expectation value v. The Sine and Cosine of the Weinberg angles are given by $c_W = g_2/\sqrt{g_1^2+g_2^2}, s_W = g_1/\sqrt{g_1^2+g_2^2}$.

[6] Ultrasoft interactions do not contribute. The corresponding discussion is found in Section 3.1 and not repeated here.

the ultrasoft decoupling in [152], though not equivalent. The above transformation proceeds on NR fields, whilst in [152] ultrasoft gluons are decoupled from the potential non-relativistic fields. Note that the Wilson lines are evaluated at $x_0 = v \cdot x = (t, \mathbf{0})$. The reason for this multipole expansion lies in the eikonal nature of the leading power soft interaction, which is not sensitive to spatial momenta of the heavy fermions.

As the soft emissions are now decoupled from the non-relativistic fields, the main issue is how to extract the Sommerfeld enhancement for a given field combination. To this end, we change from the unbroken basis above to the broken theory fields, in analogy to the discussion for the wino potentials in Chapter 3. We define the K-matrix that relates unbroken theory states ab, to broken theory two-particle states I (e.g., $(33) \to (00)$ for the wino)

$$\chi^{c\dagger}_{va} \chi_{vb} = K_{ab,I} [\chi^{c\dagger}_{v} \chi_{v}]_I \,. \tag{6.20}$$

The K-matrix is a model-dependent quantity. For the wino, it can be found in [101] (Eq. (2.10)) and for the Higgsino in [149] (Appendix C). After this basis change, we can treat the Sommerfeld effect in analogy with previous Sections or [86]. Generically, the squared matrix element entering the cross-section will be of the form

$$\chi^{\dagger}_{ve_4} \Gamma \chi^{c}_{ve_3} \, \chi^{c\dagger}_{ve_2} \Gamma \chi_{ve_1} \,, \tag{6.21}$$

with Γ operating on the spinor index of χ_v. Γ is given by either 1 or σ^i for fermions depending on if the annihilation operator is a spin-0 or 1 operator, respectively. The potential does not change the spin or angular momentum (at least to NLO), therefore we can assume both Γ's to be identical for the squared annihilation matrix element. Hence, we can evaluate the NRDM squared matrix element of angular momentum $L = 0$ and a given spin S to transition to wave-functions [86]

$$\begin{aligned} &\langle \chi_i \chi_j | \, \chi^{\dagger}_{ve_4} \Gamma \chi^{c}_{ve_3} \, \chi^{c\dagger}_{ve_2} \Gamma \chi_{ve_1} \, | \chi_i \chi_j \rangle = \langle \chi_i \chi_j | \, \chi^{\dagger}_{ve_4} \Gamma \chi^{c}_{ve_3} | 0 \rangle \, \langle 0 | \chi^{c\dagger}_{ve_2} \Gamma \chi_{ve_1} \, | \chi_i \chi_j \rangle \\ &= \Big[\langle \xi^{c\dagger}_j \Gamma \xi_i \rangle \, (\psi^{(0,S)}_{e_4 e_3,\, ij} + (-1)^S \psi^{(0,S)}_{e_3 e_4,\, ij}) \Big]^* \langle \xi^{c\dagger}_j \Gamma \xi_i \rangle \, (\psi^{(0,S)}_{e_1 e_2,\, ij} + (-1)^S \psi^{(0,S)}_{e_2 e_1,\, ij}) \,, \end{aligned} \tag{6.22}$$

where we do not sum over ij. The spinors ξ_i are the Pauli spinors corresponding to χ_i. The symbol $\langle \dots \rangle$ denotes the spin sum. The wave-functions are normalized such that in the absence of a potential $\psi^{(L,S)}_{e_1 e_2, ij} \to \delta_{e_1 i} \delta_{e_2 j}$, i.e., to the free scattering solutions of the Schrödinger equation. Both possible contractions contribute to the matrix element, as can be seen by the appearance of $\psi^{(0,S)}_{e_1 e_2, ij}$, and $\psi^{(0,S)}_{e_2 e_1, ij}$. The relative sign $(-1)^S$ arises from the exchange properties (in general $(-1)^{L+S}$). The wave-function is related via

$$\psi^{(0,S)}_{e_1 e_2,\, ij} = [\psi_E(0)]^*_{e_1 e_2,\, ij} \tag{6.23}$$

to the $L = 0$ solution of the Schrödinger equation

$$\left(\left[-\frac{\boldsymbol{\nabla}^2}{2\mu_I} - (E - M_I + 2m_\chi) \right] \delta_{IK} + V_{IK}(r) \right) [\psi_E(\mathbf{r})]_{K,ij} = 0 \tag{6.24}$$

at the origin, where the Schrödinger equation and all terms are to be understood as discussed at length for the PNRDM Lagrangian in Section 3.1. The solution is again obtained using the methods laid out in [86]. For the indirect detection process $\chi^0 \chi^0 \to \gamma + X$ that we consider, we can specify, the external states $I = ij = (00)$. The other two-particle states, e.g. $(+-)$, $(-+)$ in the case of the wino, appear only virtually inside the ladder and as part of the effective annihilation matrix (see below). At the current stage, the basis is still formulated in the redundant basis of method-I. However, as customary and also done in earlier Chapters, we switch to the method-II representation removing redundant states [86] (cf. Section 3.1). The necessary Sommerfeld factors that multiply the cross-section are defined as

$$S_{IJ} = \Big[\psi^{(0,S)}_{J,\, 00} \Big]^* \psi^{(0,S)}_{I,\, 00} \,. \tag{6.25}$$

6.3 Hard operators

As used above, the hard annihilation process is described by the effective Lagrangian

$$\mathcal{L}_{\text{ann}} = \frac{1}{2m_\chi} \sum_i \int ds\, dt\, \hat{C}_i(s,t,\mu)\, \mathcal{O}_i(s,t,\mu)\,, \tag{6.26}$$

with operators of the generic form

$$\mathcal{O}_i = \chi_v^{c\dagger} \Gamma_i^{\mu\nu} T_i^{AB} \chi_v\, \mathcal{A}^A_{\perp c,\mu}(sn_+) \mathcal{A}^B_{\perp \bar{c},\nu}(tn_-)\,. \tag{6.27}$$

Fields without position argument are to be evaluated at $x = 0$. The spin structures are denoted by $\Gamma_i^{\mu\nu}$ and the colour structures by T_i^{AB}. As expected (cf. Section 6.1), the operators are non-local, as the (anti-)collinear fields are integrated along the light-cone.

Here, we only list the annihilation operators. A detailed discussion on the completeness of the basis and the derivation of the operators can be found in [101, 149], and is not repeated here. It is convenient to distinguish the annihilation into hypercharge and SU(2) bosons. Therefore, we refrain from using the shortcut notation above, and identify $\mathcal{W}^C = \mathcal{A}^C$ for $C = 1, 2, 3$ and $\mathcal{B} = \mathcal{A}^4$. The complete list of operators reads

$$\mathcal{O}_1 = \chi_v^{c\dagger} \Gamma^{\mu\nu} \chi_v\, \mathcal{W}^B_{\perp c,\mu}(sn_+) \mathcal{W}^B_{\perp \bar{c},\nu}(tn_-)\,, \tag{6.28}$$

$$\mathcal{O}_2 = \frac{1}{2} \chi_v^{c\dagger} \Gamma^{\mu\nu} \{T^B_{\text{SU}(2)}, T^C_{\text{SU}(2)}\} \chi_v\, \mathcal{W}^B_{\perp c,\mu}(sn_+) \mathcal{W}^C_{\perp \bar{c},\nu}(tn_-)\,, \tag{6.29}$$

$$\mathcal{O}_3 = \chi_v^{c\dagger} \sigma^\alpha (n_{-\,\alpha} - n_{+\,\alpha}) T^A_{\text{SU}(2)} \chi_v\, \epsilon^{ABC} \mathcal{W}^{\mu\,B}_{\perp c}(sn_+) \mathcal{W}^C_{\perp \bar{c},\mu}(tn_-)\,, \tag{6.30}$$

$$\mathcal{O}_4 = \chi_v^{c\dagger} \Gamma^{\mu\nu} T^C_{\text{SU}(2)} \chi_v\, [\mathcal{W}^C_{\perp c,\mu}(sn_+) \mathcal{B}_{\perp \bar{c},\nu}(tn_-) + \mathcal{W}^C_{\perp \bar{c},\mu}(tn_-) \mathcal{B}_{\perp c,\nu}(sn_+)]\,, \tag{6.31}$$

$$\mathcal{O}_5 = \chi_v^{c\dagger} \sigma^\alpha (n_{-\,\alpha} - n_{+\,\alpha}) T^C_{\text{SU}(2)} \chi_v\, [\mathcal{W}^{\mu\,C}_{\perp c}(sn_+) \mathcal{B}_{\perp \bar{c},\mu}(tn_-) - \mathcal{W}^C_{\perp \bar{c},\mu}(tn_-) \mathcal{B}_{\perp c,\nu}(sn_+)]\,, \tag{6.32}$$

$$\mathcal{O}_6 = \chi_v^{c\dagger} \Gamma^{\mu\nu} \chi_v\, \mathcal{B}_{\perp c,\mu}(sn_+) \mathcal{B}_{\perp \bar{c},\nu}(tn_-)\,. \tag{6.33}$$

Of the above, the operators $\mathcal{O}_i$ with $i = 1, 2, 4, 6$ are spin-0 and $i = 3, 5$ spin-1 operators. Therefore, the latter operators are irrelevant for the indirect detection calculation, as the spin-1 initial state is forbidden for identical real particle states $\chi^0\chi^0$. The spinors χ_v^a are to be understood as non-relativistic Majorana fields for Majorana multiplets. For Dirac multiplets (with possible hypercharge), χ_v^a are understood as non-relativistic Dirac fields η_v^a, ζ_v^a as a particle and corresponding anti-particle field, respectively, following the convention of [84]. For Dirac DM, one should symmetrize[7]

$$\chi_v^{c\dagger} \Gamma^{\mu\nu} T_i^{BC} \chi_v \quad \longrightarrow \quad \zeta_v^{c\dagger} \Gamma^{\mu\nu} T_i^{BC} \eta_v + \eta_v^{c\dagger} \Gamma^{\mu\nu} T_i^{BC} \zeta_v\,, \tag{6.34}$$

which ensures the desired normalization (i.e., same matching coefficients for Dirac and Majorana DM). Furthermore, in this way, we obtain the same results for equivalent states, e.g. $(+-) \leftrightarrow (-+)$, for the method-I soft function.

The spin-0 matrix structure in the operator basis is given by

$$\Gamma^{\mu\nu} = \frac{i}{4} [\sigma^\mu, \sigma^\nu]\, \sigma^\alpha\, (n_{-\alpha} - n_{+\alpha}) = \frac{1}{2i} [\sigma^m, \sigma^n]\, \sigma \cdot \mathbf{n} \overset{d=4\,\text{only}}{=} \frac{1}{2} \epsilon^{\mu\nu\alpha\beta} n_{+\alpha} n_{-\beta} = \epsilon_\perp^{\mu\nu} \tag{6.35}$$

---

[7] In [102], the operator basis for Dirac DM was presented with a factor two, instead of this symmetrization. For the hard-matching procedure, both are effectively equivalent. However, the soft function calculation sensitively depends on the precise understanding of the NR spinors.

where the conventions are m, n being the spatial components of the Lorentz indices μ, ν respectively. The signs of the Levi-Civita symbol are fixed according to $\epsilon^{0123} = -1$ and the light-cone vectors are chosen as $n^\mu_\pm = (1, 0, 0, \mp 1)^T$.

In terms of the above discussed soft field redefinitions using Wilson lines, the operators generically read

$$\mathcal{O}_i = \chi_v^{c\dagger} \Gamma_i^{\mu\nu} [Y_v^\dagger T_i^{AB} Y_v] \chi_v \, \mathcal{Y}_+^{AV} \mathcal{Y}_-^{BW} \mathcal{A}^V_{\perp c,\mu}(sn_+) \mathcal{A}^W_{\perp \bar{c},\nu}(tn_-) \,. \tag{6.36}$$

6.4 Factorization of the endpoint spectrum

With the above annihilation operators, field definitions and decoupling transformations, we are in a position to factorize the differential cross-section for $\chi\chi \to \gamma + X$ in an arbitrary fermionic minimal DM model. To that end, we take a different path than the one presented in [101, 149], where the differential cross-section is factorized and the respective elements, such as soft functions and so on, are defined as they appear in the factorization procedure. We provide the definitions of these functions ahead of time. Their form will be justified by the factorization procedure presented in the end, thereby providing a posteriori justification of the function definitions.

6.4.1 Hard Wilson coefficients

The hard coefficients, as they appear in the effective annihilation Lagrangian Eq. (6.26) $\hat{C}(s, t, \mu)$, are inconvenient to use, as they are still connected via s, t to the gauge boson fields. Using translational invariance, we can shift the gauge boson fields in the annihilation operators

$$\begin{aligned} \langle \gamma(p_\gamma) | \, \mathcal{A}^W_{\perp \bar{c},\nu}(tn_-) \, |0\rangle &= e^{itn_- \cdot p_\gamma} \, \langle \gamma(p_\gamma) | \, \mathcal{A}^W_{\perp \bar{c},\nu}(0) \, |0\rangle \,, \\ \langle X_c | \, \mathcal{A}^V_{\perp c,\mu}(sn_+) \, |0\rangle &= e^{isn_+ \cdot p_{X_c}} \, \langle X_c | \, \mathcal{A}^V_{\perp c,\mu}(0) \, |0\rangle \,. \end{aligned} \tag{6.37}$$

The corresponding translation factors can be used to define a new C_i by performing the s, t integration. The relevant combination that will appear in the T-matrix element is

$$C_i(n_+ p_X, n_- p_\gamma, \mu) = \int ds dt \, e^{isn_+ \cdot p_{X_c} + itn_- \cdot p_\gamma} \, \hat{C}_i(s, t, \mu) \,. \tag{6.38}$$

Using the leading power relations $n_+ p_X \approx n_- p_\gamma \approx 2m_\chi$, we therefore define the hard Wilson coefficients as

$$C_i(\mu) = C_i(2m_\chi, 2m_\chi, \mu) \,. \tag{6.39}$$

6.4.2 Anti-collinear (photon) jet function

In the anti-collinear direction, the gauge boson field in $\mathcal{O}_i$ is required to be a photon. The linear combination

$$-\, g^\perp_{\nu\nu'} \, Z^{YW}_\gamma = \sum_\lambda \langle 0 | \mathcal{A}^Y_{\perp \bar{c},\nu'}(0) | \gamma(p_\gamma, \lambda) \rangle \langle \gamma(p_\gamma, \lambda) | \mathcal{A}^W_{\perp \bar{c},\nu}(0) | 0 \rangle \,, \tag{6.40}$$

is relevant and will hereafter be referred to as photon jet function. λ gives the photon polarizations, and as we contract the field with a photon, we recognize from the previous definitions, that only $\mathcal{A}^3_{\perp,\bar{c}}$, and $\mathcal{A}^4_{\perp,\bar{c}} = \mathcal{B}_{\perp,\bar{c}}$ have non-vanishing contractions. Therefore, we only encounter the photon jet functions Z^{33}_γ, Z^{34}_γ, Z^{43}_γ, and Z^{44}_γ. As they describe fields of virtuality $\mu \sim m_W$ and rapidity $\nu \sim 2m_\chi$, the jet functions require both virtuality and rapidity regularization. They are sensitive to the electroweak scale and hence, need to be calculated using the non-zero SM masses at the electroweak scale m_W, m_Z, m_H, m_t.

The different index combinations $33, 34, 43, 44$ are all related by simple coupling factors, as in the end, only the contraction between $\mathcal{A}^3, \mathcal{B}$ and γ changes. In other words, all index combinations contain the same correction/jet function due to the underlying photon, multiplied with a coupling factor associated with the annihilation operator. Finally, let us mention the origin of the notation Z_γ for the photon jet function. If normalized by appropriate coupling factors, e.g., $Z_\gamma^{33}/\hat{s}_W^2$ can be interpreted as the on-shell field renormalization factor of the photon in anti-collinear light-cone gauge $n_- \cdot \mathcal{A}_{\bar{c}}^B = 0$ [100].

6.4.3 Recoiling jet function

The unobserved recoiling jet function can be defined as

$$\begin{aligned}
-g^{\perp}_{\mu\mu'}\, J^{XV}(p^2, m_W) &= \frac{1}{\pi}\,\mathrm{Im}\big[-g^{\perp}_{\mu\mu'}\, i\mathcal{J}^{XV}(p^2, m_W)\big] \\
&\equiv \frac{1}{\pi}\,\mathrm{Im}\Big[\, i\int d^4x\, e^{ip\cdot x}\langle 0|\mathbf{T}\{\mathcal{A}^X_{\perp c,\mu'}(x)\,\mathcal{A}^V_{\perp c,\mu}(0)\}|0\rangle\,\Big] \\
&= \frac{1}{2\pi}\int d^4x\, e^{ip\cdot x}\,\langle 0|\,\mathcal{A}^X_{\perp c,\mu'}(x)\,\mathcal{A}^V_{\perp c,\mu}(0)\,|0\rangle\,, \qquad (6.41)
\end{aligned}$$

where the meaning and the EFT calculation of this object changes between the narrow and intermediate resolution case. For intermediate resolution, the fields are of hard-collinear virtuality, expressed through their dependence on $p^2 \sim m_\chi m_W$. Therefore, the calculation has to be carried out in the unbroken SCET-I type EFT. Furthermore, in principle, there is a sensitivity to the electroweak scale through the massive SM particles inside the jet. Therefore, for intermediate resolution, the object needs to be further factorized into a hard-collinear jet-function only sensitive to p^2, and a collinear function that is also sensitive to m_W [98, 101]. To leading power in m_W^2/p^2, we find

$$J^{XV}(p^2, m_W) = J_{\mathrm{int}}(p^2)\, J_m^{XV}(m_W) + \mathcal{O}(m_W^2/p^2)\,. \qquad (6.42)$$

As argued above, the hard-collinear jet function $J_{\mathrm{int}}(p^2)$ is an object to be calculated in the unbroken theory. Therefore, it resembles the standard gluon jet function known in QCD and has no rapidity divergence. The collinear mass jet-function is independent of the jet energy but can depend on both virtuality and rapidity. Fortunately, for intermediate resolution, we find that this object is given by

$$J_m^{XV}(m_W) = \delta^{XV} + \mathcal{O}(\alpha_2^2)\,, \qquad (6.43)$$

to the one-loop order. From a conceptual standpoint, it is also reasonable to assume that this form holds to all orders, as the observable under consideration has no sensitivity to any of the internal jet dynamics. We will, therefore use $J_m^{XV}(m_W) = \delta^{XV}$ to simplify the final factorization theorem.[8]

As a convenient notation for later applications, it turns out to be useful to split into U(1) and SU(2) components using

$$J^{XV} = \left(\delta^{XV} - \delta^{X4}\delta^{V4}\right) J_{\mathrm{int}}^{\mathrm{SU(2)}} + \delta^{X4}\delta^{V4} J_{\mathrm{int}}^{\mathrm{U(1)}}\,. \qquad (6.44)$$

The narrow resolution jet function obeys the same definition as the intermediate resolution one but with all fields of collinear virtuality. Therefore, there is no further factorization procedure, and the object can be directly calculated from the definition (6.41). Similar, to the photon jet function above, the index combinations $33, 34, 43, 44$ are possible. Note that in the narrow case, the recoiling jet function does depend on the electroweak scale masses and requires both virtuality and rapidity regularization [100].

---

[8] Details on the calculation of J_m can be found in Appendix B.1 of [101].

6.4.4 Soft function

The soft-function will collect the Wilson line contributions that arise from the decoupling transformations outlined for the gauge bosons and heavy fermions in Sections 6.1 and 6.2. For convenience, we define the soft operator following the linear combination that appears after decoupling in each operator $\mathcal{O}_i$ (6.36) and the projection onto the physical states using the K-matrix (6.20)

$$\mathcal{S}^i_{I,VW}(x) = K_{ab,I}\,[Y_v^\dagger T_i^{AB} Y_v]_{ab}(x)\,\mathcal{Y}_+^{AV}(x)\mathcal{Y}_-^{BW}(x)\,, \tag{6.45}$$

where we use $\mathcal{Y}_\pm$ to highlight that the Wilson lines for the gauge bosons are to be understood in the adjoint representation. Similar to the recoiling jet function, the soft function depends on the resolution regime. We start by defining the momentum space soft function for intermediate resolution, which is given by

$$\langle 0|\,\bar{\mathbf{T}}[[\mathcal{S}^\dagger]^j_{J,XY}(x)]\,\mathbf{T}[\mathcal{S}^i_{I,VW}(0)]\,|0\rangle \equiv \int \frac{d^4k}{(2\pi)^4}\, e^{-ik\cdot x}\, \boldsymbol{W}^{ij}_{IJ,VWXY}(k)\,. \tag{6.46}$$

The object, that finally appears in the factorization formula is the integrated soft-function defined as

$$\begin{aligned} W^{ij}_{IJ,VWXY}(\omega) &= \frac{1}{2}\int \frac{d(n_+k)d^2k_\perp}{(2\pi)^4}\, \boldsymbol{W}^{ij}_{IJ,VWXY}(k) \\ &= \frac{1}{4\pi}\int d(n_+y)\, e^{i\omega n_+\cdot y/2}\,\langle 0|\,\bar{\mathbf{T}}[[\mathcal{S}^\dagger]^j_{J,XY}(y_-)]\,\mathbf{T}[\mathcal{S}^i_{I,VW}(0)]\,|0\rangle\,. \end{aligned} \tag{6.47}$$

The open indices on this soft function $VWXY$ will be contracted with the photon and recoiling jet functions. As seen above, of the photon jet function indices WY, only the combinations $33, 34, 43, 44$ are non-zero, and for the recoiling jet function, we find that the $X = V$ (6.43). Even though it does not considerably simplify the final factorization theorem, it is convenient to define

$$W^{\mathrm{SU(2)},ij}_{IJ,WY}(\omega) = \left(\delta^{XV} - \delta^{X4}\delta^{V4}\right) W^{ij}_{IJ,VWXY}(\omega) \tag{6.48}$$

$$W^{\mathrm{U(1)},ij}_{IJ,WY}(\omega) = \delta^{X4}\delta^{V4} W^{ij}_{IJ,VWXY}(\omega) \tag{6.49}$$

depending on if the soft function will be contracted with the SU(2) or U(1) recoiling jet of (6.44). This has the advantage to make the origin of the soft function structures transparent and keeps notational consistency with [100, 101, 102, 149].

In the narrow resolution case, as the kinematics do not allow for real soft radiation, the above definitions also apply, however with the replacement

$$\begin{aligned} &\sum\!\!\!\!\!\!\int_{X_s} \langle 0|\,[\mathcal{S}^\dagger]^j_{J,XY}(x)\,|X_s\rangle\,\langle X_s|\,\mathcal{S}^i_{I,VW}(0)\,|0\rangle \\ &\to \quad \langle 0|\,[\mathcal{S}^\dagger]^j_{J,XY}(0)\,|0\rangle\,\langle 0|\,\mathcal{S}^i_{I,VW}(0)\,|0\rangle \equiv D^i_{I,VW}\, D^{j\,*}_{J,XY}\,. \end{aligned} \tag{6.50}$$

Therefore, in this case, we consider soft Wilson coefficients D, which have no dependence on ω anymore.[9] As the narrow resolution recoiling jet function, allows for the index combinations $33, 34, 43, 44$, these can take the values $D^i_{I,33}, D^i_{I,34}, D^i_{I,43}, D^i_{I,44}$, different from the intermediate resolution case above.

---

[9] In principle, there is also an underlying ultrasoft function convolved with the narrow resolution recoiling jet function. In our case, however, the ultrasoft radiation is restricted to be photonic and hence only couples to the total charge of the two-particle states. Therefore, the ultrasoft function is trivially $S_\gamma(\omega) = \delta(\omega)$ at leading power, and the convolution becomes trivial [100].

6.4.5 Derivation of the factorization theorem

The above definitions allow us to present a short derivation of the final factorization formula. We start from the definition of the differential cross-section in terms of the T-matrix element

$$\frac{d(\sigma v_{\mathrm{rel}})}{dE_\gamma} = \frac{1}{4}\frac{1}{4m_\chi^2} \sum\!\!\!\!\!\!\int_X \int \frac{d^3\mathbf{p}_\gamma}{(2\pi)^3 2p_\gamma^0}\, (2\pi)^4 \delta^{(4)}(p_{\chi\bar{\chi}} - p_\gamma - p_X)\delta(E_\gamma - |\mathbf{p}_\gamma|) \left|T_{\chi^0\chi^0\to\gamma X}\right|^2 . \tag{6.51}$$

The sum-integral symbol in X implies a summation over all kinematically possible final states X with momentum p_X together with the corresponding phase-space integral. We use χ^0 as a proxy for the lightest neutral DM two-particle state, as is relevant in models with several neutral states, e.g., the Higgsino. The spin sums are understood implicitly, and the factor 1/4, as usual, arises from the initial state spin-average. Furthermore, as discussed before the momentum of the two-particle state $\chi\chi$ is $p_{\chi\chi} = (2m_\chi + E)v$, such that at leading power, we have the factor $1/(4m_\chi^2)$. To this point, the definition is generic, and the T-matrix element can be evaluated in the full or effective theory. After integrating out hard modes, the T-matrix element is only non-vanishing anymore for the operators in the annihilation Lagrangian Eq. (6.26)

$$T_{\chi^0\chi^0\to\gamma X} = \frac{1}{2m_\chi} \sum_{i=1,2} \int dsdt\, \hat{C}_i(s,t,\mu)\, 2m_\chi \langle\gamma(p_\gamma)X_c X_s|\, \mathcal{O}_i \,|[\chi\chi]_{00}\rangle\,. \tag{6.52}$$

Let us consider the operator matrix element inside the T-matrix and apply the soft decoupling transformations (6.36), which in turn lead to

$$\begin{aligned}\langle\gamma(p_\gamma)X_c X_s|\, \mathcal{O}_i \,|[\chi\chi]_{00}\rangle =& \langle\gamma(p_\gamma)|\, \mathcal{A}^W_{\perp\bar{c},\nu}(tn_-)\,|0\rangle\langle X_c|\, \mathcal{A}^V_{\perp c,\mu}(sn_+)\,|0\rangle \\ &\times\, \langle X_s|\,[Y_v^\dagger T_i^{AB} Y_v]_{ab}\, \mathcal{Y}_+^{AV}\mathcal{Y}_-^{BW}\,|0\rangle\, K_{ab,I}\,\langle 0|\,[\chi_v^{c\dagger}\Gamma_i^{\mu\nu}\chi_v]_I\,|[\chi\chi]_{00}\rangle\,. \end{aligned} \tag{6.53}$$

Squaring this, using the translational invariance for the fields to redefine the hard coefficients (6.38) and putting it into the differential cross-section (6.51), we find

$$\begin{aligned}\frac{d(\sigma v_{\mathrm{rel}})}{dE_\gamma} =& \sum_{i.j=1,2} C_i(\mu)C_j^*(\mu) \sum_{I,J} \frac{1}{4}\frac{1}{4m_\chi^2}\int \frac{d^3\mathbf{p}_\gamma}{(2\pi)^3 2p_\gamma^0}\, \delta(E_\gamma - |\mathbf{p}_\gamma|) \\ &\times \int d^4x\, e^{i(p_{\chi\chi}-p_\gamma)\cdot x}\, \langle[\chi\chi]_{00}(p_{\chi\chi})|\, [\chi_v^{c\dagger}\Gamma_j^{\mu'\nu'}\chi_v]_J^\dagger\,|0\rangle\, \langle 0|\,[\chi_v^{c\dagger}\Gamma_i^{\mu\nu}\chi_v]_I\,|[\chi\chi]_{00}(p_{\chi\chi})\rangle \\ &\times \langle 0|\,\mathcal{A}^Y_{\perp\bar{c},\nu'}\,|\gamma(p_\gamma)\rangle\langle\gamma(p_\gamma)|\,\mathcal{A}^W_{\perp\bar{c},\nu}\,|0\rangle \sum\!\!\!\!\!\!\int_{X_c} e^{-ip_{X_c}\cdot x}\,\langle 0|\,\mathcal{A}^X_{\perp c,\mu'}\,|X_c\rangle\langle X_c|\,\mathcal{A}^V_{\perp c,\mu}\,|0\rangle \\ &\times \sum\!\!\!\!\!\!\int_{X_s} e^{-ip_{X_s}\cdot x}\, K_{ab,I}K^\dagger_{a'b',J}\,\langle 0|\,\mathcal{Y}_+^{\dagger A'X}\mathcal{Y}_-^{\dagger B'Y}\,[Y_v^\dagger T_j^{A'B'}Y_v]^\dagger_{a'b'}\,|X_s\rangle \\ &\times\quad \langle X_s|\,[Y_v^\dagger T_i^{AB}Y_v]_{ab}\,\mathcal{Y}_+^{AV}\mathcal{Y}_-^{BW}\,|0\rangle\,. \end{aligned} \tag{6.54}$$

The non-relativistic matrix element can be simplified by using the transition to the Sommerfeld factors (6.22) and (6.25)

$$\begin{aligned}&\langle[\chi\chi]_{00}(p_{\chi\chi})|\,[\chi_v^{c\dagger}\Gamma_j^{\mu'\nu'}\chi_v]_J^\dagger\,|0\rangle\,\langle 0|\,[\chi_v^{c\dagger}\Gamma_i^{\mu\nu}\chi_v]_I\,|[\chi\chi]_{00}(p_{\chi\chi})\rangle \\ &=\, 4\,\langle\xi_0^{c\dagger}\Gamma_j^{\mu'\nu'}\xi_0\rangle^*\,\langle\xi_0^{c\dagger}\Gamma_i^{\mu\nu}\xi_0\rangle\, S_{IJ}\,, \end{aligned} \tag{6.55}$$

note that after this step, we may use $p_{\chi\chi} = (2m_\chi + E)v \approx 2m_\chi v$, as only the Sommerfeld factors are sensitive to the kinetic energy of the two-particle state, which is irrelevant for all further considerations. Using the exponential phases, i.e., translational invariance in (6.54) to shift the fields from 0 to the given position, we arrive at

$$
\begin{aligned}
\frac{d(\sigma v_{\rm rel})}{dE_\gamma} = \sum_{I,J} S_{IJ} & \sum_{i,j=1,2,4,6} C_i(\mu) C_j^*(\mu) \frac{1}{4}\frac{1}{4m_\chi^2} \int \frac{d^3\mathbf{p}_\gamma}{(2\pi)^3 2p_\gamma^0}\,\delta(E_\gamma - |\mathbf{p}_\gamma|) \\
& \times\, 4\,\langle \xi_0^{c\dagger}\Gamma_j^{\mu'\nu'}\xi_0\rangle^*\,\langle \xi_0^{c\dagger}\Gamma_i^{\mu\nu}\xi_0\rangle \\
& \times\, \langle 0|\,\mathcal{A}^Y_{\perp\bar{c},\nu'}(0)\,|\gamma(p_\gamma)\rangle\langle\gamma(p_\gamma)|\,\mathcal{A}^W_{\perp\bar{c},\nu}(0)\,|0\rangle \\
& \times \int d^4x\, e^{i(p_{\chi\chi}-p_\gamma)\cdot x}\,\langle 0|\,\mathcal{A}^X_{\perp c,\mu'}(x)\,\mathcal{A}^V_{\perp c,\mu}(0)\,|0\rangle \\
& \times \sum\!\!\!\!\!\!\!\int_{X_s} \langle 0|\,[\mathcal{S}^\dagger]^j_{J,XY}(x)\,|X_s\rangle\,\langle X_s|\,\mathcal{S}^i_{I,VW}(0)\,|0\rangle\,.
\end{aligned} \tag{6.56}
$$

This form puts us almost in a position to use the function definitions above. The photon jet function definition (6.40) can be directly applied. Furthermore, we can use that

$$
\begin{aligned}
& \int d^4x\, e^{i(p_{\chi\chi}-p_\gamma)\cdot x}\,\langle 0|\,\mathcal{A}^X_{\perp c,\mu'}(x)\,\mathcal{A}^V_{\perp c,\mu}\,|0\rangle \times \sum\!\!\!\!\!\!\!\int_{X_s} \langle 0|\,[\mathcal{S}^\dagger]^j_{J,XY}(x)\,|X_s\rangle\,\langle X_s|\,\mathcal{S}^i_{I,VW}(0)\,|0\rangle \\
&\quad = -2\pi\, g^\perp_{\mu\mu'} \int d^4x \int \frac{d^4p}{(2\pi)^4}\int\frac{d^4k}{(2\pi)^4}\, e^{i(p_{\chi\chi}-p_\gamma-p-k)\cdot x}\, J^{XV}(p^2, m_W)\, \boldsymbol{W}^{ij}_{IJ,VWXY}(k) \\
&\quad = -2\pi\, g^\perp_{\mu\mu'} \int \frac{d^4k}{(2\pi)^4}\, J^{XV}(4m_\chi(m_\chi - E_\gamma - n_-k/2), m_W)\, \boldsymbol{W}^{ij}_{IJ,VWXY}(k) \\
&\quad = -2\pi\, g^\perp_{\mu\mu'} \int d\omega J^{XV}(4m_\chi(m_\chi - E_\gamma - \omega/2), m_W)\, W^{ij}_{IJ,VWXY}(\omega)\,,
\end{aligned} \tag{6.57}
$$

Transitioning from the second to third line, we used that at leading power $p^2 \to (p_{\chi\chi} - p_\gamma - k)^2 \approx 4m_\chi(m_\chi - E_\gamma - n_-k/2)$. As both the recoiling jet function (6.41) and the photon-jet function (6.40), supply factors of the metric tensor, we can further make use of the simplification

$$
\langle \xi_0^{c\dagger}\Gamma_j^{\mu\nu}\xi_0\rangle^*\,\langle \xi_0^{c\dagger}\Gamma_{i,\mu\nu}\xi_0\rangle = \epsilon_\perp^{\mu\nu}\epsilon_{\perp,\mu\nu}\langle \xi_0^{c\dagger}\xi_0\rangle^*\,\langle \xi_0^{c\dagger}\xi_0\rangle = 4\,. \tag{6.58}
$$

where we used that for the relevant operators in indirect detection $\mathcal{O}_1, \mathcal{O}_2, \mathcal{O}_4, \mathcal{O}_6$, the spin structure is always $\Gamma^{\mu\nu} = \epsilon_\perp^{\mu\nu}$, as expected for spin-0 operators. Furthermore, as there is also no explicit dependence on p_γ anymore, the integral

$$
\int \frac{d^3\mathbf{p}_\gamma}{(2\pi)^3 2p_\gamma^0}\,\delta(E_\gamma - |\mathbf{p}_\gamma|) = \frac{E_\gamma}{4\pi^2}\,, \tag{6.59}
$$

can be carried out. Collecting all definitions and factors, we arrive at

$$
\frac{d(\sigma v_{\rm rel})}{dE_\gamma} = 2\sum_{I,J} S_{IJ}\,\Gamma_{IJ}(E_\gamma) \tag{6.60}
$$

with the annihilation matrix defined by

$$
\begin{aligned}
\Gamma^{\rm int}_{IJ} = \frac{1}{(\sqrt{2})^{n_{\rm id}}}\frac{1}{4}\frac{2}{\pi m_\chi} & \sum_{i,j=1,2,4,6} C_i(\mu) C_j^*(\mu) Z_\gamma^{WY}(\mu,\nu) \\
\times \int d\omega\, \Big[& J^{\rm SU(2)}_{\rm int}(2m_\chi(2m_\chi - 2E_\gamma - \omega), \mu)\, W^{{\rm SU(2)},ij}_{IJ,WY}(\omega,\mu,\nu) \\
& + J^{\rm U(1)}_{\rm int}(2m_\chi(2m_\chi - 2E_\gamma - \omega), \mu)\, W^{{\rm U(1)},ij}_{IJ,WY}(\omega,\mu,\nu)\Big]
\end{aligned} \tag{6.61}
$$

where the factor $\frac{1}{(\sqrt{2})^{n_{\mathrm{id}}}}$ is introduced, as we calculate S_{IJ} using method-II [86]. If the Sommerfeld factors and annihilation matrices are calculated in method-I, this factor and the overall factor of two in (6.60) have to be dropped. Note that the colour structures T_i^{AB}, inside the soft functions, automatically pick the appropriate photon jet function components by setting all other soft function elements to zero.

For narrow resolution, one can proceed in a completely analogous fashion (using $X_s = 0$). Without repeating all the steps, using the appropriate definitions given before, we arrive at

$$\begin{aligned}\Gamma_{IJ}^{\mathrm{nrw}} = {} & \frac{1}{(\sqrt{2})^{n_{\mathrm{id}}}} \frac{1}{4} \frac{2}{\pi m_\chi} \sum_{i,j=1,2,4,6} C_i(\mu) C_j^*(\mu) Z_\gamma^{WY}(\mu,\nu) \\ & \times D_{I,VW}^{i}(\mu,\nu) D_{J,XY}^{j*}(\mu,\nu) J_{\mathrm{nrw}}^{VX}(4m_\chi(m_\chi - E_\gamma))\end{aligned} \tag{6.62}$$

where we in addition to the above considerations also uses that the ultrasoft function is $\delta(\omega)$ to all orders at leading power.

7

Resummation of the endpoint photon spectrum

In this Chapter, we discuss the resummation of the endpoint spectrum in wino and Higgsino dark matter annihilation up to the NLL' order, i.e., next-to-leading-logarithmic resummation (NLL) and the full one-loop fixed order correction (NLO). We focus on results initially derived by the author or with substantial contributions of the author. A complete and in detail presentation can be found in the corresponding publications for wino [101], and Higgsino [102] dark matter. Some of the narrow resolution results are also presented in [100]. Furthermore, we discuss a few subtleties and technical details that were omitted in the corresponding publications. Similar considerations using Sudakov resummation for various models, other resolution regimes, and effective theory setups can be found, e.g., in [93, 94, 95, 96, 97, 98, 99].

7.1 Hard coefficients

The hard matching coefficients onto the operators $\mathcal{O}_{1-6}$ in Eq. (6.33), are determined in the unbroken theory. There are various ways of determining the matching coefficients. In this Section, we present the calculation of the author using a tensor reduction and various computer algebra packages and tools. The calculation was independently done by C. Hasner using a different technique utilizing projectors thereby providing a strong cross-check on the results (for details, see Appendix A [101] or Section 6.1 of [149]).[1] To this end, the unbroken SM in addition with a Dirac/Majorana multiplet of arbitrary hypercharge Y and SU(2) representation, represented by the quadratic Casimir of the representation $c_2(j) = j \cdot (j+1)$ is created in `FeynRules` [153, 154, 155]. The corresponding model is exported into the `FeynArts` format and used for amplitude generation with `FeynArts` [125] supplied to `FeynCalc` [156, 157, 158]. These amplitudes are then further simplified using the `FeynHelpers` add-on [159] to `FeynCalc`, which supplies `Package-X` [127] that is used for the analytical evaluation of one-loop integrals.

The matching is performed at threshold. However, this leads to the unfortunate complication that propagators may be linearly dependent, i.e., the Gram determinant that appears in the ordinary PV-tensor-reduction [160] vanishes. As the Gram determinants appear in the denominator, the algorithm fails for some of the topologies. Fortunately, in `FeynCalc` a special partial fractioning algorithm `ApartFF` [161] is also supplied that allows reducing linear dependent propagators, so precisely what is needed to obtain a tensor reduced result. Finally, the analytic result for the reduced amplitudes is extracted using `Package-X`. It can be read off by accounting for the appropriate transition from relativistic spinors/gamma matrices to their non-relativistic

---

[1] The results for the wino model (or more general for arbitrary SU(2) representation without hypercharge), i.e., the matching coefficients C_1, C_2, was given in [100], respectively using a different operator basis in [97].

counterparts, which is done by hand and also checked against `FeynOnium` [162]. Other simplifications that arise during the process, e.g. the simplifications of SU(2) generators, are applied at all intermediate steps.

Using the above procedure, the matching coefficients for the operators in Eqs. (6.33) are

$$
\begin{aligned}
C_1(\mu) &= \frac{\hat{g}_2^4(\mu)}{16\pi^2}\, c_2(j) \left[(2-2i\pi)\ln\frac{\mu^2}{4m_\chi^2} - \left(4-\frac{\pi^2}{2}\right)\right], \\
C_2(\mu) &= \hat{g}_2^2(\mu) + \frac{\hat{g}_2^2(\mu)\,\hat{g}_1^2(\mu)Y^2}{16\pi^2}\left(\frac{\pi^2}{2}-10\right) \\
&\quad + \frac{\hat{g}_2^4(\mu)}{16\pi^2}\left[16-\frac{\pi^2}{6}+c_2(j)\left(\frac{\pi^2}{2}-10\right)-(6-2i\pi)\ln\frac{\mu^2}{4m_\chi^2}-2\ln^2\frac{\mu^2}{4m_\chi^2}\right], \\
C_3(\mu)|_{\text{Dirac}} &= \frac{\hat{g}_2^2(\mu)\,\hat{g}_1^2(\mu)Y^2}{16\pi^2}\left(-4+2\pi^2-16\ln 2\right) + \frac{\hat{g}_2^4(\mu)}{16\pi^2}\left[\frac{20}{3}-2\pi^2+8\ln 2\right. \\
&\quad \left. + c_2(j)\left(-4+2\pi^2-16\ln 2+(2j+1)\left(\frac{26}{9}-\frac{\pi^2}{3}+\frac{2}{9}n_G\right)\right)\right], \\
C_4(\mu) &= -\hat{g}_2(\mu)\hat{g}_1(\mu)Y - \frac{\hat{g}_2(\mu)\,\hat{g}_1^3(\mu)Y^3}{16\pi^2}\left(\frac{\pi^2}{2}-10\right) \\
&\quad - \frac{\hat{g}_2^3(\mu)\hat{g}_1(\mu)Y}{16\pi^2}\left[\frac{\pi^2}{6}+6+c_2(j)\left(\frac{\pi^2}{2}-10\right)-2\ln\frac{\mu^2}{4m_\chi^2}-\ln^2\frac{\mu^2}{4m_\chi^2}\right], \\
C_5(\mu) &= 0\,, \\
C_6(\mu) &= \hat{g}_1^2(\mu)Y^2 + \frac{\hat{g}_2^2(\mu)\hat{g}_1^2(\mu)Y^2}{16\pi^2}\,c_2(j)\left(\frac{\pi^2}{2}-10\right) + \frac{\hat{g}_1^4(\mu)Y^4}{16\pi^2}\left(\frac{\pi^2}{2}-10\right), \qquad (7.1)
\end{aligned}
$$

with $n_G = 3$ the number of fermion generations. The fermion generations only appear for C_3, as they arise in s-channel topologies, which however, only contribute to spin-one operators in the non-relativistic limit, i.e., $\mathcal{O}_3, \mathcal{O}_5$. Furthermore, note that for the same reason, C_3 is the only matching coefficient that depends on the Dirac/Majorana nature of the DM fermions. $C_3(\mu)|_{\text{Dirac}}$ in (7.1) applies for a Dirac fermion. The same calculation using a Majorana multiplet (which implies $Y = 0$) yields

$$
\begin{aligned}
C_3(\mu)|_{\text{Majorana}} &= \frac{\hat{g}_2^4(\mu)}{16\pi^2}\left[\frac{20}{3}-2\pi^2+8\ln 2\right. \\
&\quad \left. + c_2(j)\left(-4+2\pi^2-16\ln 2+(2j+1)\left(\frac{4}{3}-\frac{\pi^2}{6}+\frac{2}{9}n_G\right)\right)\right]. \qquad (7.2)
\end{aligned}
$$

Before moving on to resummation of the Wilson coefficients C_i, let us discuss a few subtleties connected to the matching coefficients C_3, C_5, both of which, however, do not contribute to the indirect detection prediction, as they correspond to spin-one operators.

The tree-level contribution to the Wilson coefficient C_3 vanishes. However, despite the vanishing tree-level coefficient, mass renormalization counterterms contribute to the matching coefficient and do not cancel. The tree-level cancellation stems from a cancellation between s- and t, u-channel diagrams. However, the DM mass counterterm insertion only exists for the t, u-channel, which in the end renders C_3 finite. A similar observation is made for the corresponding quarkonium calculation in QCD [163]. The same result arises using bare perturbation theory, where the appearance of the counterterm is subtle. The tree-level diagrams contain the bare mass explicitly from the propagators. Enforcing the on-shell condition for the external DM fermions sets their mass to the one-loop renormalized values. Therefore, the tree-level diagrams do not cancel exactly between s, t, u-channel, but the t, u-channel acquire a contribution from the difference of bare and renormalized mass, providing the mass counterterm contribution needed.

Finally, for $\mathcal{O}_5$, we find a vanishing matching coefficient at the one-loop order. The underlying reason is the Landau-Yang theorem, that albeit not applying in non-abelian gauge theories [163, 164], is applicable in this case. The reason why the Landau-Yang theorem is violated in non-abelian theories is, in essence, the final state bosons internal quantum number. Therefore, structures involving the group structure constant are constructible. At least to one-loop and possibly beyond, the group structure constant cannot arise from the underlying Feynman diagrams, as one of the final state bosons is abelian.

Let us now turn to the resummation of the Wilson coefficients C_i. In the following, we focus on the operators relevant for resummation of the DM indirect detection contribution, namely $\mathcal{O}_{1,2,4,6}$. The evolution is similar to the QCD analogue [165] and can be achieved by a straightforward adaption to the SU(2) and hypercharge case. The operators $\mathcal{O}_{1,2}$ are defined in a basis that is not a weak isospin eigenbasis, making their renormalization group evolution off-diagonal. The evolution of the operators $\mathcal{O}_{4,6}$ is already diagonal in isospin space. Therefore, it is convenient to rotate to the isospin eigenbasis, perform the resummation, and rotate back to the original basis, achieving the evolution as in QCD. The diagonal basis of operators $\mathcal{O}'$ is given by [100]

$$\mathcal{O}' = \mathbb{R}\,\mathcal{O} = \begin{pmatrix} \hat{V} & \mathbb{0}_{2\times 2} \\ \mathbb{0}_{2\times 2} & \mathbb{1}_{2\times 2} \end{pmatrix}^T \mathcal{O}\,, \quad \hat{V} = \begin{pmatrix} 1 & -\frac{c_2(j)}{3} \\ 0 & 1 \end{pmatrix} \tag{7.3}$$

where $\mathcal{O} = (\mathcal{O}_1, \mathcal{O}_2, \mathcal{O}_4, \mathcal{O}_6)^T$ and analogously for $\mathcal{O}'$. The evolved Wilson coefficients can therefore be cast in the form $C(\mu) = (C_1(\mu), C_2(\mu), C_4(\mu), C_6(\mu))^T$

$$C(\mu) = \mathbb{R} \begin{pmatrix} U_1^{(0)}(\mu_h, \mu) & 0 & 0 & 0 \\ 0 & U_2^{(2)}(\mu_h, \mu) & 0 & 0 \\ 0 & 0 & U_4^{(1)}(\mu_h, \mu) & 0 \\ 0 & 0 & 0 & U_6^{(0)}(\mu_h, \mu) \end{pmatrix} \mathbb{R}^{-1}\, C(\mu_h)\,. \tag{7.4}$$

The evolution factors $U_i^{(J)}(\mu_a, \mu_b)$ in terms of the isospin J of the operator in $\mathcal{O}'$ obey the evolution equation

$$\frac{d}{d\ln\mu} U_i^{(J)}(\mu_h, \mu) = \left(\Gamma_{\mathrm{SU}(2),i}^{(J)} + \Gamma_{\mathrm{U}(1),i}\right) U_i^{(J)}(\mu_h, \mu)\,, \tag{7.5}$$

with $\Gamma_{\mathrm{SU}(2),i}^{(J)}$ and $\Gamma_{\mathrm{U}(1),i}$ of the form [165]

$$\begin{aligned} \Gamma_{\mathrm{SU}(2),i}^{(J)} &= \frac{1}{2}\gamma_{\mathrm{cusp}} \left[c_2(\mathrm{ad})\, n_{i,\mathrm{SU}(2)} \left(\ln\frac{4m_\chi^2}{\mu^2} - i\pi \right) + i\pi c_2(J) \right] + \gamma_{\mathrm{ad}}\, n_{i,\mathrm{SU}(2)} + \gamma_{H,s}^{J}\,, \\ \Gamma_{\mathrm{U}(1),i} &= \gamma_{\mathrm{U}(1)}\, n_{i,\mathrm{U}(1)}\,, \end{aligned} \tag{7.6}$$

where $n_{i,\mathrm{SU}(2)}$ and $n_{i,\mathrm{U}(1)}$ give the number of SU(2) and U(1) gauge fields in operator $\mathcal{O}_i$ and $c_2(\mathrm{ad}) = 2$ is the quadratic Casimir of the adjoint representation. The evolution factors then are numerically solved to obtain the resummed Wilson coefficients. The cusp anomalous dimension appears in the same way to all orders [166], thereby meaning only a one-loop matching calculation is necessary for NLL' resummation. It is given at two-loops by

$$\gamma_{\mathrm{cusp}} = \frac{\hat{\alpha}_2}{4\pi}\gamma_{\mathrm{cusp}}^{(0)} + \left(\frac{\hat{\alpha}_2}{4\pi}\right)^2 \gamma_{\mathrm{cusp}}^{(1)} + \mathcal{O}(\hat{\alpha}_2^3)$$

$$= \frac{\hat{\alpha}_2}{4\pi} \cdot 4 + \left(\frac{\hat{\alpha}_2}{4\pi}\right)^2 \left[\left(\frac{268}{9} - \frac{4\pi^2}{3}\right) c_2(\text{ad}) - \frac{80}{9} n_G - \frac{16}{9}\right] + \mathcal{O}(\hat{\alpha}_2^3) . \tag{7.7}$$

The factors are analogous to QCD, with the addition of the Higgs contribution $-16/9$ at two-loop, extracted from the ϵ-scalar contribution of [167]. In addition, the following one-loop anomalous dimensions appear

$$\gamma^J_{H,s} = \frac{\hat{\alpha}_2}{4\pi} c_2(J) \, \gamma^{(0)}_{H,s} + \mathcal{O}(\hat{\alpha}_2^2) = \frac{\hat{\alpha}_2}{4\pi} c_2(J) \; (-2) + \mathcal{O}(\hat{\alpha}_2^2) \tag{7.8}$$

$$\gamma_{\text{ad}} = \frac{\hat{\alpha}_2}{4\pi} \gamma^{(0)}_{\text{SU}(2)} + \mathcal{O}(\hat{\alpha}_2^2) = \frac{\hat{\alpha}_2}{4\pi} \left(-\beta_{0,\text{SU}(2)}\right) + \mathcal{O}(\hat{\alpha}_2^2) \tag{7.9}$$

$$\gamma_{\text{U}(1)} = \frac{\hat{\alpha}_1}{4\pi} \gamma^{(0)}_{\text{U}(1)} + \mathcal{O}(\hat{\alpha}_1^2) = \frac{\hat{\alpha}_1}{4\pi} \left(-\beta_{0,\text{U}(1)}\right) + \mathcal{O}(\hat{\alpha}_1^2) \tag{7.10}$$

where the beta function coefficients are, as for the NLO potentials in previous Chapters, $\beta_{0,\text{SU}(2)} = \frac{43}{6} - \frac{4}{3} n_G$ and $\beta_{0,\text{U}(1)} = \frac{1}{6} + \frac{20}{9} n_G$.

The above resummation prescriptions are general and apply to all minimal DM models. Before turning to the other functions of the factorization theorem, let us remark a few details. In the Higgsino model, for which the numerical results are discussed in the subsequent Chapter, the operators $\mathcal{O}_1, \mathcal{O}_2$ are not linearly independent, as the doublet SU(2) generators are part of the fundamental representation, i.e., proportional to the Pauli matrices $\left\{\sigma^A/2, \sigma^B/2\right\} = \delta^{AB}/2$. Therefore, in this case, it is convenient to define

$$\tilde{C}_1 = \left(C_1 + \frac{1}{4} C_2\right)\Big|_{j=1/2} , \qquad \tilde{C}_4 = C_4|_{j=1/2} , \qquad \tilde{C}_6 = C_6|_{j=1/2} , \tag{7.11}$$

and work from there (the resummation discussion above, however, is not affected by this change). Furthermore, let us mention that for compatibility with the corresponding publications [100, 101, 102], and for later notational convenience, we also introduce the hard function, which combines the squares of Wilson coefficients into a vector. The generic form is given by

$$\vec{H} = \left(C_1^* C_1, C_2^* C_1, \ldots, C_4^* C_6, C_6^* C_6\right)^T . \tag{7.12}$$

In the particular cases of interest, e.g., the wino, this vector is only non-zero for the entries containing only C_1, C_2, and we typically drop the zero entries. The advantage of this notation is that we can introduce similar notation for the soft function, thereby producing compact consistency relations. For a more detailed discussion and model-specific results on the hard coefficients, let us point to [100, 101] for the wino and [102] for the Higgsino.

7.2 Recoiling jet functions

The recoiling jet function, together with the soft function, is the resolution-dependent object that changes between narrow and intermediate resolution calculation. In this Section, we present the intermediate resolution recoiling jet function originally calculated independently between M. Vollmann and the author, and later also checked in detail by C. Hasner. Furthermore, we discuss the Dyson resummation of the narrow resolution recoiling jet function. A result outlined in Appendix B.3 of [101] but not numerically investigated there or applied to the hypercharge case.

7.2.1 Intermediate resolution recoiling jet function

The recoiling intermediate resolution jet functions are similar to their QCD/QED analogues [168, 169]. As the recoiling jet functions describe modes of hard collinear virtuality $m_\chi m_W \gg m_W^2$, they are evaluated in the unbroken theory contrary to the narrow resolution equivalent discussed below. Therefore, we consider jet functions corresponding to the unbroken hypercharge boson B and the non-abelian SU(2) analogue corresponding to the W^a as defined in (6.44). Furthermore, the fact that the recoiling jet is of hard-collinear virtuality means that it does not suffer from a rapidity divergence and therefore only has to be resummed in virtuality.

The recoiling jet function $\mathcal{J}$, in terms of the indices X, V can be split into a Wilson line and self-energy contribution

$$i\mathcal{J}^{XV}(p^2,\mu) = i\mathcal{J}^{XV}_{\text{Wilson}}(p^2,\mu) + i\mathcal{J}^{XV}_{\text{se}}(p^2,\mu)\,. \tag{7.13}$$

All contributions are proportional to δ^{XV} in the factorization theorem for $\chi\chi \to \gamma + X$. Note that there is no Wilson line contribution for the index combination $XV = 44$. Using (6.41) and (6.44), we find

$$i\mathcal{J}^{\text{SU(2)}}_{\text{Wilson}}(p^2,\mu) = \frac{1}{-p^2-i\varepsilon}\left\{1 + \left(\frac{\mu^2}{-p^2-i\varepsilon}\right)^{\epsilon}\frac{\hat{g}_2^2(\mu)}{16\pi^2}c_2(\text{ad})\left(\frac{4}{\epsilon^2}+\frac{2}{\epsilon}+4-\frac{\pi^2}{3}\right)\right\}, \tag{7.14}$$

$$\begin{aligned} i\mathcal{J}^{\text{SU(2)}}_{\text{se}}(p^2,\mu) &= \frac{1}{-p^2-i\varepsilon}\left(\frac{\mu^2}{-p^2-i\varepsilon}\right)^{\epsilon}\frac{\hat{g}_2^2(\mu)}{16\pi^2} \\ &\times\left\{\frac{1}{\epsilon}\left(\frac{5}{3}c_2(\text{ad}) - \frac{8}{3}T_F n_G - \frac{1}{3}T_s n_s\right) + \frac{31}{9}c_2(\text{ad}) - \frac{40}{9}T_F n_G - \frac{8}{9}T_s n_s\right\}, \end{aligned} \tag{7.15}$$

$$i\mathcal{J}^{\text{U(1)}}(p^2,\mu) = \frac{1}{-p^2-i\varepsilon}\left(\frac{\mu^2}{-p^2-i\varepsilon}\right)^{\epsilon}\frac{\hat{g}_1^2(\mu)}{16\pi^2}\left\{\frac{1}{\epsilon}\left(-\frac{n_s}{6}-\frac{20}{9}n_G\right) - \frac{104}{9}\right\}, \tag{7.16}$$

where $T_F = T_s = 1/2$ and $n_s = 1$. All other symbols are to be understood as defined in previous Sections and Chapters. We can then extract the recoiling jet function for intermediate resolution by obtaining the imaginary part of all $\mathcal{J}$'s. The necessary relation is given by [169]

$$\frac{1}{\pi}\text{Im}\left[(-p^2-i\varepsilon)^a\right] = -\theta(p^2)\frac{\sin(\pi a)}{\pi}\left(p^2\right)^a\,. \tag{7.17}$$

Furthermore, after taking the imaginary part, the term $1/p^2\,(p^2/\mu^2)^\epsilon$ needs to be further expanded in the dimensional regularization parameter ϵ. To this end, we introduce star distributions [170, 171] by expanding

$$\frac{1}{p^2}\left(\frac{p^2}{\mu^2}\right)^{\eta} = \frac{\delta(p^2)}{\eta} + \sum_{m=0}^{\infty}\frac{\eta^m}{m!}\left[\frac{\ln^m\frac{p^2}{\mu^2}}{p^2}\right]_*^{[\mu^2]}\,. \tag{7.18}$$

These distributions are defined acting on a test function $f(p^2)$. To each order, we can read-off the corresponding prescription by using

$$\begin{aligned} \int_0^{\mu_b^2} d(p^2) f(p^2)\cdot\frac{1}{p^2}\left(\frac{p^2}{\mu_a^2}\right)^{\eta} &= \int_0^{\mu_b^2} d(p^2)\frac{f(p^2)-f(0)}{p^2}\left(\frac{p^2}{\mu_a^2}\right)^{\eta} + \frac{f(0)}{\eta}\left(\frac{\mu_b^2}{\mu_a^2}\right)^{\eta} \\ &= \sum_{m=0}^{\infty}\frac{\eta^m}{m!}\left[\int_0^{\mu_b^2} d(p^2)\,\frac{f(p^2)-f(0)}{p^2}\ln^m\frac{p^2}{\mu_a^2} + \frac{f(0)}{\eta}\ln^{m+1}\frac{\mu_b^2}{\mu_a^2}\right] \end{aligned}$$

$$= \frac{f(0)}{\eta} + \sum_{m=0}^{\infty} \frac{\eta^m}{m!} \int_0^{\mu_b^2} d(p^2)\, f(p^2) \left[\frac{\ln^m \frac{p^2}{\mu_a^2}}{p^2} \right]_*^{[\mu_a^2]} . \tag{7.19}$$

In this way, the prescriptions for star distributions and all relations for rescalings $p^2 \to \lambda_p p^2, \mu_a^2 \to \lambda_a \mu_a^2$ inside the distributions, and so on can easily be derived.

Using the numerical values for all group factors and all the above relations, we obtain the recoiling jet function, which is given by

$$J_{\text{int}}^{\text{SU(2)}}(p^2, \mu) = \delta(p^2) + \frac{\hat{\alpha}_2(\mu)}{4\pi} \left\{ \delta(p^2) \left(\frac{70}{9} - 2\pi^2 \right) - \frac{19}{6} \left[\frac{1}{p^2} \right]_*^{[\mu^2]} + 8 \left[\frac{\ln \frac{p^2}{\mu^2}}{p^2} \right]_*^{[\mu^2]} \right\} , \tag{7.20}$$

$$J_{\text{int}}^{\text{U(1)}}(p^2, \mu) = \delta(p^2) + \frac{\hat{\alpha}_1(\mu)}{4\pi} \left\{ \delta(p^2) \left(-\frac{104}{9} \right) + \frac{41}{6} \left[\frac{1}{p^2} \right]_*^{[\mu^2]} \right\} . \tag{7.21}$$

Note the coefficients in front of the star distributions: The ordinary star distribution has a prefactor proportional to the SU(2)/U(1) beta function coefficient, as expected, as it arises from one-loop self-energy insertions. The prefactor of the log-star distribution is proportional to the leading cusp anomalous dimension coefficient $\gamma_{\text{cusp}}^{(0)} = 4$, as it originates from the universal double pole in the Wilson line contribution. The latter also explains why there is no such term for the U(1) recoiling jet function.

The resummation procedure can be done in close analogy to the QCD treatment [172, 173]. However, note that fundamentally the U(1) and SU(2) jet functions renormalization group (RG) evolution is different, as there is no cusp anomalous dimension for the former, as we discuss below. The convolution of soft and jet function in the factorization theorem makes renormalization in momentum space complicated. However, in Laplace space, the convolution is replaced by multiplication and renormalization, as well as resummation, is multiplicative. Therefore, we define the Laplace transform of $J_{\text{int}}^a(p^2, \mu)$ by

$$j_{\text{int}}^a \left(\ln \frac{\tau^2}{\mu^2}, \mu \right) = \int_0^{\infty} dp^2 e^{-lp^2} J_{\text{int}}^a(p^2, \mu), \tag{7.22}$$

where $l = 1/(e^{\gamma_E} \tau^2)$. The result in Laplace space reads

$$j_{\text{int}}^{\text{SU(2)}} \left(\ln \frac{\tau^2}{\mu^2}, \mu \right) = 1 + \frac{\hat{\alpha}_2(\mu)}{4\pi} \left(4 \ln^2 \frac{\tau^2}{\mu^2} - \frac{19}{6} \ln \frac{\tau^2}{\mu^2} + \frac{70}{9} - \frac{4\pi^2}{3} \right), \tag{7.23}$$

$$j_{\text{int}}^{\text{U(1)}} \left(\ln \frac{\tau^2}{\mu^2}, \mu \right) = 1 + \frac{\hat{\alpha}_1(\mu)}{4\pi} \left(\frac{41}{6} \ln \frac{\tau^2}{\mu^2} - \frac{104}{9} \right), \tag{7.24}$$

where we used that the Laplace transforms of the star distributions are

$$\int_0^{\infty} dp^2 e^{-lp^2} \left[\frac{1}{p^2} \right]_*^{[\mu^2]} = \ln \frac{\tau^2}{\mu^2} \quad \text{and} \quad \int_0^{\infty} dp^2 e^{-lp^2} \left[\frac{\ln \frac{p^2}{\mu^2}}{p^2} \right]_*^{[\mu^2]} = \frac{1}{2} \ln^2 \frac{\tau^2}{\mu^2} + \frac{\pi^2}{12} . \tag{7.25}$$

The renormalization group equation (RGE) is a standard ordinary differential equation in Laplace space

$$\frac{d}{d \ln \mu} j_{\text{int}}^{\text{SU(2)}} \left(\ln \frac{\tau^2}{\mu^2}, \mu \right) = \gamma_{j,\text{SU(2)}}^{\mu}\, j_{\text{int}}^{\text{SU(2)}} \left(\ln \frac{\tau^2}{\mu^2}, \mu \right) , \tag{7.26}$$

$$\frac{d}{d\ln\mu} j_{\text{int}}^{\text{U}(1)}\left(\ln\frac{\tau^2}{\mu^2},\mu\right) = \gamma^{\mu}_{j,\text{U}(1)}\, j_{\text{int}}^{\text{U}(1)}\left(\ln\frac{\tau^2}{\mu^2},\mu\right)\,, \tag{7.27}$$

with Laplace-space anomalous dimensions

$$\gamma^{\mu}_{j,\text{SU}(2)} = -4\gamma_{\text{cusp}}\ln\frac{\tau^2}{\mu^2} - 2\gamma_{J^{\text{SU}(2)}} \quad \text{and} \quad \gamma^{\mu}_{j,\text{U}(1)} = -2\gamma_{J^{\text{U}(1)}}\,. \tag{7.28}$$

γ_{J^a} is needed at the one-loop order for NLL' resummation and incorporates terms originating from the respective beta functions

$$\gamma_{J^{\text{SU}(2)}} = \frac{\hat{\alpha}_2}{4\pi}\gamma^{(0)}_{J^{\text{SU}(2)}} + \mathcal{O}(\hat{\alpha}_2^2) \qquad \text{with} \qquad \gamma^{(0)}_{J^{\text{SU}(2)}} = -\beta_{0,\text{SU}(2)}\,, \tag{7.29}$$

$$\gamma_{J^{\text{U}(1)}} = \frac{\hat{\alpha}_1}{4\pi}\gamma^{(0)}_{J^{\text{U}(1)}} + \mathcal{O}(\hat{\alpha}_1^2) \qquad \text{with} \qquad \gamma^{(0)}_{J^{\text{U}(1)}} = -\beta_{0,\text{U}(1)}\,. \tag{7.30}$$

The RGEs lead to different solutions for SU(2) and U(1) jet function, as the latter, does not receive double logarithmic corrections. Therefore, we begin with solving the SU(2) RGE (7.26)

$$\begin{aligned} j_{\text{int}}^{\text{SU}(2)}\left(\ln\frac{\tau^2}{\mu^2},\mu\right) &= \exp\left[-\int_{\ln\mu_j}^{\ln\mu} d\ln\mu'\left(4\gamma_{\text{cusp}}(\hat{\alpha}_2(\mu'))\ln\frac{\tau^2}{\mu'^2} + 2\gamma_J(\hat{\alpha}_2(\mu'))\right)\right] j_{\text{int}}\left(\ln\frac{\tau^2}{\mu_j^2},\mu_j\right) \\ &= \exp\left[4\,S(\mu_j,\mu) + 2\,A_{\gamma_J}(\mu_j,\mu)\right] j_{\text{int}}^{\text{SU}(2)}(\partial_\eta,\mu_j)\left(\frac{\tau^2}{\mu_j^2}\right)^{\eta}\,, \end{aligned} \tag{7.31}$$

where $\mu_j \sim \sqrt{2m_\chi m_W}$ is the natural scale of the intermediate resolution recoiling jet function and the integrals $S(\mu_j,\mu)$ and $A_{\gamma_J}(\mu_j,\mu)$ are defined as

$$S(\mu_j,\mu) = -\int_{\ln\mu_j}^{\ln\mu} d\ln\mu'\,\gamma_{\text{cusp}}(\hat{\alpha}_2(\mu'))\ln\frac{\mu_j^2}{\mu'^2}\,, \tag{7.32}$$

$$A_{\gamma}(\mu_j,\mu) = -\int_{\ln\mu_j}^{\ln\mu} d\ln\mu'\,\gamma(\hat{\alpha}_2(\mu'))\,. \tag{7.33}$$

The function η is defined by

$$\eta = 4A_{\gamma_{\text{cusp}}}(\mu_j,\mu)\,. \tag{7.34}$$

The functions S, A are only numerically solvable beyond LL, as from NLL on two-loop SM running couplings enter, that make an analytic solution unfeasible. In the second line, of (7.31), the logarithms in τ^2/μ^2 are traded for derivatives in η, that generate these logarithms, thereby allowing to perform the inverse Laplace transform. The necessary inverse transform is given by

$$\int_0^\infty dp^2 e^{-p^2/(\tau^2 e^{\gamma_E})}\left(p^2\right)^{\eta-1} = \Gamma(\eta)e^{\gamma_E\eta}\left(\tau^2\right)^{\eta}\,. \tag{7.35}$$

Therefore in momentum space the SU(2) intermediate resolution recoiling jet reads[2]

$$J_{\rm int}(p^2,\mu) = \exp\left[4\,S(\mu_j,\mu) + 2\,A_{\gamma_J}(\mu_j,\mu)\right] \tilde{j}_{\rm int}(\partial_\eta,\mu_j)\,\frac{e^{-\gamma_E\eta}}{\Gamma(\eta)}\frac{1}{p^2}\left(\frac{p^2}{\mu_j^2}\right)^{\eta}\,. \tag{7.37}$$

In contrast, the U(1) jet function evolves according to

$$\begin{aligned}\tilde{j}^{\rm U(1)}_{\rm int}\left(\ln\frac{\tau^2}{\mu^2},\mu\right) &= U(\mu_j,\mu)\,\tilde{j}^{\rm U(1)}_{\rm int}\left(\ln\frac{\tau^2}{\mu^2},\mu\right)\\ &= \exp\left[-2\int_{\ln\mu_j}^{\ln\mu} d\ln\mu'\,\gamma_{J^{\rm U(1)}}(\hat{\alpha}_1(\mu'))\right]\tilde{j}^{\rm U(1)}_{\rm int}\left(\ln\frac{\tau^2}{\mu^2},\mu_j\right)\,. \end{aligned}\tag{7.38}$$

However, as there is no double logarithmic correction that would depend on τ for the U(1) jet, there is no necessity to introduce the derivatives and dependencies on η, as for the SU(2) jet above. Therefore, also the backtransform to momentum space is straightforward and leads to

$$J^{\rm U(1)}_{\rm int}(p^2,\mu) = U(\mu_j,\mu) J^{\rm U(1)}_{\rm int}(p^2,\mu_j)\,, \tag{7.39}$$

where the evolution factors again need to be evaluated numerically for NLL' resummation.

7.2.2 Dyson resummed narrow resolution recoiling jet function

Contrary to the intermediate resolution case above, the recoiling jet function is a quantity sensitive to the electroweak scale and the corresponding masses in the narrow resolution calculation. The definition is in analogy to the intermediate resolution case (cf. Eq. (6.41)), however, instead of hard-collinear $\mu^2 \sim m_\chi m_W$, the relevant mode is collinear $\mu^2 \sim m_W^2$. In practice, this means that the NLL' expressions are more complicated, as several thresholds contribute, and the SM self-energies enter with masses. On the other hand though, the resummation is considerably simpler as the convolution with the ultrasoft function is trivial to all orders. Hence we omit the resummation and point to the references discussed below for a comprehensive discussion.

In previous works, the relevant recoiling jet functions were discussed at NLL' order – J^{33} in [100, 101, 149], and J^{34}, J^{44} in [102, 149]. The presentation there is sufficient for invariant jet masses away from the Z-threshold at invariant jet-mass $p^2 = m_Z^2$. In the vicinity of this threshold, the fixed-order expressions discussed there are formally ill-defined. In [101], a procedure to cure this problem using Dyson resummation was presented (cf. Appendix B.3 therein). It is also demonstrated that in this way, the cumulative cross-section is finite if the resummed expression is expanded around $p^2 \approx m_Z^2$. However, the differential cross-section remains a distributional object.[3] As it is our goal to present a differential photon spectrum, we revisit this point and give

---

[2] The expression assumes $\eta > 0$, which is always the case as long as the scales are separated enough. In parameter scans with simultaneous scale variations for very low masses m_χ, it may be that the jet scale $\mu_j \sim \sqrt{2m_\chi m_W}$, and the soft scale $\mu_s \sim m_W$, are not separated enough, e.g. for $m_\chi = 500\,\text{GeV}$, we may have $\mu_s = 2m_W > \frac{1}{2}\sqrt{2m_\chi m_W} = \mu_j$, which in turn means $\eta < 0$. In this case, the term

$$\frac{1}{p^2}\left(\frac{p^2}{\mu_j^2}\right)^{\eta} \quad \xrightarrow{\eta<0} \quad \left[\frac{1}{p^2}\left(\frac{p^2}{\mu_j^2}\right)^{\eta}\right]_* \tag{7.36}$$

needs to be replaced by a star-distribution, which is sufficient as long as $\eta > -1$, i.e., holds for all cases of relevance [172]. Below $\eta \leq -1$, further subtractions using double-star distributions would be necessary. The same problem arises for the soft function resummation below and is cured in the same fashion by introducing a corresponding star distribution.

[3] The spectrum is also distributional after removing the physical delta-distribution $\delta(p^2)$ corresponding to the tree-level photon, which is also present after Dyson resummation.

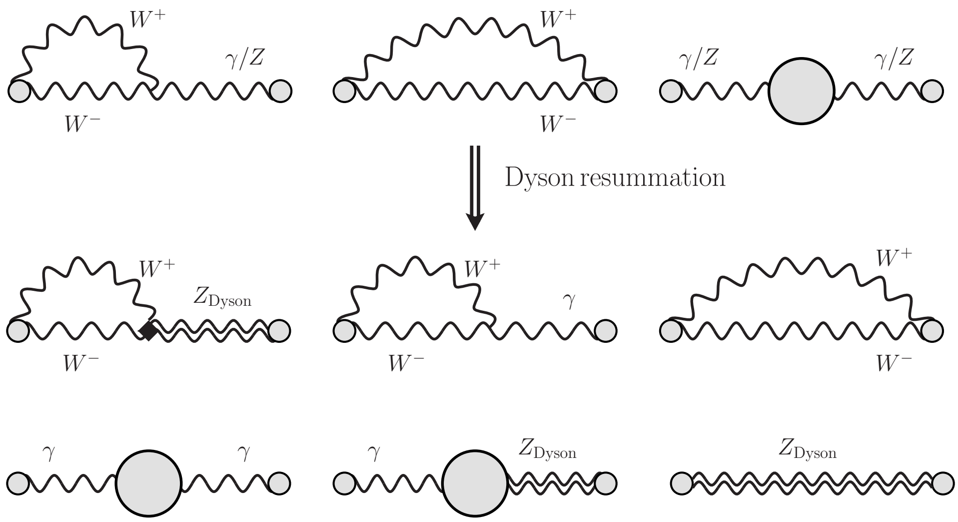

Figure 7.1: *Schematics of Dyson resummation for the narrow resolution recoiling jet function. The upper line presents the unresummed fixed-order one-loop corrections, with the left and middle diagrams stemming from Wilson-line contributions. The right diagram represents the self-energy corrections. The lower two-lines illustrate the Dyson resummed expressions schematically. The origin of the terms is the same as above. However, now Dyson resummed* Z*-propagators are represented by double-wavy lines. Note that the lower right diagram also contains the tree-level* Z *contribution that is omitted for brevity in the unresummed diagrams. Furthermore, symmetric diagrams are omitted for the Wilson line contributions and the* γZ_{Dyson} *diagram (lower middle diagram).*

a procedure that resums all the distributional terms for J^{33}, J^{34}, J^{44}, and presents us with the possibility to present a differential spectrum in the entire narrow resolution regime.

To this end, we sketch the derivation of the recoiling jet function, also in the fixed order case, to highlight the necessary modifications for Dyson resummation, without presenting the relevant fixed order expressions, that, e.g., can be found in [101, 102, 149]. Schematically, the procedure of Dyson resummation is shown in Figure 7.1.

Let us discuss the procedure on the example of J^{33}. The other jet functions work analogously with small modifications discussed below. The recoiling jet function is given as the imaginary part of $i\mathcal{J}$, where $\mathcal{J}^{33}$ is

$$\mathcal{J}^{33}_{\text{nrw}}(p^2) = \frac{-i\hat{s}_W^2}{p^2+i\varepsilon} + \frac{-i\hat{c}_W^2}{p^2-m_Z^2+i\varepsilon} + \mathcal{J}^{33}_{\text{nrw, Wilson}}(p^2) + \mathcal{J}^{33}_{\text{nrw, self-en.}}(p^2) \tag{7.40}$$

where the first two-terms correspond to the tree-level photon and Z-propagators. The latter two terms correspond to the Wilson line contribution and self-energy correction shown in the upper line of Figure 7.1, and we suppress virtuality and rapidity scale arguments throughout this Section. We begin with the self-energy contribution, which is given as

$$\begin{aligned}\mathcal{J}^{33}_{\text{nrw, self-en.}}(p^2) = {}& \hat{s}_W^2 \frac{-i}{p^2+i\varepsilon}\left(i\Sigma_T^{\gamma\gamma}(p^2)\right)\frac{-i}{p^2+i\varepsilon} + 2\hat{s}_W\hat{c}_W\frac{-i}{p^2+i\varepsilon}\left(i\Sigma_T^{\gamma Z}(p^2)\right)\frac{-i}{p^2-m_Z^2+i\varepsilon} \\ &+ \hat{c}_W^2\frac{-i}{p^2-m_Z^2+i\varepsilon}\left(i\Sigma_T^{ZZ}(p^2)\right)\frac{-i}{p^2-m_Z^2+i\varepsilon}\,,\end{aligned} \tag{7.41}$$

where the self-energies are given in Appendix A. The expressions correspond to the upper right diagram in Figure 7.1. Taking the imaginary part of the above expression, leads to various

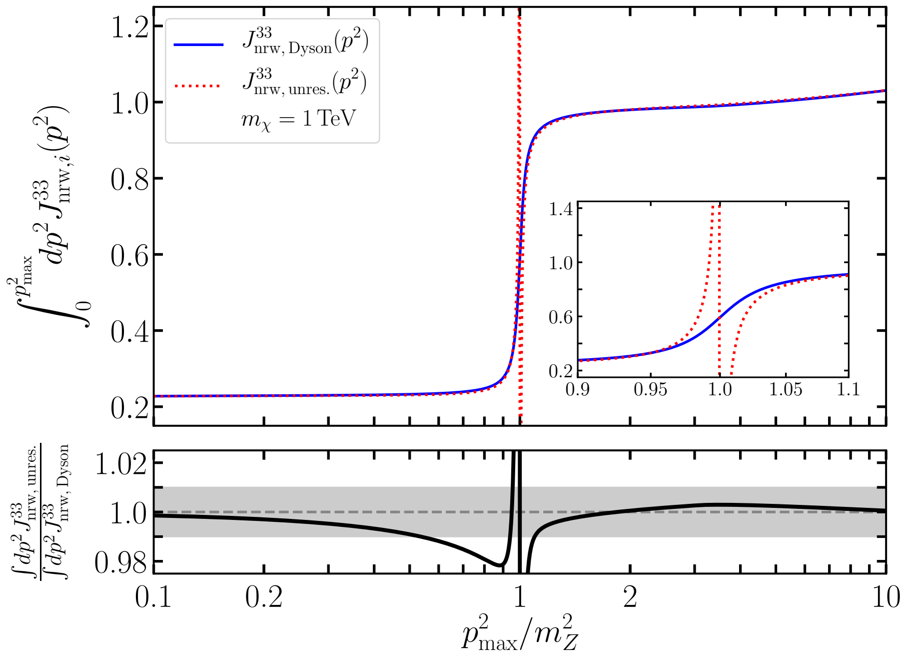

Figure 7.2: *Integrated recoiling jet function in the narrow resolution case* $\int_0^{p^2_{\max}} dp^2 J^{33}_{\mathrm{nrw}}(p^2)$ *for the Dyson resummed (blue/solid) and fixed-order (red/dotted) jet functions. The inset shows the region around the* Z*-threshold zoomed in. In the lower panel, the ratio of unresummed to resummed jet function is shown for the entire* $p^2_{\max}$ *range. The grey band indicates the one percent difference band.*

distributions, such as Dirac-delta, star or double-star distributions at fixed-order (cf. [102, 149]), that are ill-defined at and around $p^2 = m_Z^2$. The corresponding distributions also generate the necessary wave-function and mass renormalization terms that render the result finite and gauge invariant. Correspondingly, we can Dyson resum, the Z-boson propagators, which leads to

$$\begin{aligned}\mathcal{J}^{33,\mathrm{Dyson}}_{\mathrm{nrw,\,self-en.}}(p^2) &= \hat{s}_W^2 \frac{-i}{p^2 + i\varepsilon}\left(i\Sigma_T^{\gamma\gamma}(p^2)\right)\frac{-i}{p^2+i\varepsilon} \\ &\quad + 2\hat{s}_W\hat{c}_W \frac{-i}{p^2+i\varepsilon}\left(i\Sigma_T^{\gamma Z}(p^2)\right)\frac{-i}{p^2 - m_Z^2 - \delta m_Z^2 + \Sigma_T^{ZZ}(p^2)} \\ &\quad + \hat{c}_W^2 \frac{-i}{p^2 - m_Z^2 - \delta m_Z^2 + \Sigma_T^{ZZ}(p^2)} \end{aligned} \tag{7.42}$$

where δm_Z^2 is defined in Eq. (3.10). Taking the imaginary part of this expression and expanding to fixed-order reproduces the fixed-order self-energy contributions, renormalization factors and the tree-level term of the Z-boson in (7.40).

Similarly, the Wilson line contribution is distributional, as it contains terms proportional $\delta(p^2 - m_Z^2)$ from cutting the Z-propagator in Figure 7.1. These are replaced using a standard Breit-Wigner treatment, meaning that in the expressions in [101, 102, 149], one replaces

$$\delta(p^2 - m_Z^2) \quad \to \quad \frac{1}{\pi}\frac{m_Z\Gamma_Z}{(p^2 - m_Z^2)^2 + m_Z^2\Gamma_Z^2}\,. \tag{7.43}$$

In other words, Dyson resummation corresponds to undoing the narrow-width approximation $\Gamma_Z/m_Z \to 0$ in these expressions.

The resulting integrated jet function $\int_0^{p_{\max}} dp^2 J^{33}_{\rm nrw}(p^2)$ for a given $p_{\max}$ in the region around the Z-threshold is shown in Figure 7.2 (blue/solid). As a comparison, also the fixed order result (red/dotted) is shown, which breaks down in the vicinity of $p^2_{\max} \approx m_Z^2$. The actual region where this matters is very narrow, as visualized by the inset, that zooms in within 10% of the threshold value. In the subset plot, the ratio of the unresummed to the resummed result is shown, with a grey band indicating the 1% difference band. It is visible that both resummed and unresummed predictions agree on the permille level away from the Z-pole both for higher and lower $p^2_{\max}$.

Using these prescriptions produces an entirely finite differential cross-section in the narrow resolution case. Similarly, for $J^{34}_{\rm nrw}, J^{44}_{\rm nrw}$, the couplings of photon and Z-propagators need to be adjusted. However, conceptually, the same procedure applies. Note that for $J^{34}_{\rm nrw}$, the omitted symmetric Wilson line diagrams of Figure 7.1 are not present, whilst for $J^{44}_{\rm nrw}$, there is no Wilson-line contribution altogether. The equivalent plots to Figure 7.2, look similar for both $J^{34}_{\rm nrw}$ and $J^{44}_{\rm nrw}$, so we do not show them explicitly. The agreement is again on the sub percent level, away from the Z-threshold. For $J^{34}_{\rm nrw}$ above the Z-threshold, the differences may be on the level of a few percent. This is a remnant of the fact, that $J^{34}_{\rm nrw,\, tree}(p^2) \sim \delta(p^2) - \delta(p^2 - m_Z^2)$, i.e., the tree-level vanishes above the Z-threshold. Whilst the difference is still at the level of a two-loop correction for the full cross-section, the vanishing tree-level means that the relative error for $J^{34}_{\rm nrw}$ is of $\mathcal{O}(\alpha_{1,2})$. Therefore, the ratio becomes generically larger, as the difference is between two small, nearly vanishing numbers. On the final cross-section prediction, the differences arising from $J^{34}_{\rm nrw}$ do not play a role and are mostly even smaller than permille level.

As both the fixed-order and the Dyson resummed result agree within a few permille accuracy away from the Z-threshold, we will always use the Dyson resummed prediction in plots and figures from hereon. The differences away from threshold are well within the typical theoretical uncertainties obtained by scale variations in the next Chapter. However, formally, the Dyson-resummed expression suffers some conceptual problems away from threshold that we mention in the following, even though their numerical impact, as seen above, is negligible.

Dyson resummation of the Z-threshold is appropriate if $p^2 - m_Z^2 \sim m_Z \Gamma_Z$, i.e., as soon as the width plays a role in the Z-boson propagator. Numerically, using the SM Z-width, this means that Dyson resummation is necessary within $2 - 3\,\%$ of the threshold value (cf. inset Figure 7.2). However, away from threshold, Dyson resummation can be problematic, as it mixes orders in perturbation theory and is therefore not entirely systematic.

Also, let us mention that in principle, the Dyson resummed result is not gauge invariant, which only matters as soon as the W^+W^--threshold is crossed. Beforehand, only massless fermionic self-energy terms develop a non-vanishing imaginary part. These fermionic contributions are gauge invariant by themselves. At the W^+W^--threshold, also the electroweak self-energies (cf. Eq. (A.35)), develop a non-vanishing imaginary part that contributes to the Dyson resummed jet function. For definiteness, we therefore always use Feynman gauge $\xi_\gamma = \xi_W = \xi_Z = 1$, above $p^2 = 4m_W^2$. The non-gauge invariance could be cured, e.g., by only resumming fermionic self-energy contributions and keeping electroweak, i.e., gauge- and Higgs-boson loops at fixed order. However, as we find that the results agree on the permille level with the gauge invariant fixed order result if we use Feynman gauge, we refrain from doing so. A more systematic treatment avoiding possible ambiguities in Dyson resummation is possible in terms of the complex mass scheme [174]. For a detailed review of Dyson resummation in the SM and the application of the complex mass scheme to the SM propagators, see [130]. In any case, the fixed-order result can always be used away from the Z-threshold if one is worried about potentially large non-gauge invariant terms.

7.3 Soft function - wino

In this Section, we present the calculation of the soft-function $W^{ij}_{IJ}(\omega)$, as defined in Eq. (6.47), for the wino intermediate resolution case. The calculation was initially done by the author and independently checked by C. Hasner. The soft function is an object of natural virtuality and rapidity scales $\mu_s \sim \nu_s \sim m_W$, i.e., it is to be calculated in the broken electroweak theory. Here we follow an idea laid out in [101], and present the calculation for one specific matrix element $W^{22}_{(+-)(+-)}$, to which all relevant integral structures and topologies contribute. Thereby, we illustrate the NLL resummation and especially the treatment of the one-loop real contributions at NLL' order. The detailed integrals and their calculation, other soft function components and some additional details are presented in Appendix E to keep the discussion as brief as possible. Finally, before starting the discussion, let us mention that the virtual contributions to the soft function were already given in [100] for the narrow resolution case in the form of soft matching coefficients.

The matrix element for the operator combination 22 and in the $(+-) \to (+-)$ entry reads at the one-loop order

$$\begin{aligned}W^{\text{wino},22}_{(+-)(+-)}(\omega,\mu,\nu) = \delta(\omega) + \frac{\hat{\alpha}_2(\mu)}{4\pi}\Bigg[&\delta(\omega)\left(-8\ln\frac{m_W}{\mu} - 16\ln\frac{m_W}{\mu}\ln\frac{m_W}{\nu}\right)\\ &-\frac{6}{\omega}\ln\left(\frac{m_W^2+\omega^2}{m_W^2}\right) - \frac{2\omega}{m_W^2+\omega^2} + \left[\frac{1}{\omega}\right]_*^{[m_W]} 8\ln\frac{\mu^2}{m_W^2}\Bigg]\,, \end{aligned}\tag{7.44}$$

where we used $W^{\text{SU(2)},ij}_{IJ,WY} = W^{\text{SU(2)},ij}_{IJ,33} = W^{\text{wino},ij}_{IJ}$ for the wino, to simplify notation. Similar to the intermediate recoiling jet function case discussed above, the resummation is most convenient in Laplace space, where a multiplication replaces the convolution between soft and recoiling jet function. The necessary Laplace transforms and backtransforms are defined as

$$w(s) = \mathcal{L}\left\{W(\omega)\right\} = \int_0^\infty d\omega\, e^{-\omega s}\, W(\omega)\,, \tag{7.45}$$

$$W(\omega) = \mathcal{L}^{-1}\left\{w(s)\right\} = \frac{1}{2\pi i}\int_{c-i\infty}^{c+i\infty} ds\, e^{s\omega}\, w(s)\,. \tag{7.46}$$

The real emission contributions to the soft function require additional Laplace transforms beyond the delta-function one, necessary for the virtual contributions. Collecting the structures, e.g., from Eq. (7.44) or the integrals in Appendix E, we find ($s = 1/(e^{\gamma_E}\kappa)$)

$$\begin{aligned}\mathcal{L}\left\{\delta(\omega)\right\} &= 1\,,\\ \mathcal{L}\left\{\left[\frac{1}{\omega}\right]_*^{[m_W]}\right\} &= \ln\frac{\kappa}{m_W}\,,\\ \mathcal{L}\left\{\frac{1}{\omega}\ln\left(\frac{m_W^2+\omega^2}{m_W^2}\right)\right\} &= \mathrm{si}^2\left(m_W s\right) + \mathrm{ci}^2\left(m_W s\right) \equiv \tilde{G}(s)\,,\\ \mathcal{L}\left\{\frac{\omega}{m_W^2+\omega^2}\right\} &= \cos(m_W s)\,\mathrm{ci}(m_W s) - \sin(m_W s)\,\mathrm{si}(m_W s) \equiv \tilde{Q}(s)\,,\end{aligned}\tag{7.47}$$

where the functions si, ci are defined as

$$\mathrm{si}(x) \equiv -\int_x^\infty dt\,\frac{\sin(t)}{t}, \quad \text{and} \quad \mathrm{ci}(x) \equiv -\int_x^\infty dt\,\frac{\cos(t)}{t}\,. \tag{7.48}$$

Similar, to the hard function case above, it is convenient to introduce a vector notation for the Laplace transformed soft functions

$$\vec{w}_{IJ} = \left(w^{11}_{IJ}, w^{12}_{IJ}, w^{21}_{IJ}, w^{22}_{IJ}\right)^T . \tag{7.49}$$

Beyond the NLL' order, this vector has to be extended, as at two-loops, the Wilson coefficients $C_{4,6}$ in (7.1), do not necessarily vanish anymore for the wino. Thereby, there is also the possibility of soft coefficients, such as w^{14}, w^{46}, and similar. To simplify the notation and keep the size of the anomalous dimension matrices small, we drop the contributions that vanish at NLL' here.

The rapidity renormalization group (RRG) [110, 111] equations for the soft functions are simple and can be read off from all coefficients. We find

$$\frac{d}{d\ln\nu}\vec{w}_{IJ}(s,\mu,\nu) = \mathbf{\Gamma}^{\nu}_{W}\,\vec{w}_{IJ}(s,\mu,\nu)\,, \tag{7.50}$$

with the fixed-order one-loop rapidity anomalous dimension is given by

$$\mathbf{\Gamma}^{\nu}_{W} = \frac{\hat{\alpha}_2}{4\pi}\,4\gamma^{(0)}_{\text{cusp}}\,\ln\frac{m_W}{\mu}\,\mathbf{1}_4\,, \tag{7.51}$$

where the non-logarithmic anomalous dimension piece is zero at one-loop. Before solving the soft RRG (7.50), let us note that the solution crucially depends on the resummation order, between virtuality and rapidity resummation, as the anomalous dimension contains logarithms of the form $\hat{\alpha}_2^n \ln^m(\mu/m_W)$ for $m \leq n$ at higher orders [111]. If the virtuality scale is resummed before the rapidity scale, these logarithms are large and require resummation. We can circumvent this issue by noting that any observable has to be independent of both μ,ν at fixed order, hence

$$\left[\frac{d}{d\ln\mu}, \frac{d}{d\ln\nu}\right] = 0\,. \tag{7.52}$$

In combination with the virtuality anomalous dimension below, we derive the constraint

$$\frac{d}{d\ln\mu}\mathbf{\Gamma}^{\nu}_{W} = \frac{d}{d\ln\nu}\mathbf{\Gamma}^{\mu}_{W} = 4\gamma_{\text{cusp}}\,. \tag{7.53}$$

From this requirement, we solve for the rapidity anomalous dimension to obtain

$$\mathbf{\Gamma}^{\nu}_{W}(\mu) = \int^{\ln\mu} d\ln\mu'\,\frac{d}{d\ln\nu}\mathbf{\Gamma}^{\mu}_{W}(\mu',\nu)\,+\,\text{const.}\,, \tag{7.54}$$

where the integration constant is fixed such that the fixed-order non-cusp piece of the anomalous dimension is reproduced, which in the case at hand vanishes. The above procedure sums the running couplings logarithms $\ln\mu/m_W$ to all orders in perturbation theory. With the integrated rapidity anomalous dimension, the RRG (7.50) is solved, and we find

$$\vec{w}_{IJ}(s,\mu,\nu) = \exp\left[\mathbf{\Gamma}^{\nu}_{W}(\mu)\ln\frac{\nu}{\nu_s}\right]\vec{w}_{IJ}(s,\mu,\nu_s)\,. \tag{7.55}$$

At which order this factor enters the soft function resummation depends on the order of μ,ν-resummation. If rapidity is resummed first, the logarithms $\ln\mu/m_W$ are small, and hence rapidity evolution is an NLL contribution, whilst the virtuality evolution below is a LL contribution. If, on the other hand, we resum first in virtuality, the running coupling logarithms are large, and the contribution from rapidity evolution is already present at LL, whilst virtuality resummation starts at NLL.

The RRG is diagonal in operator space to all orders. The diagonality is forced, as the dependence on the rapidity scale has to cancel against the corresponding dependence of the photon jet, which is a scalar object, associated with the operator index pair.[4] Depending on the resummation scheme, either the soft function, the photon jet function, or both can be evolved rapidity. As the resummation factors are diagonal, and as long as rapidity is resummed first, the evolution does not depend on which of the functions is resummed.[5] By convention for wino and Higgsino, we chose that rapidity is first resummed and that the photon jets are evolved. Therefore, we can always set the rapidity evolution of the wino soft function to unity from hereon.

The soft function virtuality evolution is diagonal in the cusp part. However, the non-cusp part is non-diagonal in operator space, as expected. The off-diagonal fixed-order dependence of the hard contribution needs to be cancelled by the soft function. The RG equation is

$$\frac{d}{d\ln\mu}\vec{w}_{IJ}(s,\mu,\nu) = \mathbf{\Gamma}^{\mu}_{W}\,\vec{w}_{IJ}(s,\mu,\nu)\,, \tag{7.56}$$

with anomalous dimension

$$\mathbf{\Gamma}^{\mu}_{W} = 4\,\gamma_{\text{cusp}}\ln\frac{\kappa}{\nu}\,\mathbf{1}_4 + \begin{pmatrix} 0 & 0 & 0 & 0 \\ -2\gamma_W & 3\gamma_W & 0 & 0 \\ -2\gamma_W^* & 0 & 3\gamma_W^* & 0 \\ 0 & -2\gamma_W^* & -2\gamma_W & 3\gamma_W + 3\gamma_W^* \end{pmatrix}. \tag{7.57}$$

The coefficients γ_W at one-loop order are

$$\gamma_W^{(0)} = (2 + 2\pi i)\,c_2(j)\,, \tag{7.58}$$

which is sufficient for NLL' resummation. Similar to the hard coefficients above, the RG equation can be solved by diagonalizing the anomalous dimension matrix, solving the RG equation and then rotating back to the original basis. The solution takes the form

$$\vec{w}_{IJ}(s,\mu,\nu) = \boldsymbol{R}^{-1}\,\boldsymbol{U}_W(\mu,\mu_s)\,\boldsymbol{R}\,\vec{w}_{IJ}(s,\mu_s,\partial_\eta)\left(\frac{\kappa}{\nu}\right)^{\eta}\,, \tag{7.59}$$

with the diagonal evolution matrix $\boldsymbol{U}_W$

$$\boldsymbol{U}_W = \begin{pmatrix} 1 & 0 & 0 & 0 \\ 0 & \exp\left[3A_{\gamma_W}\right] & 0 & 0 \\ 0 & 0 & \exp\left[3A_{\gamma_W^*}\right] & 0 \\ 0 & 0 & 0 & \exp\left[3(A_{\gamma_W} + A_{\gamma_W^*})\right] \end{pmatrix}, \tag{7.60}$$

and the diagonalization matrix $\boldsymbol{R}$ and its inverse $\boldsymbol{R}^{-1}$

$$\boldsymbol{R} = \begin{pmatrix} \frac{2}{3} & 0 & 0 & 0 \\ -\frac{2}{3} & 1 & 0 & 0 \\ -\frac{2}{3} & 0 & 1 & 0 \\ \frac{2}{3} & -1 & -1 & \frac{3}{2} \end{pmatrix}, \quad \boldsymbol{R}^{-1} = \begin{pmatrix} \frac{3}{2} & 0 & 0 & 0 \\ 1 & 1 & 0 & 0 \\ 1 & 0 & 1 & 0 \\ \frac{2}{3} & \frac{2}{3} & \frac{2}{3} & \frac{2}{3} \end{pmatrix}. \tag{7.61}$$

---

[4] Note that at higher orders, from two-loops on, additional hard, soft and photon jet functions corresponding to the projection on the hypercharge boson B contribute, i.e., the above vectors are extended. The rapidity evolution remains diagonal. However, the anomalous dimension is not proportional to the unit matrix anymore, as only the SU(2) bosons and their projection receive corrections proportional to the cusp anomalous dimension.

[5] In principle, the virtuality resummation does, but as the cusp part is diagonal, in the case of the wino, there is also no difference in this case using the above conventions.

The functions A_{γ_W} and η were already defined for the recoiling jet function in Eq. (7.33). To complete the resummation procedure, we need to transform back to momentum space, i.e., perform the inverse Laplace transform of Eq. (7.59). As the evolution factor $\mathbf{U}_W$ does not depend on κ, we define

$$\hat{\vec{W}}_{IJ}(\omega,\mu_s,\nu) = \mathcal{L}^{-1}\left[\vec{w}_{IJ}(s,\mu_s,\partial_\eta)\left(\frac{\kappa}{\nu}\right)^\eta\right], \tag{7.62}$$

as the inverse Laplace transform of all structures containing a κ-dependence. The following inverse Laplace transforms appear[6]

$$\mathcal{L}^{-1}\left[\left(\frac{\kappa}{\nu}\right)^\eta\right] = \frac{e^{-\gamma_E\eta}}{\Gamma(\eta)}\left(\frac{\omega}{\nu}\right)^\eta\frac{1}{\omega}, \tag{7.63}$$

$$\begin{aligned} F(\omega) &\equiv \mathcal{L}^{-1}\left[\left(\frac{\kappa}{\nu}\right)^\eta \tilde{G}(e^{-\gamma_E}/\kappa)\right] \\ &= \left(\frac{e^{-\gamma_E}}{\nu}\right)^\eta \frac{\omega^{1+\eta}}{\Gamma(2+\eta)m_W^2}\,{}_4F_3\left(1,1,1,\frac{3}{2};1+\frac{\eta}{2},\frac{3}{2}+\frac{\eta}{2},2;-\frac{\omega^2}{m_W^2}\right), \end{aligned} \tag{7.64}$$

$$\begin{aligned} P(\omega) &\equiv \mathcal{L}^{-1}\left[\left(\frac{\kappa}{\nu}\right)^\eta \tilde{Q}(e^{-\gamma_E}/\kappa)\right] \\ &= \left(\frac{e^{-\gamma_E}}{\nu}\right)^\eta \frac{\omega^{1+\eta}}{m_W^2\Gamma(2+\eta)}\,{}_3F_2\left(1,1,\frac{3}{2};1+\frac{\eta}{2},\frac{3}{2}+\frac{\eta}{2};-\frac{\omega^2}{m_W^2}\right). \end{aligned} \tag{7.65}$$

Therefore, for the example matrix element (7.44), the resummed matrix element including the inverse Laplace transform is given by

$$\begin{aligned} \hat{W}^{\text{wino},22}_{(+-)(+-)}(\omega,\mu_s,\nu) = &\left[1+\frac{\hat{\alpha}_2}{4\pi}\left(\left(-16\ln\frac{m_W}{\mu_s}\,\partial_\eta\right)-8\ln\frac{m_W}{\mu_s}\right)\right]\frac{e^{-\gamma_E\eta}}{\Gamma(\eta)}\frac{1}{\omega}\left(\frac{\omega}{\nu}\right)^\eta \\ &+\frac{\hat{\alpha}_2}{4\pi}\left[-6F(\omega)-2P(\omega)\right]. \end{aligned} \tag{7.66}$$

The results for all other index combinations are given in Appendix E. Combining the back-transforms with the evolution factors for virtuality (7.59) and the resummed one-loop soft coefficients (7.62), we find that the virtuality resummed soft function in momentum space takes the form[7]

$$\vec{W}^{\text{wino}}_{IJ}(\omega,\mu,\nu) = \boldsymbol{R}^{-1}\,\boldsymbol{U}_W(\mu,\mu_s)\,\boldsymbol{R}\,\hat{\vec{W}}^{\text{wino}}_{IJ}(\omega,\mu_s,\nu). \tag{7.67}$$

7.4 Further functions

Beyond the functions discussed above, several other pieces enter the various factorization formulas for the resolution regimes and models (cf. Eqs. (6.61) and (6.62)). Up to this point, we presented mainly results that were either originally calculated or cross-checked by the author. In some cases, the author's contribution was also more connected to the implementation into code and similar, in which case we typically omitted the function. This Section provides an overview of the omitted functions and where they can be extracted in the corresponding papers. The results

---

[6] This spans all structures possible that appear for NLL' resummation of minimal DM, except $\mathcal{L}^{-1}[1] = \delta(\omega)$, which appears in addition if hypercharge bosons are involved in the annihilation operators.

[7] Where as indicated above, by convention, we do not resum the soft function in rapidity, as the photon jet functions are evolved from their rapidity scale $\nu_h \sim 2m_\chi$ to the soft rapidity scale $\nu_s \sim m_W$.

complete the ingredients necessary for the wino and Higgsino prediction, and we implicitly use them in the numerical results presented in the next Chapter.

The hard coefficients and their renormalization group evolution are presented above in Section 7.1 and hold for arbitrary hypercharge and SU(2) representation. The same holds for the intermediate resolution recoiling jet functions. However, the narrow resolution recoiling jet functions are only discussed in their Dyson resummed form above. Also, we focussed on the Dyson resummation modifications and did not discuss pieces that are not Dyson resummed, e.g., stemming from $\Sigma_T^{\gamma\gamma}$ or the Wilson line contributions. The corresponding expressions and the full-fixed order form for $J^{33}_{\text{nrw}}(p^2)$ are found in [100] and discussed in detail in [101] Appendix B.2. The same jet functions including mixed hypercharge SU(2) $J^{34}_{\text{nrw}}(p^2)$ and pure hypercharge contributions $J^{44}_{\text{nrw}}(p^2)$ are given in Appendix C.3.2 of [102].

The photon jet functions are discussed in [101] Section 3.2 for Z_γ^{33} (first given in [100]), and in [102] Appendix C.2 for $Z_\gamma^{34}, Z_\gamma^{44}$. Finally, the missing soft function contributions are found in Section 2.2.2 [100] for the wino narrow resolution case, and for the Higgsino narrow and intermediate resolution case in [102] Appendix C.4. In general, the complete presentation of all results connected to Sudakov resummation concerning the wino case are given in [100, 101] and for the Higgsino in [102].

7.5 Renormalization group invariance

An important check on the calculation arises through so-called consistency relations. These arise, as the cross-section in the factorization theorem should not depend on the arbitrary scales μ, ν, and much rather resum logarithms of the natural scales of these functions, e.g., $\ln \mu_h/\mu_s$, and similar. Therefore, we require that

$$\frac{d}{d\ln\mu}\frac{d(\sigma v_{\text{rel}})}{dE_\gamma} = 0 \quad \text{and} \quad \frac{d}{d\ln\nu}\frac{d(\sigma v_{\text{rel}})}{dE_\gamma} = 0\,. \tag{7.68}$$

As we evaluate the Sommerfeld factor on-shell, we drop it from the following considerations. However, note that the discussion also holds if the potentials in the $\overline{\text{MS}}$-scheme, as described in Section 3.4.3, are used. As discussed above, the main difficulty in resummation arises for intermediate resolution, as the soft and recoiling jet function are convolved. We use the same trick as above, namely transform to Laplace space, where a simple multiplication represents this convolution. We perform the Laplace transform with respect to $e_\gamma = 2(m_\chi - E_\gamma)$ (Laplace variable t). In the wino case, the convolution is resolved as

$$\begin{aligned}
&\mathcal{L}\left[\int_0^\infty d\omega\, J^{\text{SU}(2)}_{\text{int}}(2m_\chi(e_\gamma-\omega))\, W^{\text{wino},ij}_{IJ}(\omega)\right] \\
&= \int_0^\infty de_\gamma\, e^{-te_\gamma}\int_0^\infty d\omega\, J^{\text{SU}(2)}_{\text{int}}(2m_\chi(e_\gamma-\omega))\, W^{\text{wino},ij}_{IJ}(\omega) \\
&= \int_0^\infty \frac{dp^2}{2m_\chi}\, e^{-tp^2/2m_\chi} J^{\text{SU}(2)}_{\text{int}}(p^2)\int_0^\infty d\omega\, e^{-t\omega}\, W^{\text{wino},ij}_{IJ}(\omega) \\
&= \frac{1}{2m_\chi}\, j^{\text{SU}(2)}_{\text{int}}\left(\ln\frac{2m_\chi}{te^{\gamma_E}\mu^2}\right) w^{ij}_{IJ}(t)\,.
\end{aligned} \tag{7.69}$$

Furthermore, we substitute $p^2 = 2m_\chi(e_\gamma-\omega) \geq 0$ in the third line and omitted resummation scales for brevity. Using the Laplace transform above, the consistency relations for the wino read

$$\frac{d}{d\ln\mu}\left[\vec{H}(\mu)\cdot\vec{w}_{IJ}(t,\mu,\nu)Z_\gamma(\mu,\nu)j^{\text{SU}(2)}_{\text{int}}\left(\ln\frac{2m_\chi}{te^{\gamma_E}\mu^2},\mu\right)\right] = 0 \tag{7.70}$$

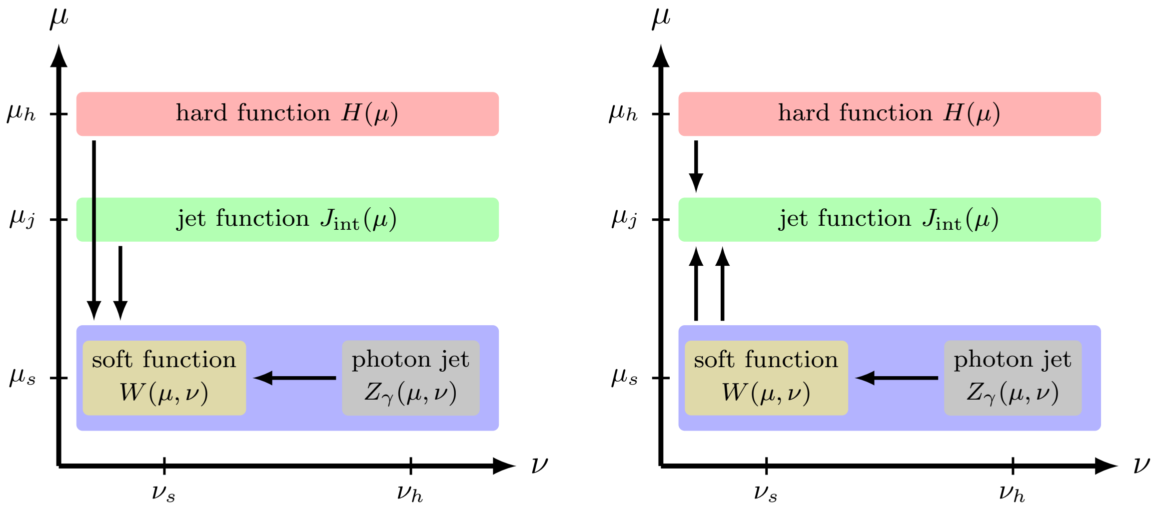

Figure 7.3: *Schematics of the resummation paths for the intermediate resolution case in virtuality μ and rapidity ν. Two possible resummation schemes, hereafter, scheme 1 (left) and 2 (right) are shown.*

$$\frac{d}{d\ln\nu}\left[\vec{H}(\mu)\cdot\vec{w}_{IJ}(t,\mu,\nu)Z_\gamma(\mu,\nu)j_{\rm int}^{\rm SU(2)}\left(\ln\frac{2m_\chi}{te^{\gamma_E}\mu^2},\mu\right)\right]=0 \tag{7.71}$$

where we used $\vec{H}=\left(|C_1|^2,C_2^*C_1,C_1^*C_2,|C_2|^2\right)^T$ and $\vec{w}_{IJ}=\left(w_{IJ}^{11},w_{IJ}^{12},w_{IJ}^{21},w_{IJ}^{22}\right)^T$. Similarly, the consistency relation for the intermediate resolution Higgsino calculation can be derived (albeit with a few more functions). In practice, the consistency relations require that the sum of all anomalous dimensions in Laplace space has to vanish order by order in perturbation theory. This has to hold for virtuality and rapidity anomalous dimensions separately

$$\sum_i\gamma_i^\mu=0\quad\text{and}\quad\sum_i\gamma_i^\nu=0 \tag{7.72}$$

where i runs over the elements of the factorization theorem. In the narrow resolution case, as there is only a trivial convolution, the requirements Eq. (7.68), directly lead to consistency relations. However, the sum of all anomalous dimensions still needs to cancel order by order in perturbation theory. For a more in-depth investigation, see Section 3.5 of [101] and especially [149] Section 6.5, where the relations in each resolution case are spelt out for both wino and Higgsino.

Beyond the wino/Higgsino case, for minimal DM, the consistency equations also allow to derive the renormalization group equations up to NLL and ultimately determine all factors without an additional loop calculation. The recoiling and photon jet functions are associated with the operators' final states and do not depend on the DM representation or hypercharge. The only two matrix-valued functions are the hard and soft functions. Due to the knowledge of the hard coefficients for arbitrary SU(2) representation and hypercharge, we can thereby bootstrap the soft anomalous dimension using consistency relations. Therefore, in the end, only a tree-level calculation of the soft function matrix element is necessary to generalize the above results to arbitrary minimal DM at NLL. The NLL' order would require the exact linear combination of soft function integrals, dependent on the SU(2) representation and hypercharge.

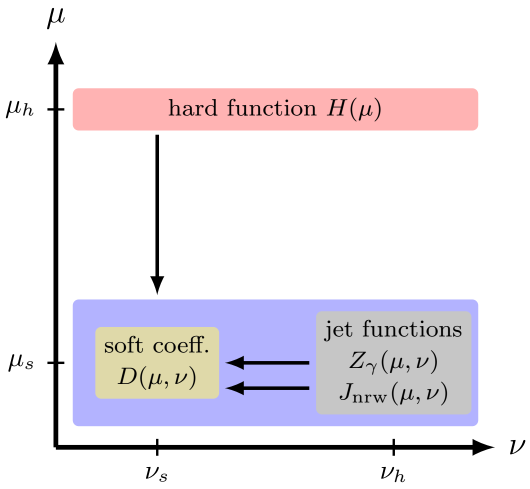

Figure 7.4: *Schematics of the resummation path for the narrow resolution case in virtuality μ and rapidity ν (details see text).*

7.6 Resummation schemes

In this work and the corresponding papers, two resummation schemes are investigated for the intermediate resolution calculation. The schematics of resummation in both schemes is shown in Figure 7.3. In resummation scheme 1 (left panel), all functions are evolved in virtuality to the soft scale $\mu_s \sim m_W$. In addition, the rapidity scale of the photon jet $\nu_h \sim 2m_\chi$ is evolved to the soft function rapidity scale $\nu_s \sim m_W$. At the NLL' order in this resummation scheme, non-trivial convolutions between the resummed intermediate resolution jet and the fixed order one-loop soft function contributions arise, which present the main challenge in numerical implementation of the results (cf. Section 7.7).

The second possibility for the resummation scheme, hereafter resummation scheme 2, is depicted in the right panel of Figure 7.3. In this more conventional scheme, all functions are resummed to the intermediate virtuality scale of the recoiling jet function $\mu_j \sim \sqrt{2m_\chi m_W}$. The rapidity scales are resummed as in resummation scheme 1. In practice, the difficulty for a code implementation at NLL' order lies in the convolutions between recoiling jet and soft functions, where the recoiling jet function one-loop contributions remain unresummed.

The precise form of the rapidity evolution factors and the virtuality resummation factors involving a rapidity scale (cf. Section 7.3) depends on the order of resummation in resummation scheme 2. Technically, we find it simpler to first resum in rapidity and only afterwards in virtuality. In practice, this means that the rapidity evolution factors enter at NLL order, whilst virtuality resummation for all functions starts at LL. In resummation scheme 1, as none of the rapidity dependent functions is evolved in virtuality, the order between rapidity and virtuality resummation can be interchanged without affecting the outcome (rapidity resummation starts naturally at NLL in this scheme).

In the end, regardless of the resummation scheme chosen, we find that the numerical differences at NLL' are of $\mathcal{O}(0.1\%)$ in both wino and Higgsino calculation, meaning below expected uncertainties from higher orders, power corrections and so on. The origin of this agreement on permille and sub permille level was investigated with a logarithmic expansion to two-loops for the wino in [101].

For the narrow resolution calculation, the recoiling jet function is of the same virtuality as the soft coefficients, meaning there are only two natural virtuality scales in the factorization theorem, i.e., the hard μ_h and soft μ_s virtuality. The resummation path chosen is shown in Figure 7.4. The hard function is evolved in virtuality to the soft-scale, and the photon and the recoiling jet function resummed to the soft rapidity scale. Note that rapidity resummation starts again at NLL, and rapidity/virtuality resummation can be interchanged at will, as for resummation scheme 1 above.

7.7 NLL' resummation intermediate resolution - an example

In practice, the implementation of the intermediate resolution case into code is more challenging, even though, at first glance, the corresponding functions look equally complicate, or in the case of the recoiling jet function, even simpler than their narrow counterparts. The reason for this additional complexity lies in the convolution between soft and recoiling jet function in the intermediate resolution case. In contrast, in the narrow resolution case, there is no such non-trivial convolution.

It is convenient not to work with the differential cross-section for numerical purposes but with the cumulative counterpart. The differential cross-section is distributional valued in terms of delta, star, log-star, double-star distributions, making it hard to represent the results numerically. Therefore, it is convenient, in numerics, to consider the integrated cross-section and, if a differential result is desired, to interpolate the cumulative cross-section for various values of photon energy and take the derivative on this interpolation. Thereby, we circumvent the issue of how to handle the distributions numerically. The problem only arises at NLL', where the rich structure in terms of hypergeometric functions, derivatives in η, distributions, and so on leads to various complications.

In the following, we discuss an instructive example on the intermediate resolution convolutions that arises in the second resummation scheme discussed above and is analytically solvable. In general, if the hypergeometric functions (cf. Eq. (7.65)) are involved, this is not possible analytically. At least one of the integrals, either in $d\omega$ or dE_γ has to be performed numerically. As an example, we present the following convolution

$$f(E^\gamma_{\text{res}}) = \int_{m_\chi - E^\gamma_{\text{res}}}^{m_\chi} dE_\gamma \int_0^{2(m_\chi - E_\gamma)} d\omega \left[\frac{e^{-\gamma_E \eta}}{\Gamma(\eta)} \frac{1}{\omega} \left(\frac{\omega}{\nu_s}\right)^\eta\right] \cdot \left[\frac{\ln \frac{p^2}{\mu_j^2}}{p^2}\right]_*^{[\mu_j^2]} \tag{7.73}$$

with $p^2 = 4m_\chi(m_\chi - E_\gamma - \omega/2)$ and η as defined in Eq. (7.34), assumed to be positive. Other structurally more complicated and only numerically possible convolutions are evaluated in analogy. In the appearing convolutions, it is typically useful to disentangle one function from one of the integrals (though in the case discussed here, not necessary) using the geometric identity

$$\int_0^a dy \int_0^y dx f(y-x) g(x) \quad \overset{x'=x,\underline{y'}=y-x}{=} \quad \int_0^a dy' f(y') \int_0^{a-y'} dx' g(x') \, . \tag{7.74}$$

By the above reasoning the integral in ω can be performed, and we find ($\tilde{E}_\gamma = m_\chi - E_\gamma$)

$$f(E^\gamma_{\text{res}}) = \frac{\left(\frac{2E^\gamma_{\text{res}}}{\nu_s e^{\gamma_E}}\right)^\eta}{4m_\chi \Gamma(1+\eta)} \left\{ \int_0^{E^\gamma_{\text{res}}} d\tilde{E}_\gamma \left[\frac{\left(1 - \frac{\tilde{E}_\gamma}{E^\gamma_{\text{res}}}\right)^\eta - 1}{\tilde{E}_\gamma} \ln \frac{4m_\chi \tilde{E}_\gamma}{\mu_j^2}\right] + \frac{1}{2} \ln^2 \frac{4m_\chi E^\gamma_{\text{res}}}{\mu_j^2} \right\} \, . \tag{7.75}$$

The remaining integral can also be evaluated analytically. Combining all factors, we find a compact expression in terms of logarithms and Polygamma functions $\psi^{(m)}(x) = \frac{d^{m+1}}{dx^{m+1}} \ln \Gamma(x)$, where $\Gamma(x)$ is the ordinary Gamma function

$$f(E^\gamma_{\text{res}}) = \frac{1}{8m_\chi\Gamma(1+\eta)}\left(\frac{2E^\gamma_{\text{res}}}{\nu_s}\right)^\eta \left[\left(\psi^{(0)}(\eta+1) - \ln\frac{4m_\chi E^\gamma_{\text{res}}}{\mu_j^2 e^{\gamma_E}}\right)^2 - \psi^{(1)}(\eta+1) + \frac{\pi^2}{6}\right] . \tag{7.76}$$

Finally, one might be tempted to declare the first resummation scheme of Section 7.6 simpler, as naively no hypergeometric functions appear, as the soft function remains unresummed. However, the hypergeometric structures arise after performing the ω, E_γ-integrals, and are not simpler than in the second resummation scheme. Consider, for example, the convolution

$$g(E^\gamma_{\text{res}}) = \int_{m_\chi - E^\gamma_{\text{res}}}^{m_\chi} dE_\gamma \int_0^{2(m_\chi - E_\gamma)} d\omega \left[\frac{1}{\omega}\ln\left(\frac{m_W^2+\omega^2}{m_W^2}\right)\right]\cdot\left[\frac{e^{-\eta\gamma_E}}{\Gamma(\eta)}\frac{1}{p^2}\left(\frac{p^2}{\mu_j^2}\right)^2\right] \tag{7.77}$$

with p^2 as defined above. Using again the geometric identity above, we can perform the ω-integral and find

$$g(E^\gamma_{\text{res}}) = \int_0^{E^\gamma_{\text{res}}} d\tilde{E}_\gamma \left(\frac{\left(\frac{4m_\chi\tilde{E}_\gamma}{\mu_j^2 e^{\gamma_E}}\right)^\eta \tilde{E}_\gamma}{m_\chi m_W^2 \Gamma\left(2+\eta\right)}\right) {}_4F_3\left(1,1,1,\frac{3}{2};1+\frac{\eta}{2},\frac{3+\eta}{2},2;-\left(\frac{2\tilde{E}_\gamma}{m_W}\right)^2\right) \tag{7.78}$$

which is a similar hypergeometric function to the one arising in the soft function calculation, cf. (7.65). Thereby, the first resummation scheme is not considerably simpler than the second resummation scheme, and in both cases, at least some convolutions have to be performed numerically.

8

Endpoint spectrum for $\chi\chi \to \gamma + X$

In this Chapter, we present the endpoint spectra for both wino and Higgsino dark matter annihilation, using the results of the previous Chapters for the NLO potentials (Chapters 3, 4) and the Sudakov logarithm resummation (Chapters 6, 7). Furthermore, we extend the results by matching to the `PPPC4DM` [175], which extends our result beyond the vicinity of the endpoint, thereby allowing us to provide the complete differential spectrum for both models. The differential cross-sections are suited as an input for future data analyses at indirect detection experiments, such as CTA [66, 67, 113], and many others.

Throughout this Chapter, we use the numerical values for couplings and masses already given in Chapter 3. Additionally, we use $\hat{\alpha}_3(m_Z) = 0.1181$, $\hat{\lambda}_t(m_Z) = 0.952957$, $\hat{\lambda}(m_Z) = 0.132944$ as input parameters for the necessary two-loop running couplings, and the $\overline{\text{MS}}$-top mass $\overline{m}_t(\overline{m}_t) = 163.35\,\text{GeV}$ (corresponding to the top pole mass $m_{t,\text{os}} = 173.1\,\text{TeV}$ at four loops), in the resummation calculation.[1] Furthermore, as discussed in Section 4.4, the Higgsino dark model requires two mass splittings to remain a viable dark matter candidate. For concreteness, we fix these to $\delta m = \alpha_{\text{em}} m_Z/2 \approx 355\,\text{MeV}$ and $\delta m_N = 20\,\text{MeV}$. The former mass splitting is taken at the value expected by one-loop radiative corrections (cf. Appendix A.1.3 and [176]). The latter is chosen so that it is large enough to evade direct detection bounds and inhibit $\chi_2^0\chi_2^0$ from being an on-shell state for typical galactic velocities $v \sim 10^{-3}$. Furthermore, it is also small enough that the mixing into δm via dimension-5 operators is expected to be small. The Sudakov resummation is unaffected by the chosen mass splittings. The Sommerfeld enhancement calculation and the resulting resonance positions depend on the chosen values. We use a DM velocity of $v = 10^{-3}$ for all plots. However, the resulting shifts apply equally to LO and NLO Sommerfeld factors, therefore not affecting the overall results of Sudakov resummation. For a discussion of the implications on Higgsino model building and the mass splitting dependence, see [177].

All plots and numerical results are generated with a private `Mathematica` code written by the author. To ensure a blind check, each result generated by the code was compared, with an independent implementation by one of the authors' collaborators. The Sommerfeld factor code was compared with corresponding implementations of M. Beneke and M. Vollmann. The narrow resolution codes originally were written and compared between C. Hasner and M. Vollmann. The narrow resolution code of M. Vollmann was adapted by the author and substantially modified with regards to performance and cross-compatibility with the intermediate resolution code. Furthermore, the authors' code also includes the Dyson resummation of the Z-threshold for the narrow resolution recoiling jet, which remains the only non-double checked module. The

---

[1] The values in this thesis are updated with respect to the corresponding publications [100, 101, 102], namely the $\overline{\text{MS}}$-Weinberg angle Eq. (3.36), which leads to slightly different numerical values. The change is practically invisible on the typical logarithmic scale of the plots.

implementation of the intermediate resolution case has been checked between C. Hasner and the author. Finally, the results for the `PPPC4DM` matching and modification, as discussed in Appendix F, were compared between M. Vollmann and the author.

The code includes two resummation schemes for the intermediate resolution Sudakov annihilation rate. Both agree, within 0.1% for NLL' accuracy. The reason for this excellent agreement was investigated in [101] for the wino model, expanding the logarithmic results to two loops. For concreteness in this Chapter, we use the second resummation scheme of Section 7.6 for intermediate resolution results.

Finally, we use the NLO potential prediction throughout this Chapter, unless remarked otherwise, thereby providing the most precise predictions for the observables discussed to date. The analogues for the energy spectrum and cumulative cross-section plots using the LO potential for the Sommerfeld enhancement prediction can be found in [100, 101] for the wino and in [102] for the Higgsino model.

8.1 Wino endpoint spectrum

We begin the analysis of the numerical results by considering the cumulative endpoint cross-section, defined as the differential cross-section integrated over a bin of size E^γ_{res} from the endpoint

$$\langle \sigma v \rangle \left(E^\gamma_{\text{res}}\right) = \int_{m_\chi - E^\gamma_{\text{res}}}^{m_\chi} dE_\gamma \, \frac{d(\sigma v)}{dE_\gamma} \,. \tag{8.1}$$

In Figure 8.1, we show the numerical values for a mass range of $m_\chi = (0.5 - 20)$ TeV, which covers the thermal mass and also the window of interest for the narrow and intermediate resolution regimes in view of the projected CTA resolution (cf. Figure 2.2). The plot is generated using the intermediate resolution regime and $E^\gamma_{\text{res}} = m_W$. However, it looks similar for different E^γ_{res} or using the narrow resolution calculation with overall magnitude changes. The upper panel of the figure shows the cross-section prediction. As already outlined in the earlier discussion, one can recognize the characteristic first two Sommerfeld resonances (cf. Section 3.5). As seen there, the resonances are shifted from 2.283 (8.773) TeV to 2.419 (9.355) TeV, for first and second resonance, respectively.

The black/dotted line represents the tree-prediction, which refers to Γ_{IJ} in the tree-level approximation, meaning no resummation effects taken into account. As an indication, we also show the tree result using LO Sommerfeld factors (solid/light-grey), which is a result known in the literature [74] by now over 15 years. Furthermore, the other lines show the various resummation levels LL, NLL and NLL', which generically are suppressed with respect to the naive tree-level prediction. The error bands are extracted using a conservative procedure by simultaneously varying the resummation scales within factors of two around their central values. We distribute 21 points logarithmically between $[1/2\mu_{\text{central}}, 2\mu_{\text{central}}]$ (ten points above and below the central value, respectively), where μ_{central} is one of the resummation scales. Using this procedure, we create a 21^5 point grid for each mass value, from which we extract the maximal and minimal value as the error bands.

To better assess the Sudakov resummations overall effect, we show the ratio of cross-sections in the various resummation approximations to the tree prediction in the lower panel (all curves using NLO Sommerfeld effect). In this way, the effect of the Sommerfeld factors is subtracted,[2] and the Sudakov resummation effect size are separately visible. We observe the characteristic

---

[2] A full separation of both effects is, of course, not possible, as it is the Sommerfeld factors S_{IJ}, that give access to the resummed matrix elements other than $\Gamma_{(00)(00)}$. However, the ratio effectively refers to $\sum_{IJ}(S_{IJ}\Gamma^{\text{res.}}_{IJ})/(S_{IJ}\Gamma^{\text{tree}}_{IJ})$

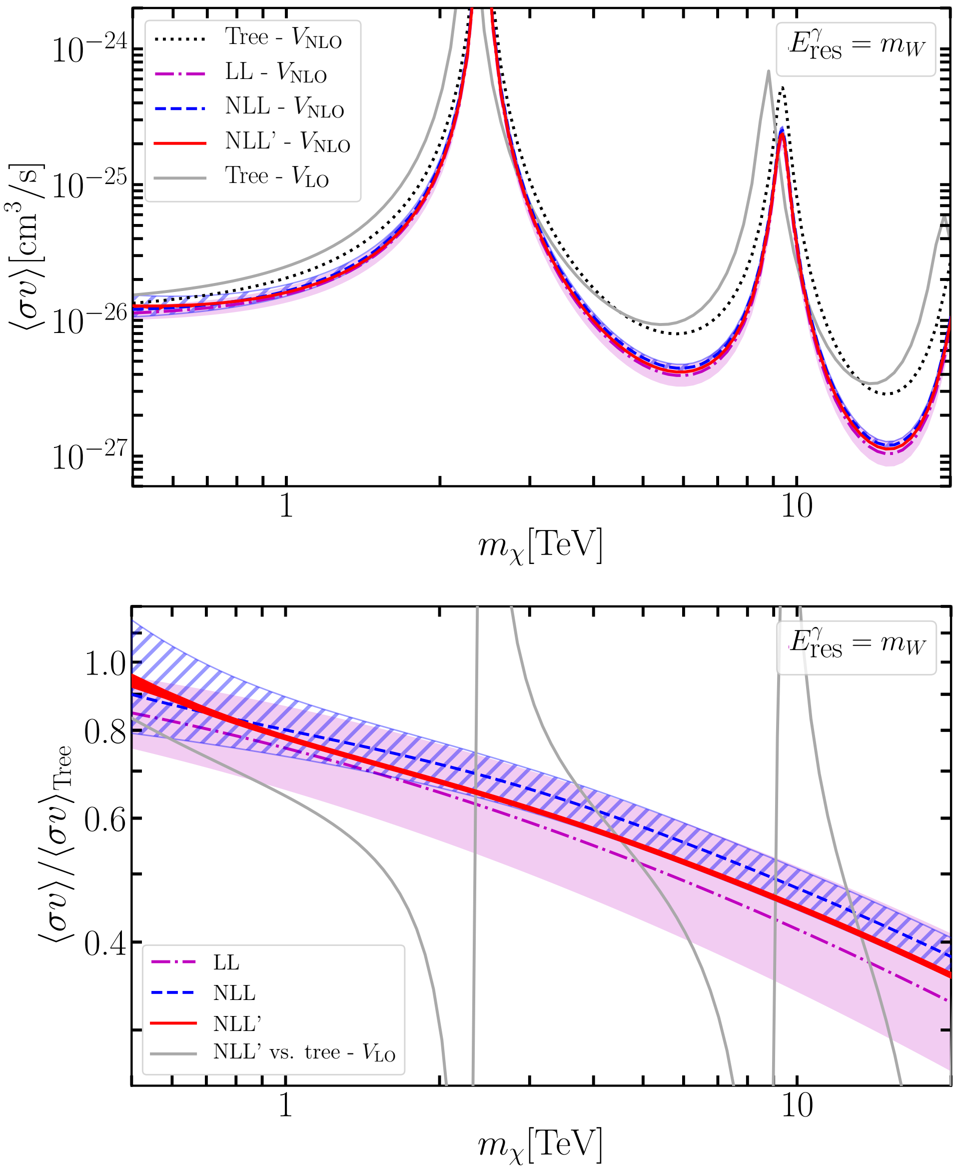

Figure 8.1: *The cumulative cross-section* (8.1) *as a function of mass* m_χ *for an energy resolution* $E^\gamma_{\rm res} = m_W$*. The lines show the LL (purple/dash-dotted), NLL (blue/dashed), NLL' (red/solid) resummed predictions. As an indication also the unresummed tree-level predictions using the NLO potential (black/dotted) and LO potential (solid/light-grey) are shown. The error bands are given by the hatched/shaded regions and extracted as described in the text. For the NLL' resummed prediction, the uncertainty band is given by the thickness of the red line.*

Sudakov suppression of the cross-section for all resummation levels. As expected, the effect is larger for high masses, as the resummed logarithms depend on the DM and electroweak mass scale ratio. The size of the error bands is successively reduced in the transition from LL → NLL → NLL', e.g. for $m_\chi = 2\,\text{TeV}$ from $16\,\% \to 7\,\% \to 1\,\%$.

The effect is sizeable, reaching from a $5-10\%$ suppression for the lowest mass values depicted to suppression by more than a factor of two for masses of 10 TeV and higher. At the mass value

---

meaning that both tree and resummed expressions are weighed by the same factors, giving a good indication on the resummation effects. The ratios are similar for LO, and NLO potentials which confirms this point.

2.842 TeV for which the wino would constitute all of DM if produced via thermal freeze-out, derived in Chapter 5, the logarithmic resummation at NLL' reduces the cross-section by 37 % for $E^{\gamma}_{\text{res}} = m_W$ or 49 % for $E^{\gamma}_{\text{res}} = m_W^2/m_\chi$.

Finally, let us point to the (solid/light-grey) line in the lower panel that depicts the ratio of the NLL' prediction (without error bands) to the tree-level result using the LO potential, previously in the literature [74]. The effect is significant over practically the entire mass range under consideration. It emphasizes the need for both NLO potential and Sudakov resummation to obtain an accurate prediction for the cross-section $\chi^0\chi^0 \to \gamma + X$.

To make this more quantitative, we find for the two mass values 2 TeV (10 TeV) the ratio to the tree-only rate is $0.653^{+0.112}_{-0.095}$ ($0.417^{+0.095}_{-0.077}$) at LL, $0.717^{+0.053}_{-0.053}$ ($0.477^{+0.031}_{-0.033}$) at NLL, and $0.676^{+0.007}_{-0.005}$($0.448^{+0.005}_{-0.004}$) at NLL'. To investigate the contribution of individual terms to the final cross-section prediction, we consider

$$\langle\sigma v\rangle = 2\times\Big[\mathbf{S}_{\mathbf{(00)(00)}}\,[\sigma v]_{(00)(00)} + 2\,\mathrm{Re}\Big[\mathbf{S}_{\mathbf{(00)}(+-)}\,[\sigma v]_{(00)(+-)}\Big] + \mathbf{S}_{(+-)(+-)}\,[\sigma v]_{(+-)(+-)}\Big] \tag{8.2}$$

where we define

$$[\sigma v]_{IJ}\,(E^{\gamma}_{\text{res}}) = \int_{m_\chi - E^{\gamma}_{\text{res}}}^{m_\chi} dE_\gamma\,\Gamma_{IJ}(E_\gamma)\,. \tag{8.3}$$

At $m_\chi = 2$ TeV ($E^{\gamma}_{\text{res}} = m_W$) with Sommerfeld factors in bold, we have

$$\begin{aligned}\langle\sigma v\rangle = 2\times\Bigg[\Bigg[&\left\{\begin{array}{l}\mathbf{34.246}\\ \mathbf{17.085}\end{array}\right. \times 1.1552 + 2\,\mathrm{Re}\Bigg[\Bigg[\left\{\begin{array}{l}\mathbf{42.101}\\ \mathbf{20.025}\end{array}\right. \times(-0.8718+5.4288i)\Bigg]\Bigg]\\ &+\left\{\begin{array}{l}\mathbf{51.756}\\ \mathbf{23.469}\end{array}\right. \times 29.242\Bigg] \times 10^{-28}\text{cm}^3/\text{s} = \left\{\begin{array}{l}2.9592\\ 1.3442\end{array}\right. \times 10^{-25}\text{cm}^3/\text{s}\,,\end{aligned} \tag{8.4}$$

where the upper/lower line corresponds to the LO/NLO potential prediction. Regardless of Sommerfeld calculation, the (00)(00) terms make up $\sim 3\%$, the (00)(+−) terms $\sim -5\%$, and the (+−)(+−) terms $\sim 102\%$ of the cross-section prediction. The terms contribute similarly at other values of E^{γ}_{res}, also using the narrow resolution prediction. The Sommerfeld factors are all of the same order. Therefore the cross-section prediction is dominated by the double-logarithmic suppression of the $\Gamma_{(+-)(+-)}$ matrix element, which is the only one to start at LO. For lower masses, the picture is different, as the Sommerfeld effect is less strong, leading to hierarchy in the Sommerfeld matrix elements. For $m_\chi = 500$ GeV, we have

$$\begin{aligned}\langle\sigma v\rangle = 2\times\Bigg[\Bigg[&\left\{\begin{array}{l}\mathbf{1.1345}\\ \mathbf{1.1186}\end{array}\right. \times 1.1159 + 2\,\mathrm{Re}\Bigg[\Bigg[\left\{\begin{array}{l}\mathbf{0.35103}\\ \mathbf{0.32519}\end{array}\right. \times(-0.8969+7.2167i)\Bigg]\Bigg]\\ &+\left\{\begin{array}{l}\mathbf{0.10861}\\ \mathbf{0.09453}\end{array}\right. \times 60.676\Bigg] \times 10^{-27}\text{cm}^3/\text{s} = \left\{\begin{array}{l}1.4453\\ 1.2802\end{array}\right. \times 10^{-26}\text{cm}^3/\text{s}\,.\end{aligned} \tag{8.5}$$

The importance of the terms has changed considerably compared to the former case. For $m_\chi = 500$ GeV, the (00)(00) elements contribute with 18% (20%) at LO (NLO) in the Sommerfeld calculations. The (00)(+−) elements contribute with −8% (−9%), and the (+−)(+−) element 91% (90%).

The above values and plots were all extracted for a fixed energy resolution E^{γ}_{res} and varying DM mass m_χ. It is only natural to consider the opposite situation, namely, fix the DM mass and vary the energy resolution, i.e., the detector bin size. In Figure 8.2, we show the cumulative cross-section as a function of the detector resolution E^{γ}_{res}. We depict the narrow (blue/dotted)

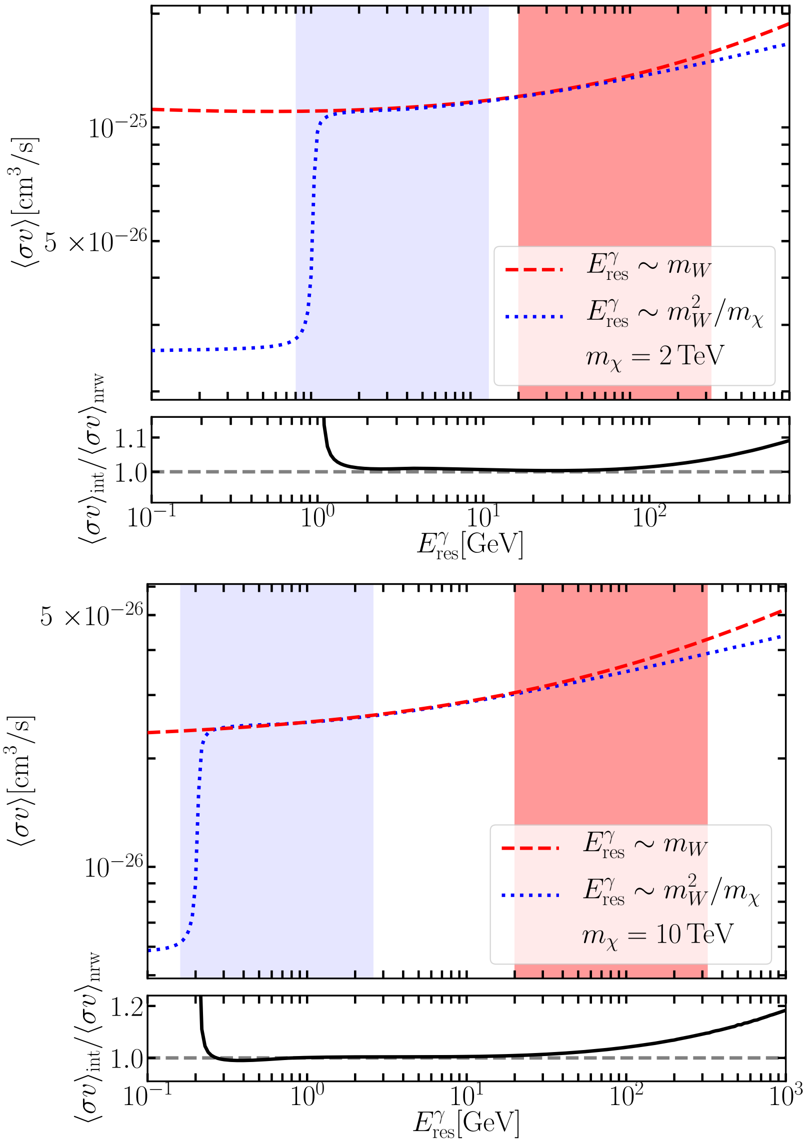

Figure 8.2: *Cumulative cross-section Eq.* (8.1) *for the masses* $m_\chi = 2\,\mathrm{TeV}$ *(lower panel), and* $m_\chi = 10\,\mathrm{TeV}$ *(upper panel), for central values of all resummation scales. The blue/dotted line corresponds to the narrow-resolution prediction, whilst the red/dashed line is the value extracted using the intermediate resolution EFT. The shaded areas represent the estimated regions of validity of the corresponding EFTs (more details in the text), with the color-coding as blue (light-grey) for the narrow resolution EFT and red (dark-grey) for the intermediate resolution EFT. The subtended panel shows the ratio of intermediate to narrow cross-section prediction.*

and intermediate (red/dashed) resolution predictions and indicate their parametric, i.e. by power-counting, expected validity regions by the respective shaded areas. These are chosen as $[m_W/4, 4m_W]$ for the intermediate resolution calculation, and $[m_W^2/(4m_\chi), 4m_W^2/m_\chi]$ in the narrow resolution case. In fact, the narrow resolution calculation also extends to smaller resolutions, all the way down to $E^{\gamma}_{\mathrm{res}} \to 0$, as long as we can ignore light fermion masses.[3]

---

[3] At some point, the effective theory would need to be matched onto a theory containing massive light quarks and leptons. Conceptually though, this is straightforward and would only modify the unobserved narrow resolution

We observe for both mass values, depicted in Figure 8.2, that the narrow and intermediate resolution prediction match nicely for an extended region above the γZ-threshold. More quantitatively, this is also visualized by the subtended ratio plot. For an extended region, of about two orders of magnitude for $m_\chi = 2\,\mathrm{TeV}$ $(10\,\mathrm{TeV})$, the two calculations stay close. The steep rise in the prediction at $E^\gamma_{\mathrm{res}} = m_Z^2/(4m_\chi^2)$ is due to γZ becoming kinematically possible inside the energy bin. We use the Dyson resummed recoiling jet to produce the prediction, as the fixed order result is ill-defined at threshold, as described in detail in Section 7.2.2. In principle, the narrow resolution calculation also passes through the thresholds for $W^+W^-, ZH, t\bar{t}$. As these channels open up only at NLO and further the plot shows the integrated cross-section, these are not visible on the scale of the plot.

In contrast, the intermediate resolution calculation, which is not sensitive to any masses in the recoiling jet function, is clearly not applicable below the γZ-threshold.[4] However, it still provides an accurate prediction well into the narrow resolution regime, as does the narrow calculation for most of the region of validity of the intermediate resolution calculation. Even beyond the validity of the intermediate calculation, e.g., for the highest value depicted $E^\gamma_{\mathrm{res}} = 1\,\mathrm{TeV}$, the two calculations only differ by $\mathcal{O}(10\,\%)$. Whilst this is somewhat expected for lower masses, as the regions of validity are close to each other, matching the predictions also works for higher masses. For those, the regions of validity are well separated, e.g., in the lower panel of Figure 8.2. In fact, this suggests that we can merge the two calculations, providing an accurate prediction, from the endpoint to at least $E^\gamma_{\mathrm{res}} = 4m_W$. Such a merging procedure is described in Appendix F, together with a merging procedure to the EW parton shower calculation provided with the `PPPC4DM`-package [175].

Finally, we take a look at the differential spectrum $d(\sigma v)/dx$, where x is defined as $x = E_\gamma/m_\chi$. To create this spectrum, we use the above cumulative prediction, construct an interpolating function from it, and then finally take the derivative. The reason why we do not directly use the differential prediction, as provided by our factorization formula, lies in the fact that the appearing delta and star-distributions are somewhat hard to handle in numerical calculations, which we circumvent by using the above procedure. Let us note that the procedure is a mere convenience choice and not a conceptual limitation. With additional effort, the direct use of the factorization formula in the numerical code should be possible.

In Figure 8.3, we show the differential prediction using NLL' resummation and the NLO potentials for a selection of mass values. The plots show, the narrow resolution differential spectrum in blue/dash-dotted, the intermediate resolution prediction in red/dotted and the `PPPC4DM` [175] implemented as in Appendix F in teal/solid. The merged prediction of the three regimes is shown in green/dashed. The spectra can be integrated to obtain the cumulative predictions, similar to Figure 8.2. However, we note that the "zeroth"-bin would need to be added due to delta-function contribution from the $\gamma\gamma$-final state and the respective virtual corrections to this final state.

---

recoiling jet function. The procedure would be similar to the corresponding modifications for the NLO potential, cf. Section 3.4.1. The regime, where the first modifications are expected, starts around $E^\gamma_{\mathrm{res}} \sim m_b^2/m_\chi^2$, i.e., around the threshold for a photon splitting into $b\bar{b}$, meaning about two orders of magnitude in E^γ_{res} below the γZ-threshold. Note that our prediction, due to the massless light-fermions, suffers from a log-divergence, for $E^\gamma_{\mathrm{res}} \to 0$, which, however, is very mild and would be cured by matching onto theories with massive light fermions.

[4] Additional, to the missing sensitivity to the γZ-threshold, for very small E^γ_{res} also the resolution-dependent logarithms in the intermediate resolution calculation become inaccurate. Using a log-expansion to two-loops, the functions $\theta_{f_R}, \varphi_{f_R}, \lambda_R, \kappa_R$ vanish for $E^\gamma_{\mathrm{res}} \to 0$, the logarithm l_R changes sign at $2E^\gamma_{\mathrm{res}}/m_W = 1$, and logarithmically diverges for $E^\gamma_{\mathrm{res}} \to 0$. At some point, this leads to an increasing cross-section prediction for smaller bin size, which is, of course, unphysical, though never relevant, as it happens typically below the γZ-threshold, where the narrow resolution calculation is to be applied. For more details and the definition of the functions, see the logarithmic expansion to two-loops in [101].

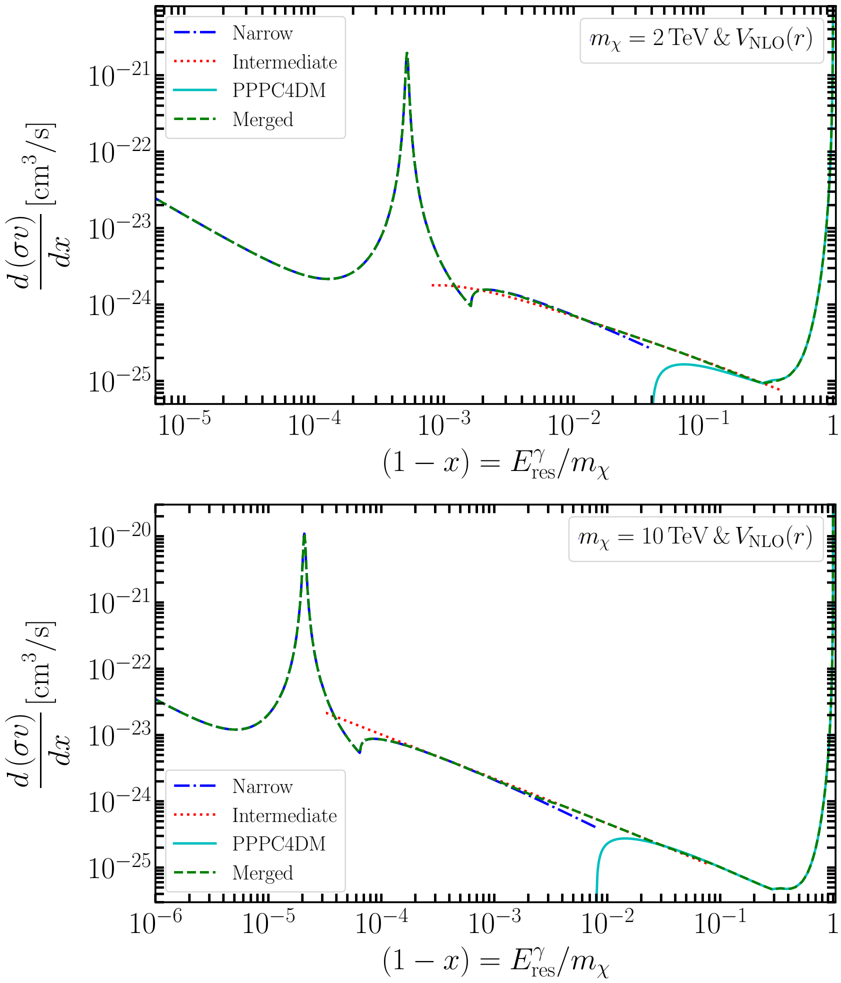

Figure 8.3: *Differential spectra* $\frac{d(\sigma v)}{dx}$ *as function of* $(1-x) = E^{\gamma}_{\text{res}}/m_\chi$ *for DM masses of* $m_\chi = 2\,\text{TeV}$ *and* $10\,\text{TeV}$*. In addition to the merged spectrum (green/dashed), as described in the text, we also show the narrow (blue/dash-dotted), intermediate (red/dotted), and* `PPPC4DM` *prediction (teal/solid) from which the merged spectrum was created.*

Starting from the right, i.e., for small $1-x$, we observe the rising differential cross-section towards the endpoint, that originates from light-fermionic splittings, i.e., $\chi\chi \to \gamma f \bar{f}$. Then at $1-x = m_Z^2/(4m_\chi^2)$, we recognise the Dyson resummed γZ final state, entering the spectrum. Following this, at $1-x = m_W^2/m_\chi^2$, there is a kink in the narrow and merged spectra. This kink arises from the onset of the γW^+W^- final state. In principle, at $1-x = (m_Z+m_H)^2/(4m_\chi^2)$ and m_t^2/m_χ^2, also the γZH and $\gamma t\bar{t}$-final states enter the spectrum. However, even zooming into the respective regions, it is tough to see respective kinks, as their contribution is tiny in comparison to the W^+W^- threshold.

The intermediate resolution spectrum is not sensitive to any recoiling jet masses, i.e., no such thresholds are seen. However, the slope encodes the aforementioned particles in the recoiling jet splittings (now taken as massless) and further allows for soft isotropic W-boson radiation. Finally, in the `PPPC4DM` [175], the full electroweak collinear splittings, multiplied on the tree-level annihilation matrices into $W^+W^-, ZZ, \gamma Z$, and $\gamma\gamma$ contribute. For $x \to 1$, these diverge as expected for the fully inclusive DM annihilation spectrum. In the low mass regime between $500\,\text{GeV} - 1\,\text{TeV}$, the merging can look a bit odd to the human eye. However, as discussed in

Appendix F, this does not significantly affect the cumulative prediction integrated over a bin.

Let us mention, that a matching/merging into the wide resolution case $E^{\gamma}_{\text{res}} \gg m_W$, implemented in [98, 99], would be interesting as well, before matching onto the `PPPC4DM` prediction. However, given the expected resolutions for, e.g., CTA [112], this should only be relevant for $m_\chi \gtrsim 10\,\text{TeV}$ (cf. Figure 2.2). In any case, we would expect that the wide and intermediate calculation would match onto each other similar to the intermediate and narrow calculations, such that the errors by only using the `PPPC4DM` and our calculations should be small even beyond $m_\chi \gtrsim 10\,\text{TeV}$.

8.2 Higgsino endpoint spectrum

In a similar fashion to the above discussion for wino dark matter, the respective results can also be considered for Higgsino dark matter. We again start with the cumulative cross-section at an energy resolution of $E^{\gamma}_{\text{res}} = m_W$, shown in Figure 8.4. In contrast to the wino, the Sommerfeld enhancement is considerably weaker for the Higgsino. We can intuitively understand this considering the high-energy regime of the potentials that resembles QCD/QED. In this regime, the potentials and states can be diagonalized, similar to the singlet/octet decomposition in QCD, and their strength is proportional to the Casimir of the representation. For the SU(2)-part of the potentials, the Casimir invariant is $c_2(j) = j \cdot (j+1)$, with j the size of the multiplet. Meaning the high-energy potentials are quadratically dependent on the multiplet-size, i.e., neglecting hypercharge effects, the SU(2) potentials are four times stronger for the wino than for the Higgsino at small distances. Therefore, it is not surprising that the enhancement factors are roughly an order of magnitude smaller (away from resonance) than for comparable wino masses and that in the mass range from $(0.5 - 20)\,\text{TeV}$ only one resonance is seen. By a similar argument, the resummation effects are expected to be smaller for the Higgsino.

The corresponding ratio plot comparing to the tree-prediction is shown in the lower plot of Figure 8.4. For large mass values, the picture is similar to the wino. A generic suppression regardless of resummation level is seen. At low masses, the picture is completely different. The Sudakov suppression, still present for LL resummation, turns into an enhancement for the NLL and NLL' resummed predictions.

The reason for the low mass enhancement can be attributed to the interplay of two points. First, at large masses, as for the wino, the Sommerfeld elements S_{IJ} are all of similar size. Therefore, the $\Gamma_{(+-)(+-)}$ element, which is the only one to possess a tree-level contribution, dominates the annihilation rate. As the $(+-)(+-)$-term receives the standard double logarithmic suppression, the high mass annihilation cross-section is suppressed. At low masses, the Sommerfeld enhancement is considerably weaker, and the channels are not mixed democratically. The hierarchy between the Sommerfeld elements can therefore compensate for loop factors suppressing $(11/22)(11/22)$, and to a different extent $(11/22)(+-)$ channels, that start at higher-order in α_1 and α_2. This allows for partial cancellations and enhancements among the matrix elements.

The second reason for the enhancement behaviour is rooted in the size of Sudakov resummation. For small masses, i.e., smaller ratios of dark matter mass scale and electroweak scale, it is not guaranteed that the leading logarithms make up the dominant contribution to the cross-section. Furthermore, in the neutral annihilation channels, the leading logarithms are of positive sign, which can overwhelm the suppression in the $(+-)(+-)$ channel, and the negative interference in the $(11)(+-)$ and $(22)(+-)$ channels. Let us note that the effect only appears for the intermediate resolution calculation and the narrow resolution calculation above the γZ threshold, as discussed in detail below.

However, before proceeding with the discussion on the origin of the low-mass enhancement,

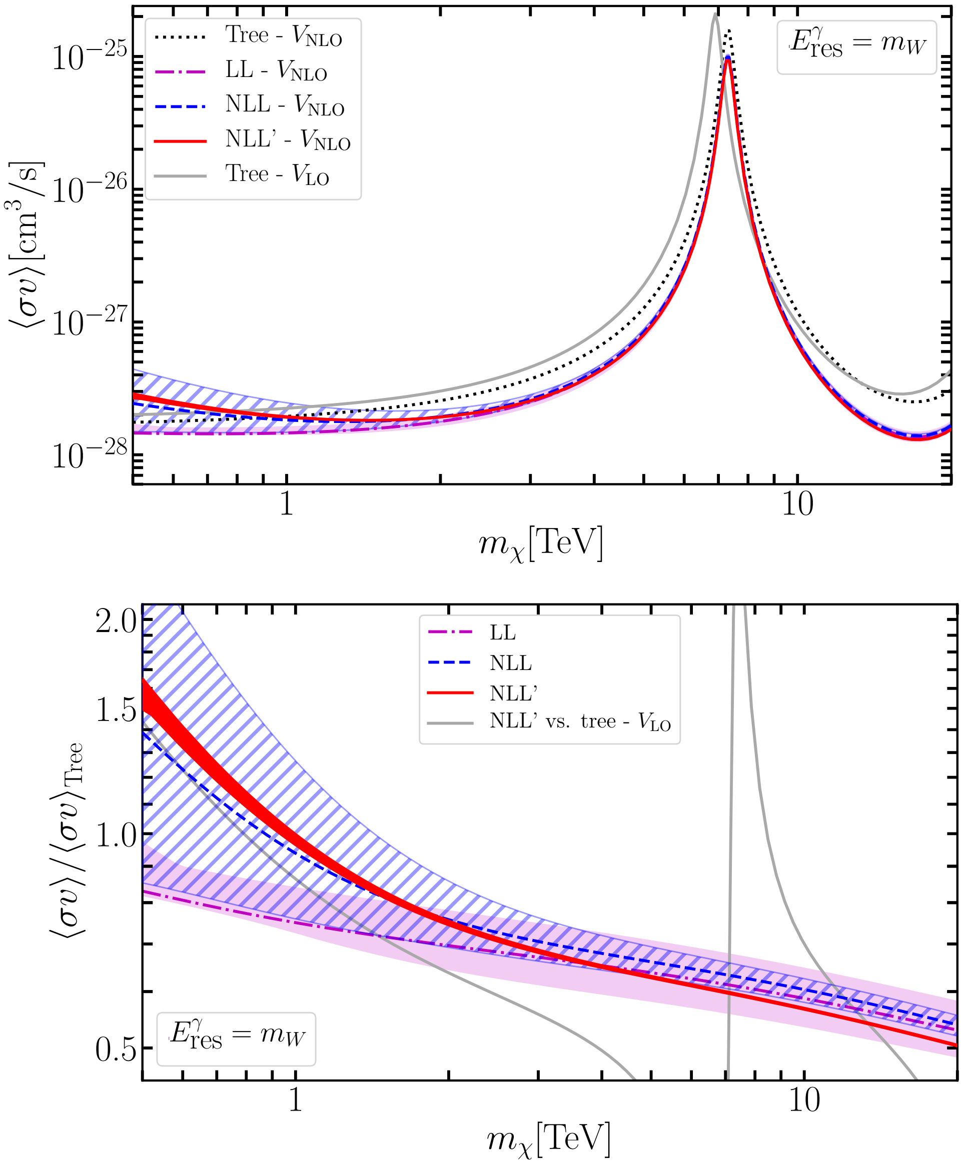

Figure 8.4: *The cumulative cross-section* (8.1) *as a function of mass m_χ for an energy resolution $E^{\gamma}_{\mathrm{res}} = m_W$. The lines show the LL (purple/dash-dotted), NLL (blue/dashed), NLL' (red/solid) resummed predictions. As indication also the unresummed tree-level predictions using the NLO potential (black/dotted) and LO potential (solid/light-gray) are shown. The error bands are given by the hatched/shaded regions and extracted as described in the text. For the NLL' resummed prediction the uncertainty band is given by the thickness of the red line.*

we discuss some more explicit results highlighting the numerical size of the enhancement and suppression effects at the relevant mass scales. We begin with the two benchmark mass values chosen as 1 TeV (10 TeV), i.e., the mass value that approximately reproduces the thermal Higgsino and a high mass value. The ratio to the tree for a resolution of $E^{\gamma}_{\mathrm{res}} = m_W$, i.e. Sommerfeld-only rate is $0.750^{+0.091}_{-0.025}$ $(0.587^{+0.062}_{-0.052})$ at LL, $0.939^{+0.327}_{-0.180}$ $(0.604^{+0.022}_{-0.024})$ at NLL and $0.993^{+0.010}_{-0.034}$ $(0.567^{+0.004}_{-0.003})$ at NLL'. The theoretical uncertainty for the thermal Higgsino $m_\chi = 1\,\mathrm{TeV}$ is therefore ±8% at LL, ±27 % at NLL and ±2 % at NLL'.

To emphasize, this we examine the NLL' cross-section at $m_\chi = 1\,\mathrm{TeV}$ (with definitions as for the wino case above), we write

$$\begin{aligned}\langle\sigma v\rangle = 2\times\Big\{&\mathbf{S}_{(\mathbf{11})(\mathbf{11})}\,[\sigma v]_{(11)(11)} + 2\,\mathrm{Re}\Big[\mathbf{S}_{(\mathbf{11})(\mathbf{22})}\,[\sigma v]_{(11)(22)}\Big] \\ &+2\,\mathrm{Re}\Big[\mathbf{S}_{(\mathbf{11})(+-)}\,[\sigma v]_{(11)(+-)}\Big] + \mathbf{S}_{(\mathbf{22})(\mathbf{22})}\,[\sigma v]_{(22)(22)} \\ &+2\,\mathrm{Re}\Big[\mathbf{S}_{(\mathbf{22})(+-)}\,[\sigma v]_{(22)(+-)}\Big] + \mathbf{S}_{(+-)(+-)}\,[\sigma v]_{(+-)(+-)}\Big\}\,. \qquad (8.6)\end{aligned}$$

The individual elements are (upper/lower components correspond to LO/NLO potential Sommerfeld coefficients, respectively)

$$\begin{aligned}\langle\sigma v\rangle = 2\times&\Bigg[\left\{\begin{matrix}\mathbf{1.0486}\\ \mathbf{1.0436}\end{matrix}\right. \times 1.0955 + 2\,\mathrm{Re}\Bigg[\left\{\begin{matrix}\mathbf{0.1326}\\ \mathbf{0.1256}\end{matrix}\right. \times 1.0955\Bigg] \\ &+2\,\mathrm{Re}\Bigg[\left\{\begin{matrix}\mathbf{0.1481}\\ \mathbf{0.1382}\end{matrix}\right. \times(-3.8233+7.6627i)\Bigg] + \left\{\begin{matrix}\mathbf{0.01676}\\ \mathbf{0.01512}\end{matrix}\right. \times 1.0955 \\ &+2\,\mathrm{Re}\Bigg[\left\{\begin{matrix}\mathbf{0.01872}\\ \mathbf{0.01664}\end{matrix}\right. \times(-3.8233+7.6627i)\Bigg] + \left\{\begin{matrix}\mathbf{0.02092}\\ \mathbf{0.01831}\end{matrix}\right. \times 115.81\Bigg]\times 10^{-29}\mathrm{cm}^3/\mathrm{s} \\ =&\left\{\begin{matrix}5.2086\\ 4.7423\end{matrix}\right. \times 10^{-29}\mathrm{cm}^3/\mathrm{s} \qquad (8.7)\end{aligned}$$

which illustrates the above points. The hierarchy between the elements S_{IJ}, which ranges from $\mathbf{S}_{(\mathbf{11})(\mathbf{11})} \approx 1$, to the off-diagonal contributions that are ~ 0.1, to finally ~ 0.01 for the $(22)(22), (+-)(+-)$ elements, is compensated by a roughly opposite hierarchy between the $[\sigma v]$ elements, making the contributions between the various elements I, J democratic.

The tree-level cancellation for all channels involving (11) or (22) (hereafter, referred to as combined neutral state (00)), originates from the cancellation between the three operators $\mathcal{O}_{1,4,6}$, and other than for the wino case, is not preserved by renormalization group evolution. The operators have different anomalous dimension and do not mix. Choosing a different basis, e.g. the mass basis, where the cancellation for the (00) elements is part of the Wilson coefficient, does not remedy the situation, as in that case, the annihilation operators link to γ, Z, instead of the unbroken gauge bosons. As photon and Z are not electroweak eigenstates and mix, the same effect is observed in this basis as well.

The consequence of this non-preservation under RG evolution is therefore, a double-logarithm $L^2 = \ln^2(4m_\chi^2/m_W^2)$ in the one-loop elements for $(00)(00), (00)(+-), (+-)(00)$, even though the tree-level term cancels. Therefore, the first non-vanishing terms at NLL for (00)(00) that are of order $\mathcal{O}(\alpha_{1,2}^4)$ carry an L^4 enhancement, whilst for the wino, the corresponding annihilation matrix element $\Gamma^{\mathrm{NLL}}_{(00)(00)}$ only contains at most L^2 terms at $\mathcal{O}(\hat\alpha_2^4)$.[5] The underlying reason for the different logarithmic structure lies in the non-zero hypercharge of the Higgsino model, which allows for tree-level Z with neutral DM couplings. Therefore, $\chi_i^0\chi_i^0 \to ZZ$ is already non-vanishing at the tree-level.

Finally, the largeness of the NLL error band is also traceable to the L^4 leading terms in the (00)(00) element at $\mathcal{O}(\hat\alpha_{1,2}^4)$. The existence of L^4 terms implies that at NLL, the L^2 and L terms are not yet accurately summed. Therefore, they are dependent on the individual scales, which together with a large π^2-enhanced coefficient for L [101] leads to the error band. The origin of the π^2-terms is the imaginary part of the one-loop anomalous dimensions, which was

---

[5] In principle, the lowest order term that contributes to this channel arises from $\chi_i^0\chi_i^0 \to \gamma W^+W^-$, which is of order $\mathcal{O}(\hat\alpha_{1,2}^3)$ for both wino and Higgsino. However, this process enters through the one-loop corrections, i.e., at NLL' order.

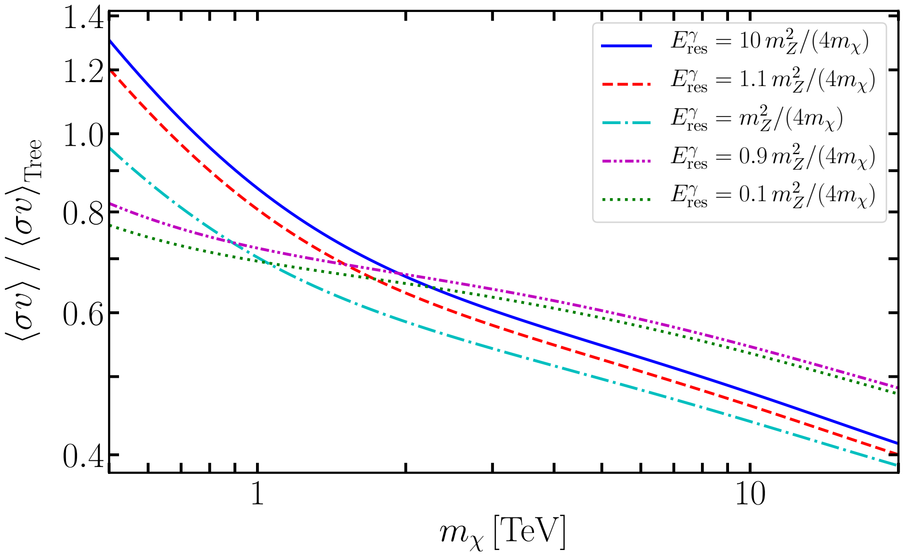

Figure 8.5: *Ratio of NLL' resummed narrow resolution cumulative cross-section vs. the tree (Sommerfeld-only) prediction, for the mass range* $(0.5-20)$ TeV *and various values of detector energy bin. All values are extracted for central resummation scales. Note that, below the* γZ *threshold, also the tree-level prediction in the ratio changes.*

understood as a Glauber-mode that is part of the soft function in [99] for the wino case, and here causes $\mathcal{O}(1)$ scale variations at low masses. A similar scale-dependence is also present for the LL terms. However, in that case, an accidental cancellation between (00)(00) and (00)(+−) results in an asymmetric and much smaller error band. At NLL' order, the inclusion of the one-loop fixed-order terms cancels the large scale variation, leading to a drastic reduction in the error band size.

The above arguments also hold in the narrow resolution case, above the γZ threshold, as in that case, the recoiling jet-function $J^{34}_{\text{nrw}} \sim \mathcal{O}(\hat{\alpha}_{1,2})$ compared to the recoiling jets $J^{33}_{\text{nrw}}, J^{44}_{\text{nrw}}$ making the cancellation similar to the above discussed intermediate resolution discussion. Below the Z-pole, however, $J^{34}_{\text{nrw}} \sim \mathcal{O}(1)$ of the same order as the other recoiling jet functions. The cancellation now proceeds differently, and the enhancement effectively ceases. Physically, this is a manifestation of the fact, that if the Z-boson cannot appear in the final state, we can choose the mass basis for the annihilation operators. The photon and Z do not mix on-shell for invariant jet masses $p^2 < m_Z^2$, meaning that the L^4 term for the (00)(00) element above, is turned into an L^2 term, similar to the wino case.

To visualize this fact, we plot in Figure 8.5 the same ratio plot for the mass spectrum above (cf. Figure 8.4 - lower panel). However, now for different resolutions around the Z-pole and using the narrow resolution calculation at NLL'. We show the prediction, away from the γZ-threshold, namely at a tenth and ten times the threshold value. Furthermore, we show two values, at ten percent below and above the threshold value and directly at the Z-pole.[6] As indicated above, below the γZ threshold, the enhancement ceases, and the situation is similar to the wino case.

The cumulative cross-section for Higgsino dark matter matches the narrow and intermediate resolution predictions, similar to the wino above, as shown in Figure 8.6. Also, most of the other comments made for the wino above apply. We remark that the matching of narrow and

---

[6] Note that we choose the tree-level for $E^{\gamma}_{\text{res}} = m_Z^2/(4m_\chi^2)$ at the value above the Z-pole as a convention. In principle, any value between the tree-level before and after the γZ threshold is possible, as the tree-level recoiling jet functions are not well-defined at $p^2 = m_Z^2$ due to the appearing delta-function.

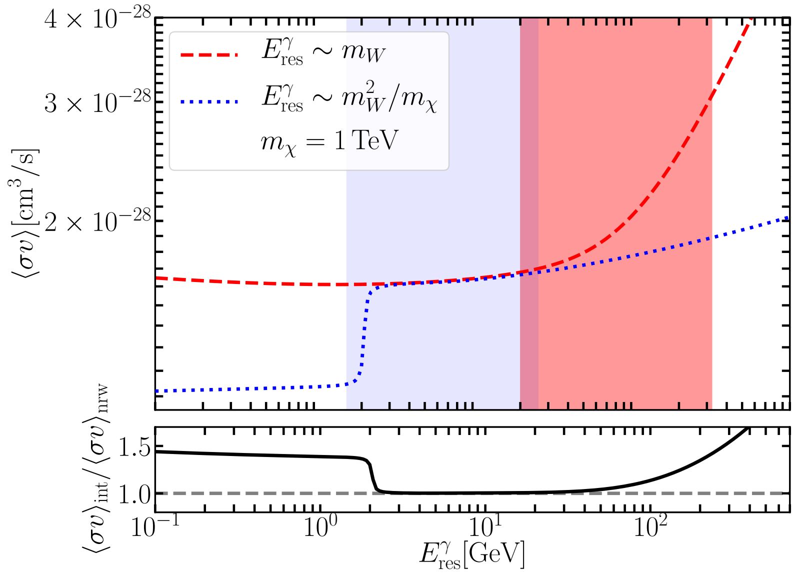

Figure 8.6: *Cumulative cross-section Eq.* (8.1) *for the expected thermal Higgsino mass* $m_\chi = 1\,\mathrm{TeV}$*, for central values of all resummation scales. The blue/dotted line, corresponds to the narrow-resolution prediction, whilst the red/dashed line, is the value extracted using the intermediate resolution EFT. The shaded areas represent the estimated regions of validity of the corresponding EFTs (more details in the text), with the color-coding as blue (light-grey) for the narrow resolution EFT and red (dark-grey) for the intermediate resolution EFT. The subtended panel shows the ratio of intermediate to narrow cross-section prediction.*

intermediate resolution calculation is slightly worse for the Higgsino, especially for lower masses. Over the region of validity of the narrow resolution calculation, both calculations match on the percent to sub percent level, also visualized by the subtended ratio plot. However, starting with the onset of the intermediate resolution validity, deviations on the percent level arise, different from the wino, where the matching extends well into the intermediate regime.

Still, the results in both resolution regimes agree well enough with each other, such that we can again match both predictions and create a differential spectrum also beyond the endpoint region, as described above for the wino and in Appendix F. The resulting spectrum is shown in Figure 8.7.

Similar to the wino above, the resummed Z-pole at $1 - x = m_Z^2/(4m_\chi^2)$ presents the main feature of the differential spectrum. Note, however, that in the Higgsino case, in addition to the function J^{33}_{nrw} in the recoiling jet, also the combinations J^{34}_{nrw} and J^{44}_{nrw} contribute. Similar to the wino, we also recognize the γW^+W^- threshold, and also the other thresholds $\gamma ZH, \gamma t\bar{t}$ remain invisible on the scale of the plot. Even though the merging into the intermediate resolution calculation works rather well, it is not quite as good as in the wino case. The reason is similar to the cumulative cross-section above. Finally, the matching onto the `PPPC4DM` [175] also works, however, again with some difficulties at low masses. Nevertheless, this does not change the prediction obtained from integrating the differential spectrum considerably. For high masses, the matching is again essentially perfect on the scale of the plot (cf. lower panel of Figure 8.7).

In summary, the above results allow for an analysis of the indirect detection prediction. Contrary to the wino, the suppression for the thermal mass value is only about 1% for an energy resolution of $E^{\gamma}_{\mathrm{res}} = m_W$ and the NLO potential. However, this suppression can be altered, e.g., by a smaller bin size, or even be turned into an enhancement if the energy bin is enlarged (cf. Figure 8.5). Using NLL' resummation, we decreased the theoretical scale uncertainty to the

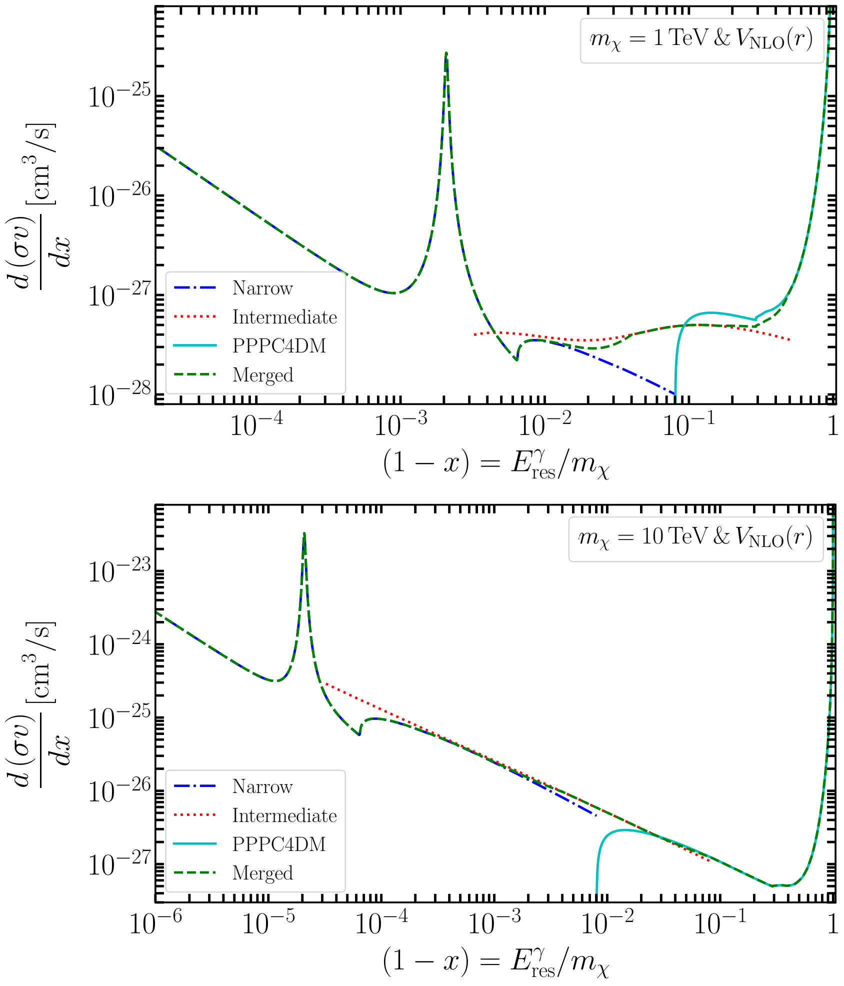

Figure 8.7: *Differential spectra* $\frac{d(\sigma v)}{dx}$ *as function of* $(1-x) = E^\gamma_{\rm res}/m_\chi$ *for DM masses of . In addition to the merged spectrum (green/dashed), as described in the text, we also show the narrow (blue/dash-dotted), intermediate (red/dotted), and* `PPPC4DM` *prediction (teal/solid) from which the merged spectrum was created.*

percent level, which for a practical experimental analysis should be sufficient. At this level, of uncertainty, one might worry about power corrections, e.g., from terms proportional m_W/m_χ, which for the TeV Higgsino would be of order $m_W/m_\chi \sim 0.1 \times (1\,\mathrm{TeV}/m_\chi)$ and might spoil the accuracy of the calculation. Fortunately, as discussed in [102], the power corrections for the annihilation cross-section are of order $\mathcal{O}(m_W^2/m_\chi^2)$, and also come with a small coefficient. Therefore, the power corrections are not expected to lessen the percent accuracy of the NLL' result. For a detailed discussion, including explicit terms and further details, see [102].

9

Conclusions and Outlook

This thesis investigates the effect of electroweak corrections on WIMP relic abundance and indirect detection signal using effective field theories. While typical electroweak corrections are expected to amount to changes of a few percent, we demonstrated that the impact of electroweak corrections is sizeable and oftentimes well beyond the naive estimate.

We calculated the one-loop correction to the potential using potential non-relativistic dark matter theory [84], first for the pure wino model and following this for general arbitrary SM multiplets also including hypercharge. For the wino, we find that even though the potential is corrected only on the few percent level, the phenomenological implications for indirect detection are sizeable for the entire thermal mass range interesting. The reason is identified as a shift in the zero-energy resonances of the Sommerfeld effect due to the slightly weaker potential, leading to $\mathcal{O}(> 10\,\%)$ corrections for essentially all mass values.

Similarly, we have investigated the effect of the NLO Sommerfeld effect on the relic abundance prediction. The effect is of the order of a few percent, as the NLO potentials affect the early and late time Sommerfeld effect differently. In addition, we included $\mathcal{O}(v^2)$ [85] corrections to the annihilation matrices, thereby nevertheless providing the most precise prediction for the thermal pure wino mass $m_\chi = 2.842\,\text{TeV}$ to date.

Apart from examining various field-theoretical aspects of the NLO potential correction, we also proved that the one-loop corrections to the electroweak potentials are universal, in the sense that the correction is proportional to the tree-level potential ("Casimir-like" scaling). The universality holds not only for the pure SU(2) sector of the SM but also pertains to a possible hypercharge generalization. The calculation was performed assuming general SM multiplets without any reference to DM. Therefore, the result is relevant for all TeV-scale (and beyond) particles coupled to the electroweak gauge group. In this sense, we have uncovered a "low-energy" property of the electroweak SM bosons.

The second large electroweak correction in TeV-WIMP annihilation are electroweak Sudakov double logarithms of DM mass to electroweak scale that require resummation. We performed this resummation within the soft-collinear effective theory framework, first showing how the differential cross-section factorizes for generic fermionic minimal DM models in two detector resolution regimes. We provided the factorization formula for narrow resolution, where $E^\gamma_{\text{res}} \sim m_W^2/m_\chi$, and for intermediate resolution $E^\gamma_{\text{res}} \sim m_W$. Secondly, we specialized on two often discussed models in the literature, the pure wino and Higgsino, and performed resummation to the next-to-leading logarithmic prime order, thereby combining next-to-leading logarithmic resummation with the full one-loop fixed order result.

The predictions after resummation show a suppression effect of about 30 % for the thermal wino cross-section at $E^\gamma_{\text{res}} = m_W$. Similar results are obtained for the thermal Higgsino, though the suppression effect is smaller due to the lower DM mass. Furthermore, in the Higgsino case, the result is highly resolution-dependent. While for resolutions below $E^{\gamma}_{\text{res}} \lesssim m_Z^2/(4m_\chi^2)$, the generic suppression picture of the wino persists, at higher resolutions, the cross-section may even be enhanced due to the delicate interplay of Sommerfeld and Sudakov resummation effects, as well as, some subtleties originating from non-zero hypercharge in EWSB.

The residual theoretical uncertainty is on the level of $\lesssim 1\,\%$ for the thermal wino and about $2\,\%$ for the thermal Higgsino. Generically for essentially all resolutions, the theoretical uncertainty of the NLL' result stays within the $1\,\%$ range, except for very low masses where the enhancement effect can lead to slightly larger error bars. Furthermore, the calculation revealed that considering only NLL resummation is not sufficient for the Higgsino DM model, as there are significant uncertainties of up to a factor of two for low masses $m_\chi \sim 500\,\text{GeV}$. In general, the precision of the results in both models is more than sufficient, given the potential astrophysical uncertainties that may enter a complete indirect detection analysis.

In addition to Sudakov resummation and the NLO potential, which were also examined separately in the corresponding publications [100, 101, 102, 103, 104], in this thesis, we show for the first time the combined effect of both results. Consequently, we provide the most precise predictions for the indirect detection process $\chi^0\chi^0 \to \gamma + X$ in these models to date. For the entire TeV-mass range, the effects on the cross-section are large and emphasize the need for including EW corrections to make precise predictions for DM indirect detection.

In this thesis, we furthermore examined the differential spectrum for the full range of kinematically possible photon energies. To this extent, we merged our calculations for the narrow and intermediate resolution, which provides an accurate prediction from the endpoint to at least $E^{\gamma}_{\text{res}} \approx 4m_W$. Together with the spectra provided in the `PPPC4DM` [175], that tabulates the results of EW parton shower calculations and is merged with our result, we provide the entire photon spectrum from $E_\gamma = m_\chi$ to $E_\gamma \to 0$. In this form, the differential spectra can serve as an input for future analyses, e.g., a reanalysis of the H.E.S.S. data set [65] or also in the upcoming CTA experiment [67]. According to projections, the CTA experiment will then be able to confirm or rule out the thermal wino, even under conservative assumptions on possible astrophysical inputs, such as DM halo profiles. Also, for the thermal Higgsino, CTA might be able to probe a large part of the theoretical parameter space. However, it is not yet clear if the model can definitely be confirmed or ruled out in this case.

The frameworks developed in this thesis also allow for the treatment of more general models. It might be interesting to investigate models where EW bound states have a sizeable impact in the future. For example, in the minimal fermionic quintuplet, bound states play a significant role in the DM relic abundance and may further impact the indirect detection prediction [119]. In such a case, both the Sudakov resummation and the NLO potential may provide large modifications of the results in the literature. The resummation framework and the NLO potential allow to challenge electroweak TeV-WIMPs for essentially all models within the minimal DM paradigm.

A

NLO loop topologies - NREFT

In this Appendix, we collect the NLO topologies and integrals necessary to determine the one-loop corrections to the potential presented in Chapters 3 and 4. The result and presentation are similar to Appendix A of the corresponding publication [104].

A.1 Feynman gauge results

We begin collecting the results in Feynman gauge for the diagram topologies presented in Figures 3.1, 3.2, 3.3. To shorten notation, we use the vector $v^\mu = (1, \mathbf{0})$ and the abbreviation for the loop integral measure

$$[dl] = \tilde{\mu}^{2\epsilon} \frac{d^d l}{(2\pi)^d} = \left(\frac{\mu^2 e^{\gamma_E}}{4\pi} \right)^\epsilon \frac{d^d l}{(2\pi)^d} \,, \tag{A.1}$$

where $d = 4 - 2\epsilon$ and γ_E is the Euler-Mascheroni constant. The loop integrals can be calculated using the standard methods for non-relativistic effective theories. Note that for all topologies involving pinched poles at $v \cdot l = \pm i\varepsilon$, the residues of these poles must not be taken into account. In the case at hand this only affects ordinary box topologies, for which these residues are part of the leading order potential ladder.

A.1.1 Box topologies

We first consider the box topologies, e.g., in the first line of Figure 3.1. Crossed-box diagrams are related trivially by a minus sign to the box topologies. We define the triangle function $\lambda(a, b, c) = (a - b - c)^2 - 4bc$. In the case of two unequal-mass bosons, we obtain

$$\begin{aligned} I_{\text{box}}(\alpha_i, m_i; \alpha_j, m_j) &= i g_i^2 g_j^2 \int [dl] \; \frac{-i}{l^2 - m_i^2 + i\varepsilon} \cdot \frac{-i}{(l+q)^2 - m_j^2 + i\varepsilon} \cdot \frac{i}{v \cdot l + i\varepsilon} \cdot \frac{i}{-v \cdot l + i\varepsilon} \\ &= \frac{4\alpha_i \alpha_j}{\lambda^{1/2}(-\mathbf{q}^2, m_i^2, m_j^2)} \ln \left[\frac{m_i^2 + m_j^2 + \mathbf{q}^2 + \lambda^{1/2}(-\mathbf{q}^2, m_i^2, m_j^2)}{2 m_i m_j} \right] . \end{aligned} \tag{A.2}$$

The box integral with masses is finite in $d = 4$. $\mathbf{q}^2 \approx -q^2$ denotes the exchanged potential three-momentum. If the masses of the exchanged bosons are equal, the expression takes the simpler form

$$I_{\text{box}}(\alpha_i, m_i; \alpha_j, m_i) = \frac{4\alpha_i \alpha_j}{|\mathbf{q}| \sqrt{4m_i^2 + \mathbf{q}^2}} \ln \left[\frac{2m_i^2 + \mathbf{q}^2 + \sqrt{4m_i^2 \mathbf{q}^2 + \mathbf{q}^4}}{2m_i^2} \right] . \tag{A.3}$$

Furthermore, there are also situations in which either one or two of the exchange bosons are massless. In these cases, the topologies are divergent and require regularization. Expanding in ϵ and retaining finite terms, we find

$$I_{\text{box}}(\alpha_i, m_i; \alpha_j, 0) = -\frac{2\alpha_i\alpha_j}{m_i^2+\mathbf{q}^2}\left(\frac{1}{\epsilon}+\ln\left[\frac{\mu^2}{m_i^2+\mathbf{q}^2}\right]+\ln\left[\frac{m_i^2}{m_i^2+\mathbf{q}^2}\right]\right), \tag{A.4}$$

$$I_{\text{box}}(\alpha_i, 0; \alpha_j, 0) = -\frac{4\alpha_i\alpha_j}{\mathbf{q}^2}\left(\frac{1}{\epsilon}+\ln\frac{\mu^2}{\mathbf{q}^2}\right). \tag{A.5}$$

A.1.2 Vertex corrections

The soft correction to the vertex (e.g., first diagram second row of Figure 3.1) is known as it appears also in soft corrections to exclusive DM annihilation [101], and is also discussed in the context of the wino soft function in Appendix E. We choose

$$I_{\text{vertex}}(\alpha_i, m_i) = g_i^2\int[dl]\,\frac{-i}{l^2-m_i^2+i\varepsilon}\cdot\frac{i}{v\cdot l+i\varepsilon}\cdot\frac{i}{-v\cdot l-i\varepsilon} = -\frac{\alpha_i}{2\pi}\left(\frac{1}{\epsilon}+\ln\frac{\mu^2}{m_i^2}\right). \tag{A.6}$$

The soft vertex correction involving the triple gauge vertex (cf. Figure 3.1) vanishes in Feynman gauge, as the vertices project on the zero-component of the propagator

$$I_{3\,\text{gauge}}^{\gamma/Z/W} = 0\,. \tag{A.7}$$

A.1.3 DM field renormalization

The field and mass renormalization of the heavy DM field can be obtained in analogy to HQET. We find

$$\begin{aligned} I_{\text{heavy DM}}(g_i, m_i) &= g_i^2\int[dl]\,\frac{-i}{l^2-m_i^2+i\varepsilon}\,\frac{i}{v\cdot(l+p)+i\varepsilon} \\ &= \frac{i\,\alpha_i\,v\cdot p}{2\pi}\left(\frac{1}{\epsilon}+\ln\frac{\mu^2}{m_i^2}\right)-\frac{i\,\alpha_i\,m_i}{2}+\mathcal{O}\left((v\cdot p)^2\right). \end{aligned} \tag{A.8}$$

From the term proportional to $v\cdot p$, we extract the on-shell static fermion field renormalization constants. For the wino, they read

$$\delta Z_{\chi^0} = \frac{\alpha_2}{4\pi}\left[\frac{2}{\epsilon}-2\ln\frac{m_W^2}{\mu^2}\right], \tag{A.9}$$

$$\delta Z_{\chi^+} = \delta Z_{\chi^-} = \frac{\alpha_2}{4\pi}\left[\frac{1+c_W^2}{\epsilon}-\ln\frac{m_W^2}{\mu^2}-c_W^2\ln\frac{m_Z^2}{\mu^2}\right]. \tag{A.10}$$

The $v\cdot p$ independent term generates the one-loop mass difference between the neutral and charged DM fermions in the non-relativistic theory. In the wino case, we find [178]

$$\delta m_{\chi^0} = -\alpha_2 m_W\,, \tag{A.11}$$

$$\delta m_{\chi^+} = -\frac{\alpha_2}{2}m_W-\frac{\alpha_2 c_W^2}{2}m_Z\,, \tag{A.12}$$

$$\delta m_{\chi} = \delta m_{\chi^+}-\delta m_{\chi^-} = \frac{1-c_W}{2}\alpha_2 m_W\,. \tag{A.13}$$

A.1.4 Gauge boson self-energies

The self-energies in Feynman gauge are not given explicitly for brevity, as we give the self-energies in R_ξ-gauge in the following Section. They can e.g. be found in [101, 128].

A.2 Expressions in R_ξ-gauge

All gauge parameter dependent parts of the diagram topologies and counterterms can be expressed in terms of the Passarino-Veltman (PV) functions [160] (expanded to $\mathcal{O}(\epsilon^0)$)

$$\begin{aligned}
A_0(m) &= m^2\left[\frac{1}{\epsilon}+\ln\frac{\mu^2}{m^2}+1\right]\,,\\
B_0(p^2,0,0) &= \frac{1}{\epsilon}+\ln\left(-\frac{\mu^2}{p^2}\right)+2\,,\\
B_0(p^2,0,m) &= \frac{1}{\epsilon}+\ln\frac{\mu^2}{m^2}+2-\left(1-\frac{m^2}{p^2}\right)\ln\left(1-\frac{p^2}{m^2}\right)\,,\\
B_0(p^2,m,m) &= \frac{1}{\epsilon}+\ln\frac{\mu^2}{m^2}+2+\sqrt{1-\frac{4m^2}{p^2}}\ln\left(\frac{2m^2-p^2+\sqrt{p^2(p^2-4m^2)}}{2m^2}\right)\,,\\
B_0(p^2,m_1,m_2) &= \frac{1}{\epsilon}-\frac{m_1^2-m_2^2}{2p^2}\ln\frac{m_1^2}{m_2^2}+\frac{1}{2}\left(\ln\frac{\mu^2}{m_1^2}+\ln\frac{\mu^2}{m_2^2}\right)+2\\
&\quad+\frac{\lambda^{1/2}(m_1^2,m_2^2,p^2)}{p^2}\ln\left(\frac{m_1^2+m_2^2-p^2+\lambda^{1/2}(m_1^2,m_2^2,p^2)}{2m_1m_2}\right)\,, \qquad \text{(A.14)}
\end{aligned}$$

where $\lambda(a,b,c)$ is the triangle function defined above. We use the abbreviation $\Delta_i=1-\xi_i$, where ξ_i denotes the gauge fixing parameter for boson $i=\gamma,W,Z$. The integrals I_X provided below in general gauge are defined in terms of those for $\xi_i=1$ by substituting

$$\frac{g_{\mu\nu}}{l^2-m_i^2} \quad\to\quad \frac{g_{\mu\nu}-\Delta_i\frac{l_\mu l_\nu}{l^2-\xi_i m_i^2}}{l^2-m_i^2} \qquad \text{(A.15)}$$

in the appropriate gauge boson propagators.

A.2.1 Box topologies

The massive boxes evaluate to

$$\begin{aligned}
&I^\xi_{\text{box}}(\alpha_i,m_i;\alpha_j,m_j)=I^{\xi=1}_{\text{box}}(\alpha_i,m_i;\alpha_j,m_j)\\
&+\frac{\alpha_i\alpha_j}{12\mathbf{q}^2}\Bigg[\Delta_j\frac{A_0(m_i)-A_0(\xi_i^{1/2}m_i)}{m_i^2}+\Delta_i\frac{A_0(m_j)-A_0(\xi_j^{1/2}m_j)}{m_j^2}\\
&\qquad-\frac{1}{m_i^2m_j^2}\Bigg(\Big(12\mathbf{q}^2(m_i^2+m_j^2)-\lambda(-\mathbf{q}^2,m_i^2,m_j^2)\Big)B_0(-\mathbf{q}^2,m_i,m_j)\\
&\qquad\qquad+\Big(\lambda(-\mathbf{q}^2,m_i^2,\xi_jm_j^2)-12\mathbf{q}^2m_i^2\Big)B_0(-\mathbf{q}^2,m_i,\xi_j^{1/2}m_j)\\
&\qquad\qquad+\Big(\lambda(-\mathbf{q}^2,m_j^2,\xi_im_i^2)-12\mathbf{q}^2m_j^2\Big)B_0(-\mathbf{q}^2,m_j,\xi_i^{1/2}m_i)\\
&\qquad\qquad-\lambda(-\mathbf{q}^2,\xi_im_i^2,\xi_jm_j^2)\;B_0(-\mathbf{q}^2,\xi_i^{1/2}m_i,\xi_j^{1/2}m_j)\Bigg)\Bigg]\,, \qquad \text{(A.16)}
\end{aligned}$$

where the gauge parameter with index i is associated with the boson of mass m_i. For one vanishing mass (where Δ_j, ξ_j are associated to the massless boson coupling with α_j)

$$\begin{aligned}
&I^{\xi}_{\text{box}}(\alpha_i, m_i; \alpha_j, 0) = I^{\xi=1}_{\text{box}}(\alpha_i, m_i; \alpha_j, 0) \\
&- \alpha_i\alpha_j \left[\Delta_j \frac{2(A_0(m_i) - \mathbf{q}^2) + (\mathbf{q}^2 - m_i^2)B_0(-\mathbf{q}^2, 0, m_i)}{(\mathbf{q}^2 + m_i^2)^2}\right. \\
&\qquad + \frac{B_0(-\mathbf{q}^2, 0, m_i) - B_0(-\mathbf{q}^2, 0, \xi_i^{1/2} m_i)}{m_i^2} \\
&\qquad - \frac{\Delta_j}{4\mathbf{q}^2 m_i^2}\Big(A_0(m_i) - A_0(\xi_i^{1/2} m_i) + (\mathbf{q}^2 - m_i^2)B_0(-\mathbf{q}^2, 0, m_i) \\
&\qquad\qquad \left. - (\mathbf{q}^2 - \xi_i m_i^2)\; B_0(-\mathbf{q}^2, 0, \xi_i^{1/2} m_i)\Big)\right] . \qquad \text{(A.17)}
\end{aligned}$$

The massless box is given by (Δ_i, ξ_i and Δ_j, ξ_j are associated to massless bosons coupling with α_i and α_j, respectively)

$$\begin{aligned}
I^{\xi}_{\text{box}}(\alpha_i, 0; \alpha_j, 0) &= I^{\xi=1}_{\text{box}}(\alpha_i, 0; \alpha_j, 0) \\
&\quad - \frac{\alpha_i\alpha_j}{\mathbf{q}^2}\left[\frac{\Delta_i\Delta_j}{2} + (\Delta_i + \Delta_j)(B_0(-\mathbf{q}^2, 0, 0) - 2)\right] . \qquad \text{(A.18)}
\end{aligned}$$

A.2.2 Vertex topologies

The ordinary soft vertex correction reads in general covariant gauge

$$I^{\xi}_{\text{vertex}}(\alpha_i, m_i) = I^{\xi=1}_{\text{vertex}}(\alpha_i, m_i) - \frac{\alpha_i}{4\pi}\frac{A_0(m_i) - A_0(\xi_i^{1/2} m_i)}{m_i^2} . \qquad \text{(A.19)}$$

The non-abelian vertex correction involving the triple gauge boson vertex vanishes in Feynman gauge. In arbitrary R_ξ-gauge it is, however, non-zero. Which gauge bosons are involved, depends on the tree-level potential exchange. For tree-level photon and Z-exchange, the loop contains two W-bosons and, hence only depends on ξ_W. If the tree-level exchange boson is a W-boson, the loop is a mixture of W and either photon or Z, i.e., depends on two gauge parameters, and either one or two masses. The integral with W/Z bosons in the loop is given by

$$\begin{aligned}
I^{WZ}_{3\,\text{gauge}} &= -i g_2^2 c_W^2 \int [dl] \frac{i}{v\cdot l + i\varepsilon} \frac{-i\left(g_{0\mu} - \Delta_W \frac{l_0 l_\mu}{l^2 - \xi_W m_W^2 + i\varepsilon}\right)}{l^2 - m_W^2 + i\varepsilon} \frac{-i\left(g_{0\nu} - \Delta_Z \frac{l_0 (l+q)_\nu}{(l+q)^2 - \xi_Z m_Z^2 + i\varepsilon}\right)}{(l+q)^2 - m_Z^2 + i\varepsilon} \\
&\qquad \times g_{0\rho}\left(g^{\mu\nu}(-2l - q)^\rho + g^{\nu\rho}(l + 2q)^\mu + g^{\rho\mu}(l - q)^\nu\right) \\
&= \frac{\alpha_2 c_W^2}{4\pi}\frac{1}{12}\left[2\left(\Delta_W + \Delta_Z\right) + \left(\Delta_Z - 11 + (\Delta_Z - 1)\frac{m_W^2}{\mathbf{q}^2} + \frac{m_Z^2}{\mathbf{q}^2}\right)\frac{A_0(m_W)}{m_W^2}\right. \\
&\quad - \left(\Delta_Z - 11 + (\Delta_W - 1)\frac{m_W^2}{\mathbf{q}^2} + \frac{m_Z^2}{\mathbf{q}^2}\right)\frac{A_0(\xi_W^{1/2} m_W)}{m_W^2} \\
&\quad + \left(\Delta_W - 11 + \frac{m_W^2}{\mathbf{q}^2} + (\Delta_W - 1)\frac{m_Z^2}{\mathbf{q}^2}\right)\frac{A_0(m_Z)}{m_Z^2} \\
&\quad - \left(\Delta_W - 11 + \frac{m_W^2}{\mathbf{q}^2} + (\Delta_Z - 1)\frac{m_Z^2}{\mathbf{q}^2}\right)\frac{A_0(\xi_Z^{1/2} m_Z)}{m_Z^2}
\end{aligned}$$

$$
\begin{aligned}
&+\Bigg(c_W^2\frac{\mathbf{q}^4}{m_W^4}-9(1+c_W^2)\frac{\mathbf{q}^2}{m_W^2}-\frac{9c_W^4-2c_W^2+9}{c_W^2}+\frac{s_W^4}{c_W^4}(1+c_W^2)\frac{m_W^2}{\mathbf{q}^2}\Bigg)B_0(-\mathbf{q}^2,m_W,m_Z)\\
&-\Bigg(c_W^2\frac{\mathbf{q}^4}{m_W^4}+(2(1-\Delta_Z)-9c_W^2)\frac{\mathbf{q}^2}{m_W^2}+\frac{(\Delta_Z-1)^2-9c_W^4}{c_W^2}\\
&\qquad\qquad+\frac{(c_W^2+(\Delta_Z-1))^2}{c_W^2}\frac{m_W^2}{\mathbf{q}^2}\Bigg)B_0(-\mathbf{q}^2,m_W,\xi_Z^{1/2}m_Z)\\
&-\Bigg(c_W^2\frac{\mathbf{q}^4}{m_W^4}+(2c_W^2(1-\Delta_W)-9)\frac{\mathbf{q}^2}{m_W^2}+\frac{c_W^4(\Delta_W-1)^2-9}{c_W^2}\\
&\qquad\qquad+\frac{(1+c_W^2(\Delta_W-1))^2}{c_W^4}\frac{m_W^2}{\mathbf{q}^2}\Bigg)B_0(-\mathbf{q}^2,\xi_W^{1/2}m_W,m_Z)\\
&+\Bigg(c_W^2\frac{\mathbf{q}^4}{m_W^4}+2(c_W^2(1-\Delta_W)+1-\Delta_Z)\frac{\mathbf{q}^2}{m_W^2}\\
&\qquad\qquad+\frac{(c_W^2(\Delta_W-1)+1-\Delta_Z)^2}{c_W^2}\Bigg)B_0(-\mathbf{q}^2,\xi_W^{1/2}m_W,\xi_Z^{1/2}m_Z)\Bigg]\,.
\end{aligned}
\tag{A.20}
$$

If the Z-boson is replaced by the massless photon, we find

$$
\begin{aligned}
I^{W\gamma}_{3\,\text{gauge}}=\frac{\alpha}{4\pi}\Bigg[&\frac{2\Delta_\gamma\mathbf{q}^2}{\mathbf{q}^2+m_W^2}+\frac{\Delta_W}{6}\\
&+\Bigg(\frac{2\Delta_\gamma\mathbf{q}^2}{\mathbf{q}^2+m_W^2}+\frac{(3\Delta_\gamma-1)m_W^2}{12\mathbf{q}^2}-\frac{21\Delta_\gamma+11}{12}\Bigg)\frac{A_0(m_W)}{m_W^2}\\
&+\Bigg(\frac{11-3\Delta_\gamma}{12}+\frac{(1-\Delta_W)m_W^2}{12\mathbf{q}^2}\Bigg)\frac{A_0(\xi_W^{1/2}m_W)}{m_W^2}\\
&+\Bigg(\Bigg[\frac{2\Delta_\gamma\mathbf{q}^2}{\mathbf{q}^2+m_W^2}-\frac{11+21\Delta_\gamma}{12}\Bigg]\frac{\mathbf{q}^2}{m_W^2}+\frac{1+6\Delta_\gamma}{6}+\frac{1-3\Delta_\gamma}{12}\frac{m_W^2}{\mathbf{q}^2}\Bigg)B_0(-\mathbf{q}^2,0,m_W)\\
&+\frac{1}{12}\Bigg((11-3\Delta_\gamma)\frac{\mathbf{q}^2}{m_W^2}+(1-\Delta_W)(3\Delta_\gamma-2)-(\Delta_W-1)^2\frac{m_W^2}{\mathbf{q}^2}\Bigg)B_0(-\mathbf{q}^2,0,\xi_W^{1/2}m_W)\Bigg]\,.
\end{aligned}
\tag{A.21}
$$

Finally, if both bosons involved are W-bosons, we have

$$
\begin{aligned}
I^{WW}_{3\,\text{gauge}}=\frac{\alpha}{4\pi s_W^2}\Bigg[&\frac{\Delta_W}{3}+\Bigg(\frac{\Delta_W}{6}\frac{\mathbf{q}^2+m_W^2}{\mathbf{q}^2}-\frac{11}{6}\Bigg)\frac{A_0(m_W)-A_0(\xi_W^{1/2}m_W)}{m_W^2}\\
&+\Bigg(\frac{1}{12}\frac{\mathbf{q}^4}{m_W^4}-\frac{3}{2}\frac{\mathbf{q}^2}{m_W^2}-\frac{4}{3}\Bigg)B_0(-\mathbf{q}^2,m_W,m_W)\\
&-\frac{\mathbf{q}^2+m_W^2}{6\mathbf{q}^2}\Bigg(\frac{\mathbf{q}^4}{m_W^4}-2(4+\Delta_W)\frac{\mathbf{q}^2}{m_W^2}+\Delta_W^2\Bigg)B_0(-\mathbf{q}^2,m_W,\xi_W^{1/2}m_W)\\
&+\Bigg(\frac{1}{12}\frac{\mathbf{q}^4}{m_W^4}+\frac{1-\Delta_W}{3}\frac{\mathbf{q}^2}{m_W^2}\Bigg)B_0(-\mathbf{q}^2,\xi_W^{1/2}m_W,\xi_W^{1/2}m_W)\Bigg]\,.
\end{aligned}
\tag{A.22}
$$

A.2.3 DM field renormalization

The heavy DM field renormalization constants for the wino in R_ξ-gauge are

$$
\delta Z^{\xi}_{\chi^0}=\delta Z^{\xi=1}_{\chi^0}+\frac{\alpha_2}{4\pi}\frac{A_0(m_W)-A_0(\xi_W^{1/2}m_W)}{m_W^2}\,,
\tag{A.23}
$$

$$\delta Z^{\xi}_{\chi^+} = \delta Z^{\xi=1}_{\chi^+} + \frac{\alpha_2}{8\pi}\frac{A_0(m_W)-A_0(\xi_W^{1/2}m_W)}{m_W^2} + \frac{\alpha_2 c_W^2}{8\pi}\frac{A_0(m_Z)-A_0(\xi_Z^{1/2}m_Z)}{m_Z^2}\,. \tag{A.24}$$

A.2.4 Gauge boson self-energies

The transverse self-energies (including tadpole diagrams) are split into the three separately gauge invariant pieces discussed in the main text according to

$$\Sigma_T^{ij} = \Sigma_{T,\,\text{light ferm.}}^{ij} + \Sigma_{T,\,\text{3rd gen. quarks}}^{ij} + \Sigma_{T,\,\text{electroweak}}^{ij}\,. \tag{A.25}$$

The photon self-energy

The fermionic self-energy contributions are

$$\Sigma_{T,\,\text{light ferm.}}^{\gamma\gamma}(p^2) = \frac{\alpha}{4\pi}\frac{76}{9}p^2\left[B_0(p^2,0,0)-\frac{1}{3}\right]\,, \tag{A.26}$$

$$\begin{aligned}\Sigma_{T,\,\text{3rd gen. quarks}}^{\gamma\gamma}(p^2) = \frac{\alpha}{4\pi}&\left[\frac{32}{9}\left(m_t^2 - A_0(m_t)\right) + \frac{4}{9}p^2\left(B_0(p^2,0,0)-\frac{5}{3}\right)\right.\\ &\left. +\frac{16}{9}\left(p^2+2m_t^2\right)B_0(p^2,m_t,m_t)\right]\,.\end{aligned} \tag{A.27}$$

The electroweak part of the self-energy reads

$$\begin{aligned}\Sigma_{T,\,\text{electroweak}}^{\gamma\gamma}(p^2) &= \frac{\alpha}{4\pi}\left[-4m_W^2 + \frac{2}{3}p^2\Delta_W\right.\\ &+\left(\frac{12-\Delta_W}{3}+\frac{\Delta_W-10}{6}\frac{p^2}{m_W^2}\right)A_0(m_W)\\ &+\left(\frac{\Delta_W}{3}+\frac{10-\Delta_W}{6}\frac{p^2}{m_W^2}\right)A_0(\xi_W^{1/2}m_W)\\ &+\left(-4-\frac{17}{3}\frac{p^2}{m_W^2}+\frac{4}{3}\frac{p^4}{m_W^4}+\frac{1}{12}\frac{p^6}{m_W^6}\right)m_W^2B_0(p^2,m_W,m_W)\\ &+\left(\frac{\Delta_W^2}{3}+\frac{16+4\Delta_W-\Delta_W^2}{6}\frac{p^2}{m_W^2}-\frac{3+\Delta_W}{3}\frac{p^4}{m_W^4}-\frac{1}{6}\frac{p^6}{m_W^6}\right)m_W^2B_0(p^2,m_W,\xi_W^{1/2}m_W)\\ &\left.+\left(\frac{\Delta_W-1}{3}\frac{p^4}{m_W^4}+\frac{1}{12}\frac{p^6}{m_W^6}\right)m_W^2B_0(p^2,\xi_W^{1/2}m_W,\xi_W^{1/2}m_W)\right]\,.\end{aligned} \tag{A.28}$$

The photon-Z self-energy

$$\Sigma_{T,\,\text{light ferm.}}^{\gamma Z}(p^2) = \frac{\alpha}{4\pi s_W c_W}\frac{38s_W^2-38c_W^2+11}{9}p^2\left(B_0(p^2,0,0)-\frac{1}{3}\right)\,, \tag{A.29}$$

$$\begin{aligned}\Sigma_{T,\,\text{3rd gen. quarks}}^{\gamma Z}(p^2) = \frac{\alpha}{4\pi s_W c_W}&\left[-\frac{2}{9}p^2+\frac{4}{9}\left(1+4s_W^2-4c_W^2\right)\left(m_t^2-A_0(m_t)\right)\right.\\ &-\frac{1}{9}\left(1+2c_W^2-2s_W^2\right)p^2\left(B_0(p^2,0,0)-\frac{5}{3}\right)\\ &\left.+\frac{2}{9}\left(1+4s_W^2-4c_W^2\right)\left(p^2+2m_t^2\right)B_0(p^2,m_t,m_t)\right]\,,\end{aligned} \tag{A.30}$$

$$
\begin{aligned}
\Sigma^{\gamma Z}_{T,\text{electroweak}}(p^2) &= \frac{\alpha}{4\pi s_W c_W}\left[\frac{p^2}{9}\left(1-6c_W^2\Delta_W\right)+\frac{m_W^2}{3}(12c_W^2-2+\Delta_W)\right.\\
&+\left(-\frac{\Delta_W}{6}\frac{m_W^2}{p^2}-\frac{1}{6}\left(1+c_W^2(24-2\Delta_W)\right)+\frac{c_W^2(10-\Delta_W)}{6}\frac{p^2}{m_W^2}\right)A_0(m_W)\\
&+\left(\frac{\Delta_W}{6}\frac{m_W^2}{p^2}+\frac{1}{6}\left(5-2c_W^2\Delta_W\right)-\frac{c_W^2(10-\Delta_W)}{6}\frac{p^2}{m_W^2}\right)A_0(\xi_W^{1/2}m_W)\\
&-c_W^2\left(p^2-4m_W^2\right)\left(1+\frac{5}{3}\frac{p^2}{m_W^2}+\frac{1}{12}\frac{p^4}{m_W^4}\right)B_0(p^2,m_W,m_W)\\
&+\left(c_W^2\left(1-\frac{p^2}{m_W^2}\right)^2+s_W^2\right)\left(\frac{\Delta_W^2}{6}\frac{m_W^2}{p^2}+\frac{4+\Delta_W}{3}+\frac{1}{6}\frac{p^2}{m_W^2}\right)m_W^2B_0(p^2,m_W,\xi_W^{1/2}m_W)\\
&\left.-\frac{c_W^2}{12}\frac{p^4}{m_W^4}\left(p^2-4m_W^2(1-\Delta_W)\right)B_0(p^2,\xi_W^{1/2}m_W,\xi_W^{1/2}m_W)\right]\,. \qquad \text{(A.31)}
\end{aligned}
$$

The Z-boson self-energy

The fermionic contributions are given by

$$
\Sigma^{ZZ}_{T,\text{light ferm.}}(p^2) = \frac{\alpha}{4\pi s_W^2c_W^2}\frac{49-98c_W^2+76c_W^4}{9}p^2\left[B_0(p^2,0,0)-\frac{1}{3}\right]\,, \qquad \text{(A.32)}
$$

$$
\begin{aligned}
\Sigma^{ZZ}_{T,\text{3rd gen. quarks}}(p^2) =& \frac{\alpha}{4\pi s_W^2c_W^2}\left[\frac{p^2(1+8c_W^2)}{18}+\frac{17-8c_W^2(1+4s_W^2)}{9}\left(m_t^2-A_0(m_t)\right)\right.\\
&+\frac{1+4s_W^2+8c_W^4}{18}p^2\left(B_0(p^2,0,0)-\frac{5}{3}\right) \qquad \text{(A.33)}\\
&\left.+\left(\frac{9+8s_W^2(1-4c_W^2)}{18}(2m_t^2+p^2)-\frac{3}{2}m_t^2\right)B_0(p^2,m_t,m_t)\right]\,.
\end{aligned}
$$

The Z- and W-boson self-energies receive contributions from tadpole diagrams. In terms of the gauge invariant parts, the tadpoles belong to the electroweak contributions and are related by a simple prefactor such that

$$
\begin{aligned}
\Sigma_T^{WW,\,\text{tadpole}} &= c_W^2\Sigma_T^{ZZ,\,\text{tadpole}}\\
&= \frac{\alpha}{4\pi s_W^2}\left[(2c_W^2m_W^2+m_Z^2)\frac{m_Z^2}{m_H^2}-\frac{3}{4}A_0(m_H)+6\frac{m_t^2}{m_H^2}A_0(m_t)-3\frac{m_W^2}{m_H^2}A_0(m_W)\right.\\
&\left.-\frac{3}{2}\frac{m_Z^2}{m_H^2}A_0(m_Z)-\frac{1}{2}A_0(\xi_W^{1/2}m_W)-\frac{1}{4}A_0(\xi_Z^{1/2}m_Z)\right]\,. \qquad \text{(A.34)}
\end{aligned}
$$

The electroweak part is then given by

$$
\begin{aligned}
\Sigma^{ZZ}_{T,\text{electroweak}}(p^2) &= \frac{\alpha}{4\pi s_W^2c_W^2}\left[\frac{(s_W^2-c_W^2+6c_W^4\Delta_W)p^2}{9}-\frac{m_H^2+m_Z^2}{6}\right.\\
&-\frac{m_W^2}{3}\left(1+2c_W^2(4c_W^2-2s_W^2+\Delta_W)\right)\\
&+\left(\frac{1}{6}-\frac{m_H^2-m_Z^2}{12p^2}\right)A_0(m_H)-\left(\frac{1}{12}-\frac{m_H^2-m_Z^2}{12p^2}\right)A_0(m_Z)+\frac{1}{4}A_0(\xi_Z^{1/2}m_Z)
\end{aligned}
$$

$$
\begin{aligned}
&+\frac{1}{6}\left((\Delta_W-10)c_W^4\frac{p^2}{m_W^2}+c_W^2-s_W^2+2c_W^4(12-\Delta_W)+(c_W^2-s_W^2)\Delta_W\frac{m_W^2}{p^2}\right)A_0(m_W)\\
&+\frac{1}{6}\left((10-\Delta_W)c_W^4\frac{p^2}{m_W^2}+(3-10c_W^2+2c_W^4\Delta_W)+(s_W^2-c_W^2)\Delta_W\frac{m_W^2}{p^2}\right)A_0(\xi_W^{1/2}m_W)\\
&+\left(\frac{1}{12}\frac{p^2}{m_Z^2}+\frac{5}{6}-\frac{m_H^2}{6m_Z^2}+\frac{1}{12}\left(\frac{m_H^2}{m_Z^2}-1\right)^2\frac{m_Z^2}{p^2}\right)m_Z^2B_0(p^2,m_H,m_Z)\\
&-\left(4+\frac{17}{3}\frac{p^2}{m_W^2}-\frac{4}{3}\frac{p^4}{m_W^4}-\frac{1}{12}\frac{p^6}{m_W^6}\right)c_W^4m_W^2B_0(p^2,m_W,m_W)\\
&+\left(-\frac{c_W^4}{6}\frac{p^6}{m_W^6}-\frac{c_W^4(3+\Delta_W)}{3}\frac{p^4}{m_W^4}+\frac{s_W^2-c_W^2+c_W^4(16+4\Delta_W-\Delta_W^2)}{6}\frac{p^2}{m_W^2}\right.\\
&\quad\left.+\frac{(s_W^2-c_W^2)(4+\Delta_W)+c_W^4\Delta_W^2}{3}+\frac{(s_W^2-c_W^2)\Delta_W^2}{6}\frac{m_W^2}{p^2}\right)m_W^2B_0(p^2,m_W,\xi_W^{1/2}m_W)\\
&-\frac{1}{12}\left(1-\frac{p^4}{m_Z^4}\right)\Big(p^2-4m_W^2(1-\Delta_W)\Big)B_0(p^2,\xi_W^{1/2}m_W,\xi_W^{1/2}m_W)\Bigg]+\Sigma_T^{ZZ\,\text{tadpole}}\,. \qquad \text{(A.35)}
\end{aligned}
$$

The W-boson self-energy

The fermionic contributions are gauge invariant and given by

$$
\Sigma^{WW}_{T,\text{light ferm.}}(p^2)=\frac{\alpha}{4\pi s_W^2}\,3p^2\left[B_0(p^2,0,0)-\frac{1}{3}\right], \qquad \text{(A.36)}
$$

$$
\begin{aligned}
\Sigma^{WW}_{T,\text{3rd gen. quarks}}(p^2)=\frac{\alpha}{4\pi s_W^2}&\left[\frac{m_t^2}{2}\frac{m_t^2}{p^2}-\frac{p^2}{3}+\left(1-\frac{m_t^2}{2p^2}\right)\Big(m_t^2-A_0(m_t)\Big)\right.\\
&\left.+\left(-\frac{1}{2}\frac{m_t^2}{p^2}-\frac{1}{2}+\frac{p^2}{m_t^2}\right)m_t^2B_0(p^2,0,m_t)\right]. \qquad \text{(A.37)}
\end{aligned}
$$

The electroweak contribution is

$$
\begin{aligned}
&\Sigma^{WW}_{T,\text{electroweak}}(p^2)=\frac{\alpha}{4\pi s_W^2}\Bigg[\frac{p^2}{9}\Big(-1+18s_W^2\Delta_\gamma+3\Delta_W+3c_W^2\Delta_Z\Big)\\
&-\frac{m_H^2+m_Z^2+18m_W^2}{6}-\frac{\Delta_Wm_W^2+c_W^2\Delta_Zm_W^2}{3}+\left(\frac{1}{6}-\frac{m_H^2-m_W^2}{12p^2}\right)A_0(m_H)\\
&+\left(\frac{-10+3s_W^2\Delta_\gamma+c_W^2\Delta_Z}{12}\frac{p^2}{m_W^2}+\frac{12-c_W^2\Delta_Z+9s_W^2\Delta_\gamma}{6}\right.\\
&\qquad\qquad\left.+\frac{m_H^2+m_Z^2(s_W^2-c_W^2)+m_W^2(c_W^2\Delta_Z+3s_W^2\Delta_\gamma)}{12p^2}\right)A_0(m_W)\\
&+\left(\frac{10-3s_W^2\Delta_\gamma-c_W^2\Delta_Z}{12}\frac{p^2}{m_W^2}-\frac{2-\Delta_W}{6}+\frac{3s_W^2\Delta_\gamma-2\Delta_W+c_W^2\Delta_Z}{12}\frac{m_W^2}{p^2}\right)A_0(\xi_W^{1/2}m_W)\\
&+\left(\frac{c_W^2(\Delta_W-10)}{12}\frac{p^2}{m_Z^2}+\frac{8c_W^4+(17-2\Delta_W)c_W^2-s_W^2}{12}\right.\\
&\qquad\qquad\left.+\frac{c_W^4(1+s_W^2)\Delta_W-s_W^2(s_W^2-c_W^2-2c_W^2(s_W^2-6))}{12}\frac{m_Z^2}{p^2}\right)A_0(m_Z)
\end{aligned}
$$

$$
\begin{aligned}
&+\left(\frac{c_W^2(10-\Delta_W)}{12}\frac{p^2}{m_Z^2}+\frac{3-8c_W^4+2c_W^2(\Delta_Z-1)}{12}\right.\\
&\qquad\left.+\frac{c_W^2(2(1-\Delta_Z)+c_W^2(\Delta_W-2))}{12}\frac{m_W^2}{p^2}\right)A_0(\xi_Z^{1/2}m_Z)\\
&+\left(\frac{10-3\Delta_\gamma}{12}\left(\frac{m_W^2}{p^2}+1+\frac{p^2}{m_W^2}+\frac{p^4}{m_W^4}\right)-\frac{22+3\Delta_\gamma}{6}\frac{m_W^2+p^2}{m_W^2}\right)s_W^2m_W^2B_0(p^2,0,m_W)\\
&+\left(\frac{10-3\Delta_\gamma}{12}\left(\frac{m_W^2}{p^2}+1+\frac{p^2}{m_W^2}-\frac{p^4}{m_W^4}\right)+\frac{(\Delta_W-2)^2}{6}\left(1-\frac{m_W^2}{p^2}\right)-\frac{1}{3}\frac{m_W^2}{p^2}\right.\\
&\quad\left.+\left(\frac{\Delta_\gamma}{2}-\frac{4}{3}\right)\frac{p^2}{m_W^2}+\frac{3\Delta_\gamma\Delta_W-4\Delta_W}{12}\left(\frac{m_W^2}{p^2}-\frac{p^2}{m_W^2}\right)\right)s_W^2m_W^2B_0(p^2,0,\xi_W^{1/2}m_W)\\
&+\frac{1}{12}\left(\left(\frac{m_H^2}{m_W^2}-1\right)^2\frac{m_W^2}{p^2}+2\left(5-\frac{m_H^2}{m_W^2}\right)+\frac{p^2}{m_W^2}\right)m_W^2B_0(p^2,m_H,m_W)\\
&+\left(\frac{(1+c_W^2(10+c_W^2))s_W^4}{12}\frac{m_Z^2}{p^2}+\frac{2(1+c_W^2)}{3}(c_W^4-4c_W^2+s_W^2)\right.\\
&\qquad\left.-\frac{9+c_W^2(16+9c_W^2)}{6}\frac{p^2}{m_Z^2}+\frac{2(1+c_W^2)}{3}\frac{p^4}{m_Z^4}+\frac{1}{12}\frac{p^6}{m_Z^6}\right)m_Z^2B_0(p^2,m_W,m_Z)\\
&-\frac{c_W^2}{12}\left((c_W^2+(\Delta_Z-1))^2\frac{m_Z^2}{p^2}+10c_W^2+2(\Delta_Z-1)+\frac{p^2}{m_Z^2}\right)\\
&\qquad\qquad\times\left(1-\frac{p^2}{m_W^2}\right)^2m_W^2B_0(p^2,m_W,\xi_Z^{1/2}m_Z)\\
&-\frac{1}{12}\left((1+c_W^2(\Delta_W-1))^2\frac{m_Z^2}{p^2}+10+2c_W^2(\Delta_W-1)+\frac{p^2}{m_Z^2}\right)\\
&\qquad\qquad\times\left(\left(1-\frac{p^2}{m_Z^2}\right)^2-s_W^4\right)m_Z^2B_0(p^2,m_Z,\xi_W^{1/2}m_W)\\
&+\frac{1}{12}\left(-c_W^4(c_W^2(1-\Delta_W)+(\Delta_Z-1))^2\frac{m_Z^2}{p^2}-2c_W^4(c_W^2(\Delta_W-1)+\Delta_Z-1)\right.\\
&\qquad+((1-\Delta_Z)+c_W^2(\Delta_W-2))(1-\Delta_Z+c_W^2\Delta_W)\frac{p^2}{m_Z^2}\\
&\qquad\left.+2((\Delta_Z-1)+c_W^2(\Delta_W-1))\frac{p^4}{m_Z^4}+\frac{p^6}{m_Z^6}\right)m_Z^2B_0(p^2,\xi_W^{1/2}m_W,\xi_Z^{1/2}m_Z)\Bigg]\\
&+\Sigma_T^{WW,\,\text{tadpole}}\,. \qquad\qquad (\text{A.38})
\end{aligned}
$$

B

Fourier transforms of momentum space potentials

In this Appendix, we collect the analytic Fourier transformations necessary to tranform the NLO potentials from momentum to position space, similar to Appendix B in the corresponding publication [104]. The position space representation then allows to solve the Schrödinger equation and thereby obtain the Sommerfeld factors. If analytic transformations are possible, we give these, whilst we also describe how to determine stable numerical Fourier transforms in cases, in which no analytic transform is possible or known.

As the NLO potential correction is rotationally invariant, we may rewrite the Fourier transfrom (3.6) as

$$V(r = |\mathbf{x}|) = \int \frac{d^3\mathbf{k}}{(2\pi)^3}\, e^{i\mathbf{k}\cdot\mathbf{x}}\, \tilde{V}(\mathbf{k}) = \frac{1}{2\pi^2 r}\int_0^\infty d|\mathbf{k}|\, |\mathbf{k}|\, \sin(|\mathbf{k}|r)\, \tilde{V}(|\mathbf{k}|)\,. \tag{B.1}$$

B.1 Analytic transforms

All structures, except for logarithms involving the triangle functions discussed below, that arise in the momentum space NLO potentials can be Fourier transformed using the expressions in Table B.1. To get to the listed structures, it can be necessary to apply, e.g., partial-fractioning identities, such as

$$\frac{1}{AB} = \frac{1}{B-A}\left(\frac{1}{A} - \frac{1}{B}\right)\,. \tag{B.2}$$

Furthermore, an analytic evaluation in some cases requires rewriting logarithms using

$$\frac{1}{(\mathbf{k}^2+m^2)^n}\left(\frac{\mathbf{k}^2+m^2}{m^2}\right)^{\epsilon} = \frac{1}{(\mathbf{k}^2+m^2)^n} + \epsilon\,\frac{\ln\left(\frac{\mathbf{k}^2+m^2}{m^2}\right)}{(\mathbf{k}^2+m^2)^n} + \mathcal{O}(\epsilon^2)\,. \tag{B.3}$$

Moreover, some transforms are also related by taking derivatives. For example, the transform of

$$\frac{1}{(\mathbf{k}^2+m_W^2)^2} = -\frac{\partial}{\partial(m_W^2)}\frac{1}{\mathbf{k}^2+m_W^2}\,, \tag{B.4}$$

can be obtained by recognizing the transform of the Yukawa potential and afterwards taking the derivative. Finally, the derivative of the Bessel K_ν function for $\nu = \pm 1/2$ which is the case relevant here

$$\left.\frac{\partial K_\nu(z)}{\partial \nu}\right|_{\nu=\pm 1/2} = \pm\sqrt{\frac{\pi}{2z}}\,\Gamma(0,2z)\,e^{z}\,, \quad \text{where} \quad \Gamma(s,z) = \int_z^\infty dt\, t^{s-1}e^{-t} \tag{B.5}$$

$\tilde{V}(\mathbf{k})$	$V(r)$
$\frac{1}{\mathbf{k}^2}$	$\frac{1}{4\pi r}$
$\frac{1}{(\mathbf{k}^2)^n}$	$\frac{\Gamma(2-2n)\sin(n\pi)}{2\pi^2 r^{3-2n}} \qquad (n<3/2)$
$\frac{1}{\mathbf{k}^2+m^2}$	$\frac{1}{4\pi r}e^{-m\,r}$
$\frac{1}{(\mathbf{k}^2+m^2)^2}$	$\frac{1}{8\pi m}e^{-m\,r}$
$\frac{1}{(\mathbf{k}^2+m^2)^n}$	$\frac{2^{-n-\frac{1}{2}}m^{\frac{3}{2}-n}r^{n-\frac{3}{2}}K_{\frac{3}{2}-n}(mr)}{\pi^{3/2}\Gamma(n)} \qquad (n\geq 1/2)$
$\frac{\ln\frac{\mathbf{k}^2+m_W^2}{m_W^2}}{\mathbf{k}^2+m_W^2}$	$\frac{e^{m_W r}\,\Gamma(0,2m_W r)}{4\pi r}-\frac{e^{-m_W r}}{8\pi r}\ln\left(\frac{m_W^2 r^2 e^{2\gamma_E}}{4}\right)$
$\frac{\ln\frac{\mathbf{k}^2+m_W^2}{m_W^2}}{(\mathbf{k}^2+m_W^2)^2}$	$\frac{e^{-m_W r}}{8\pi m_W}-\frac{e^{m_W r}\Gamma(0,2m_W r)}{8\pi m_W}-\frac{e^{-m_W r}}{16\pi m_W}\ln\left(\frac{m_W^2 r^2 e^{2\gamma_E}}{4}\right)$
$\frac{1}{\mathbf{k}^2+m_W^2}\left(\frac{\mathbf{k}^2}{m_t^2}\right)^{\epsilon}$	$\frac{\sin(\pi\epsilon)\Gamma(2\epsilon)\,(m_t r)^{-2\epsilon}\ {}_1F_2\left(1;\frac{1}{2}-\epsilon,1-\epsilon;\frac{1}{4}r^2m_W^2\right)}{2\pi^2 r}$ $-\frac{\sec(\pi\epsilon)\left(\frac{m_W^2}{m_t^2}\right)^{\epsilon}\sinh\left(rm_W\right)}{4\pi r}$
$\frac{\ln\frac{\mathbf{k}^2+m_t^2}{m_t^2}}{\mathbf{k}^2+m_W^2}$	$-\frac{1}{4\pi r}\Big(e^{m_W r}\mathrm{Ei}(-(m_t+m_W)r)+e^{-m_W r}\mathrm{Ei}((m_W-m_t)r)$ $+e^{-m_W r}\ln\frac{m_t^2}{m_t^2-m_W^2}\Big) \qquad (m_t>m_W)$

Table B.1: *Table of Fourier transforms. K_n denotes the modified Bessel function of the second kind,* Ei *the exponential integral function, ${}_nF_m$ the generalized hypergeometric function.*

is the incomplete Gamma function.

As an example on how to obtain the analytic Fourier transforms, we discuss an example that appears in channels, where a massive gauge-boson is exchanged at tree-level. The terms are responsible for the long-distance asymptotic behaviour in such channels, if only a massive exchange is present at tree-level. We consider the linear combination presented in (3.27) (similar terms appear for the Z-only exchange Eqs. (4.29) and (4.31)). Using the second to last result of Table B.1 and relations among derivatives of special functions, the $\mathcal{O}(\epsilon)$ term evaluates to

$$\frac{\ln\frac{\mathbf{k}^2}{m_W^2}}{\mathbf{k}^2+m_W^2}\to-\frac{1}{4\pi r}\left[e^{m_W r}\mathrm{Ei}(-m_W r)+e^{-m_W r}\mathrm{Ei}(m_W r)\right] \tag{B.6}$$

For $r \to \infty$ the right hand side of (B.6) has the behaviour

$$-\frac{1}{2\pi m_W^2}\left(\frac{1}{r^3}+\frac{6}{m_W^2 r^5}+\mathcal{O}\left(r^{-7}\right)\right). \tag{B.7}$$

In (3.27), we have the linear combination

$$\ln\frac{\mathbf{k}^2}{m_W^2}\left[\frac{m_W^2}{(\mathbf{k}^2+m_W^2)^2}-\frac{1}{\mathbf{k}^2+m_W^2}\right]=-\ln\frac{\mathbf{k}^2}{m_W^2}\frac{\partial}{\partial(m_W^2)}\frac{m_W^2}{\mathbf{k}^2+m_W^2} \tag{B.8}$$

which explains why the asymptotics is proportional to r^{-5}. In the case of the $\overline{\text{MS}}$-scheme in momentum space (see footnote 14 in Chapter 3) the second term on the left-hand side of (B.8) is not present. Therefore in this case the asymptotic behaviour goes as r^{-3} (cf. Eq. (3.43)). Similarly, for Z-exchange in overall charged two-particle states, the γ-Z-mixing also gives rise, to such terms, ultimately resulting in an r^{-3} asymptotic behaviour (cf. Eq. (4.32)).

B.2 Numerical transforms

In cases, where the logarithms of the triangle function, arising, e.g., from box-topologies or self-energies, the analytic Fourier transform is not readily available. In the following, we discuss using an example, how to obtain stable numerical transforms in such cases.

The example arises from the self-energies, namely from the Higgs-Z loops, and is given by

$$\frac{\lambda^{1/2}(-\mathbf{k}^2,m_H^2,m_Z^2)}{\mathbf{k}^2(\mathbf{k}^2+m_Z^2)}\ln\left[\frac{\mathbf{k}^2+m_H^2+m_Z^2+\lambda^{1/2}(-\mathbf{k}^2,m_H^2,m_Z^2)}{2m_H m_Z}\right]. \tag{B.9}$$

The naive numerical transform using (B.1) is not always stable, depending on the precise value of r. For $\mathbf{k}\to 0$, (B.9) scales as $1/\mathbf{k}^2$. In the final expression, however, it may happen that the corresponding $1/r$ behaviour in position space cancels against another term in the complete expression for the NLO potential. The subleading terms are exponentially suppressed for large r, which is hard to resolve numerically. We solve this issue by undoing the Feynman-parameter integration that led to the logarithm, writing

$$\begin{aligned}&\frac{\lambda^{1/2}(-\mathbf{k}^2,m_H^2,m_Z^2)}{\mathbf{k}^2(\mathbf{k}^2+m_Z^2)}\ln\left[\frac{\mathbf{k}^2+m_H^2+m_Z^2+\lambda^{1/2}(-\mathbf{k}^2,m_H^2,m_Z^2)}{2m_H m_Z}\right]\\&\quad=\frac{\lambda(-\mathbf{k}^2,m_H^2,m_Z^2)}{\mathbf{k}^2(\mathbf{k}^2+m_Z^2)}\int_0^1 dx\,\frac{1}{2(m_Z^2+(\mathbf{k}^2+m_H^2-m_Z^2)x-\mathbf{k}^2x^2)}\,.\end{aligned} \tag{B.10}$$

We then subtract the Coulombic behavior in the limit $\mathbf{k}\to 0$ by adding the term[1]

$$-\frac{m_H^2-m_Z^2}{2m_Z^2\mathbf{k}^2}\ln\frac{m_H^2}{m_Z^2}\,. \tag{B.11}$$

The Fourier integral over $|\mathbf{k}|$ can now be performed analytically, resulting in

$$\int_0^1 dx\,\frac{1}{8\pi r(m_Z^2(1-x)^2+m_H^2x)}\left[e^{-m_Z r}\frac{m_H^2(4m_Z^2-m_H^2)}{m_Z^2}\right.$$

---

[1] In some cases such a subtraction can even be necessary, e.g., for terms that behave as $1/\mathbf{k}^4$. Only the full NLO potential is guaranteed to have a $\mathbf{k}\to 0$ behaviour which is not more singular than $(\ln\mathbf{k}^2)/\mathbf{k}^2$. Sometimes, the integrand of the Feynman-parameter representation is more singular than $1/\mathbf{k}^2$ even though the integral is not, and to perform the analytic transform the subtraction of an expression that vanishes after integration over Feynman parameters is necessary.

$$+\, e^{-r\sqrt{\frac{m_Z^2}{x}+\frac{m_H^2}{1-x}}}\, \frac{\left(m_Z^2(1-x)^2 - m_H^2 x^2\right)^2}{(1-x)x(m_Z^2(1-x)+m_H^2 x)} \Bigg] \,. \tag{B.12}$$

The above expression looks complicated, however, the numerical integration that has to be performed is now only an integral from $x = 0$ to 1 instead of an integral from $|\mathbf{k}| = 0$ to ∞. This stabilizes the large-r tail as the exponential suppression of the final result is already captured in the integrand before the Feynman-parameter integration, and the numerical difficulty of accurately determining the exponential tail is thus circumvented.

C

Expressions for asymptotic behaviour

In Sections 3.4.1 and 4.3.1, we discussed the asymptotic behaviour of the NLO correction to the potentials in the limits $r \to 0$ and $r \to \infty$. In this Appendix, we provide the mass-dependent functions appearing in the main text. The arctan terms in the expressions below stem from simplifying the real parts of self-energies.

C.1 The $r \to 0$ asymptotics - wino

$$\begin{aligned}
A(m_W, m_Z, m_t) =& -\frac{80 s_W^2}{27} + \frac{(64 c_W^2 - 16)}{9}\frac{m_t^2}{m_Z^2} - \frac{1}{2 c_W^2 s_W^2}\frac{m_t^4}{m_Z^4} - \frac{3 + 2 s_W^2}{6 s_W^2}\ln\frac{m_t^2}{m_Z^2} \\
&+ \left(\frac{c_W^2}{s_W^2} - \frac{m_t^2}{2 s_W^2 m_Z^2}\left(3 - \frac{m_t^4}{m_W^4}\right)\right)\ln\frac{m_t^2}{m_t^2 - m_W^2} \\
&- \sqrt{\frac{4 m_t^2}{m_Z^2} - 1}\ \arctan\left[\frac{\sqrt{4 m_t^2 - m_Z^2}\, m_Z}{2 m_t^2 - m_Z^2}\right] \\
&\times \left(\frac{4}{3} - \frac{1}{2 s_W^2} - \frac{16 s_W^2}{9} + \left(\frac{8}{3} + \frac{1}{2 s_W^2} - \frac{32 s_W^2}{9}\right)\frac{m_t^2}{m_Z^2}\right) \qquad \text{(C.1)}
\end{aligned}$$

$$\begin{aligned}
B(m_W, m_Z, m_H) =& \frac{125}{6} - \frac{1}{12 c_W^2} - \frac{80 s_W^2}{3} - 8 c_W^2 s_W^2 - \frac{m_H^4}{12 m_W^2 m_Z^2} \\
&+ \left(-\frac{s_W^2}{c_W^2} + \frac{1 - c_W^4}{6 c_W^4}\frac{m_H^2}{m_Z^2}\right)\frac{m_H^4}{4 s_W^2 m_Z^4}\ln\frac{m_H^2}{m_Z^2} \\
&+ \left(-\frac{1 + 11 c_W^2}{2 c_W^2} + \frac{13 + 10 c_W^2}{6 s_W^2} - \frac{1 + 2 c_W^2}{24 c_W^4 s_W^2}\right. \\
&\qquad \left. - \frac{3 m_H^2}{4 m_Z^2 s_W^2} + \frac{m_H^4}{4 m_W^2 m_Z^2 s_W^2} - \frac{m_H^6}{24 m_W^4 m_Z^2 s_W^2}\right)\ln\frac{m_W^2}{m_Z^2} \\
&+ \sqrt{\frac{4 m_W^2}{m_Z^2} - 1}\arctan\left[\frac{\sqrt{\frac{4 m_W^2}{m_Z^2} - 1}}{\frac{2 m_W^2}{m_Z^2} - 1}\right]\left(-\frac{1}{12} - \frac{29 c_W^2}{3} - 4 c_W^4 + \frac{33 c_W^2}{4 s_W^2}\right) \\
&+ \sqrt{\frac{4 m_W^2}{m_Z^2} - 1}\arctan\left[\sqrt{\frac{4 m_W^2}{m_Z^2} - 1}\right]\left(4 + \frac{4}{3 c_W^2} - \frac{25}{3 s_W^2} + \frac{1}{12 c_W^4 s_W^2}\right)
\end{aligned}$$

$$
\begin{aligned}
&- \sqrt{\frac{4m_Z^2}{m_H^2} - 1}\arctan\left[\sqrt{\frac{4m_Z^2}{m_H^2} - 1}\right]\left(\frac{m_H^2}{m_Z^2 s_W^2} - \frac{m_H^4}{3m_Z^4 s_W^2} + \frac{m_H^6}{12m_Z^6 s_W^2}\right) \\
&+ \sqrt{\frac{4m_W^2}{m_H^2} - 1}\arctan\left[\sqrt{\frac{4m_W^2}{m_H^2} - 1}\right] \\
&\times \left(\frac{m_H^2}{m_Z^2 s_W^2} - \frac{m_H^4}{3m_W^2 m_Z^2 s_W^2} + \frac{m_H^6}{12m_W^4 m_Z^2 s_W^2}\right) \qquad \text{(C.2)}
\end{aligned}
$$

C.2 The $r \to \infty$ asymptotics - wino

$$
\begin{aligned}
C(m_W, m_Z, m_H) &= \frac{109}{8} - \frac{299 s_W^2}{72} - \frac{3029 s_W^4}{90} + \frac{104 s_W^6}{3} - 8 s_W^8 - \frac{3c_W^2 m_H^2}{8m_Z^2} - \frac{s_W^2 m_H^4}{12 m_Z^4} \\
&+ \ln\frac{m_H^2}{m_Z^2}\frac{c_W^2 m_H^2}{m_H^2 - m_Z^2}\left(\frac{3}{2} + \frac{(s_W^2 - 3c_W^2)m_H^2}{4m_W^2} - \frac{(1 + 7c_W^2 s_W^2)m_H^4}{24 m_W^4} + \frac{c_W^2(1 + c_W^2 s_W^2)m_H^6}{24 m_W^6}\right) \\
&- \frac{\ln\frac{m_W^2}{m_Z^2}}{24 c_W^2 s_W^2}\left(1 + 14c_W^2 - 106 c_W^4 + 2c_W^6 + 18 c_W^4 \frac{m_H^2}{m_Z^2} - 6c_W^2\frac{m_H^4}{m_Z^4} + \frac{m_H^6}{m_Z^6}\right) \\
&+ \sqrt{\frac{4m_W^2}{m_Z^2} - 1}\arctan\sqrt{\frac{4m_W^2}{m_Z^2} - 1}\left(\frac{4}{3} + 4c_W^2 + \frac{1}{12 c_W^2 s_W^2} - \frac{25 c_W^2}{3 s_W^2}\right) \\
&+ \sqrt{\frac{4m_W^2}{m_Z^2} - 1}\arctan\left[\frac{\sqrt{\frac{4m_W^2}{m_Z^2} - 1}}{\frac{2m_W^2}{m_Z^2} - 1}\right] c_W^2\left(-\frac{55}{4} + \frac{33}{4s_W^2} - \frac{13 s_W^2}{3} + \frac{41 s_W^4}{3} - 4s_W^6\right) \\
&+ \sqrt{\frac{4m_W^2}{m_H^2} - 1}\frac{c_W^2 m_H^2}{s_W^2 m_Z^2}\arctan\left[\sqrt{\frac{4m_W^2}{m_H^2} - 1}\right]\left(1 - \frac{m_H^2}{3m_W^2} + \frac{m_H^4}{12 m_W^4}\right) \\
&- \sqrt{\frac{4m_Z^2}{m_H^2} - 1}\frac{m_H^2}{m_Z^2}\frac{c_W^2 + s_W^2 c_W^2}{s_W^2}\arctan\left[\sqrt{\frac{4m_Z^2}{m_H^2} - 1}\right]\left(1 - \frac{m_H^2}{3m_Z^2} + \frac{m_H^4}{12 m_Z^4}\right) \qquad \text{(C.3)}
\end{aligned}
$$

$$
\begin{aligned}
D(m_W, m_Z, m_t) &= \frac{80 s_W^2}{27} + \left(\frac{16}{9} - \frac{64 c_W^2}{9} - \frac{1}{4c_W^2}\right)\frac{m_t^2}{m_Z^2} + \frac{c_W^2 - s_W^2}{2s_W^2}\frac{m_t^4}{m_W^4} \\
&+ \frac{c_W^2 - s_W^2}{s_W^2}\ln\frac{m_t^2}{m_t^2 - m_W^2}\left(-1 + \frac{3m_t^2}{2m_W^2} - \frac{m_t^6}{2m_W^6}\right) + \frac{3c_W^2 - s_W^2}{6s_W^2}\ln\frac{m_t^2}{m_Z^2} \\
&+ \sqrt{\frac{4m_t^2}{m_Z^2} - 1}\arctan\left[\frac{\sqrt{\frac{4m_t^2}{m_Z^2} - 1}}{\frac{2m_t^2}{m_Z^2} - 1}\right] \\
&\times\left(\frac{16 c_W^2}{9} - \frac{17}{18 s_W^2} + \frac{4c_W^2}{9s_W^2} + \left(\frac{32 c_W^2}{9} - \frac{7}{18 s_W^2} + \frac{8c_W^2}{9s_W^2}\right)\frac{m_t^2}{m_Z^2}\right) \qquad \text{(C.4)}
\end{aligned}
$$

$$
\begin{aligned}
E(m_W, m_Z, m_H) &= -\frac{145}{12} + \frac{2 + 29 c_W^2}{24 c_W^4} + \frac{56 c_W^2}{3} + 8c_W^4 - \frac{3}{8}\frac{m_H^2}{m_W^2} + \frac{s_W^2}{12}\frac{m_H^4}{m_W^4} \\
&+ \ln\frac{m_H^2}{m_Z^2}\frac{m_H^2}{m_H^2 - m_W^2}\left(\frac{3}{2} + \frac{c_W^2 - 4}{4}\frac{m_H^2}{m_W^2} + \frac{7s_W^2 - c_W^4}{24}\frac{m_H^4}{m_W^4} + \frac{c_W^4 - s_W^2}{24}\frac{m_H^6}{m_W^6}\right)
\end{aligned}
$$

$$
\begin{aligned}
&+\ln\frac{m_W^2}{m_Z^2}\left(\frac{65}{12}\frac{c_W^2-s_W^2}{c_W^2 s_W^2}+\frac{1}{24 s_W^2 c_W^6}+\frac{1}{2 s_W^2 c_W^4}-\frac{3}{4}+\frac{3}{4}\frac{s_W^2-c_W^2}{s_W^2}\frac{m_H^2}{m_W^2}\right.\\
&\qquad\left.+\frac{c_W^2-s_W^2}{4 s_W^2}\frac{m_H^4}{m_W^4}+\frac{s_W^2-c_W^2}{24 s_W^2}\frac{m_H^6}{m_W^6}-\frac{3}{4}\frac{m_W^2}{m_H^2-m_W^2}\right)\\
&+\sqrt{\frac{4m_W^2}{m_H^2}-1}\arctan\left[\sqrt{\frac{4m_W^2}{m_H^2}-1}\right]\frac{c_W^2-s_W^2}{s_W^2}\left(\frac{m_H^2}{m_W^2}-\frac{1}{3}\frac{m_H^4}{m_W^4}+\frac{1}{12}\frac{m_H^6}{m_W^6}\right)\\
&-\sqrt{\frac{4m_Z^2}{m_H^2}-1}\arctan\left[\sqrt{\frac{4m_Z^2}{m_H^2}-1}\right]\frac{1}{s_W^2}\left(\frac{m_H^2}{m_Z^2}-\frac{1}{3}\frac{m_H^4}{m_Z^4}+\frac{1}{12}\frac{m_H^6}{m_Z^6}\right)\\
&+\sqrt{\frac{4m_W^2}{m_Z^2}-1}\arctan\left[\sqrt{\frac{4m_W^2}{m_Z^2}-1}\right]\frac{c_W^2-s_W^2}{c_W^2}\left(\frac{4-17c_W^2}{3c_W^2 s_W^2}-\frac{4c_W^2}{s_W^2}+\frac{1}{12 c_W^4 s_W^2}\right)\\
&+\sqrt{\frac{4m_W^2}{m_Z^2}-1}\arctan\left[\frac{\sqrt{\frac{4m_W^2}{m_Z^2}-1}}{\frac{2m_W^2}{m_Z^2}-1}\right]\left(\frac{33}{4s_W^2}-22+\frac{53 s_W^2}{3}-4s_W^4\right)
\end{aligned}
\tag{C.5}
$$

C.3 The $r \to \infty$ asymptotics - arbitrary SM representation

$$
\begin{aligned}
F(m_W,m_Z,m_H)={}&\frac{151 s_W^2}{360}-\frac{1049 c_W^2}{72}+\frac{80 s_W^2 c_W^2}{3}-8s_W^4-\frac{3}{8}\frac{m_H^2}{m_Z^2}+\frac{1}{12}\frac{m_H^4}{m_Z^4}\\
&+\frac{1}{12}\ln\frac{m_W^2}{m_Z^2}-\frac{\ln\frac{m_H^2}{m_Z^2}}{12\left(\frac{m_H^2}{m_Z^2}-1\right)}\left(-\frac{3}{2}\frac{m_H^2}{m_Z^2}+\frac{m_H^4}{m_Z^4}-\frac{7}{24}\frac{m_H^6}{m_Z^6}+\frac{1}{24}\frac{m_H^8}{m_Z^8}\right)\\
&+\sqrt{\frac{4m_Z^2}{m_H^2}-1}\arctan\left[\sqrt{\frac{4m_Z^2}{m_H^2}-1}\right]\left(-\frac{m_H^2}{m_Z^2}+\frac{1}{3}\frac{m_H^4}{m_Z^4}-\frac{1}{12}\frac{m_H^6}{m_Z^6}\right)\\
&+\sqrt{\frac{4m_W^2}{m_Z^2}-1}\arctan\left[\frac{\sqrt{\frac{4m_W^2}{m_Z^2}-1}}{\frac{2m_W^2}{m_Z^2}-1}\right]\left(-\frac{1}{12}-\frac{4}{3}c_W^2+\frac{17}{3}c_W^4+4c_W^6\right)
\end{aligned}
\tag{C.6}
$$

$$
\begin{aligned}
I(m_W,m_Z,m_H)={}&\frac{1349 s_W^2}{90}-\frac{s_W^2}{12 c_W^4}-\frac{11 s_W^2}{8 c_W^2}+\frac{56 c_W^2 s_W^2}{3}+8c_W^4 s_W^2\\
&+\frac{3s_W^2}{8}\frac{m_H^2}{m_W^2}-\frac{(1+c_W^2)s_W^2}{12}\frac{m_H^4}{m_W^4}\\
&+\ln\frac{m_W^2}{m_Z^2}\left(\frac{1}{12}+\frac{17}{4c_W^2}-\frac{7}{12c_W^4}-\frac{1}{24c_W^6}-\frac{3}{4}\frac{m_H^2}{m_W^2}+\frac{1}{4}\frac{m_H^4}{m_W^4}-\frac{1}{24}\frac{m_H^6}{m_W^6}\right)\\
&+\ln\frac{m_H^2}{m_Z^2}\frac{m_H^2}{m_H^2-m_Z^2}\left(-\frac{3s_W^2}{2c_W^2}+\frac{s_W^2(1+4c_W^2)}{4c_W^2}\frac{m_H^2}{m_W^2}+\frac{7c_W^6-6c_W^2-1}{24c_W^2}\frac{m_H^4}{m_W^4}+\frac{1-c_W^6}{24}\frac{m_H^6}{m_W^6}\right)\\
&+\sqrt{\frac{4m_W^2}{m_Z^2}-1}\arctan\left[\sqrt{\frac{4m_W^2}{m_Z^2}-1}\right]\left(\frac{1}{12c_W^6}+\frac{4}{3c_W^4}-\frac{17}{3c_W^2}-4\right)
\end{aligned}
$$

$$\begin{aligned}
&+\sqrt{\frac{4m_W^2}{m_Z^2}-1}\,\arctan\left[\frac{\sqrt{\frac{4m_W^2}{m_Z^2}-1}}{\frac{2m_W^2}{m_Z^2}-1}\right]\left(-\frac{1}{12}-\frac{4c_W^2}{3}+\frac{17c_W^4}{3}+4c_W^6\right)\\
&+\sqrt{\frac{4m_W^2}{m_H^2}-1}\,\arctan\left[\sqrt{\frac{4m_W^2}{m_H^2}-1}\right]\left(\frac{m_H^2}{m_W^2}-\frac{1}{3}\frac{m_H^4}{m_W^4}+\frac{1}{12}\frac{m_H^6}{m_W^6}\right)\\
&+\sqrt{\frac{4m_Z^2}{m_H^2}-1}\,\arctan\left[\sqrt{\frac{4m_Z^2}{m_H^2}-1}\right]\left(-\frac{m_H^2}{m_Z^2}+\frac{1}{3}\frac{m_H^4}{m_Z^4}-\frac{1}{12}\frac{m_H^6}{m_Z^6}\right)
\end{aligned}\tag{C.7}$$

C.4 The $r \to 0$ asymptotics - arbitrary SM representation

$$\begin{aligned}
G(m_W,m_Z,m_t)=&-\frac{80c_W^2}{27}+\frac{16c_W^2(1-4c_W^2)}{9}\frac{m_t^2}{m_W^2}+\frac{c_W^2}{2s_W^2}\frac{m_t^4}{m_W^4}+\ln\frac{m_t^2}{m_Z^2}\left(\frac{1}{2s_W^2}-\frac{13}{9}\right)\\
&+\frac{1}{s_W^2}\sqrt{\frac{4m_t^2}{m_Z^2}-1}\,\arctan\left[\frac{\sqrt{\frac{4m_t^2}{m_Z^2}-1}}{\frac{2m_t^2}{m_Z^2}-1}\right]\left(-\frac{17}{18}+\frac{20c_W^2}{9}-\frac{16c_W^4}{9}-\left(\frac{7}{18}-\frac{40c_W^2}{9}+\frac{32c_W^4}{9}\right)\frac{m_t^2}{m_Z^2}\right)\\
&+\frac{c_W^2}{s_W^2}\ln\frac{m_t^2}{m_t^2-m_W^2}\left(-1+\frac{3}{2}\frac{m_t^2}{m_W^2}-\frac{1}{2}\frac{m_t^6}{m_W^6}\right)
\end{aligned}\tag{C.8}$$

$$\begin{aligned}
H(m_W,m_Z,m_H)=&\frac{80c_W^2}{3}-\frac{1}{12c_W^2}-\frac{1}{2}-8c_W^2s_W^2-\frac{c_W^2}{12}\frac{m_H^4}{m_W^4}\\
&+\frac{c_W^2}{s_W^2}\ln\frac{m_H^2}{m_W^2}\left(\frac{1}{24}\frac{m_H^6}{m_W^6}-\frac{1}{4}\frac{m_H^4}{m_W^4}\right)+\frac{1}{s_W^2}\ln\frac{m_H^2}{m_Z^2}\left(-\frac{1}{24}\frac{m_H^6}{m_Z^6}+\frac{1}{4}\frac{m_H^4}{m_Z^4}\right)\\
&+\frac{1}{s_W^2}\ln\frac{m_W^2}{m_Z^2}\left(\frac{c_W^2}{6}-\frac{1}{24c_W^4}-\frac{7}{12c_W^2}+\frac{25}{6}-\frac{3}{4}\frac{m_H^2}{m_Z^2}\right)\\
&+\frac{1}{s_W^2}\sqrt{\frac{4m_W^2}{m_Z^2}-1}\,\arctan\left[\sqrt{\frac{4m_W^2}{m_Z^2}-1}\right]\left(-4c_W^2+\frac{1}{12c_W^4}+\frac{4}{3c_W^2}-\frac{17}{3}\right)\\
&+\frac{1}{s_W^2}\sqrt{\frac{4m_W^2}{m_Z^2}-1}\,\arctan\left[\frac{\sqrt{\frac{4m_W^2}{m_Z^2}-1}}{\frac{2m_W^2}{m_Z^2}-1}\right]\left(-\frac{1}{12}-\frac{4c_W^2}{3}+\frac{17c_W^4}{3}+4c_W^6\right)\\
&+\frac{c_W^2}{s_W^2}\sqrt{\frac{4m_W^2}{m_H^2}-1}\,\arctan\left[\sqrt{\frac{4m_W^2}{m_H^2}-1}\right]\left(\frac{1}{12}\frac{m_H^6}{m_W^6}-\frac{1}{3}\frac{m_H^4}{m_W^4}+\frac{m_H^2}{m_W^2}\right)\\
&+\frac{1}{s_W^2}\sqrt{\frac{4m_Z^2}{m_H^2}-1}\,\arctan\left[\sqrt{\frac{4m_Z^2}{m_H^2}-1}\right]\left(-\frac{1}{12}\frac{m_H^6}{m_Z^6}+\frac{1}{3}\frac{m_H^4}{m_Z^4}-\frac{m_H^2}{m_Z^2}\right)
\end{aligned}\tag{C.9}$$

D

NLO potentials arbitrary representations - Technical details

This Appendix presents the derivation of the prefactors for arbitrary minimal DM, which is necessary to construct the NLO results discussed in Chapter 4. We do not repeat the calculation of loop integrals, as all loop integrals are proportional to corresponding wino topologies, discussed at length in Appendix A. The notation for the channels is as laid out in the main text, in particular in Chapter 4.

D.1 Self-energies and counterterms

Some terms are trivially related to the tree-level potentials. Such terms are the self-energies and all counterterms except the wave-function renormalization, which we treat together with the vertex corrections in the next Section. For the W-potentials, self-energies and counterterms lead to

$$\delta V^{W}_{(ij),(kl)}\Big|_{\text{self-en./ct.}} = V^{W}_{(ij),(kl)}\left(2\delta Z_e - 2\frac{\delta s_W}{s_W} + \frac{\Sigma_T^{WW}(-\mathbf{k}^2) - \delta m_W^2}{\mathbf{k}^2 + m_W^2}\right). \tag{D.1}$$

The T^3T^3 contribution receives the correction

$$\begin{aligned}\delta V^{T3T3}_{(ij),(ij)}\Big|_{\text{self-en./ct.}} &= +\frac{4\pi\alpha}{\mathbf{k}^2}\left(T^3_{R,ii}T^3_{R,jj}\right)\left(2\delta Z_e + \frac{\Sigma_T^{\gamma\gamma}(-\mathbf{k}^2)}{\mathbf{k}^2}\right)\\ &+ \frac{4\pi\alpha}{\mathbf{k}^2 + m_Z^2}\left(T^3_{R,ii}T^3_{R,jj}\right)\frac{c_W^2}{s_W^2}\left(2\delta Z_e + 2\frac{\delta c_W}{c_W} - 2\frac{\delta s_W}{s_W} + \frac{\Sigma_T^{ZZ}(-\mathbf{k}^2) - \delta m_Z^2}{\mathbf{k}^2 + m_Z^2}\right)\\ &+ \frac{4\pi\alpha}{\mathbf{k}^2(\mathbf{k}^2 + m_Z^2)}\left(T^3_{R,ii}T^3_{R,jj}\right)\frac{-2c_W}{s_W}\Sigma_T^{\gamma Z}(-\mathbf{k}^2)\,. \end{aligned}\tag{D.2}$$

For the mixed T^3Y contribution, we have

$$\begin{aligned}\delta V^{T3Y}_{(ij),(ij)}\Big|_{\text{self-en./ct.}} &= +\frac{4\pi\alpha}{\mathbf{k}^2}\left(T^3_{R,ii}Y_j + T^3_{R,jj}Y_i\right)\left(2\delta Z_e + \frac{\Sigma_T^{\gamma\gamma}(-\mathbf{k}^2)}{\mathbf{k}^2}\right)\\ &- \frac{4\pi\alpha}{\mathbf{k}^2 + m_Z^2}\left(T^3_{R,ii}Y_j + T^3_{R,jj}Y_i\right)\left(2\delta Z_e + \frac{\Sigma_T^{ZZ}(-\mathbf{k}^2) - \delta m_Z^2}{\mathbf{k}^2 + m_Z^2}\right)\\ &+ \frac{4\pi\alpha}{\mathbf{k}^2(\mathbf{k}^2 + m_Z^2)}\left(T^3_{R,ii}Y_j + T^3_{R,jj}Y_i\right)\left(\frac{s_W}{c_W} - \frac{c_W}{s_W}\right)\Sigma_T^{\gamma Z}(-\mathbf{k}^2)\,. \end{aligned}\tag{D.3}$$

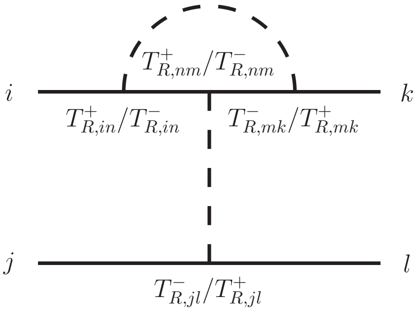

Figure D.1: *Example of a vertex correction to the W-Yukawa potential.*

Finally the Y^2 contribution results in

$$\begin{aligned}\delta V^{YY}_{(ij),(ij)}\Big|_{\text{self-en./ct.}} &= +\frac{4\pi\alpha}{\mathbf{k}^2}\left(Y_iY_j\right)\left(2\delta Z_e + \frac{\Sigma_T^{\gamma\gamma}(-\mathbf{k}^2)}{\mathbf{k}^2}\right) \\ &\quad + \frac{4\pi\alpha}{\mathbf{k}^2+m_Z^2}\frac{s_W^2}{c_W^2}\left(Y_iY_j\right)\left(2\delta Z_e - 2\frac{\delta c_W}{c_W} + 2\frac{\delta s_W}{s_W} + \frac{\Sigma_T^{ZZ}(-\mathbf{k}^2)-\delta m_Z^2}{\mathbf{k}^2+m_Z^2}\right) \\ &\quad + \frac{4\pi\alpha}{\mathbf{k}^2(\mathbf{k}^2+m_Z^2)}\left(Y_iY_j\right)\frac{2s_W}{c_W}\Sigma_T^{\gamma Z}(-\mathbf{k}^2)\,. \end{aligned} \tag{D.4}$$

D.2 Vertex and wave-function correction

We treat the vertex contribution and the wave-function correction together. The reason is that both corrections only contain poles and logarithms but no finite pieces. Also, as we will see, there is a partial cancellation necessary to prove the universal behaviour of the potential correction.

The wave-function correction for a fermion/scalar i in the multiplet reads

$$\begin{aligned}\delta Z_{\chi_i} &= \left\{T_R^+, T_R^-\right\}_{ii}\frac{\alpha_2}{4\pi}\left(\frac{1}{\epsilon} - \ln\frac{m_W^2}{\mu^2} + \frac{A_0(m_W) - A_0(\xi_W^{1/2}m_W)}{2m_W^2}\right) \\ &\quad + \frac{\alpha}{4\pi}\left(\frac{c_W}{s_W}T^3_{R,ii} - \frac{s_W}{c_W}Y_i\right)^2\left(\frac{1}{\epsilon} - \ln\frac{m_Z^2}{\mu^2} + \frac{A_0(m_Z) - A_0(\xi_Z^{1/2}m_Z)}{2m_Z^2}\right)\,, \end{aligned} \tag{D.5}$$

see Appendix A.1.3 for the wino result and integrals.

The vertex correction is assembled in the standard way. As an example, we discuss the diagram given in Figure D.1. Useful identities are

$$\left[T_R^3, T_R^+\right] = -T_R^+\,, \qquad \left[T_R^3, T_R^-\right] = T_R^-\,, \qquad \left[T_R^+, T_R^-\right] = -T_R^3\,. \tag{D.6}$$

The diagram results in

$$\begin{aligned}&\Big[\left(T_R^+T_R^+T_R^-\right)_{ik}T^-_{R,jl} + \left(T_R^+T_R^-T_R^-\right)_{ik}T^+_{R,jl} + \left(T_R^-T_R^+T_R^+\right)_{ik}T^-_{R,jl} + \left(T_R^-T_R^-T_R^+\right)_{ik}T^+_{R,jl}\Big] \\ &\quad\times I_{\text{vertex}}(\alpha_2, m_W)\frac{(-1)^{n_Q}(4\pi\alpha_2)}{\mathbf{k}^2+m_W^2} \\ &= \Big[\left(T_R^+T_R^-\right)_{kk}T^+_{R,ik}T^-_{R,jl} + \left(T_R^+T_R^-\right)_{ii}T^-_{R,ik}T^+_{R,jl} + \left(T_R^-T_R^+\right)_{ii}T^+_{R,ik}T^-_{R,jl} \\ &\quad + \left(T_R^-T_R^+\right)_{kk}T^-_{R,ik}T^+_{R,jl}\Big]\, I_{\text{vertex}}(\alpha_2, m_W)\frac{(-1)^{n_Q}(4\pi\alpha_2)}{\mathbf{k}^2+m_W^2}\,. \end{aligned} \tag{D.7}$$

As $T^\pm$ are creation and annihilation operators, the linear combination $T^\pm T^\mp$ is a diagonal matrix, therefore we can simplify $(T_R^+T_R^+T_R^-)_{ik}T^-_{jl} = (T_R^+T_R^-)_{kk}T^+_{R,ik}T^-_{R,jl}$, which makes the connection to the tree-level apparent. Together with the loop attached to the lower line, the W-loops are then proportional to the tree-level potential. The same diagram involving a Z-boson in the loop is trivially proportional to the tree-level, as the index at the upper line did not change due to Z-exchange.

For the W-exchange channel, we find for vertex and wave-function correction

$$\begin{aligned}
\delta V^W_{(ij),(kl)}\Big|_{\text{WF/vertex}} &= V^W_{(ij),(kl)}\left(\delta Z_{\chi_i}+\delta Z_{\chi_j}+\delta Z_{\chi_k}+\delta Z_{\chi_l}\right)\\
&+\left[\left\{T_R^+,T_R^-\right\}_{ii}+\left\{T_R^+,T_R^-\right\}_{kk}+\left\{T_R^+,T_R^-\right\}_{jj}+\left\{T_R^+,T_R^-\right\}_{ll}\right]V^W_{(ij),(kl)}I_{\text{vertex}}(\alpha_2,m_W)\\
&+\left[\frac{1}{2}\left(T^3_{R,ii}-T^3_{R,jj}-T^3_{R,kk}+T^3_{R,ll}\right)T^+_{R,ik}T^-_{R,jl}\right.\\
&\quad\left.+\frac{1}{2}\left(-T^3_{R,ii}+T^3_{R,jj}+T^3_{R,kk}-T^3_{R,ll}\right)T^-_{R,ik}T^+_{R,jl}\right](-1)^{n_Q}\frac{4\pi\alpha_2}{\mathbf{k}^2+m_W^2}I_{\text{vertex}}(\alpha_2,m_W)\\
&+V^W_{(ij),(kl)}I_{\text{vertex}}\left(\alpha\left(\frac{c_W}{s_W}T^3_{R,ii}-\frac{s_W}{c_W}Y_i\right)\left(\frac{c_W}{s_W}T^3_{R,kk}-\frac{s_W}{c_W}Y_k\right),m_Z\right)\\
&+V^W_{(ij),(kl)}I_{\text{vertex}}\left(\alpha\left(\frac{c_W}{s_W}T^3_{R,jj}-\frac{s_W}{c_W}Y_j\right)\left(\frac{c_W}{s_W}T^3_{R,ll}-\frac{s_W}{c_W}Y_l\right),m_Z\right)\\
&=V^W_{(ij),(kl)}\frac{\alpha_2}{2\pi}\left(\frac{1+c_W^2}{\epsilon}-\ln\frac{m_W^2}{\mu^2}-c_W^2\ln\frac{m_Z^2}{\mu^2}\right.\\
&\qquad\left.+\frac{A_0(m_W)-A_0(\xi_W^{1/2}m_W)}{2m_W^2}+c_W^2\frac{A_0(m_Z)-A_0(\xi_Z^{1/2}m_Z)}{2m_Z^2}\right)
\end{aligned}\tag{D.8}$$

the crucial observation here is that wave-function and vertex correction cancel such that there is always the same term in the bracket, multiplying the tree-level potential. Furthermore note that $Y_i = Y_k$ and $Y_j = Y_l$. To obtain the final result, we have made use of the fact that

$$T^+_{R,ik}(T^3_{R,kk}-T^3_{R,ii}) = T^+_{R,ik}\qquad T^-_{R,ik}(T^3_{R,kk}-T^3_{R,ii}) = -T^-_{R,ik}\,,\tag{D.9}$$

and that vertex and wave-function poles/logarithms cancel except for the common remnant. Similar observations hold in the γ/Z exchange channels. To find the necessary cancellations, we make use of

$$\left(T_R^+T_R^3T_R^-+T_R^-T_R^3T_R^+\right)_{ii} = -T^3_{R,ii}+\left\{T_R^+,T_R^-\right\}_{ii}T^3_{R,ii}\,.\tag{D.10}$$

The terms proportional T^3T^3 receive the correction

$$\begin{aligned}
\delta V^{T3T3}_{(ij),(ij)}\Big|_{\text{vertex/WF}} &= V^{T3T3}_{(ij),(ij)}\left(2\delta Z_{\chi_i}+2\delta Z_{\chi_j}\right)\\
&+V^{T3T3}_{(ij),(ij)}\left(-2+\left\{T_R^+,T_R^-\right\}_{ii}+\left\{T_R^+,T_R^-\right\}_{jj}\right)I_{\text{vertex}}(\alpha_2,m_W)\\
&+V^{T3T3}_{(ij),(ij)}I_{\text{vertex}}\left(\alpha\left(\frac{c_W}{s_W}T^3_{R,ii}-\frac{s_W}{c_W}Y_i\right)^2,m_Z\right)\\
&+V^{T3T3}_{(ij),(ij)}I_{\text{vertex}}\left(\alpha\left(\frac{c_W}{s_W}T^3_{R,jj}-\frac{s_W}{c_W}Y_j\right)^2,m_Z\right)\\
&=V^{T3T3}_{(ij),(ij)}\frac{\alpha_2}{\pi}\left(\frac{1}{\epsilon}+\ln\frac{\mu^2}{m_W^2}+\frac{A_0(m_W)-A_0(\xi_W^{1/2}m_W)}{2m_W^2}\right)\,.
\end{aligned}\tag{D.11}$$

For T^3Y-terms we find

$$\begin{aligned}
\delta V^{T3Y}_{(ij),(ij)}\Big|_{\text{vertex/WF}} &= V^{T3Y}_{(ij),(ij)}\left(2\delta Z_{\chi_i} + 2\delta Z_{\chi_j}\right) \\
&+ V^{T3Y}_{(ij),(ij)}\left(-1 + \left\{T^+_R, T^-_R\right\}_{ii} + \left\{T^+_R, T^-_R\right\}_{jj}\right) \\
&+ V^{T3Y}_{(ij),(ij)} I_{\text{vertex}}\left(\alpha\left(\frac{c_W}{s_W}T^3_{R,ii} - \frac{s_W}{c_W}Y_i\right)^2, m_Z\right) \\
&+ V^{T3Y}_{(ij),(ij)} I_{\text{vertex}}\left(\alpha\left(\frac{c_W}{s_W}T^3_{R,jj} - \frac{s_W}{c_W}Y_j\right)^2, m_Z\right) \\
&= V^{T3Y}_{(ij),(ij)}\frac{\alpha_2}{2\pi}\left(\frac{1}{\epsilon} + \ln\frac{\mu^2}{m_W^2} + \frac{A_0(m_W) - A_0(\xi_W^{1/2} m_W)}{2m_W^2}\right)
\end{aligned} \tag{D.12}$$

and finally for Y^2 terms, we have the vanishing combination

$$\begin{aligned}
\delta V^{YY}_{(ij),(ij)}\Big|_{\text{vertex/WF}} &= V^{YY}_{(ij),(ij)}\left(2\delta Z_{\chi_i} + 2\delta Z_{\chi_j}\right) \\
&+ V^{YY}_{(ij),(ij)}\left(\left\{T^+_R, T^-_R\right\}_{ii} + \left\{T^+_R, T^-_R\right\}_{jj}\right) I_{\text{vertex}}(\alpha_2, m_W) \\
&+ V^{YY}_{(ij),(ij)} I_{\text{vertex}}\left(\alpha\left(\frac{c_W}{s_W}T^3_{R,ii} - \frac{s_W}{c_W}Y_i\right)^2, m_Z\right) \\
&+ V^{YY}_{(ij),(ij)} I_{\text{vertex}}\left(\alpha\left(\frac{c_W}{s_W}T^3_{R,jj} - \frac{s_W}{c_W}Y_j\right)^2, m_Z\right) \\
&= 0\,.
\end{aligned} \tag{D.13}$$

D.3 Triple gauge vertex topologies

The structure of the triple gauge boson diagrams allows, in the case of the W-Yukawa potential, only $W\gamma$ and WZ loops, as between the upper and lower line of the diagram, one charge unit needs to be transferred. The structures appearing are the same as in the case of the wino, with adjusted couplings. Note that, in addition, now further diagrams are in principle possible, as multiply charged fermions are possible within general multiplets.

$$\begin{aligned}
\delta V^{W}_{(ij),(kl)}\Big|_{\text{triple}-\text{vertex}} &= (-1)^{n_Q}\frac{4\pi\alpha_2}{\mathbf{k}^2 + m_W^2}\left(I^{W\gamma}_{3\,\text{gauge}} + I^{WZ}_{3\,\text{gauge}}\right) \\
&\times\left(T^+_{R,ik}T^-_{R,jl} - T^-_{R,ik}T^+_{R,jl}\right)\left(T^3_{R,kk} - T^3_{R,ii} + T^3_{R,ll} - T^3_{R,jj}\right) \\
&= V^{W}_{(ij),(kl)}\left(2I^{W\gamma}_{3\,\text{gauge}} + 2I^{WZ}_{3\,\text{gauge}}\right)\,,
\end{aligned} \tag{D.14}$$

where the various minus signs in the first equality stem from particle exchange for the triple gauge boson vertex. Note that the abelian piece $\sim Y$ cancels among the diagrams. To obtain the tree-level structure in the last line, we used Eq. (D.9) which flips the crucial signs. Similarly, for γ/Z exchange, only a WW-loop is possible. We again decompose the correction into the T^3T^3 proportional terms

$$\begin{aligned}
\delta V^{T3T3}_{(ij),(ij)}\Big|_{\text{triple}-\text{vertex}} &= \left(\frac{4\pi\alpha}{\mathbf{k}^2} + \frac{4\pi\alpha}{\mathbf{k}^2 + m_Z^2}\frac{c_W^2}{s_W^2}\right) T^3_{R,ii}T^3_{R,jj}\left(2I^{WW}_{3\,\text{gauge}}\right) \\
&= V^{T3T3}_{(ij),(ij)}\left(2I^{WW}_{3\,\text{gauge}}\right)
\end{aligned} \tag{D.15}$$

where we have used that the triple-vertex changes sign under exchange of $W^+ \leftrightarrow W^-$, leading to structures of the form $[T_R^+, T_R^-] = -T_R^3$. Furthermore, there are the T^3Y terms

$$\begin{aligned}
\delta V^{T3Y}_{(ij),(ij)}\Big|_{\text{triple-vertex}} &= \left(\frac{4\pi\alpha}{\mathbf{k}^2} - \frac{4\pi\alpha}{\mathbf{k}^2 + m_Z^2}\right)\left(T^3_{R,ii}Y_j + T^3_{R,jj}Y_i\right) I^{WW}_{3\,\text{gauge}} \\
&= V^{T3Y}_{(ij),(ij)} I^{WW}_{3\,\text{gauge}} \qquad \text{(D.16)}
\end{aligned}$$

and finally Y^2

$$\delta V^{YY}_{(ij),(ij)}\Big|_{\text{triple-vertex}} = 0, \qquad \text{(D.17)}$$

which is understood from the unbroken theory. The triple gauge vertex stems from the $W^aW^bW^c$ interaction. Two DM-gauge boson interactions are fixed to W, which leaves only one vertex to mix W^3 into a photon or Z, therefore at maximum, we have T^3Y, but no Y^2 contribution.

D.4 Box topologies

For the W-Yukawa potential, the box corrections must involve exactly one W-boson, due to charge conservation. Therefore there are four box and four crossed box diagrams possible. The contribution reads

$$\begin{aligned}
\delta V^{W}_{(ij),(kl)}\Big|_{\text{boxes}} &= I_{\text{box}}\left((-1)^{n_Q}\alpha_2(T^+_{R,ik}T^-_{R,jl} + T^-_{R,ik}T^+_{R,jl}), m_W; \alpha(T^3_{R,kk}+Y_k)(T^3_{R,ll}+Y_l), 0\right) \\
&+ I_{\text{box}}\left((-1)^{n_Q}\alpha_2(T^+_{R,ik}T^-_{R,jl} + T^-_{R,ik}T^+_{R,jl}), m_W; \alpha\frac{c_W^2T^3_{R,kk} - s_W^2Y_k}{s_Wc_W}\frac{c_W^2T^3_{R,ll} - s_W^2Y_l}{s_Wc_W}, m_Z\right) \\
&+ I_{\text{box}}\left(\alpha(T^3_{R,ii}+Y_i)(T^3_{R,jj}+Y_j), 0; (-1)^{n_Q}\alpha_2(T^+_{R,ik}T^-_{R,jl} + T^-_{R,ik}T^+_{R,jl}), m_W\right) \\
&+ I_{\text{box}}\left(\alpha\frac{c_W^2T^3_{R,ii} - s_W^2Y_i}{s_Wc_W}\frac{c_W^2T^3_{R,jj} - s_W^2Y_j}{s_Wc_W}, m_Z; (-1)^{n_Q}\alpha_2(T^+_{R,ik}T^-_{R,jl} + T^-_{R,ik}T^+_{R,jl}), m_W\right) \\
&- I_{\text{box}}\left(\alpha(T^3_{R,ii}+Y_i)(T^3_{R,ll}+Y_l), 0; (-1)^{n_Q}\alpha_2(T^+_{R,ik}T^-_{R,jl} + T^-_{R,ik}T^+_{R,jl}), m_W\right) \\
&- I_{\text{box}}\left(\alpha\frac{c_W^2T^3_{R,ii} - s_W^2Y_i}{s_Wc_W}\frac{c_W^2T^3_{R,ll} - s_W^2Y_l}{s_Wc_W}, m_Z; (-1)^{n_Q}\alpha_2(T^+_{R,ik}T^-_{R,jl} + T^-_{R,ik}T^+_{R,jl}), m_W\right) \\
&- I_{\text{box}}\left((-1)^{n_Q}\alpha_2(T^+_{R,ik}T^-_{R,jl} + T^-_{R,ik}T^+_{R,jl}), m_W; \alpha(T^3_{R,kk}+Y_k)(T^3_{R,jj}+Y_j), 0\right) \\
&- I_{\text{box}}\left((-1)^{n_Q}\alpha_2(T^+_{R,ik}T^-_{R,jl} + T^-_{R,ik}T^+_{R,jl}), m_W; \alpha\frac{c_W^2T^3_{R,kk} - s_W^2Y_k}{s_Wc_W}\frac{c_W^2T^3_{R,jj} - s_W^2Y_j}{s_Wc_W}, m_Z\right)
\end{aligned} \qquad \text{(D.18)}$$

we used the factor $(-1)^{n_Q}$ already present for the tree-level potential to determine the sign due to fermion flow (the signs for γ/Z are determined by T^3 and Y). The first four lines give the box contributions, whilst the last four lines denote crossed box contributions. The proportionality to the tree-level contribution is evident, as each box diagram depends on $(-1)^{n_Q}(T^+T^- + T^-T^+)$ in the W-couplings. Furthermore, note that $Y_i = Y_k$ and $Y_j = Y_l$, which together with the linearity of I_{box} in the couplings leads to

$$\begin{aligned}
\delta V^{W}_{(ij),(kl)}\Big|_{\text{boxes}} &= (-1)^{n_Q}(T^+_{R,ik}T^-_{R,jl} + T^-_{R,ik}T^+_{R,jl})\left(T^3_{R,ii}(T^3_{R,jj} - T^3_{R,ll}) + T^3_{R,kk}(T^3_{R,ll} - T^3_{R,jj})\right) \\
&\times \left[I_{\text{box}}\left(\alpha_2, m_W; \alpha, 0\right) + I_{\text{box}}\left(\alpha_2, m_W; \alpha\frac{c_W^2}{s_W^2}, m_Z\right)\right]
\end{aligned}$$

$$= (-1)^{n_Q} (T^+_{R,ik} T^-_{R,jl} + T^-_{R,ik} T^+_{R,jl}) \left[-I_{\text{box}}\left(\alpha_2, m_W; \alpha, 0\right) - I_{\text{box}}\left(\alpha_2, m_W; \alpha \frac{c_W^2}{s_W^2}, m_Z\right)\right] \tag{D.19}$$

where we observe that the hypercharge contribution drops, which is unsurprising, noting the non-vanishing unbroken theory contribution arises from $T^a T^b \otimes T^a T^b - T^a T^b \otimes T^b T^a$. The colour factor is the same as for the tree-level potential $V^W_{(ij),(kl)}$.

In the γ/Z-channels, only W-boson boxes are present. The reason is that possible γ/Z boxes, if possible, are always accompanied by the respective crossed box counterparts. As there would be no W's involved, i.e., the heavy DM content internally does not change, the crossed boxes exactly cancel the regular box diagrams. We follow the decomposition in the previous Sections and define corrections for $T^3 T^3$, $T^3 Y$ and Y^2. The W-boxes are needed to cancel the gauge dependence for $T^3 T^3$, which is non-surprising considering the unbroken theory diagrams $T^a T^b T^a T^b$ that they originate from. The correction for the other linear combinations vanishes

$$\begin{aligned}
\delta V^{T3T3}_{(ij),(ij)}\Big|_{\text{boxes}} &= I_{\text{box}}\left(\alpha_2 T^+_{R,in} T^-_{R,jm}, m_W; \alpha_2 T^-_{R,ni} T^+_{R,mj}, m_W\right) \\
&\quad + I_{\text{box}}\left(\alpha_2 T^-_{R,in} T^+_{R,jm}, m_W; \alpha_2 T^+_{R,ni} T^-_{R,mj}, m_W\right) \\
&\quad - I_{\text{box}}\left(\alpha_2 T^+_{R,in} T^-_{R,mj}, m_W; \alpha_2 T^-_{R,ni} T^+_{R,jm}, m_W\right) \\
&\quad - I_{\text{box}}\left(\alpha_2 T^-_{R,in} T^+_{R,mj}, m_W; \alpha_2 T^+_{R,ni} T^-_{R,jm}, m_W\right) \\
&= -T^3_{R,ii} T^3_{R,jj} I_{\text{box}}(\alpha_2, m_W; \alpha_2, m_W) \\
\delta V^{T3Y}_{(ij),(ij)}\Big|_{\text{boxes}} &= 0 \\
\delta V^{YY}_{(ij),(ij)}\Big|_{\text{boxes}} &= 0\,.
\end{aligned} \tag{D.20}$$

Note that here the factor $(-1)^{n_Q}$ does not appear, as two W-bosons are involved and therefore $(-1)^{2n_Q} = 1$. The contribution is proportional to the tree-level $T^3 T^3$ contribution and confirms the findings of the wino case. We have used that I_{box} is linear in the couplings and that

$$\begin{aligned}
&\left(T^+_R T^-_R\right)_{ii} \left(T^-_R T^+_R\right)_{jj} + \left(T^-_R T^+_R\right)_{ii} \left(T^+_R T^-_R\right)_{jj} - \left(T^+_R T^-_R\right)_{ii} \left(T^+_R T^-_R\right)_{jj} - \left(T^-_R T^+_R\right)_{ii} \left(T^-_R T^+_R\right)_{jj} \\
&= \left(T^+_R T^-_R\right)_{ii} \left[T^-_R, T^+_R\right]_{jj} + \left(T^-_R T^+_R\right)_{ii} \left[T^+_R, T^-_R\right]_{jj} = T^3_{R,jj} \left[T^+_R, T^-_R\right]_{ii} = -T^3_{R,ii} T^3_{R,jj}\,.
\end{aligned} \tag{D.21}$$

D.5 No one-loop induced potentials

The above considerations cover off-diagonal channels with charge transfer from upper to lower line of one, e.g. $\chi^0\chi^0 \to \chi^+\chi^-$ for the wino and diagonal channels with T^3 and Y couplings. In principle, there are two further possibilities, which have no tree-level potential. One possibility is a channel with charge change two from upper to lower line, e.g. in the quintuplet $\chi^{\pm\pm}\chi^{\pm\pm} \to \chi^0\chi^0$. The second possibility is a channel without charge change, but vanishing tree-level, e.g., the $\chi^0\chi^0 \to \chi^0\chi^0$ channel in the wino. Channels with higher charge change are not possible at one-loop, as these would involve more than two W-bosons.

Both cases can only be realized with box diagrams. The charge zero transitions are covered by $T^3 T^3$ (the box part) above and vanish if the tree-level potential vanishes, as can easily be seen from the expressions above (D.20). Similarly, for charge change two between the upper and lower line

$$\delta V^{\Delta \text{Q}=2}_{(ij),(kl)} = I_{\text{box}}\left(\alpha_2 T^+_{R,in} T^-_{R,jm}, m_W; \alpha_2 T^+_{R,nk} T^-_{R,ml}, m_W\right)$$

$$
\begin{aligned}
&+ I_{\rm box}\left(\alpha_2 T^-_{R,in} T^+_{R,jm}, m_W; \alpha_2 T^-_{R,nk} T^+_{R,ml}, m_W\right) \\
&- I_{\rm box}\left(\alpha_2 T^+_{R,in} T^-_{R,ml}, m_W; \alpha_2 T^+_{R,nk} T^-_{R,jm}, m_W\right) \\
&- I_{\rm box}\left(\alpha_2 T^-_{R,in} T^+_{R,ml}, m_W; \alpha_2 T^-_{R,nk} T^+_{R,jm}, m_W\right) \\
=\,& 0
\end{aligned}
\tag{D.22}
$$

as expected. Therefore, the NLO correction does not introduce any potentials in channels that are not present at tree-level.

E

The wino soft function

In this Appendix, we present the one-loop calculation of the wino DM soft function, similar to the corresponding Appendix C in [101]. In particular, we provide the technical details on the soft function omitted in the main text (cf. Section 7.3) and give the necessary loop integrals for real and virtual contributions. Furthermore, we introduce the rapidity regularization scheme used throughout the main text. The soft integral results in this Appendix were independently calculated by A. Broggio, C. Hasner, and the author. The linear combinations of integrals and the resulting soft function coefficients were checked between C. Hasner and the author.

E.1 Rapidity regularization

Throughout this thesis, we use the rapidity regulator introduced in [110, 111], for all integrals and functions of virtuality $\mu \sim m_W$ that suffer from rapidity divergences. From a technical standpoint, this regulator amounts to changing the loop integrals from

$$\tilde{\mu}^{4-d} \int \frac{d^d k}{(2\pi)^d} = \int [dk] \quad \longrightarrow \quad \int [dk] \, \frac{\nu^\eta}{|2k^3|^\eta} \,, \tag{E.1}$$

with ν the analogue of the dimensional regularization scale μ, and $\tilde{\mu}$ defined as in (A.1). The newly introduced regulator needs to be expanded in the region under consideration, meaning $|2k^3| = |(n_+ - n_-) \cdot k| \to |n_\pm k|$ in the (anti-)collinear limits. When calculating a specific integral, we can proceed as in standard dimensional regularization. However, the limit $\eta \to 0$ always has to be taken before $\epsilon \to 0$, i.e., $\eta/\epsilon^n \to 0$ for all n. Physically, this order of limits arises from the requirement that the rapidity regularization has to keep the integrals on their invariant mass hyperbola [111]. Furthermore, the sum of all rapidity poles in η necessarily cancels, as the full theory is rapidity finite. If one considers the effective theory integrals as asymptotic expansions of the finite full theory result, it is clear that the sum has to be finite in η. Finally, let us remark that the above regulator preserves gauge invariance within the individually regulated sectors. The result can be proven using exponentiation into Wilson lines [111].

E.2 Wino soft function

The integrated soft function in the factorization theorem is defined in (6.47). For wino dark matter at NLL', further simplifications are possible, as, e.g., only the 33 components of the photon jet function contributes. Therefore, we find it convenient to calculate (6.48)

$$W^{\mathrm{SU(2)},ij}_{IJ,WY} \quad \overset{\text{wino NLL'}}{\longrightarrow} \quad W^{\mathrm{SU(2)},ij}_{IJ,33} = W^{\mathrm{wino},ij}_{IJ} \tag{E.2}$$

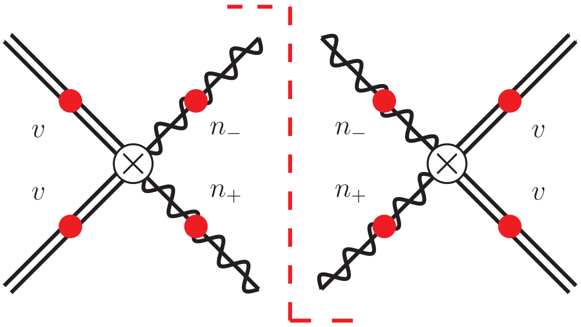

Figure E.1: *Diagrammatic representation of the one-loop soft function.*

which covers all non-zero elements at NLL' order. From a practical point, the calculation is also more convenient if all Wilson lines can be evaluated at the same point. Therefore, we shift the Wilson lines in (6.47) to $x = 0$ and then perform the n_+y integration resulting in a delta distribution

$$W_{IJ}^{\text{wino},ij}(\omega) = \sum\!\!\!\!\!\!\!\int_{X_s} \delta(\omega - n_-p_{X_s}) \left\langle 0 \right| \bar{\mathbf{T}}[[\mathcal{S}^\dagger]^j_{J,V3}(0)] \left| X_s \right\rangle \left\langle X_s \right| \mathbf{T}[\mathcal{S}^i_{I,V3}(0)] \left|0\right\rangle . \tag{E.3}$$

For nomenclature, we will use the diagrammatic representation sketched in Figure E.1. The one-loop correction is associated with the connection of any two distinct (red) dots on the legs. The integrals are then named after the legs, they are connected to, and are categorized as real or virtual, depending on if they cross the cut (red/dashed). Therefore, for example, the soft gauge boson that connects one of the v dots on the left, with n_+ to the right of the cut, is called *vn_+ real integral.*

To conclude this preface on the integral calculation, let us introduce the phase-space measure for real integrals in light-cone coordinates

$$\begin{aligned}\int d^dk\, \theta(k^0)\delta(k^2 - m_W^2) &= \frac{1}{2}\int_0^\infty dn_+k \int_0^\infty dn_-k \int d^{d-2}k_\perp \delta(n_+k\, n_-k + k_\perp^2 - m_W^2) \\ &= \frac{\Omega_{d-2}}{2}\int_0^\infty dn_+k \int_0^\infty dn_-k \int_0^\infty dk_T\, k_T^{d-3}\delta(n_+k\, n_-k - k_T^2 - m_W^2)\,,\end{aligned} \tag{E.4}$$

where $k_T^2 = -k_\perp^2 > 0$, and the delta- and theta-functions from the Cutkosky rules enforce $n_+k, n_-k \geq 0$.

E.2.1 Virtual soft integrals

In this Section, the virtual integrals necessary for the soft function calculation are discussed. Some of the results shown here are also presented in [98] in agreement with the results below.

The n_+n_- virtual integral

We begin with the n_+n_- virtual integral, i.e., the connection of n_+n_- line without crossing the cut in Figure E.1. Therefore, $p_{X_s} = 0$, and after expanding the Wilson lines to the one-loop order, we find

$$I^{\text{virt.}}_{n_+n_-} = -i\hat{g}_2^2\delta(\omega)(n_+\cdot n_-)\int [dk] \frac{\nu^\eta}{[k^2 - m_W^2 + i\varepsilon][n_-k + i\varepsilon][n_+k - i\varepsilon]|2k^3|^\eta}\,. \tag{E.5}$$

To evaluate the integral we begin by performing the contour integral in k^0. To identify the location of the residues, we write the integral as

$$
\begin{aligned}
I^{\text{virt.}}_{n_+n_-} = -2i\hat{g}_2^2\delta(\omega)\tilde{\mu}^{2\epsilon} \int \frac{dk^0 dk^3 d^{d-2}k_\perp}{(2\pi)^d} \frac{\nu^\eta}{|2k^3|^\eta} \\
\times \frac{1}{[(k^0)^2 - E_k^2 + i\varepsilon][k^0 - k^3 + i\varepsilon][k^0 + k^3 - i\varepsilon]}\,,
\end{aligned}
\tag{E.6}
$$

where $E_k^2 = (k^3)^2 + k_T^2 + m_W^2$. The location of the poles in k^0 depends on the sign of k^3. Therefore, we distinguish the positive and negative k^3 regime, which has the additional advantage, that we can remove the absolute value in the rapidity regularization factor $|2k^3|^\eta$. For $k^3 > 0$ there are four poles in k^0 located at $\pm(E_k - i\varepsilon)$, and $\pm(k^3 - i\varepsilon)$, two in the upper and two in the lower half-plane. We close the contour in the lower half-plane, thereby picking up a factor $-2\pi i$. For $k^3 < 0$, the poles in $\pm(k^3 - i\varepsilon)$ move from positive to negative k^0 domain, and vice versa. Therefore, after k^0 integration, we are left with

$$
\begin{aligned}
I^{\text{virt.}}_{n_+n_-} = 2i\hat{g}_2^2\delta(\omega)\tilde{\mu}^{2\epsilon} \int \frac{d^{d-2}k_\perp}{(2\pi)^d} \Bigg\{ \int_0^\infty dk^3 \frac{\nu^\eta}{(2k^3)^\eta} \frac{2\pi i}{k_T^2 + m_W^2} \left[\frac{1}{2E_k} - \frac{1}{2k^3 - i\varepsilon}\right] \\
+ \int_{-\infty}^0 dk^3 \frac{\nu^\eta}{(-2k^3)^\eta} \frac{2\pi i}{k_T^2 + m_W^2} \left[\frac{1}{2E_k} - \frac{1}{2k^3 - i\varepsilon}\right] \Bigg\}\,.
\end{aligned}
\tag{E.7}
$$

The first terms in the two square brackets (E.7) give the same contribution, as can be seen by replacing $k^3 \to -k^3$ in either. The following integrals in k^3 and $k_\perp$ are straightforward and yield

$$
-\frac{\hat{g}_2^2}{4\pi^2}\delta(\omega)\left(\frac{\mu}{m_W}\right)^{2\epsilon} e^{\gamma_E\epsilon}\left(\frac{\nu}{m_W}\right)^\eta \frac{\Gamma(\frac{1}{2} - \frac{\eta}{2})\Gamma(\epsilon + \frac{\eta}{2})}{2^\eta\,\pi^{\frac{1}{2}}\,\eta}\,.
\tag{E.8}
$$

The second terms in the square brackets of (E.7) lead to a purely imaginary part that is associated with an electroweak Glauber mode [179], as pointed out in [99]. However, the soft function correctly captures this term, making further factorization unnecessary. The k^3 integral in these terms leads to

$$
\begin{aligned}
\int dk^3 \frac{(-2\pi i)\nu^\eta}{[2k^3 - i\varepsilon]|2k^3|^\eta} &= \int_0^\infty dk^3 \frac{(-2\pi i)\nu^\eta}{(2k^3)^\eta}\left[\frac{1}{2k^3 - i\varepsilon} + \frac{1}{-2k^3 - i\varepsilon}\right] \\
&= (-i\pi)\nu^\eta \pi \csc(\pi\eta)\big((-i\varepsilon)^{-\eta} - (i\varepsilon)^{-\eta}\big) = (2\pi^2)\nu^\eta \csc(\pi\eta)\,\varepsilon^{-\eta}\sin(\eta\,\pi/2) \\
&= \pi^2 + \mathcal{O}(\eta)\,,
\end{aligned}
\tag{E.9}
$$

independent of $i\varepsilon$ to $\mathcal{O}(\eta^0)$. Performing the final $k_\perp$ integral, and summing both contributions leads to the final result

$$
\begin{aligned}
I^{\text{virt.}}_{n_+n_-} &= -\frac{\hat{g}_2^2\delta(\omega)}{4\pi^2}\left(\frac{\mu}{m_W}\right)^{2\epsilon}\left(\frac{\nu}{m_W}\right)^\eta e^{\gamma_E\epsilon}\left[\frac{\Gamma(\frac{1}{2} - \frac{\eta}{2})\Gamma(\epsilon + \frac{\eta}{2})}{2^\eta\,\pi^{\frac{1}{2}}\,\eta} - \frac{\Gamma(\epsilon + \frac{\eta}{2})}{\Gamma(1 + \frac{\eta}{2})}\left(\frac{i\pi}{2} + \mathcal{O}(\eta)\right)\right] \\
&= -\frac{\hat{\alpha}_2}{2\pi}\delta(\omega)\bigg[-\frac{1}{\epsilon^2} + \frac{2}{\epsilon\eta} - \frac{i\pi}{\epsilon} + \frac{2}{\epsilon}\ln\frac{m_W}{\mu} - \frac{2}{\epsilon}\ln\frac{m_W}{\nu} - \frac{4}{\eta}\ln\frac{m_W}{\mu} \\
&\qquad + \frac{\pi^2}{12} + 2\pi i\ln\frac{m_W}{\mu} - 2\ln^2\frac{m_W}{\mu} + 4\ln\frac{m_W}{\mu}\ln\frac{m_W}{\nu}\bigg]\,.
\end{aligned}
\tag{E.10}
$$

vn_+ and vn_- virtual integrals

The virtual integrals vn_+ and vn_- yield the same integral, as the soft function is symmetric under exchange of $n_+ \leftrightarrow n_-$, in the virtual parts. The relevant integral for this initial-final state virtual soft correction is

$$I^{\text{virt.}}_{vn_+} = -i\hat{g}_2^2 \delta(\omega)(v\cdot n_+)\int [dk] \frac{\nu^\eta}{[k^2 - m_W^2 + i\varepsilon][n_+k - i\varepsilon][v\cdot k - i\varepsilon]|2k^3|^\eta}\,. \tag{E.11}$$

As above for $I^{\text{virt.}}_{n_+n_-}$, the integral can be performed using residue calculus. The contour integration in k^0 again has four poles in the complex plane. Only one of these is located in the lower half-plane at $E_k - i\varepsilon$. Therefore, we close the contour in the lower half-plane, for both positive and negative k^3-region, as distinguished by the rapidity factor. The sum of both k^3 cases can be easily integrated in $k^3, k_\perp$, and yields

$$\begin{aligned} I^{\text{virt}}_{vn_+} &= -\frac{\hat{g}_2^2}{8\pi^2}\delta(\omega)\left(\frac{\mu}{m_W}\right)^{2\epsilon}\left(\frac{\nu}{m_W}\right)^{\eta} e^{\gamma_E\epsilon}\,\frac{\Gamma(\frac{1}{2}-\frac{\eta}{2})\Gamma(\epsilon+\frac{\eta}{2})}{2^\eta\,\pi^{\frac{1}{2}}\,\eta} \\ &= -\frac{\hat{\alpha}_2}{4\pi}\delta(\omega)\left[-\frac{1}{\epsilon^2}+\frac{2}{\epsilon\eta}+\frac{2}{\epsilon}\ln\frac{m_W}{\mu}-\frac{2}{\epsilon}\ln\frac{m_W}{\nu}-\frac{4}{\eta}\ln\frac{m_W}{\mu}\right. \\ &\qquad \left. +\frac{\pi^2}{12}+4\ln\frac{m_W}{\mu}\ln\frac{m_W}{\nu}-2\ln^2\frac{m_W}{\mu}\right]\,. \end{aligned} \tag{E.12}$$

The vv virtual integral

The final virtual integral corresponds to the connection of the two heavy DM Wilson lines. The integral reads

$$I^{\text{virt.}}_{vv} = -i\hat{g}_2^2\delta(\omega)(v\cdot v)\int [dk]\frac{1}{[k^2-m_W^2+i\varepsilon][k^0+i\varepsilon][k^0-i\varepsilon]}\,. \tag{E.13}$$

The integral is rather simple to evaluate. However, one has to note that the pinched $k^0 = \pm i\varepsilon$ poles are not supposed to be picked up. The reason is that they reproduce the potential region and are already taken into account when solving the Schrödinger equation with the LO potential. The integral evaluates to

$$I^{\text{virt.}}_{vv} = -\frac{\hat{\alpha}_2}{2\pi}\delta(\omega)\left[\frac{1}{\epsilon}+\ln\frac{\mu^2}{m_W^2}\right]\,. \tag{E.14}$$

E.2.2 Real soft integrals

The real integrals are defined in analogy to the virtual integrals, replacing the gauge boson propagators with

$$\frac{1}{k^2-m_W^2+i\varepsilon} \to -2\pi i\,\delta(k^2-m_W^2)\,\theta(k^0)\,, \tag{E.15}$$

following the Cutkosky rules. Rapidity regularization is still necessary and leads to the appearance of star distributions [170]. For star distribution definitions and identities, we point to Section 7.2.1 in the main text, where the treatment is discussed in the context of the intermediate resolution recoiling jet function. Again some of the integrals are also discussed in [98], with which the results agree.

The n_+n_- real integral

Beginning with the n_+n_- real integral

$$I^{\text{real}}_{n_+n_-} = (n_+\cdot n_-)\,\hat{g}_2^2 \int [dk]\, \frac{-2\pi\delta\left(k^2-m_W^2\right)\theta(k^0)}{(n_+k)(n_-k)}\delta(\omega-n_-k)\frac{\nu^\eta}{|2k^3|^\eta}\,, \tag{E.16}$$

we perform the trivial n_-k integration over the delta-function $\delta(\omega-n_-k)$. This leaves

$$I^{\text{real}}_{n_+n_-} = -\frac{\hat{\alpha}_2 e^{\gamma_E\epsilon}}{2\pi^{2-\epsilon}}\,\mu^{2\epsilon}\nu^\eta \int d(n_+k)\, d^{d-2}k_T\, \frac{\delta(\omega n_+k - k_T^2 - m_W^2)\theta(\omega+n_+k)}{\omega n_+k\,|n_+k-\omega|^\eta}\,. \tag{E.17}$$

The second integral in n_+k is also simple due to the additional delta function. Note that the Heaviside function can be dropped, as it only ensures $n_+k>-\omega$. However, as ω is positive, and as furthermore $k_T^2+m_W^2>0$, the Heaviside function does not introduce any restriction beyond the information encoded in the delta-function. The integral becomes

$$I^{\text{real}}_{n_+n_-} = -\frac{\hat{\alpha}_2 e^{\gamma_E\epsilon}}{\pi\Gamma(1-\epsilon)}\,\mu^{2\epsilon}\omega^{\eta-1}\nu^\eta \int_0^\infty dk_T\, \frac{k_T^{1-2\epsilon}}{k_T^2+m_W^2}\frac{1}{|k_T^2+m_W^2-\omega^2|^\eta}\,. \tag{E.18}$$

To carry out the integral over k_T, we have to remove the absolute value and distinguish the various cases. Above, we have pulled a factor of ω^η into the absolute value as ω is positive. The relevant cases for the absolute value are: Either $m_W>\omega$, in which, case the absolute value can be dropped, as $k_T, m_W>0$. Secondly, if $\omega>m_W$, then the integrand is split into an integral from 0 to $\sqrt{\omega^2-m_W^2}$ with a factor $(-1)^\eta$ to remove the absolute value, and a second integral from $\sqrt{\omega^2-m_W^2}$ to ∞, where the absolute value can be dropped altogether.

For additional emphasis, on the arising structures, we substitute the dimensionless quantities $k_T'=k_T/m_W$ and $\omega'=\omega/m_W$. The integral then reads

$$I^{\text{real}}_{n_+n_-} = -\frac{\hat{\alpha}_2}{\pi}\left(\frac{\mu^2 e^{\gamma_E}}{m_W^2}\right)^\epsilon \left(\frac{\nu\omega}{m_W^2}\right)^\eta \frac{1}{\omega\Gamma(1-\epsilon)}\int_0^\infty dk_T'\frac{k_T'^{1-2\epsilon}}{(k_T'^2+1)\,|k_T'^2+1-\omega'^2|^\eta}\,. \tag{E.19}$$

We begin with $\omega'<1$, in which case the absolute value can be dropped and we find for the integration

$$\begin{aligned}I^{\text{real}}_{n_+n_-} = -\frac{\hat{\alpha}_2}{2\pi}\left(\frac{\mu^2 e^{\gamma_E}}{m_W^2}\right)^\epsilon \left(\frac{\nu\omega}{m_W^2}\right)^\eta \frac{1}{\omega\Gamma(1-\epsilon)}&\Big\{(\omega')^{-2\eta}\,\Gamma(\epsilon+\eta)\Gamma(1-\epsilon-\eta)\\ &+\left(1-\omega'^2\right)^{1-\epsilon-\eta}\frac{\Gamma(1-\epsilon)\Gamma(\epsilon+\eta-1)}{\Gamma(\eta)}\,{}_2F_1\left(1,1-\epsilon,2-\epsilon-\eta,1-\omega'^2\right)\Big\}\end{aligned} \tag{E.20}$$

with ${}_2F_1$ the hypergeometric function, exact to all orders in both ϵ and η. The terms in the curly brackets are finite for $\omega,\eta\to0$, hence the only rapidity poles may arise from $\omega^{\eta-1}m_W^{-\eta} = \frac{\delta(\omega)}{\eta}+\left[\frac{1}{\omega}\right]_*^{[m_W]}+\mathcal{O}(\eta)$. The delta-distribution term, therefore requires an expansion up to $\mathcal{O}(\eta)$ in the curly brackets. However, in this term due to the multiplication with $\delta(\omega')$, we can set $\omega'=0$, which allows to simplify the hypergeometric function. The term involving the star distribution requires to keep ω' general, however, only terms up to $\mathcal{O}(\eta^0)$ have to be retained in the curly bracket. Hence, we can write

$$I^{\text{real}}_{n_+n_-} = -\frac{\hat{\alpha}_2}{2\pi}\left(\frac{\mu^2 e^{\gamma_E}}{m_W^2}\right)^\epsilon \left(\frac{\nu\,\omega}{m_W^2}\right)^\eta \frac{\Gamma(\epsilon+\eta)}{\omega\Gamma(1+\eta)}+\mathcal{O}(\eta,\epsilon)$$

$$
\begin{aligned}
= -\frac{\hat{\alpha}_2}{2\pi}\Bigg[\delta(\omega)\bigg(& -\frac{1}{\epsilon^2}+\frac{1}{\epsilon\,\eta}+\frac{1}{\eta}\ln\frac{\mu^2}{m_W^2}+\frac{1}{\epsilon}\left(-\ln\frac{\mu^2}{m_W^2}+\ln\frac{\nu}{m_W}\right) \\
& +\frac{\pi^2}{12}-\frac{1}{2}\ln^2\frac{\mu^2}{m_W^2}+\frac{1}{2}\ln\frac{\mu^2}{m_W^2}\ln\frac{\nu^2}{m_W^2}\bigg) \\
& +\left[\frac{1}{\omega}\right]_*^{[m_W]}\left(\frac{1}{\epsilon}+\ln\frac{\mu^2}{m_W^2}\right)\Bigg]\,. \qquad \text{(E.21)}
\end{aligned}
$$

In the second case $\omega' > 1$, we will show that the integral can be written in the same form as above, i.e., that the same result applies for all $\omega \geq 0$. Therefore, going back to the k_T integral, we distinguish the two regions

$$
\begin{aligned}
\int_0^\infty dk'_T \frac{k_T'^{1-2\epsilon}}{(k_T'^2+1)\,|k_T'^2+1-\omega'^2|^\eta} = & \int_0^{\sqrt{\omega'^2-1}} dk'_T \frac{k_T'^{1-2\epsilon}}{(k_T'^2+1)\,(k_T'^2+1-\omega'^2)^\eta} \\
& + \int_{\sqrt{\omega'^2-1}}^\infty dk'_T \frac{k_T'^{1-2\epsilon}}{(k_T'^2+1)\,(-k_T'^2-1+\omega'^2)^\eta}\,. \qquad \text{(E.22)}
\end{aligned}
$$

The two resulting integrals can be evaluated to

$$
\begin{aligned}
& \int_0^{\sqrt{\omega'^2-1}} dk'_T \frac{k_T'^{1-2\epsilon}}{(k_T'^2+1)\,(k_T'^2+1-\omega'^2)^\eta} \\
& \quad = \frac{(\omega'^2-1)^{1-\epsilon-\eta}}{2}\frac{\Gamma(1-\epsilon)\Gamma(1-\eta)}{\Gamma(2-\epsilon-\eta)}\,{}_2F_1(1,1-\epsilon,2-\epsilon-\eta,1-\omega'^2)\,, \\
& \int_{\sqrt{\omega'^2-1}}^\infty dk'_T \frac{k_T'^{1-2\epsilon}}{(k_T'^2+1)\,(-k_T'^2-1+\omega'^2)^\eta} \\
& \quad = \frac{(\omega'^2-1)^{-\epsilon}\,(1-\omega'^2)^{-\eta}}{2}\frac{\Gamma(1-\eta)\Gamma(\epsilon+\eta)}{\Gamma(1+\epsilon)}\,{}_2F_1\left(1,\epsilon+\eta,1+\epsilon,\frac{1}{1-\omega'^2}\right)\,. \qquad \text{(E.23)}
\end{aligned}
$$

The following discussion is analogous to the previous discussion on $\omega' < 1$. If appropriately expanded to $\mathcal{O}(\eta,\epsilon)$, the same result as in (E.21) is found.

The vn_+ real integral

For real integrals, contrary to the virtual calculation above, vn_+ and vn_- yield distinct results. The vn_+ real integral is given by

$$
I_{vn_+}^{\text{real}} = (v\cdot n_+)\hat{g}_2^2\int[dk]\frac{\left(-2\pi\delta(k^2-m_W^2)\theta(k^0)\right)}{(v\cdot k)(n_+k)}\delta(\omega-n_-k)\frac{\nu^\eta}{|2k^3|^\eta}\,. \qquad \text{(E.24)}
$$

The integration in the light-cone components n_+k, n_-k can be performed using both delta-functions

$$
I_{vn_+}^{\text{real}} = -\frac{\hat{\alpha}_2}{\pi}\frac{\mu^{2\epsilon}e^{\epsilon\gamma_E}}{\Gamma(1-\epsilon)}\nu^\eta\omega^{\eta+1}\int_0^\infty dk_T\frac{k_T^{1-2\epsilon}}{k_T^2+m_W^2}\frac{1}{\omega^2+k_T^2+m_W^2}\frac{1}{|\omega^2-k_T^2-m_W^2|^\eta}\,. \qquad \text{(E.25)}
$$

Other than in the n_+n_- case above, there is no rapidity divergence for $\omega,\eta\to 0$, as marked by the different prefactor $\omega^{\eta+1}$ which is finite in these limits. Therefore, we can perform the integral setting η to 0, which results in a standard easily solved integral

$$
I_{vn_+}^{\text{real}} = -\frac{\hat{\alpha}_2 e^{\epsilon\gamma_E}}{2\pi\omega}\mu^{2\epsilon}\Gamma(\epsilon)\left(m_W^{-2\epsilon}-(m_W^2+\omega^2)^{-\epsilon}\right)+\mathcal{O}(\eta)
$$

$$= -\frac{\hat{\alpha}_2}{2\pi}\frac{1}{\omega}\ln\left(\frac{m_W^2+\omega^2}{m_W^2}\right) + \mathcal{O}(\eta,\epsilon)\,, \tag{E.26}$$

which is finite. When combining this integral with other terms that contain, e.g., star-distributions, we may replace $\frac{1}{\omega} \to \left[\frac{1}{\omega}\right]_*$, as the integral is finite for $\omega \to 0$, meaning ω^{-1} is equivalent to the star-distribution in this particular case.

The vn_- real integral

The integral for the vn_- real combination can be derived from the two previous integrals. To this end, we use the identity

$$\frac{(n_+\cdot n_-)}{(n_+k)(n_-k)} - \frac{(v\cdot n_+)}{(v\cdot k)(n_+k)} = \frac{(v\cdot n_-)}{(n_-k)(v\cdot k)}\,, \tag{E.27}$$

which means that the integral obeys the relation

$$I_{vn_-}^{\text{real}} = I_{n_+n_-}^{\text{real}} - I_{vn_+}^{\text{real}}\,. \tag{E.28}$$

The vv real integral

Finally, we consider the real contribution connecting the two heavy DM Wilson lines. The starting expression is

$$I_{vv}^{\text{real}} = (v\cdot v)\,\hat{g}_2^2\int[dk]\frac{1}{(v\cdot k)^2}(-2\pi\delta(k^2-m_W^2)\theta(k^0))\delta(\omega-n_-k)\frac{\nu^\eta}{|2k^3|^\eta}\,. \tag{E.29}$$

As before, the light-cone components of the loop integral can easily be evaluated using the two delta-functions, and yield

$$I_{vv}^{\text{real}} = -\frac{2\hat{\alpha}_2}{\pi}\frac{\mu^{2\epsilon}e^{\epsilon\gamma_E}\nu^\eta}{\Gamma(1-\epsilon)}\omega^{\eta+1}\int_0^\infty dk_T\frac{k_T^{1-2\epsilon}}{(\omega^2+k_T^2+m_W^2)^2}\frac{1}{|\omega^2-k_T^2-m_W^2|^\eta}\,. \tag{E.30}$$

As for the vn_+ integral, the integral is finite in the limits $\omega,\eta\to 0$. Therefore, we can again expand to $\mathcal{O}(\eta)$, which allows to perform the k_T integral

$$\begin{aligned} I_{vv}^{\text{real}} &= -\frac{2\hat{\alpha}_2}{\pi}\frac{\mu^{2\epsilon}e^{\epsilon\gamma_E}}{\Gamma(1-\epsilon)}\,\omega\int_0^\infty dk_T\frac{k_T^{1-2\epsilon}}{(\omega^2+k_T^2+m_W^2)^2} + \mathcal{O}(\eta) \\ &= -\frac{\hat{\alpha}_2}{\pi}\epsilon\,\Gamma(\epsilon)\mu^{2\epsilon}e^{\epsilon\gamma_E}\omega\left(\frac{1}{m_W^2+\omega^2}\right)^{1+\epsilon} + \mathcal{O}(\eta) \\ &= -\frac{\hat{\alpha}_2}{\pi}\frac{\omega}{m_W^2+\omega^2} + \mathcal{O}(\eta,\epsilon)\,. \end{aligned} \tag{E.31}$$

The same result can also be obtained by retaining the full η-dependence and then expanding the hypergeometric functions that arise in this case. The integral is finite in both dimensional and rapidity regularization. The latter is expected, as the rapidity divergences are associated with the overlap of soft and (anti-)collinear contributions. As the heavy DM does not contribute to the (anti-)collinear physics, a rapidity divergence is not expected in the first place.

E.3 Wino soft functions in momentum space

In this Appendix we give the individual components of the index-contracted soft function as defined in (6.48) and (E.3) for the wino model. For the operator combination $ij = 11$ we find

$$\begin{aligned}
W^{\mathrm{wino},11}_{(00)(00)}(\omega,\mu,\nu) &= W^{\mathrm{wino},11}_{(00)(+-)}(\omega,\mu,\nu) = W^{11}_{(+-)(00)}(\omega,\mu,\nu) = W^{11}_{(+-)(+-)}(\omega,\mu,\nu) \\
&= \delta(\omega) + \frac{\hat{\alpha}_2}{4\pi}\left[\delta(\omega)(-16)\ln\frac{m_W}{\mu}\ln\frac{m_W}{\nu} + \left[\frac{1}{\omega}\right]_*^{[m_W]}(-16)\ln\frac{m_W}{\mu}\right].
\end{aligned} \tag{E.32}$$

The operator combinations $ij = \{12, 21\}$ are given by

$$\begin{aligned}
W^{\mathrm{wino},12}_{(00)(00)}(\omega,\mu,\nu) &= W^{\mathrm{wino},21*}_{(00)(00)}(\omega,\mu,\nu) \\
&= \frac{\hat{\alpha}_2}{4\pi}\left[\delta(\omega)\,(8+8\pi i)\ln\frac{m_W}{\mu} + \left[\frac{1}{\omega}\right]_*^{[m_W]} 8\ln\left(\frac{m_W^2+\omega^2}{m_W^2}\right)\right], \\
W^{\mathrm{wino},12}_{(00)(+-)}(\omega,\mu,\nu) &= W^{\mathrm{wino},21*}_{(+-)(00)}(\omega,\mu,\nu) \\
&= \delta(\omega) + \frac{\hat{\alpha}_2}{4\pi}\left[\delta(\omega)\left((4+4\pi i)\ln\frac{\mu}{m_W} - 16\ln\frac{m_W}{\mu}\ln\frac{m_W}{\nu}\right)\right. \\
&\qquad \left. + \left[\frac{1}{\omega}\right]_*^{[m_W]}\left(-4\ln\left(\frac{m_W^2+\omega^2}{m_W^2}\right) + 8\ln\frac{\mu^2}{m_W^2}\right)\right], \\
W^{\mathrm{wino},12}_{(+-)(00)}(\omega,\mu,\nu) &= W^{\mathrm{wino},21*}_{(00)(+-)}(\omega,\mu,\nu) = W^{\mathrm{wino},12}_{(00)(00)}(\omega,\mu,\nu)\,, \\
W^{\mathrm{wino},12}_{(+-)(+-)}(\omega,\mu,\nu) &= W^{\mathrm{wino},21*}_{(+-)(+-)}(\omega,\mu,\nu) \\
&= W^{\mathrm{wino},12}_{(00)(+-)}(\omega,\mu,\nu) + \frac{\hat{\alpha}_2}{4\pi}\left[\frac{1}{\omega}\right]_*^{[m_W]}(-2)\ln\left(\frac{m_W^2+\omega^2}{m_W^2}\right).
\end{aligned} \tag{E.33}$$

Finally, the operator combination $ij = 22$ is

$$\begin{aligned}
W^{\mathrm{wino},22}_{(00)(00)}(\omega,\mu,\nu) &= \frac{\hat{\alpha}_2}{4\pi}\left[\frac{1}{\omega}\right]_*^{[m_W]}\left(8\ln\left(\frac{m_W^2+\omega^2}{m_W^2}\right) - 8\frac{\omega^2}{m_W^2+\omega^2}\right), \\
W^{\mathrm{wino},22}_{(00)(+-)}(\omega,\mu,\nu) &= W^{\mathrm{wino},22*}_{(+-),(00)}(\omega,\mu,\nu) \\
&= \frac{\hat{\alpha}_2}{4\pi}\left[\delta(\omega)\,(8-8\pi i)\ln\frac{m_W}{\mu} + \left[\frac{1}{\omega}\right]_*^{[m_W]}\left(4\ln\left(\frac{m_W^2+\omega^2}{m_W^2}\right) + 4\frac{\omega^2}{m_W^2+\omega^2}\right)\right] \\
W^{\mathrm{wino},22}_{(+-)(+-)}(\omega,\mu,\nu) &= \delta(\omega) + \frac{\hat{\alpha}_2}{4\pi}\left[\delta(\omega)\left(-8\ln\frac{m_W}{\mu} - 16\ln\frac{m_W}{\mu}\ln\frac{m_W}{\nu}\right)\right. \\
&\qquad \left. + \left[\frac{1}{\omega}\right]_*^{[m_W]}\left(-6\ln\left(\frac{m_W^2+\omega^2}{m_W^2}\right) - 2\frac{\omega^2}{m_W^2+\omega^2} + 8\ln\frac{\mu^2}{m_W^2}\right)\right].
\end{aligned} \tag{E.34}$$

Let us remark, that I_{vv}^{real} only contributes to the $ij = 22$ operator combination. The reason lies in the fact, that for operator $\mathcal{O}_1$ (6.28) the relevant Wilson line structure reads

$$\left[Y_v^\dagger T_1^{AB} Y_v\right]_{ab} = \delta^{AB}\left[Y_v^\dagger Y_v\right]_{ab} = \delta^{AB}\delta_{ab}\,, \tag{E.35}$$

to all orders. Correspondingly, the virtual heavy DM Wilson line only correction $I_{vv}^{\mathrm{virt.}}$ cannot appear for $ij = 11$.

E.4 Expressions for the resummed wino soft coefficients $\hat{W}^{ij}_{IJ}$

In this Section, we collect all inverse Laplace transformed soft coefficients $\hat{W}^{\text{wino}}$, that are necessary for NLL' resummation. The corresponding discussion of the respective Laplace transformations and functions is given in Section 7.3, and the coefficients $\hat{W}^{\text{wino}}_{IJ}$ defined in (7.62). The inverse Laplace transforms $F(\omega), P(\omega)$ are defined in (7.64), (7.65), respectively. For the index combination $ij = 11$, the coefficients read

$$\begin{aligned}\hat{W}^{11}_{(00)(00)}(\omega,\mu_s,\nu) &= \hat{W}^{11}_{(00)(+-)}(\omega,\mu_s,\nu) = \hat{W}^{11}_{(+-)(00)}(\omega,\mu_s,\nu) = \hat{W}^{11}_{(+-)(+-)}(\omega,\mu_s,\nu)\\ &= \left(1+\frac{\hat{\alpha}_2}{4\pi}\,(-16)\ln\frac{m_W}{\mu_s}\,\partial_\eta\right)\frac{e^{-\gamma_E\eta}}{\Gamma(\eta)}\frac{1}{\omega}\left(\frac{\omega}{\nu}\right)^{\eta}\,. \end{aligned}\tag{E.36}$$

We emphasize that η is defined in (7.34) and is not to be confused with the rapidity regulator used for the loop integral calculation (cf. Section E.1). For the operator combination $ij = 12$, we find

$$\begin{aligned}\hat{W}^{12}_{(00)(00)}(\omega,\mu_s,\nu) &= \hat{W}^{12}_{(+-)(00)}(\omega,\mu_s,\nu)\\ &= \frac{\hat{\alpha}_2}{4\pi}\left[(8+8\pi i)\ln\frac{m_W}{\mu_s}\right]\frac{e^{-\gamma_E\eta}}{\Gamma(\eta)}\frac{1}{\omega}\left(\frac{\omega}{\nu}\right)^{\eta}+\frac{\hat{\alpha}_2}{4\pi}\left[8F(\omega)\right]\,,\\ \hat{W}^{12}_{(00)(+-)}(\omega,\mu_s,\nu) &= \left[1+\frac{\hat{\alpha}_2}{4\pi}\left(\left(-16\ln\frac{m_W}{\mu_s}\,\partial_\eta\right)-(4+4\pi i)\ln\frac{m_W}{\mu_s}\right)\right]\frac{e^{-\gamma_E\eta}}{\Gamma(\eta)}\frac{1}{\omega}\left(\frac{\omega}{\nu}\right)^{\eta}\\ &\quad+\frac{\hat{\alpha}_2}{4\pi}\left[-4F(\omega)\right]\,,\\ \hat{W}^{12}_{(+-)(+-)}(\omega,\mu_s,\nu) &= \hat{W}^{12}_{(00)(+-)}(\omega,\mu_s,\nu)+\frac{\hat{\alpha}_2}{4\pi}\left[-2F(\omega)\right]\,. \end{aligned}\tag{E.37}$$

The combination $ij = 21$ is related to $ij = 12$ by complex conjugation and exchange of two-particles states $IJ \to JI$, via

$$\begin{aligned}\hat{W}^{21}_{(00)(00)}(\omega,\mu_s,\nu) &= \hat{W}^{12*}_{(00)(00)}(\omega,\mu_s,\nu)\\ \hat{W}^{21}_{(00)(+-)}(\omega,\mu_s,\nu) &= \hat{W}^{12*}_{(+-)(00)}(\omega,\mu_s,\nu)\\ \hat{W}^{21}_{(+-)(00)}(\omega,\mu_s,\nu) &= \hat{W}^{12*}_{(00)(+-)}(\omega,\mu_s,\nu)\\ \hat{W}^{21}_{(+-)(+-)}(\omega,\mu_s,\nu) &= \hat{W}^{12*}_{(+-)(+-)}(\omega,\mu_s,\nu)\,. \end{aligned}\tag{E.38}$$

The last operator combination is $ij = 22$

$$\begin{aligned}\hat{W}^{22}_{(00)(00)}(\omega,\mu_s,\nu) &= \frac{\hat{\alpha}_2}{4\pi}\left[8F(\omega)-8P(\omega)\right]\,,\\ \hat{W}^{22}_{(00)(+-)}(\omega,\mu_s,\nu) &= \hat{W}^{22*}_{(+-)(00)}(\omega,\mu_s,\nu)\\ &= \left[\frac{\hat{\alpha}_2}{4\pi}\,(8-8\pi i)\ln\frac{m_W}{\mu_s}\right]\frac{e^{-\gamma_E\eta}}{\Gamma(\eta)}\frac{1}{\omega}\left(\frac{\omega}{\nu}\right)^{\eta}+\frac{\hat{\alpha}_2}{4\pi}\left[4F(\omega)+4P(\omega)\right]\,,\\ \hat{W}^{22}_{(+-)(+-)}(\omega,\mu_s,\nu) &= \left[1+\frac{\hat{\alpha}_2}{4\pi}\left(\left(-16\ln\frac{m_W}{\mu_s}\,\partial_\eta\right)-8\ln\frac{m_W}{\mu_s}\right)\right]\frac{e^{-\gamma_E\eta}}{\Gamma(\eta)}\frac{1}{\omega}\left(\frac{\omega}{\nu}\right)^{\eta}\\ &\quad+\frac{\hat{\alpha}_2}{4\pi}\left[-6F(\omega)-2P(\omega)\right]\,. \end{aligned}\tag{E.39}$$

F

Merging and differential spectra

In this Appendix, we provide the technical details on merging differential and cumulative cross-sections between the various resolution cases and the `PPPC4DM` [175] as presented in the main text (cf. Chapter 8). Furthermore, we discuss implementing the wino and Higgsino dark matter model using the `PPPC4DM`, and a technical addition to ensure an appropriate matching procedure. The technical addition and merging of `PPPC4DM` and the resummed intermediate endpoint results were originally developed by M. Vollmann (`PPPC4DM` and merging to intermediate resolution) and independently checked and implemented by the author to supply fully differential spectra away from the endpoint.

F.1 Merging procedures

To merge the differential and cumulative cross-section between narrow $E^{\gamma}_{\text{res}} \sim m_W^2/m_\chi$ and intermediate $E^{\gamma}_{\text{res}} \sim m_W$ resolution calculation, we define the following function

$$w_1(x,\varepsilon) = \begin{cases} 0 & \text{if} \quad \varepsilon < 1-x \\ \frac{1}{1-4\varepsilon}\left(1 - \frac{1-x}{\varepsilon}\right) & \text{if} \quad 4\varepsilon^2 \geq 1-x \geq \varepsilon \\ 1 & \text{if} \quad 1-x < 4\varepsilon^2 \end{cases} \tag{F.1}$$

with $\varepsilon = m_W/(2m_\chi)$, chosen as some resolution-dependent logarithms for intermediate resolution are typically dependent on $x_\gamma = 2E^{\gamma}_{\text{res}}/m_W = \frac{1}{\varepsilon} - 2E_\gamma/m_W$ (cf. Section 5 and Appendix E of [101]). We use the dimensionless variable $x = E_\gamma/m_\chi$. In this way, $x = 1$ correspond to the fully exclusive case $\chi^0\chi^0 \to \gamma\gamma$, whilst $x = 0$ describes the fully inclusive $\chi^0\chi^0$ cross-section. The above function is chosen so that it vanishes if the photon energy is within the intermediate resolution regime. The lower boundary of the intermediate resolution regime is chosen at $E^{\gamma}_{\text{res}} = m_W/2$. Other choices are possible, as well. However, the above value still leaves separation to the narrow resolution boundary chosen at $4\varepsilon^2 = m_W^2/m_\chi^2$. This choice enables a smooth merging procedure also for low DM mass value $m_\chi \sim 500\,\text{GeV}$. The narrow resolution boundary is picked such that it is well above the Z-pole at $E^{\gamma}_{\text{res}} = m_Z^2/(4m_\chi)$. In fact, we start the merging at the $W^+W^-\gamma$ threshold to ensure an extended enough merging region between narrow and intermediate resolution calculation. We tested that varying the boundaries within factors of two, without overlapping narrow and intermediate resolution regimes, produces similar results within the theoretical uncertainty determined in the main text for cumulative results. For mass values above $m_\chi \sim 1\,\text{TeV}$, this also holds for the differential spectrum. Some changes can be visible at small mass values, as the narrow and intermediate calculation do not merge perfectly in the differential spectrum for low masses. However, as stated, the differences in the cumulative cross-sections are always negligible. The cross-section is then merged, with the linear function

w_1 between the boundaries using

$$\left.\frac{d(\sigma v)}{dx}\right|_{\text{merged}} = w_1(x,\varepsilon)\, \left.\frac{d(\sigma v)}{dx}\right|_{\text{narrow}} + (1-w_1(x,\varepsilon))\, \left.\frac{d(\sigma v)}{dx}\right|_{\text{intermediate}} \tag{F.2}$$

and analogously for the cumulative cross-section. For the merging to the `PPPC4DM` implemented as discussed below, we define a second function in the same spirit

$$w_2(x,\varepsilon) = \begin{cases} 0 & \text{if} \quad \min(20\varepsilon, 0.5) \leq 1-x \leq 1 \\ 1 - \frac{1-x-\min(4\varepsilon,0.2)}{\min(20\varepsilon,0.5)-\min(4\varepsilon,0.2)} & \text{if} \quad \min(4\varepsilon, 0.2) \leq 1-x \leq \min(20\varepsilon, 0.5) \\ 1 & \text{if} \quad 0 \leq 1-x \leq \min(4\varepsilon, 0.2) \end{cases} \tag{F.3}$$

The boundaries of the validity regions are picked, such that the `PPPC4DM` prediction is taken as the true value within the boundaries of the minimum of 0.5 or 20ε, where the former is motivated for small masses where m_W and m_χ might be rather close. The latter is chosen to allow for an extended merging region between intermediate and `PPPC4DM` calculation. The lower boundary, where the intermediate resolution calculation is taken as the true value is set at the minimum of 4ε and 0.2, with the latter again necessitated to cover the low mass regime. Note that in this way, there is no overlap between narrow/intermediate and intermediate/`PPPC4DM` merging, as long as $4m_W > m_\chi$. The differential cross-section, and analogously the cumulative counterpart, are then merged according to

$$\left.\frac{d(\sigma v)}{dx}\right|_{\text{full merged}} = w_2(x,\varepsilon)\, \left.\frac{d(\sigma v)}{dx}\right|_{\text{merged}} + (1-w_2(x,\varepsilon))\, \left.\frac{d(\sigma v)}{dx}\right|_{\texttt{PPPC4DM}} . \tag{F.4}$$

F.2 PPPC4DM implementation

The `PPPC4DM` [175] provides the electroweak parton shower prediction away from the endpoint, using Monte-Carlo event generators and the EW evolution equations following [180]. In our implementation, we use

$$\begin{aligned} \left.\frac{d(\sigma v)}{dx}\right|_{\texttt{PPPC4DM}} = 2\sum_{I,J} S_{IJ} \Bigg[& \hat{\Gamma}^{WW}_{IJ}\, \frac{dN_{W_T W_T \to \gamma + X}}{dx} + \hat{\Gamma}^{ZZ}_{IJ}\, \frac{dN_{Z_T Z_T \to \gamma+X}}{dx} \\ & + \hat{\Gamma}^{\gamma Z}_{IJ}\, \frac{dN_{\gamma Z_T \to \gamma+X}}{dx} + \hat{\Gamma}^{\gamma\gamma}_{IJ}\, \frac{dN_{\gamma\gamma\to\gamma+X}}{dx} \Bigg] \end{aligned} \tag{F.5}$$

to generate the `PPPC4DM` prediction, where the functions $dN/(dx)$ are supplied within the package. The tree-level annihilation matrices $\hat{\Gamma}$ in method-II [86] are given below for the wino and Higgsino model. Finally, the Sommerfeld factors are calculated as in the main text (6.25). For definiteness, we do evaluate the tree-level annihilation matrices using running couplings at two-loops at the scale $\mu_h = 2m_\chi$.

In principle, this suffices to generate the `PPPC4DM` prediction. However, the provided interpolating tables are not very dense for $x \geq 0.7$, i.e., precisely in the region where we want to merge to the resummed endpoint results discussed in the main text. To ensure a smooth matching procedure, we therefore add further points to these tables. We identified that the dominant contribution in the merging region $1-x \ll 1$ comes from the splittings associated with the tree-level $\chi\chi \to W^+W^-$. Of the needed splitting function, the dominant contribution can be approximated by

$$\frac{dN_{W_T\to\gamma}}{d\ln x} \approx \int_x^1 dz\, D^{\text{EW}}_{W_T\to\gamma}(z)\, \frac{dN^{\text{MC}}_{\gamma\to\gamma}}{d\ln x}\left(z m_\chi, \frac{x}{z}\right) \tag{F.6}$$

where the splitting kernel D^{EW} is given by [180]

$$D^{\mathrm{EW}}_{W_T\to\gamma}(z) = \frac{\alpha}{2\pi}\cdot 2\left[\frac{z}{1-z}L(1-z) + \left(\frac{1-z}{z} + z(1-z)\right)\ln\frac{1}{\varepsilon^2}\right]. \tag{F.7}$$

This approximation merges very well with the existing points and allows a smooth merging into the region where the endpoint results have superior accuracy (cf. Chapter 8). The massive logarithm $L(x)$ following [180] is given by

$$L(x) = \ln\frac{m_\chi^2 x^2}{m_W^2} + 2\,\mathrm{Re}\left[\ln\left(1 + \sqrt{1 - \frac{m_W^2}{x^2 m_\chi^2}}\right)\right] \tag{F.8}$$

As we do not have the Monte-Carlo results available in this region, we use the leading approximation for $1 - x \to 0$, which is given by the delta-function contribution, up to corrections of the order of the electromagnetic coupling

$$\frac{dN^{\mathrm{MC}}_{\gamma\gamma\to\gamma+X}}{dx} = 2\,\delta(1-x) + \mathcal{O}(\alpha)\,. \tag{F.9}$$

Wino tree-level annihilation matrices

The necessary tree-level annihilation matrices for the wino in method-II read [74, 85]

$$\hat{\Gamma}^{WW} = \frac{\pi\hat{\alpha}_2^2}{m_\chi^2}\begin{pmatrix} 1 & \frac{1}{\sqrt{2}} \\ \frac{1}{\sqrt{2}} & \frac{1}{2}\end{pmatrix}, \qquad \hat{\Gamma}^{ZZ} = \frac{\pi\hat{\alpha}_2^2}{m_\chi^2}\begin{pmatrix} 0 & 0 \\ 0 & \hat{c}_W^4\end{pmatrix},$$

$$\hat{\Gamma}^{\gamma Z} = \frac{\pi\hat{\alpha}_2^2}{m_\chi^2}\begin{pmatrix} 0 & 0 \\ 0 & 2\hat{s}_W^2\hat{c}_W^2\end{pmatrix}, \qquad \hat{\Gamma}^{\gamma\gamma} = \frac{\pi\hat{\alpha}_2^2}{m_\chi^2}\begin{pmatrix} 0 & 0 \\ 0 & \hat{s}_W^4\end{pmatrix}, \tag{F.10}$$

where the matrix entries refer to the state vector $(00, +-)^T$

Higgsino tree-level annihilation matrices

The necessary tree-level annihilation matrices for the Higgsino in method-II read [74, 84]

$$\hat{\Gamma}^{WW} = \frac{\pi\hat{\alpha}_2^2}{16 m_\chi^2}\begin{pmatrix} 1 & 1 & \sqrt{2} \\ 1 & 1 & \sqrt{2} \\ \sqrt{2} & \sqrt{2} & 2\end{pmatrix},$$

$$\hat{\Gamma}^{ZZ} = \frac{\pi\hat{\alpha}_2^2}{16\hat{c}_W^4 m_\chi^2}\begin{pmatrix} \frac{1}{2} & \frac{1}{2} & \frac{1}{\sqrt{2}}(\hat{c}_W^2 - \hat{s}_W^2)^2 \\ \frac{1}{2} & \frac{1}{2} & \frac{1}{\sqrt{2}}(\hat{c}_W^2 - \hat{s}_W^2)^2 \\ \frac{1}{\sqrt{2}}(\hat{c}_W^2 - \hat{s}_W^2)^2 & \frac{1}{\sqrt{2}}(\hat{c}_W^2 - \hat{s}_W^2)^2 & (\hat{c}_W^2 - \hat{s}_W^2)^4\end{pmatrix},$$

$$\hat{\Gamma}^{\gamma Z} = \frac{\pi\hat{\alpha}_2^2\hat{s}_W^2}{2\hat{c}_W^2 m_\chi^2}\begin{pmatrix} 0 & 0 & 0 \\ 0 & 0 & 0 \\ 0 & 0 & (\hat{c}_W^2 - \hat{s}_W^2)^2\end{pmatrix}$$

$$\hat{\Gamma}^{\gamma\gamma} = \frac{\pi\hat{\alpha}_2^2}{m_\chi^2}\begin{pmatrix} 0 & 0 & 0 \\ 0 & 0 & 0 \\ 0 & 0 & \hat{s}_W^4\end{pmatrix}, \tag{F.11}$$

where the matrix entries refer to the state vector $(11, 22, +-)^T$.

Acknowledgements

First and foremost, I am grateful to Prof. Martin Beneke for his advice, the many inspiring discussions, and the opportunity to work on the projects presented in this thesis. I am also very much indebted to Robert Szafron for the countless discussions on effective field theories and for shaping the way how I think about them. Similarly, I am thankful to Martin Vollmann for explaining a lot of astrophysics to me and the ever so often discussion on yet another factor of two.

It was also a great pleasure to work with all my collaborators, Prof. Martin Beneke, Alessandro Broggio, Caspar Hasner, Robert Szafron and Martin Vollmann, on the projects that made this thesis possible in the first place.

Special thanks are due to Andreas Mütter for proofreading parts of this thesis and providing me with his thesis template. Furthermore, I thank Martin Vollmann for checking some of the equations and clarifying many points, especially on the log-expansion for wino and Higgsino.

Furthermore, I want to thank all the members of T31 over the years for the pleasant working atmosphere and the always interesting discussions over lunch. I particularly want to thank Sebastian Jaskiewicz for sharing countless coffee-breaks, and many exciting evenings with the occasional refreshing drink. A special thank you also goes to Elke Hutsteiner for all the help with the administrative struggles and keeping them to a minimum.

Moreover, I want to thank my officemates in 1122, especially Anja Brenner, Sebastian Ingenhütt, Andreas Mütter, Erik Parr, and Jan Toelstede, for providing an always fun working atmosphere with the sporadic distraction.

Finally, I want to thank my parents and my brother for the constant support over the years.

We have used `AxoDraw` [181] and `JaxoDraw` [182] to draw Feynman diagrams in this thesis. Furthermore, we used `NumPy` [183] and `Mathematica` [184] for creating numerical results and evaluation of parameter scans, and `Matplotlib` [185] to produce plots and figures. This work was supported by the Deutsche Forschungsgemeinschaft (SFB 1258).

Bibliography

[1] F. Zwicky, *Die Rotverschiebung von extragalaktischen Nebeln*, *Helv. Phys. Acta* **6** (1933) 110–127.

[2] **Planck** Collaboration, N. Aghanim et al., *Planck 2018 results. VI. Cosmological parameters*, *Astron. Astrophys.* **641** (2020) A6, [`arXiv:1807.0620`].

[3] V. C. Rubin and W. K. Ford, Jr., *Rotation of the Andromeda Nebula from a Spectroscopic Survey of Emission Regions*, *Astrophys. J.* **159** (1970) 379–403.

[4] V. C. Rubin, N. Thonnard, and W. K. Ford, Jr., *Rotational properties of 21 SC galaxies with a large range of luminosities and radii, from NGC 4605 /R = 4kpc/ to UGC 2885 /R = 122 kpc/*, *Astrophys. J.* **238** (1980) 471.

[5] J. A. Tyson, G. P. Kochanski, and I. P. Dell'Antonio, *Detailed mass map of CL0024+1654 from strong lensing*, *Astrophys. J. Lett.* **498** (1998) L107, [`astro-ph/9801193`].

[6] A. Refregier, *Weak gravitational lensing by large scale structure*, *Ann. Rev. Astron. Astrophys.* **41** (2003) 645–668, [`astro-ph/0307212`].

[7] W. J. Percival, S. Cole, D. J. Eisenstein, R. C. Nichol, J. A. Peacock, A. C. Pope, and A. S. Szalay, *Measuring the Baryon Acoustic Oscillation scale using the SDSS and 2dFGRS*, *Mon. Not. Roy. Astron. Soc.* **381** (2007) 1053–1066, [`arXiv:0705.3323`].

[8] D. Clowe, M. Bradac, A. H. Gonzalez, M. Markevitch, S. W. Randall, C. Jones, and D. Zaritsky, *A direct empirical proof of the existence of dark matter*, *Astrophys. J. Lett.* **648** (2006) L109–L113, [`astro-ph/0608407`].

[9] S. D. McDermott, H.-B. Yu, and K. M. Zurek, *Turning off the Lights: How Dark is Dark Matter?*, *Phys. Rev. D* **83** (2011) 063509, [`arXiv:1011.2907`].

[10] D. Harvey, R. Massey, T. Kitching, A. Taylor, and E. Tittley, *The non-gravitational interactions of dark matter in colliding galaxy clusters*, *Science* **347** (2015) 1462–1465, [`arXiv:1503.0767`].

[11] B. Audren, J. Lesgourgues, G. Mangano, P. D. Serpico, and T. Tram, *Strongest model-independent bound on the lifetime of Dark Matter*, *JCAP* **12** (2014) 028, [`arXiv:1407.2418`].

[12] A. Boyarsky, O. Ruchayskiy, and D. Iakubovskyi, *A Lower bound on the mass of Dark Matter particles*, *JCAP* **03** (2009) 005, [`arXiv:0808.3902`].

[13] M. A. Monroy-Rodríguez and C. Allen, *The end of the MACHO era- revisited: new limits on MACHO masses from halo wide binaries*, *Astrophys. J.* **790** (2014), no. 2 159, [`arXiv:1406.5169`].

[14] T. D. Brandt, *Constraints on MACHO Dark Matter from Compact Stellar Systems in Ultra-Faint Dwarf Galaxies*, *Astrophys. J. Lett.* **824** (2016), no. 2 L31, [`arXiv:1605.0366`].

[15] **Particle Data Group** Collaboration, P. Zyla et al., *Review of Particle Physics*, *PTEP* **2020** (2020), no. 8 083C01.

[16] E. Di Valentino, E. Giusarma, M. Lattanzi, O. Mena, A. Melchiorri, and J. Silk, *Cosmological Axion and neutrino mass constraints from Planck 2015 temperature and polarization data*, *Phys. Lett. B* **752** (2016) 182–185, [`arXiv:1507.0866`].

[17] E. W. Kolb and M. S. Turner, *The Early Universe*, vol. 69. 1990.

[18] A. J. S. Hamilton and M. Tegmark, *The Real space power spectrum of the PSCz survey from 0.01 to 300 h Mpc**-1*, *Mon. Not. Roy. Astron. Soc.* **330** (2002) 506, [`astro-ph/0008392`].

[19] J. S. Bullock and M. Boylan-Kolchin, *Small-Scale Challenges to the ΛCDM Paradigm*, *Ann. Rev. Astron. Astrophys.* **55** (2017) 343–387, [`arXiv:1707.0425`].

[20] A. Del Popolo and M. Le Delliou, *Small scale problems of the ΛCDM model: a short review*, *Galaxies* **5** (2017), no. 1 17, [`arXiv:1606.0779`].

[21] M. Milgrom, *A Modification of the Newtonian dynamics as a possible alternative to the hidden mass hypothesis*, *Astrophys. J.* **270** (1983) 365–370.

[22] B. Carr and F. Kuhnel, *Primordial Black Holes as Dark Matter: Recent Developments*, *Ann. Rev. Nucl. Part. Sci.* **70** (2020) 355–394, [`arXiv:2006.0283`].

[23] G. Bertone et al., *Particle Dark Matter: Observations, Models and Searches.* Cambridge Univ. Press, Cambridge, 2010.

[24] J. L. Feng, *Dark Matter Candidates from Particle Physics and Methods of Detection*, *Ann. Rev. Astron. Astrophys.* **48** (2010) 495–545, [`arXiv:1003.0904`].

[25] S. Weinberg, *A New Light Boson?*, *Phys. Rev. Lett.* **40** (1978) 223–226.

[26] F. Wilczek, *Problem of Strong P and T Invariance in the Presence of Instantons*, *Phys. Rev. Lett.* **40** (1978) 279–282.

[27] R. D. Peccei and H. R. Quinn, *CP Conservation in the Presence of Instantons*, *Phys. Rev. Lett.* **38** (1977) 1440–1443.

[28] L. Roszkowski, E. M. Sessolo, and S. Trojanowski, *WIMP dark matter candidates and searches—current status and future prospects*, *Rept. Prog. Phys.* **81** (2018), no. 6 066201, [`arXiv:1707.0627`].

[29] P. Gondolo and G. Gelmini, *Cosmic abundances of stable particles: Improved analysis*, *Nucl. Phys. B* **360** (1991) 145–179.

[30] G. Steigman, B. Dasgupta, and J. F. Beacom, *Precise Relic WIMP Abundance and its Impact on Searches for Dark Matter Annihilation*, *Phys. Rev. D* **86** (2012) 023506, [`arXiv:1204.3622`].

[31] G. Jungman, M. Kamionkowski, and K. Griest, *Supersymmetric dark matter*, *Phys. Rept.* **267** (1996) 195–373, [`hep-ph/9506380`].

[32] E. Gildener, *Gauge Symmetry Hierarchies*, *Phys. Rev. D* **14** (1976) 1667.

[33] S. Weinberg, *Gauge Hierarchies*, *Phys. Lett. B* **82** (1979) 387–391.

[34] S. P. Martin, *A Supersymmetry primer*, *Adv. Ser. Direct. High Energy Phys.* **18** (1998) 1–98, [`hep-ph/9709356`].

[35] M. Drees and M. M. Nojiri, *The Neutralino relic density in minimal $N = 1$ supergravity*, *Phys. Rev. D* **47** (1993) 376–408, [`hep-ph/9207234`].

[36] M. Beneke, C. Hellmann, and P. Ruiz-Femenía, *Heavy neutralino relic abundance with Sommerfeld enhancements - a study of pMSSM scenarios*, *JHEP* **03** (2015) 162, [`arXiv:1411.6930`].

[37] M. Cirelli, N. Fornengo, and A. Strumia, *Minimal dark matter*, *Nucl. Phys. B* **753** (2006) 178–194, [`hep-ph/0512090`].

[38] M. Cirelli, A. Strumia, and M. Tamburini, *Cosmology and Astrophysics of Minimal Dark Matter*, *Nucl. Phys. B* **787** (2007) 152–175, [`arXiv:0706.4071`].

[39] J. Hisano, S. Matsumoto, M. Nagai, O. Saito, and M. Senami, *Non-perturbative effect on thermal relic abundance of dark matter*, *Phys. Lett. B* **646** (2007) 34–38, [`hep-ph/0610249`].

[40] M. Beneke, A. Bharucha, F. Dighera, C. Hellmann, A. Hryczuk, S. Recksiegel, and P. Ruiz-Femenía, *Relic density of wino-like dark matter in the MSSM*, *JHEP* **03** (2016) 119, [`arXiv:1601.0471`].

[41] **ATLAS** Collaboration, M. Aaboud et al., *Search for long-lived charginos based on a disappearing-track signature in pp collisions at $\sqrt{s} = 13$ TeV with the ATLAS detector*, *JHEP* **06** (2018) 022, [`arXiv:1712.0211`].

[42] **CMS** Collaboration, A. M. Sirunyan et al., *Search for disappearing tracks as a signature of new long-lived particles in proton-proton collisions at $\sqrt{s} = 13$ TeV*, *JHEP* **08** (2018) 016, [`arXiv:1804.0732`].

[43] M. Low and L.-T. Wang, *Neutralino dark matter at 14 TeV and 100 TeV*, *JHEP* **08** (2014) 161, [`arXiv:1404.0682`].

[44] M. Cirelli, F. Sala, and M. Taoso, *Wino-like Minimal Dark Matter and future colliders*, *JHEP* **10** (2014) 033, [`arXiv:1407.7058`]. [Erratum: JHEP 01, 041 (2015)].

[45] S. Gori, S. Jung, L.-T. Wang, and J. D. Wells, *Prospects for Electroweakino Discovery at a 100 TeV Hadron Collider*, *JHEP* **12** (2014) 108, [`arXiv:1410.6287`].

[46] A. Berlin, T. Lin, M. Low, and L.-T. Wang, *Neutralinos in Vector Boson Fusion at High Energy Colliders*, *Phys. Rev. D* **91** (2015), no. 11 115002, [`arXiv:1502.0504`].

[47] M. Saito, R. Sawada, K. Terashi, and S. Asai, *Discovery reach for wino and higgsino dark matter with a disappearing track signature at a 100 TeV pp collider*, *Eur. Phys. J. C* **79** (2019), no. 6 469, [`arXiv:1901.0298`].

[48] R. J. Hill and M. P. Solon, *Universal behavior in the scattering of heavy, weakly interacting dark matter on nuclear targets*, *Phys. Lett. B* **707** (2012) 539–545, [`arXiv:1111.0016`].

[49] R. J. Hill and M. P. Solon, *WIMP-nucleon scattering with heavy WIMP effective theory*, *Phys. Rev. Lett.* **112** (2014) 211602, [`arXiv:1309.4092`].

[50] R. J. Hill and M. P. Solon, *Standard Model anatomy of WIMP dark matter direct detection I: weak-scale matching*, *Phys. Rev. D* **91** (2015) 043504, [`arXiv:1401.3339`].

[51] R. J. Hill and M. P. Solon, *Standard Model anatomy of WIMP dark matter direct detection II: QCD analysis and hadronic matrix elements*, *Phys. Rev. D* **91** (2015) 043505, [`arXiv:1409.8290`].

[52] J. Hisano, R. Nagai, and N. Nagata, *Effective Theories for Dark Matter Nucleon Scattering*, *JHEP* **05** (2015) 037, [`arXiv:1502.0224`].

[53] J. Hisano, K. Ishiwata, and N. Nagata, *QCD Effects on Direct Detection of Wino Dark Matter*, *JHEP* **06** (2015) 097, [`arXiv:1504.0091`].

[54] Q. Chen and R. J. Hill, *Direct detection rate of heavy Higgsino-like and Wino-like dark matter*, *Phys. Lett. B* **804** (2020) 135364, [`arXiv:1912.0779`].

[55] J. Billard, L. Strigari, and E. Figueroa-Feliciano, *Implication of neutrino backgrounds on the reach of next generation dark matter direct detection experiments*, *Phys. Rev. D* **89** (2014), no. 2 023524, [`arXiv:1307.5458`].

[56] M. Schumann, *Direct Detection of WIMP Dark Matter: Concepts and Status*, *J. Phys. G* **46** (2019), no. 10 103003, [`arXiv:1903.0302`].

[57] T. R. Slatyer, *Indirect Detection of Dark Matter*, in *Theoretical Advanced Study Institute in Elementary Particle Physics: Anticipating the Next Discoveries in Particle Physics*, 10, 2017. `arXiv:1710.0513`.

[58] J. Zavala and C. S. Frenk, *Dark matter haloes and subhaloes*, *Galaxies* **7** (2019), no. 4 81, [`arXiv:1907.1177`].

[59] M. Kachelriess and D. V. Semikoz, *Cosmic Ray Models*, *Prog. Part. Nucl. Phys.* **109** (2019) 103710, [`arXiv:1904.0816`].

[60] D. J. Thompson et al., *Calibration of the Energetic Gamma-Ray Experiment Telescope (EGRET) for the Compton Gamma-Ray Observatory*, *Astrophys. J. Suppl.* **86** (1993) 629–656.

[61] **Fermi-LAT** Collaboration, W. B. Atwood et al., *The Large Area Telescope on the Fermi Gamma-ray Space Telescope Mission*, *Astrophys. J.* **697** (2009) 1071–1102, [`arXiv:0902.1089`].

[62] T. C. Weekes et al., *VERITAS: The Very energetic radiation imaging telescope array system*, *Astropart. Phys.* **17** (2002) 221–243, [`astro-ph/0108478`].

[63] J. Aleksić et al., *Optimized dark matter searches in deep observations of Segue 1 with MAGIC*, *JCAP* **02** (2014) 008, [`arXiv:1312.1535`].

[64] **HAWC** Collaboration, A. Albert et al., *Dark Matter Limits From Dwarf Spheroidal Galaxies with The HAWC Gamma-Ray Observatory*, *Astrophys. J.* **853** (2018), no. 2 154, [`arXiv:1706.0127`].

[65] **HESS** Collaboration, H. Abdallah et al., *Search for γ-Ray Line Signals from Dark Matter Annihilations in the Inner Galactic Halo from 10 Years of Observations with H.E.S.S.*, *Phys. Rev. Lett.* **120** (2018), no. 20 201101, [`arXiv:1805.0574`].

[66] **CTA Consortium** Collaboration, M. Actis et al., *Design concepts for the Cherenkov Telescope Array CTA: An advanced facility for ground-based high-energy gamma-ray astronomy*, *Exper. Astron.* **32** (2011) 193–316, [`arXiv:1008.3703`].

[67] **CTA Consortium** Collaboration, B. S. Acharya et al., *Science with the Cherenkov Telescope Array.* WSP, 11, 2018.

[68] L. Bergstrom and P. Ullio, *Full one loop calculation of neutralino annihilation into two photons*, *Nucl. Phys. B* **504** (1997) 27–44, [`hep-ph/9706232`].

[69] Z. Bern, P. Gondolo, and M. Perelstein, *Neutralino annihilation into two photons*, *Phys. Lett. B* **411** (1997) 86–96, [`hep-ph/9706538`].

[70] P. Ullio and L. Bergstrom, *Neutralino annihilation into a photon and a Z boson*, *Phys. Rev. D* **57** (1998) 1962–1971, [`hep-ph/9707333`].

[71] A. Sommerfeld, *Über die Beugung und Bremsung der Elektronen*, *Annalen der Physik* **403** (1931), no. 3 257–330, [`https://onlinelibrary.wiley.com/doi/pdf/10.1002/andp.19314030302`].

[72] V. V. Sudakov, *Vertex parts at very high-energies in quantum electrodynamics*, *Sov. Phys. JETP* **3** (1956) 65–71.

[73] J. Hisano, S. Matsumoto, and M. M. Nojiri, *Explosive dark matter annihilation*, *Phys. Rev. Lett.* **92** (2004) 031303, [`hep-ph/0307216`].

[74] J. Hisano, S. Matsumoto, M. M. Nojiri, and O. Saito, *Non-perturbative effect on dark matter annihilation and gamma ray signature from galactic center*, *Phys. Rev. D* **71** (2005) 063528, [`hep-ph/0412403`].

[75] **PAMELA** Collaboration, O. Adriani et al., *An anomalous positron abundance in cosmic rays with energies 1.5-100 GeV*, *Nature* **458** (2009) 607–609, [`arXiv:0810.4995`].

[76] N. Arkani-Hamed, D. P. Finkbeiner, T. R. Slatyer, and N. Weiner, *A Theory of Dark Matter*, *Phys. Rev. D* **79** (2009) 015014, [`arXiv:0810.0713`].

[77] T. R. Slatyer, *The Sommerfeld enhancement for dark matter with an excited state*, *JCAP* **1002** (2010) 028, [`arXiv:0910.5713`].

[78] A. Pineda and J. Soto, *Effective field theory for ultrasoft momenta in NRQCD and NRQED*, *Nucl. Phys. B Proc. Suppl.* **64** (1998) 428–432, [`hep-ph/9707481`].

[79] M. Beneke, *New results on heavy quarks near threshold*, in *3rd Workshop on Continuous Advances in QCD (QCD 98)*, pp. 293–309, 6, 1998. `hep-ph/9806429`.

[80] M. Beneke, A. Signer, and V. A. Smirnov, *Top quark production near threshold and the top quark mass*, *Phys. Lett. B* **454** (1999) 137–146, [`hep-ph/9903260`].

[81] N. Brambilla, A. Pineda, J. Soto, and A. Vairo, *Potential NRQCD: An Effective theory for heavy quarkonium*, *Nucl. Phys. B* **566** (2000) 275, [`hep-ph/9907240`].

[82] A. Pineda and J. Soto, *The Lamb shift in dimensional regularization*, *Phys. Lett. B* **420** (1998) 391–396, [`hep-ph/9711292`].

[83] A. Pineda and J. Soto, *Potential NRQED: The Positronium case*, *Phys. Rev. D* **59** (1999) 016005, [`hep-ph/9805424`].

[84] M. Beneke, C. Hellmann, and P. Ruiz-Femenía, *Non-relativistic pair annihilation of nearly mass degenerate neutralinos and charginos I. General framework and S-wave annihilation*, *JHEP* **03** (2013) 148, [`arXiv:1210.7928`]. [Erratum: JHEP10,224(2013)].

[85] C. Hellmann and P. Ruiz-Femenía, *Non-relativistic pair annihilation of nearly mass degenerate neutralinos and charginos II. P-wave and next-to-next-to-leading order S-wave coefficients*, *JHEP* **08** (2013) 084, [`arXiv:1303.0200`].

[86] M. Beneke, C. Hellmann, and P. Ruiz-Femenía, *Non-relativistic pair annihilation of nearly mass degenerate neutralinos and charginos III. Computation of the Sommerfeld enhancements*, *JHEP* **05** (2015) 115, [`arXiv:1411.6924`].

[87] C. W. Bauer, S. Fleming, D. Pirjol, and I. W. Stewart, *An Effective field theory for collinear and soft gluons: Heavy to light decays*, *Phys. Rev. D* **63** (2001) 114020, [`hep-ph/0011336`].

[88] C. W. Bauer and I. W. Stewart, *Invariant operators in collinear effective theory*, *Phys. Lett. B* **516** (2001) 134–142, [`hep-ph/0107001`].

[89] C. W. Bauer, D. Pirjol, and I. W. Stewart, *Soft collinear factorization in effective field theory*, *Phys. Rev. D* **65** (2002) 054022, [`hep-ph/0109045`].

[90] M. Beneke, A. P. Chapovsky, M. Diehl, and T. Feldmann, *Soft collinear effective theory and heavy to light currents beyond leading power*, *Nucl. Phys. B* **643** (2002) 431–476, [`hep-ph/0206152`].

[91] J.-y. Chiu, F. Golf, R. Kelley, and A. V. Manohar, *Electroweak Sudakov corrections using effective field theory*, *Phys. Rev. Lett.* **100** (2008) 021802, [`arXiv:0709.2377`].

[92] J.-y. Chiu, A. Fuhrer, R. Kelley, and A. V. Manohar, *Factorization Structure of Gauge Theory Amplitudes and Application to Hard Scattering Processes at the LHC*, *Phys. Rev. D* **80** (2009) 094013, [`arXiv:0909.0012`].

[93] M. Bauer, T. Cohen, R. J. Hill, and M. P. Solon, *Soft Collinear Effective Theory for Heavy WIMP Annihilation*, *JHEP* **01** (2015) 099, [`arXiv:1409.7392`].

[94] M. Baumgart, I. Z. Rothstein, and V. Vaidya, *Calculating the Annihilation Rate of Weakly Interacting Massive Particles*, *Phys. Rev. Lett.* **114** (2015) 211301, [`arXiv:1409.4415`].

[95] M. Baumgart, I. Z. Rothstein, and V. Vaidya, *Constraints on Galactic Wino Densities from Gamma Ray Lines*, *JHEP* **04** (2015) 106, [`arXiv:1412.8698`].

[96] G. Ovanesyan, T. R. Slatyer, and I. W. Stewart, *Heavy Dark Matter Annihilation from Effective Field Theory*, *Phys. Rev. Lett.* **114** (2015), no. 21 211302, [`arXiv:1409.8294`].

[97] G. Ovanesyan, N. L. Rodd, T. R. Slatyer, and I. W. Stewart, *One-loop correction to heavy dark matter annihilation*, *Phys. Rev. D* **95** (2017), no. 5 055001, [`arXiv:1612.0481`]. [Erratum: Phys.Rev.D 100, 119901 (2019)].

[98] M. Baumgart, T. Cohen, I. Moult, N. L. Rodd, T. R. Slatyer, M. P. Solon, I. W. Stewart, and V. Vaidya, *Resummed Photon Spectra for WIMP Annihilation*, *JHEP* **03** (2018) 117, [`arXiv:1712.0765`].

[99] M. Baumgart, T. Cohen, E. Moulin, I. Moult, L. Rinchiuso, N. L. Rodd, T. R. Slatyer, I. W. Stewart, and V. Vaidya, *Precision Photon Spectra for Wino Annihilation*, *JHEP* **01** (2019) 036, [`arXiv:1808.0895`].

[100] M. Beneke, A. Broggio, C. Hasner, and M. Vollmann, *Energetic γ-rays from TeV scale dark matter annihilation resummed*, *Phys. Lett. B* **786** (2018) 347–354, [`arXiv:1805.0736`]. [Erratum: Phys.Lett.B 810, 135831 (2020)].

[101] M. Beneke, A. Broggio, C. Hasner, K. Urban, and M. Vollmann, *Resummed photon spectrum from dark matter annihilation for intermediate and narrow energy resolution*, *JHEP* **08** (2019) 103, [`arXiv:1903.0870`]. [Erratum: JHEP 07, 145 (2020)].

[102] M. Beneke, C. Hasner, K. Urban, and M. Vollmann, *Precise yield of high-energy photons from Higgsino dark matter annihilation*, *JHEP* **03** (2020) 030, [`arXiv:1912.0203`].

[103] M. Beneke, R. Szafron, and K. Urban, *Wino potential and Sommerfeld effect at NLO*, *Phys. Lett.* **B800** (2020) 135112, [`arXiv:1909.0458`].

[104] M. Beneke, R. Szafron, and K. Urban, *Sommerfeld-corrected relic abundance of wino dark matter with NLO electroweak potentials*, *JHEP* **02** (2021) 020, [`arXiv:2009.0064`].

[105] M. Beneke and V. A. Smirnov, *Asymptotic expansion of Feynman integrals near threshold*, *Nucl. Phys.* **B522** (1998) 321–344, [`hep-ph/9711391`].

[106] V. A. Smirnov, *Applied asymptotic expansions in momenta and masses*, *Springer Tracts Mod. Phys.* **177** (2002) 1–262.

[107] B. Jantzen, *Foundation and generalization of the expansion by regions*, *JHEP* **12** (2011) 076, [`arXiv:1111.2589`].

[108] T. Y. Semenova, A. V. Smirnov, and V. A. Smirnov, *On the status of expansion by regions*, *Eur. Phys. J. C* **79** (2019), no. 2 136, [`arXiv:1809.0432`].

[109] T. Becher and M. Neubert, *Drell-Yan Production at Small q_T, Transverse Parton Distributions and the Collinear Anomaly*, *Eur. Phys. J. C* **71** (2011) 1665, [`arXiv:1007.4005`].

[110] J.-y. Chiu, A. Jain, D. Neill, and I. Z. Rothstein, *The Rapidity Renormalization Group*, *Phys. Rev. Lett.* **108** (2012) 151601, [`arXiv:1104.0881`].

[111] J.-Y. Chiu, A. Jain, D. Neill, and I. Z. Rothstein, *A Formalism for the Systematic Treatment of Rapidity Logarithms in Quantum Field Theory*, *JHEP* **05** (2012) 084, [`arXiv:1202.0814`].

[112] **CTA Consortium** Collaboration, K. Bernlöhr et al., *Monte Carlo design studies for the Cherenkov Telescope Array*, *Astropart. Phys.* **43** (2013) 171–188, [`arXiv:1210.3503`].

[113] **CTA** Collaboration, A. Acharyya et al., *Sensitivity of the Cherenkov Telescope Array to a dark matter signal from the Galactic centre*, *JCAP* **01** (2021) 057, [`arXiv:2007.1612`].

[114] M. Beneke, Y. Kiyo, and K. Schuller, *Third-order correction to top-quark pair production near threshold I. Effective theory set-up and matching coefficients*, `arXiv:1312.4791`.

[115] G. T. Bodwin, E. Braaten, and G. P. Lepage, *Rigorous QCD analysis of inclusive annihilation and production of heavy quarkonium*, *Phys. Rev. D* **51** (1995) 1125–1171, [`hep-ph/9407339`]. [Erratum: Phys.Rev.D 55, 5853 (1997)].

[116] M. Ibe, S. Matsumoto, and R. Sato, *Mass Splitting between Charged and Neutral Winos at Two-Loop Level*, *Phys. Lett.* **B721** (2013) 252–260, [`arXiv:1212.5989`].

[117] M. Beneke, *Perturbative heavy quark - anti-quark systems*, *PoS* **hf8** (1999) 009, [`hep-ph/9911490`].

[118] P. Asadi, M. Baumgart, P. J. Fitzpatrick, E. Krupczak, and T. R. Slatyer, *Capture and Decay of Electroweak WIMPonium*, *JCAP* **1702** (2017), no. 02 005, [`arXiv:1610.0761`].

[119] A. Mitridate, M. Redi, J. Smirnov, and A. Strumia, *Cosmological Implications of Dark Matter Bound States*, *JCAP* **1705** (2017), no. 05 006, [`arXiv:1702.0114`].

[120] Y. Yamada, *Electroweak two-loop contribution to the mass splitting within a new heavy SU(2)(L) fermion multiplet*, *Phys. Lett. B* **682** (2010) 435–440, [`arXiv:0906.5207`].

[121] J. McKay and P. Scott, *Two-loop mass splittings in electroweak multiplets: winos and minimal dark matter*, *Phys. Rev. D* **97** (2018), no. 5 055049, [`arXiv:1712.0096`].

[122] W. Fischler, *Quark - anti-Quark Potential in QCD*, *Nucl. Phys. B* **129** (1977) 157–174.

[123] T. Appelquist, M. Dine, and I. Muzinich, *The static limit of quantum chromodynamics*, *Phys. Rev. D* **17** (1978) 2074.

[124] A. Billoire, *How heavy must be quarks in order to build coulombic q anti-q bound states*, *Phys. Lett. B* **92** (1980) 343–347.

[125] T. Hahn, *Generating Feynman diagrams and amplitudes with FeynArts 3*, *Comput. Phys. Commun.* **140** (2001) 418–431, [`hep-ph/0012260`].

[126] T. Hahn and M. Perez-Victoria, *Automatized one loop calculations in four-dimensions and D-dimensions*, *Comput. Phys. Commun.* **118** (1999) 153–165, [`hep-ph/9807565`].

[127] H. H. Patel, *Package-X 2.0: A Mathematica package for the analytic calculation of one-loop integrals*, *Comput. Phys. Commun.* **218** (2017) 66–70, [`arXiv:1612.0000`].

[128] A. Denner, *Techniques for calculation of electroweak radiative corrections at the one loop level and results for W physics at LEP-200*, *Fortsch. Phys.* **41** (1993) 307–420, [`arXiv:0709.1075`].

[129] J. Fleischer and F. Jegerlehner, *Radiative Corrections to Higgs Decays in the Extended Weinberg-Salam Model*, *Phys. Rev.* **D23** (1981) 2001–2026.

[130] D. Bardin and G. Passarino, *The Standard Model in the Making: Precision Study of the Electroweak Interactions.* International series of monographs on physics. Clarendon Press, 1999.

[131] M. Laine, *The Renormalized gauge coupling and nonperturbative tests of dimensional reduction*, *JHEP* **06** (1999) 020, [`hep-ph/9903513`].

[132] Y. Schröder, *The Static potential in QCD.* PhD thesis, Hamburg U., 1999.

[133] M. Veltman, *Second Threshold in Weak Interactions*, *Acta Phys. Polon. B* **8** (1977) 475.

[134] G. Feinberg and J. Sucher, *Long-Range Forces from Neutrino-Pair Exchange*, *Phys. Rev.* **166** (1968) 1638–1644.

[135] J. Grifols, E. Masso, and R. Toldra, *Majorana neutrinos and long range forces*, *Phys. Lett. B* **389** (1996) 563–565, [`hep-ph/9606377`].

[136] G. Degrassi, S. Fanchiotti, and A. Sirlin, *Relations Between the On-shell and Ms Frameworks and the M (W) - M (Z) Interdependence*, *Nucl. Phys. B* **351** (1991) 49–69.

[137] F. Jegerlehner, *Renormalizing the standard model*, *Conf. Proc. C* **900603** (1990) 476–590.

[138] K. Blum, R. Sato, and T. R. Slatyer, *Self-consistent Calculation of the Sommerfeld Enhancement*, *JCAP* **06** (2016) 021, [`arXiv:1603.0138`].

[139] E. Braaten, E. Johnson, and H. Zhang, *Zero-range effective field theory for resonant wino dark matter. Part I. Framework*, *JHEP* **11** (2017) 108, [`arXiv:1706.0225`].

[140] E. Braaten, E. Johnson, and H. Zhang, *Zero-range effective field theory for resonant wino dark matter. Part II. Coulomb resummation*, *JHEP* **02** (2018) 150, [`arXiv:1708.0715`].

[141] E. Braaten, E. Johnson, and H. Zhang, *Zero-range effective field theory for resonant wino dark matter. Part III. Annihilation effects*, *JHEP* **05** (2018) 062, [`arXiv:1712.0714`].

[142] H. Georgi, *Lie algebras in particle physics*, vol. 54. Perseus Books, Reading, MA, 2nd ed., 1999.

[143] M. Kreuzer and W. Kummer, *New Coulomb Like Gauge for Massive Gauge Fields*, *Nucl. Phys. B* **276** (1986) 466–480.

[144] J. Edsjo and P. Gondolo, *Neutralino relic density including coannihilations*, *Phys. Rev. D* **56** (1997) 1879–1894, [`hep-ph/9704361`].

[145] B. W. Lee and S. Weinberg, *Cosmological lower bound on heavy neutrino masses*, *Phys. Rev. Lett.* **39** (1977) 165–168.

[146] J. Bernstein, L. S. Brown, and G. Feinberg, *The cosmological heavy neutrino problem revisited*, *Phys. Rev. D* **32** (1985) 3261.

[147] S. Borsanyi et al., *Calculation of the axion mass based on high-temperature lattice quantum chromodynamics*, *Nature* **539** (2016), no. 7627 69–71, [`arXiv:1606.0749`].

[148] M. Laine and M. Meyer, *Standard Model thermodynamics across the electroweak crossover*, *JCAP* **07** (2015) 035, [`arXiv:1503.0493`].

[149] C. Hasner, *Resummed photon spectra from wino and Higgsino dark matter annihilation at NLL' accuracy.* PhD thesis, Munich, Tech. U., 2020.

[150] M. Beneke and T. Feldmann, *Multipole expanded soft collinear effective theory with non-abelian gauge symmetry*, *Phys. Lett. B* **553** (2003) 267–276, [`hep-ph/0211358`].

[151] M. Beneke, M. Garny, R. Szafron, and J. Wang, *Anomalous dimension of subleading-power N-jet operators*, *JHEP* **03** (2018) 001, [`arXiv:1712.0441`].

[152] M. Beneke, P. Falgari, and C. Schwinn, *Threshold resummation for pair production of coloured heavy (s)particles at hadron colliders*, *Nucl. Phys. B* **842** (2011) 414–474, [`arXiv:1007.5414`].

[153] N. D. Christensen and C. Duhr, *FeynRules - Feynman rules made easy*, *Comput. Phys. Commun.* **180** (2009) 1614–1641, [`arXiv:0806.4194`].

[154] N. D. Christensen, P. de Aquino, C. Degrande, C. Duhr, B. Fuks, M. Herquet, F. Maltoni, and S. Schumann, *A Comprehensive approach to new physics simulations*, *Eur. Phys. J. C* **71** (2011) 1541, [`arXiv:0906.2474`].

[155] A. Alloul, N. D. Christensen, C. Degrande, C. Duhr, and B. Fuks, *FeynRules 2.0 - A complete toolbox for tree-level phenomenology*, *Comput. Phys. Commun.* **185** (2014) 2250–2300, [`arXiv:1310.1921`].

[156] R. Mertig, M. Bohm, and A. Denner, *FEYN CALC: Computer algebraic calculation of Feynman amplitudes*, *Comput. Phys. Commun.* **64** (1991) 345–359.

[157] V. Shtabovenko, R. Mertig, and F. Orellana, *New Developments in FeynCalc 9.0*, *Comput. Phys. Commun.* **207** (2016) 432–444, [`arXiv:1601.0116`].

[158] V. Shtabovenko, R. Mertig, and F. Orellana, *FeynCalc 9.3: New features and improvements*, *Comput. Phys. Commun.* **256** (2020) 107478, [`arXiv:2001.0440`].

[159] V. Shtabovenko, *FeynHelpers: Connecting FeynCalc to FIRE and Package-X*, *Comput. Phys. Commun.* **218** (2017) 48–65, [`arXiv:1611.0679`].

[160] G. Passarino and M. Veltman, *One Loop Corrections for e+ e- Annihilation Into mu+ mu- in the Weinberg Model*, *Nucl. Phys. B* **160** (1979) 151–207.

[161] F. Feng, `Apart`*: A Generalized Mathematica Apart Function*, *Comput. Phys. Commun.* **183** (2012) 2158–2164, [`arXiv:1204.2314`].

[162] N. Brambilla, H. S. Chung, V. Shtabovenko, and A. Vairo, *FeynOnium: Using FeynCalc for automatic calculations in Nonrelativistic Effective Field Theories*, *JHEP* **11** (2020) 130, [`arXiv:2006.1545`].

[163] W. Beenakker, R. Kleiss, and G. Lustermans, *No Landau-Yang in QCD*, `arXiv:1508.0711`.

[164] M. Cacciari, L. Del Debbio, J. R. Espinosa, A. D. Polosa, and M. Testa, *A note on the fate of the Landau–Yang theorem in non-Abelian gauge theories*, *Phys. Lett. B* **753** (2016) 476–481, [`arXiv:1509.0785`].

[165] M. Beneke, P. Falgari, and C. Schwinn, *Soft radiation in heavy-particle pair production: All-order colour structure and two-loop anomalous dimension*, *Nucl. Phys. B* **828** (2010) 69–101, [`arXiv:0907.1443`].

[166] G. P. Korchemsky and A. V. Radyushkin, *Renormalization of the Wilson Loops Beyond the Leading Order*, *Nucl. Phys. B* **283** (1987) 342–364.

[167] A. Broggio, C. Gnendiger, A. Signer, D. Stöckinger, and A. Visconti, *SCET approach to regularization-scheme dependence of QCD amplitudes*, *JHEP* **01** (2016) 078, [`arXiv:1506.0530`].

[168] T. Becher and M. D. Schwartz, *Direct photon production with effective field theory*, *JHEP* **02** (2010) 040, [`arXiv:0911.0681`].

[169] T. Becher and G. Bell, *The gluon jet function at two-loop order*, *Phys. Lett. B* **695** (2011) 252–258, [`arXiv:1008.1936`].

[170] F. De Fazio and M. Neubert, *B —> X(u) lepton anti-neutrino lepton decay distributions to order alpha(s)*, *JHEP* **06** (1999) 017, [`hep-ph/9905351`].

[171] S. W. Bosch, B. O. Lange, M. Neubert, and G. Paz, *Factorization and shape function effects in inclusive B meson decays*, *Nucl. Phys. B* **699** (2004) 335–386, [`hep-ph/0402094`].

[172] T. Becher, M. Neubert, and B. D. Pecjak, *Factorization and Momentum-Space Resummation in Deep-Inelastic Scattering*, *JHEP* **01** (2007) 076, [`hep-ph/0607228`].

[173] T. Becher and M. Neubert, *Threshold resummation in momentum space from effective field theory*, *Phys. Rev. Lett.* **97** (2006) 082001, [`hep-ph/0605050`].

[174] R. G. Stuart, *Gauge invariance, analyticity and physical observables at the Z0 resonance*, *Phys. Lett. B* **262** (1991) 113–119.

[175] M. Cirelli, G. Corcella, A. Hektor, G. Hutsi, M. Kadastik, P. Panci, M. Raidal, F. Sala, and A. Strumia, *PPPC 4 DM ID: A Poor Particle Physicist Cookbook for Dark Matter Indirect Detection*, *JCAP* **03** (2011) 051, [`arXiv:1012.4515`]. [Erratum: JCAP 10, E01 (2012)].

[176] S. D. Thomas and J. D. Wells, *Phenomenology of Massive Vectorlike Doublet Leptons*, *Phys. Rev. Lett.* **81** (1998) 34–37, [`hep-ph/9804359`].

[177] E. J. Chun, J.-C. Park, and S. Scopel, *Non-perturbative Effect and PAMELA Limit on Electro-Weak Dark Matter*, *JCAP* **12** (2012) 022, [`arXiv:1210.6104`].

[178] H.-C. Cheng, B. A. Dobrescu, and K. T. Matchev, *Generic and chiral extensions of the supersymmetric standard model*, *Nucl. Phys. B* **543** (1999) 47–72, [`hep-ph/9811316`].

[179] I. Z. Rothstein and I. W. Stewart, *An Effective Field Theory for Forward Scattering and Factorization Violation*, *JHEP* **08** (2016) 025, [`arXiv:1601.0469`].

[180] P. Ciafaloni, D. Comelli, A. Riotto, F. Sala, A. Strumia, and A. Urbano, *Weak Corrections are Relevant for Dark Matter Indirect Detection*, *JCAP* **03** (2011) 019, [`arXiv:1009.0224`].

[181] J. A. M. Vermaseren, *Axodraw*, *Comput. Phys. Commun.* **83** (1994) 45–58.

[182] D. Binosi and L. Theussl, *JaxoDraw: A Graphical user interface for drawing Feynman diagrams*, *Comput. Phys. Commun.* **161** (2004) 76–86, [`hep-ph/0309015`].

[183] C. R. Harris, K. J. Millman, S. J. van der Walt, R. Gommers, P. Virtanen, D. Cournapeau, E. Wieser, J. Taylor, S. Berg, N. J. Smith, R. Kern, M. Picus, S. Hoyer, M. H. van Kerkwijk, M. Brett, A. Haldane, J. F. del R'ıo, M. Wiebe, P. Peterson, P. G'erard-Marchant, K. Sheppard, T. Reddy, W. Weckesser, H. Abbasi, C. Gohlke, and T. E. Oliphant, *Array programming with NumPy*, *Nature* **585** (Sept., 2020) 357–362.

[184] W. R. Inc., “Mathematica, Version 12.2.” Champaign, IL, 2020.

[185] J. D. Hunter, *Matplotlib: A 2d graphics environment*, *Computing in Science & Engineering* **9** (2007), no. 3 90–95.